DISSERTATION

submitted to the
Combined Faculties for the Natural Sciences and Mathematics
of the Ruperto-Carola-University of Heidelberg, Germany
for the degree of

Doctor of Natural Sciences

put forward by

M.Sc. Philippe d'Argent

born in Stuttgart

Oral examination: July 3th, 2019

Probing the Standard Model flavor structure with hadronic beauty and charm decays

Referees:
Prof. Dr. Ulrich Uwer
Prof. Dr. Tilman Plehn

Abstract

This dissertation investigates hadronic multi-body decays of beauty and charm mesons providing insights into both the CKM sector of the Standard Model and strong interaction dynamics at the hadronic energy scale. First, the resonant substructure of the decay $D^0 \to \pi^+\pi^-\pi^+\pi^-$ is studied. Quantum-entangled $D^0\bar{D}^0$ pairs produced in electron-positron collisions are used. The data sample corresponds to an integrated luminosity of $818\,\text{pb}^{-1}$ recorded by the CLEO-c detector. An amplitude analysis exploiting the full information provided by the five-dimensional phase space is performed to disentangle the various intermediate-state components and measure their relative phases. The global decay-rate asymmetry between D^0 and $\overline{D}^0$ decays is measured and a search for *CP* asymmetries in the amplitude components is conducted; no evidence for *CP* violation is found. The fractional *CP*-even content and related hadronic parameters are derived from the amplitude model and found to be consistent with model-independent measurements. These hadronic parameters are crucial input for a future measurement of the *CP*-violating phase γ in $B^\pm \to (D \to \pi^+\pi^-\pi^+\pi^-)K^\pm$ decays, where D represents a superposition of D^0 and $\bar{D}^0$ mesons. With currently existing proton-proton collision data collected by the LHCb experiment, a precision of around $\sigma(\gamma) \approx 12^\circ$ can be achieved, competitive with the most precise single measurement of the CKM angle γ to date. Second, hadronic multi-body decays of B_s^0 mesons are studied using proton-proton collision data corresponding to $7\,\text{fb}^{-1}$ recorded by the LHCb detector. The $B_s^0 - \overline{B}_s^0$ oscillation frequency is measured from flavor-specific $B_s^0 \to D_s^-\pi^+\pi^+\pi^-$ decays to be $\Delta m_s = (17.7651 \pm 0.0084\,(\text{stat}) \pm 0.0058\,(\text{syst}))\,\text{ps}^{-1}$, consistent with and significantly more precise than the current world-average value. Mixing-induced *CP* violation in $B_s^0 \to D_s^\pm K^\mp\pi^\pm\pi^\mp$ decays is explored by means of a time-dependent amplitude analysis. The weak phase difference between $B_s^0 \to D_s^- K^+\pi^+\pi^-$ and $\overline{B}_s^0 \to D_s^- K^+\pi^+\pi^-$ decays is determined to be $\gamma = (60 \pm 17(\text{stat+syst}))^\circ$; the most precise measurement of this quantity in the B_s meson system.

Zusammenfassung

In dieser Dissertation werden hadronische Mehrkörperzerfälle von Beauty- und Charm-Mesonen untersucht, welche neue Erkenntnisse über den CKM-Mechanismus des Standard Models und die Dynamik der starken Wechselwirkung bei niedrigen Energien liefern. Zunächst wird die Resonanzstruktur des Zerfalls $D^0 \to \pi^+\pi^-\pi^+\pi^-$ studiert. Dafür werden quantenverschränkte $D^0\bar{D}^0$ Paare verwendet, die in Elektron-Positron Kollisionen produziert wurden. Der Datensatz entspricht einer integrierten Luminosität von $818\,\mathrm{pb}^{-1}$ und wurde mit dem CLEO-c Detektor aufgenommen. Um die verschiedenen Zwischenzustände zu trennen und ihre relativen Phasen zu bestimmen wird eine Amplituden Analyse durchgeführt, welche die gesamte Information des fünf dimensionalen Phasenraums ausnutzt. Es werden die Zerfallsraten von D^0 und $\overline{D}^0$ Mesonen verglichen, um nach einer Verletzung der *CP*-Symmetrie in den Amplituden-Komponenten zu suchen, wobei keine keine signifikanten Asymmetrien gefunden werden. Hadronische Parameter werden mit Hilfe des entwickelten Amplituden-Models berechnet und mit model-unabhängigen Messungen verglichen. Die Resultate erlauben eine zukünftige Bestimmung der *CP*-verletzenden Phase γ in $B^\pm \to (D \to \pi^+\pi^-\pi^+\pi^-)K^\pm$ Zerfällen, wobei D eine Superposition von D^0 and $\bar{D}^0$ Mesonen repräsentiert. Mit den aktuell vorhandenen Proton-Proton Kollisionsdaten, die mit dem LHCb Detektor aufgezeichnet wurden, ist eine Präzision von $\sigma(\gamma) \approx 12^\circ$ erreichbar, vergleichbar mit der besten Einzelmessung des CKM-Winkels γ. Des weiteren wird eine Studie von hadronischen Mehrkörperzerfällen von B_s Mesonen beim LHCb Experiment vorgestellt. Proton-Proton Kollisionsdaten, die einer integrierten Luminosität von $7\,\mathrm{fb}^{-1}$ entsprechen, werden verwendet. Die $B_s^0 - \overline{B}_s^0$ Oszillationsfrequenz wird von $B_s^0 \to D_s^-\pi^+\pi^+\pi^-$ Zerfällen bestimmt. Der gemessene Wert, $\Delta m_s = (17.7651 \pm 0.0084\,(\mathrm{stat}) \pm 0.0058\,(\mathrm{syst}))\,\mathrm{ps}^{-1}$, ist in Übereinstimmung mit dem Weltdurchschnittswert und erheblich präziser. Durch Mischung bedingte *CP*-Verletzung im Zerfall $B_s^0 \to D_s^\pm K^\mp\pi^\pm\pi^\mp$ wird mittels einer zeitabhängigen Amplituden Analyse erforscht. Die gemessene relative schwache Phase zwischen den $B_s^0 \to D_s^- K^+\pi^+\pi^-$ und $\overline{B}_s^0 \to D_s^- K^+\pi^+\pi^-$ Zerfallsamplituden beträgt: $\gamma = (60 \pm 17(\mathrm{stat+syst}))^\circ$, welches die präziseste Messung dieses Parameters im B_s Meson System darstellt.

Preface

The analysis of $D \to \pi\pi\pi\pi$ decays uses the CLEO-c legacy data set and as such would not have been possible without the work of many former members of the CLEO collaboration. The reconstruction of the decays and the production of simulated data have been performed by Dr. Paras Naik (a former CLEO member) and Dr. Jack Benton. The author of this thesis is the main person responsible for all subsequent analysis steps and the contact author of the resulting paper which has been been published by a peer reviewed journal [1].

The analysis of $B_s \to D_s\pi\pi\pi$ and $B_s \to D_sK\pi\pi$ decays has been carried out by the author within the LHCb collaboration which implies the usage of common software to analyze the collected data. The author and a second Ph.D. student are the main contributors to the analysis. Every step of the analysis has been performed by the author. The reconstruction and selection of the decays and studies of the decay-time acceptance, decay-time resolution as well as production and detection asymmetries were performed together with the second Ph.D. student. The implementation of the (phase-space integrated) decay-time fit and the full time-dependent amplitude fit was exclusively developed by the author. He was also the main person responsible for the evaluation of the systematic uncertainties. A more technical description is available in an internal LHCb note [2].

The author was member of the Outer-Tracker detector group, where he contributed to the operation during data-taking and improved the time alignment of the detector. The author also performed measurements of performance characteristics such as the spatial resolution. These studies are not part of this thesis but are documented in a paper published by a peer reviewed journal [3], where the author of this thesis is one of the main authors.

Where has all the Antimatter gone?

"We are trying to prove ourselves wrong as quickly as possible, because only in that way can we find progress."

– Richard P. Feynman, 1965

Our current understanding of the subatomic universe is encapsulated in the Standard Model of particle physics which has been remarkably successful in predicting various phenomena with astonishing precision. Since completing the Standard Model picture with the discovery of the Higgs boson in 2012, a new era of searches for physics beyond the established theory has been heralded. As triumphant as the Standard Model might be, it fails to answer such fundamental questions as the origin of our very existence. If equal amounts of matter and antimatter were created at the big bang, where has all the antimatter gone? Why did matter survive their mutual annihilation process and not antimatter? Other cosmological concerns are the existence of dark matter and dark energy accounting for nearly 95% of the energy content in the universe, whose origins and nature are not explained either. It is thus a common conviction that the Standard Model is only a low energy approximation of a more fundamental theory. Several generations of particle colliders have been built to test the Standard Model with ever increasing precision, eventually provoking its breakdown. Direct searches for new heavy particles produced as collision products lead to important breakthroughs such as the discoveries of the charmonium resonance J/ψ, the electroweak gauge boson Z^0 or the Higgs boson. A complementary and more subtle method compares precisely measured decay properties of heavy-flavored hadrons to theory expectations. Such indirect approaches predicted the charm, beauty and top quarks long before their direct observation and were essential for the development of the theory as we know it today. Within the Standard Model, transitions between quarks are described by the Cabibbo-Kobayashi-Maskawa (CKM) matrix through their weak interaction. The CKM matrix is unitary implying that the number of quarks is conserved and that there are exactly three

generations of quarks. The unitarity condition can be displayed in the form of a triangle in the complex plane, known as the Unitarity Triangle. The sides of the triangle (magnitudes of the CKM matrix elements) determine transition rates between quark species, whereas the angles (complex phases of the CKM matrix elements) introduce an asymmetry between the decay properties of particles and antiparticles, also referred to as charge-parity (CP) violation. Albeit the CKM mechanism formally introduces an intrinsic difference between particles and antiparticles, the amount of CP violation that can be accommodated is not enough to explain the observed predominance of matter over antimatter in the universe. Additional sources of CP violation must exist, entering through higher order quantum loops, where heavy and yet unknown particles can contribute even though their mass is far beyond the energy accessible for direct production. Measurements of decay rates and CP asymmetries in a variety of decay channels allow to over-constrain the CKM parameters and as such provide a sensitive probe of the Standard Model flavor structure. New physics phenomena beyond the Standard Model might reveal themselves as internal inconsistencies of the unitarity relation such as a non-closed Unitarity Triangle or disagreeing measurements of the same CKM parameter in different decay modes. The extraction of fundamental theory parameters from experimental data necessitates in many cases a description of the strong interaction responsible for confining quarks inside hadrons. However, the underlying field theory (quantum chromodynamics) is strongly coupled at the energy regime of hadrons such that conventional perturbative methods are not applicable. To validate alternative methods, including effective theories or phenomenological approaches, a profound experimental understanding of the hadronic spectrum is critical.

This thesis investigates the hadronic multi-body decays $D^0 \to \pi^+\pi^-\pi^+\pi^-$ and $B_s^0 \to D_s^\pm K^\mp \pi^\pm \pi^\mp$ using electron-positron collision data recorded by the CLEO-c detector and proton-proton collision data recorded by the LHCb detector, respectively. While the LHCb experiment profits from the huge heavy quark production cross-section, charm mesons collected at the CLEO-c experiment have unique properties; they are produced in quantum-entangled $D^0\bar{D}^0$ pairs which allows the measurement of hadronic parameters free from theoretical uncertainties. The rich phenomenology of hadronic charm and beauty meson decays is outlined in Part I. After briefly introducing the Standard Model, the connection between weak and strong interaction dynamics is drawn which is essential to link experimental observables to Standard Model parameters. Part II presents a detailed study of the resonant substructure of $D^0 \to \pi^+\pi^-\pi^+\pi^-$ decays. The various intermediate-state

contributions are disentangled based on the spin-dependent angular distributions of the decay products, a technique known as amplitude (or Dalitz plot) analysis. Knowledge of the hadronic part allows the measurement of the *CP*-violating phase γ from $B^{\pm} \to (D \to \pi^+\pi^-\pi^+\pi^-)K^{\pm}$ decays (where D represents a superposition of D^0 and $\bar{D}^0$ mesons), which remains the least well constrained CKM angle of the Unitarity Triangle. The sensitivity of this approach, exploiting the copious amount of beauty hadrons collected at the LHCb experiment, is discussed. The excellent time resolution of the LHCb detector also permits studying the dynamics of B_s^0 meson decays as detailed in Part III. Neutral mesons can oscillate into their antiparticle counterparts via quantum loop processes opening additional mechanisms for *CP* symmetry breaking. The $B_s^0 - \overline{B}_s^0$ oscillation frequency is measured from flavor-specific $B_s^0 \to D_s^-\pi^-\pi^+\pi^-$ decays, which can be related to one side of the Unitarity Triangle. Subsequently, the *CP* violating phase $\gamma - 2\beta_s$ is extracted from $B_s^0 \to D_s^{\pm}K^{\mp}\pi^{\pm}\pi^{\mp}$ decays by means of a time-dependent amplitude analysis.

Contents

Part I

MATTER, ANTIMATTER AND THEIR TINY DIFFERENCE

CP violation in the Standard Model

1

This chapter introduces the fundamental theory and formalism on which the presented analyses are based. A thorough description is not intended and the following discussion merely scratches the surface of the *Standard Model,* which builds the foundation of modern particle physics, focusing on the aspects most relevant for this thesis; more in-depth introductions can be found in the literature, *e.g.* in Reference [4]. The formation of bound states and their spectroscopic classification are expounded followed by a discussion of the origin of matter-antimatter asymmetries and its manifestation in experimental observations.

1.1 Particle physics in a nutshell

The Standard Model is a quantum field theory that combines the *electromagnetic*, *weak* and *strong* interactions and as such provides the most complete description of the known elementary particles and their mutual interactions to date [5–7]. Despite enormous efforts, the most familiar force influencing our everyday life, gravity, is not yet incorporated. Moreover, several cosmological observations [8, 9] require the existence of dark matter and dark energy which are not explained by the Standard Model. Neither is the apparent matter-antimatter asymmetry in the universe. Nonetheless, the Standard Model delivers precise predictions at the minuscule scale of elementary particles, where it so far withstand all experimental challenges. Natural units with $\hbar = c = 1$ are used throughout the thesis.

Fundamental particles

The fundamental building blocks of matter are particles with half-integer spin which occur in two basic types called *quarks* and *leptons*, collectively referred to as *fermions*. They can be further categorized in three generations or *flavors*. Each quark generation consists of a quark with fractional electric charge[1] of $+\frac{2}{3}e$, named *up* (u), *down* (d) and *charm* (c) quark, and a quark of electric charge $-\frac{1}{3}e$,

[1] The electric charges is defined in units of the proton charge, $e \approx 1.6 \cdot 10^{-19}\,\mathrm{C}$ [10]

named *down* (d), *strange* (s) and *bottom* or *beauty* (b) quark. A pair of leptons, one with integer electric charge (*electron* e^-, *muon* μ^-, *tauon* τ^-) and an associated uncharged *neutrino* (ν_e, ν_μ, ν_τ), completes each fermion generation. The particles belonging to the first generation build up all stable matter in the universe, while fermions of the other generations are essentially heavier replicas which rapidly decay into their lighter counterparts. For each fermion a corresponding antiparticle having the same mass but opposite additive quantum numbers (such as the electric charge or quantum numbers related to lepton and quark-flavour) exists.

Interactions between the fermions are mediated by force carriers of integer spin, called *bosons*. The most familiar one of those, the *photon*, mediates the electromagnetic force and is thus responsible for binding atoms and molecules together. The photon couples to electric charge, itself being electrically neutral. Electromagnetic interactions have an infinite range due to the fact that the photon is massless. The weak force, on the other hand, mediated by the massive $W^\pm$ and Z^0 bosons, is effective only over a very short range ($\approx 10^{-18}\,\mathrm{m}$). Quarks can change their flavor exclusively via the weak interaction, the rich phenomenology of which plays a central role in this thesis and is discussed in more detail in the succeeding sections. To give a generally known example at this point, the weak force is responsible for radioactive processes such as the nuclear β-decay. The strong force is what bounds quarks in composite structures such as the proton. This happens via the exchange of (massless) *gluons* which couple to *color* charge (red, blue, green). Unlike quarks and gluons, leptons do not carry color charge such that they do not participate in strong interactions. The color charge of the gluons enables gluon-gluon couplings. At low energies, these gluon self interactions lead to a phenomenon called (color) *confinement* which implies that isolated quarks cannot be observed. Instead, quarks bind together in color-neutral[2] bound states, called *hadrons*. At the energy scale of hadrons, the theory of strong interactions, *quantum chromodynamics* (QCD), cannot be solved with perturbative methods. Thus, the prediction of hadronic properties relies on numerical calculations on a discrete space-time lattice (*lattice QCD* [11]), effective theories [12,13] or phenomenological approaches [14–16]. At high energies, quarks become asymptotically free eventually forming a quark-gluon plasma.

[2]Either the combination of a color with its respective anti-color or the combination of all three (anti-) colors result in a color-neutral state.

Symmetries

Considering symmetries of nature has always been a central, maybe the most fundamental, concept of physics. Noether's theorem states that each continuous symmetry leads to a conserved quantity [17]. The most prominent examples, known from classical mechanics, are the invariance of physical laws under translations in time, space or under spatial rotations which imply energy, momentum and angular momentum conservation, respectively. In the context of quantum field theory, electric and color charge conservation arise as consequence of the gauge invariance of the Standard Model Lagrangian. There are also three discrete symmetries which were long thought to be exact symmetries of nature: the *parity* transformation (P) inverts the spacial coordinates, $\vec{x}$, of a physical system with respect to the origin, $(t, \vec{x}) \xrightarrow{P} (t, -\vec{x})$; the *time inversion* ($T$) transformation reverses time, t, $(t, \vec{x}) \xrightarrow{T} (-t, \vec{x})$ and the *charge-conjugation* (C) effectively transforms particles into their antiparticle partners by changing the signs of all additive quantum numbers. A twofold application of these operations leads to the original state. Possible eigenvalues of the corresponding operators are thus $\eta_O = +1$ (*even*) or $\eta_O = -1$ (*odd*) with $O = \{C, P, T\}$. Provided that the physical system is invariant under a given discrete symmetry, the respective eigenvalue is conserved (in the form of a multiplicative quantum number). Both electromagnetic and strong interactions are invariant under each transformation individually. Parity violation in weak interactions was first observed in the Wu experiment [18], where electrons originating from the reaction ${}^{60}_{27}\mathrm{Co} \rightarrow {}^{60}\mathrm{Ni}^{*}\, e^{-}\, \nu_e$ are preferentially emitted in the direction opposite to the spin of the nuclei. Indeed, the weak force violates both C and P transformations maximally as it couples only to left-handed[3] particles and right-handed antiparticles. The combined CP operator transforms left-handed particles into right-handed antiparticles and was hence believed to be a symmetry of the weak interactions. However, as first demonstrated in the neutral kaon system [19], it is not. In fact, *CP* violation is one of the necessary conditions to explain the observed imbalance between matter and antimatter in the universe, formally known as baryogenesis [20]. While the origin of *CP* violation within the Standard Model is well established, as explored in the next section, an asymmetry ten million times larger than accommodated is required to explain the excess of matter in the universe [21]. This fact points to additional *CP* violating processes originating from physics beyond the Standard Model and precise measurements of *CP*-violating observables might reveal such effects.

[3] The handedness of a particle refers to the chirality which might be considered as a Lorentz-invariant version of the helicity, defined as the projection of the particle's spin onto its momentum vector. In the massless limit they coincide.

Mesonic spectrum

The internal structure of hadrons comprises a complicated interplay between *valence* quarks, which define the basic properties of the hadron such as spin and parity, as well as virtual quark antiquark pairs and virtual gluons, also called *sea* quarks and gluons. Hadrons are categorized in two main types according to their valence quark content [16]: *mesons* are composed of one quark and one antiquark ($q\bar{q}$), *baryons* are formed from three quarks (qqq) or three antiquarks ($\bar{q}\bar{q}\bar{q}$). Other more exotic combinations, such as *tetraquark* ($qq\bar{q}\bar{q}$) or *tpentaquark* states ($qqqq\bar{q}$ or $\bar{q}\bar{q}\bar{q}\bar{q}q$), are supported by the theory [16] as well and recent experimental evidence points towards their existence [22–24]. The precise nature of these states is yet unclear and further studies are necessary for an established interpretation.

Despite the rather limited combinatoric possibilities to form quark antiquark pairs out of six quark species, there is, in fact, a plethora of mesonic states realized in nature. This can be understood in analogy to the spectral emission spectrum of the hydrogen atom. The energy levels of the hydrogen atom are a result of the electromagnetic force, whereas the mesonic spectrum is caused by the strong interaction. The constituent quark model explains the existence of distinguishable mesonic states having the same quark content as a result of the spin dynamics between the valence quarks [25]. The intrinsic spins of the two quarks can either be parallel or antiparallel leading to a total spin of $S = 1$ or $S = 0$. Besides that, the di-quark system can also exhibit an orbital excitation depending on the relative angular momentum between the quarks, $L = \{0, 1, 2, \dots\}$, which is related to the parity of the hadron via the relation $P = (-1)^{L+1}$. Angular momentum configurations with $L = \{0, 1, 2\}$ are also called S-,P- and D-wave, respectively. The spin and angular momentum couple to a state of total angular momentum, J, taking on values from $|L - S|$ to $|L + S|$ in integer steps. There is also a radial excitation possible, denoted by the quantum number $N = \{1, 2, \cdots\}$, which leads to recurrences of mesonic states with higher mass but otherwise identical spin-orbit configuration. The quasi-stable ground states exhibit the energetically most favorable configuration, $J = L = S = 0$ and $N = 1$, and are denoted as pseudoscalars. These include the pion $\pi^+(u\bar{d})$, kaon $K^+(u\bar{s})$, the charm meson $D^0(c\bar{u})$, the charm-strange meson $D_s^+(c\bar{s})$, the beauty mesons $B^0(d\bar{b})$ and $B^+(u\bar{b})$ as well as the beauty-strange meson $B_s^0(s\bar{b})$; all of which are of particular importance for the presented analyses. The following convention is used throughout the thesis to refer to both a particle and its antiparticle: $\pi = \{\pi^+, \pi^-\}$, $K = \{K^+, K^-\}$, $D = \{D^0, \bar{D}^0\}$, $D_s = \{D_s^+, D_s^-\}$, $B_d = \{B^0, \bar{B}^0\}$, $B_u = \{B^+, B^-\}$ and $B_s = \{B_s^0, \overline{B}_s^0\}$. The spectroscopic classifications of mesons is generally based on their total angular momentum and parity and the naming convention is summarized in Table 1.1.

Table 1.1: Spectroscopic classification of mesons.

Type	**Notation**	$\boldsymbol{J^P}$
scalar	S	0^+
pseudoscalar	P	0^-
vector	V	1^-
axial vector	A	1^+
tensor	T_+	2^+
pseudotensor	T_-	2^-

1.2 Quark flavor transitions

Within the Standard Model, the sole[4] source of *CP* violation is accommodated in the *Cabibbo-Kobayashi-Maskawa* (CKM) quark-mixing matrix, V_{CKM} [28, 29]. It describes how quarks couple in flavor-changing processes mediated by the weak charged-current interaction. The transition probability of an up-type quark q to a down-type quark q' via exchange of a $W^\pm$ boson, $q \to W^\pm q'$, is proportional to the matrix element $V_{qq'}$ (squared). The values of these complex matrix elements are not predicted by the Standard Model. However, they are not independent since the CKM matrix is unitary, by construction, and four physical degrees of freedom are sufficient to fully describe it. As experimentally a hierarchical structure is established, it is convenient to express the CKM matrix in terms of an expansion parameter $\lambda \approx 0.2$ and three real parameters[5] A, ρ and η [28, 31]:

$$V_{\mathrm{CKM}} = \begin{pmatrix} V_{ud} & V_{us} & V_{ub} \\ V_{cd} & V_{cs} & V_{cb} \\ V_{td} & V_{ts} & V_{tb} \end{pmatrix} = \begin{pmatrix} 1 - \frac{\lambda^2}{2} & \lambda & A\lambda^3(\rho - i\eta) \\ -\lambda & 1 - \frac{\lambda^2}{2} & A\lambda^2 \\ A\lambda^3(1 - \rho - i\eta) & -A\lambda^2 & 1 \end{pmatrix} + \mathcal{O}(\lambda^4). \tag{1.1}$$

From this so-called *Wolfenstein parameterization* it is obvious that transitions within a generation are favored while transitions between two different generations are suppressed by powers of λ. The CKM matrix elements transform under the *CP* conjugation into their complex conjugates, $V_{qq'} \overset{CP}{\to} V^*_{qq'}$, and, as such, provide *the* gateway to *CP* violation in the Standard Model by means of their complex phases.

[4] There is another possible source of *CP* violation in strong interactions, however it is observed to be negligibly small, known as the strong *CP* problem [26, 27].

[5] The Wolfenstein parameters are experimentally constrained to be $\lambda = 0.224747^{+0.000254}_{-0.000059}$, $A = 0.8403^{+0.0056}_{-0.0201}$, $\bar{\rho} = 0.1577^{+0.0096}_{-0.0074}$ and $\bar{\eta} = 0.3493^{+0.0095}_{-0.0071}$, where $\bar{\rho} = \rho(1 - \lambda^2/2) + \mathcal{O}(\lambda^4)$ and $\bar{\eta} = \eta(1 - \lambda^2/2) + \mathcal{O}(\lambda^4)$ [30].

Unitarity Triangle

The unitarity of the CKM matrix, $V_{\mathrm{CKM}}^{\dagger} V_{\mathrm{CKM}} = 1$, imposes nine conditions. Three of them enforce the total probability of an up-type quark to convert to any down-type quark to be unity, *e.g.* $|V_{ud}|^2 + |V_{us}|^2 + |V_{ub}|^2 = 1$. The others imply that the products of different rows and columns must vanish and can be displayed as closed triangles in the complex plane. Most famous is the triangle, depicted in Figure 1.1, which derives from the condition $V_{ud}V_{ub}^* + V_{cd}V_{cb}^* + V_{td}V_{tb}^* = 0$, known as the *Unitarity Triangle*. It is experimentally (comparably) well accessible from decays of beauty hadrons (as detailed in Chapter 3) and all sides are of similar magnitude, λ^3. The angles of the Unitarity Triangle are defined in terms of the CKM matrix elements as:

$$\alpha \equiv \arg\left(-\frac{V_{td}V_{tb}^*}{V_{ud}V_{ub}^*}\right), \quad \beta \equiv \arg\left(-\frac{V_{cd}V_{cb}^*}{V_{td}V_{tb}^*}\right), \quad \gamma \equiv \arg\left(-\frac{V_{ud}V_{ub}^*}{V_{cd}V_{cb}^*}\right). \tag{1.2}$$

In the Wolfenstein parameterization up to order $\mathcal{O}(\lambda^4)$ all CKM matrix elements are real except for V_{td} and V_{ub}, whose arguments can be identified with the angles β and γ. Including an additional order in λ, also V_{ts} develops a small imaginary part. This allows to write the CKM matrix as follows:

$$V_{CKM} = \begin{pmatrix} |V_{ud}| & |V_{us}| & |V_{ub}|e^{-i\gamma} \\ -|V_{cd}| & |V_{cs}| & |V_{cb}| \\ |V_{td}|e^{-i\beta} & -|V_{ts}|e^{i\beta_s} & |V_{tb}| \end{pmatrix} + \mathcal{O}(\lambda^5), \tag{1.3}$$

where the angle[6] β_s is defined as $\beta_s \equiv arg\,(V_{ts}V_{tb}^*/(V_{cs}V_{cb}^*))$.

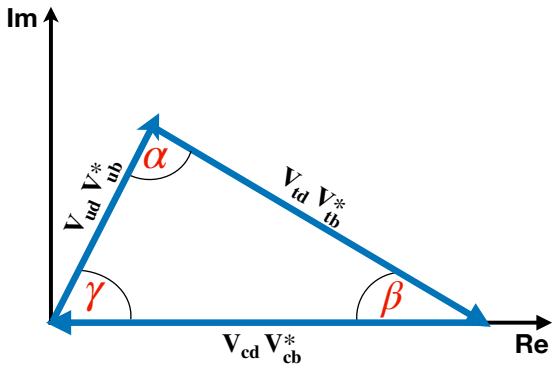

Figure 1.1: The Unitarity Triangle of the CKM matrix, derived from the condition $V_{ud}V_{ub}^* + V_{cd}V_{cb}^* + V_{td}V_{tb}^* = 0$, showing the definition of the CKM angles α, β and γ.

[6]The angle β_s does not appear in the Unitarity Triangle but in the so-called B_s-triangle formed from the second and third columns of the CKM matrix and is relevant for B_s meson mixing discussed later.

1.3 Neutral meson mixing

The neutral meson system exhibits the fascinating property of spontaneous transitions between particle and antiparticle, a phenomenon called *flavor mixing*. As the Standard Model does not allow for flavor-changing neutral currents at first-order perturbation theory (*tree-level* transitions), higher order transitions, known as *loop* processes, are required. An example is given in Figure 1.2, where two $W^{\pm}$ bosons are exchanged leading to the conversion of a B_s^0 meson to a $\bar{B}_s^0$ meson. This special kind of loop process is also called a *box-diagram* transition. All quark generations can contribute as virtual particles to the loop. Even heavy particles such as the top quark can participate through Heisenberg's uncertainty principle [32], notwithstanding that the energy might not be sufficient to directly produce them. The internal quarks may also hadronize leading to non-perturbative mixing processes via intermediate states accessible to both B_s^0 and $\bar{B}_s^0$ mesons, for example $B_s^0 \to D_s^- D_s^+ \to \overline{B}_s^0$. For the following discussion, the flavor eigenstates of the neutral mesons K^0, D^0, B^0 and B_s^0 are collectively referred to as P^0 and their antiparticles as $\bar{P}^0$, *e.g.* $P^0 = B_s^0 = |\bar{b}s\rangle$ and $\bar{P}^0 = \bar{B}_s^0 = |b\bar{s}\rangle$. These eigenstates of the strong interaction are not simultaneously eigenstates of the weak interaction. Their time-development can be described by an effective Schrödinger equation [33, 34]:

$$-i\frac{\partial}{\partial t}\begin{pmatrix}|P^0(t)\rangle\\|\bar{P}^0(t)\rangle\end{pmatrix} = (\mathbf{M} - \frac{i}{2}\mathbf{\Gamma})\begin{pmatrix}|P^0(t)\rangle\\|\bar{P}^0(t)\rangle\end{pmatrix}, \tag{1.4}$$

where $|P^0(t)\rangle$ $\left(|\bar{P}^0(t)\rangle\right)$ denotes the state of a meson at proper time t which was initially produced in a P^0 $\left(\bar{P}^0\right)$ flavor eigenstate and $\mathbf{M}$ and $\mathbf{\Gamma}$ are hermitian two-by-two matrices describing the mass and decay rate components[7] of the effective Hamiltonian, $\mathbf{H} = \mathbf{M} - \frac{i}{2}\mathbf{\Gamma}$. The off-diagonal matrix elements correspond to flavour-changing transitions, $P^0 \to \bar{P}^0$ and vice versa. Flavor-conserving processes are instead associated to the diagonal elements. The Hamiltonian itself is non-hermitian leading to complex eigenvalues. This in turn implies that the total probability is not conserved expressing the fact that the particle will eventually decay. The eigenstates of the effective Hamiltonian are an admixture of the flavor eigenstates,

$$|P_L\rangle = p|P^0\rangle + q|\bar{P}^0\rangle, \qquad |P_H\rangle = p|P^0\rangle - q|\bar{P}^0\rangle, \tag{1.5}$$

[7] The mass matrix, $\mathbf{M}$, and decay width matrix, $\mathbf{\Gamma}$, are associated to transitions via virtual (off-shell) and real (on-shell) intermediate states, respectively.

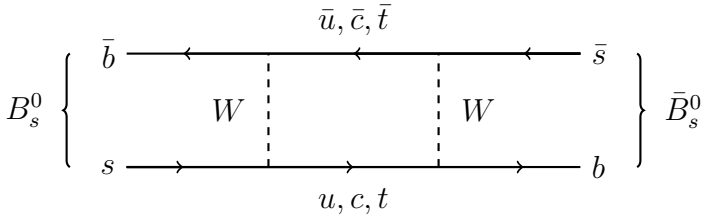

Figure 1.2: Leading order Feynman diagram of the $B_s^0 - \bar{B}_s^0$ mixing process.

where the complex coefficients are normalized to $|p|^2 + |q|^2 = 1$. The *light*, $|P_L\rangle$, and *heavy*, $|P_H\rangle$, mass eigenstates have distinct masses, m_L and m_H, and decay widths, Γ_L and Γ_H. Their arithmetic means and differences are denoted as:

$$\begin{aligned} m &= \frac{m_H + m_L}{2}, & \Gamma &= \frac{\Gamma_H + \Gamma_L}{2}, \\ \Delta m &= m_H - m_L, & \Delta\Gamma &= \Gamma_H - \Gamma_L. \end{aligned} \tag{1.6}$$

The convention is such that for the mass difference $\Delta m > 0$ holds, while the decay width difference can also be negative. The time development of the flavor eigenstates can be obtained by solving Equation 1.4 after diagonalization and inverting Equation 1.5:

$$\begin{aligned} |P^0(t)\rangle &= g_+(t)|P^0\rangle + \frac{q}{p}\, g_-(t)|\bar{P}^0\rangle \\ |\bar{P}^0(t)\rangle &= g_+(t)|\bar{P}^0\rangle + \frac{p}{q}\, g_-(t)|P^0\rangle, \end{aligned} \tag{1.7}$$

with the coefficients $g_\pm(t) = \frac{1}{2}\left(e^{-i\,m_L\,t}e^{-\Gamma_L/2\,t} \pm e^{-i\,m_H\,t}e^{-\Gamma_H/2\,t}\right)$. This means an initially produced pure P^0 or $\bar{P}^0$ meson will propagate in time as a superposition of flavor eigenstates. The probability to observe it, at proper time t, in a certain flavor eigenstate is given by:

$$\begin{aligned} \left|\langle P^0|P^0(t)\rangle\right|^2 &= e^{-\Gamma t}/2\,[\cosh(\Delta\Gamma/2\,t) + \cos(\Delta m\,t)] = \left|\langle \bar{P}^0|\bar{P}^0(t)\rangle\right|^2 \\ |\langle \bar{P}^0|P^0(t)\rangle|^2 &= \left|\frac{q}{p}\right|^2 e^{-\Gamma t}/2\,[\cosh(\Delta\Gamma/2\,t) - \cos(\Delta m\,t)] \\ |\langle P^0|\bar{P}^0(t)\rangle|^2 &= \left|\frac{p}{q}\right|^2 e^{-\Gamma t}/2\,[\cosh(\Delta\Gamma/2\,t) - \cos(\Delta m\,t)] \end{aligned} \tag{1.8}$$

A non-zero decay rate difference modulates the typical exponential decay law in form of a hyperbolic cosine term, whereas the mass difference can be identified as the oscillation frequency (also called *mixing frequency* for historic reasons) via which periodic transitions between the flavor eigenstates proceed. The characteristic mixing behaviors of the neutral meson systems relevant for this thesis are demonstrated in Figure 1.3. Neutral charm mesons show neither a sizable

	D^0	B^0	B_s^0
m[MeV]	1864.83 ± 0.05	5279.55 ± 0.26	5366.84 ± 0.30
$\tau[ps]$	0.4101 ± 0.0015	1.520 ± 0.004	1.509 ± 0.004
Δm[ps^{-1}]	$0.0095^{+0.0041}_{-0.0044}$	0.5065 ± 0.0019	17.757 ± 0.021
$\Delta\Gamma/\Gamma$	$+0.0129^{+0.0014}_{-0.0018}$	$+0.002 \pm 0.010$	-0.132 ± 0.008

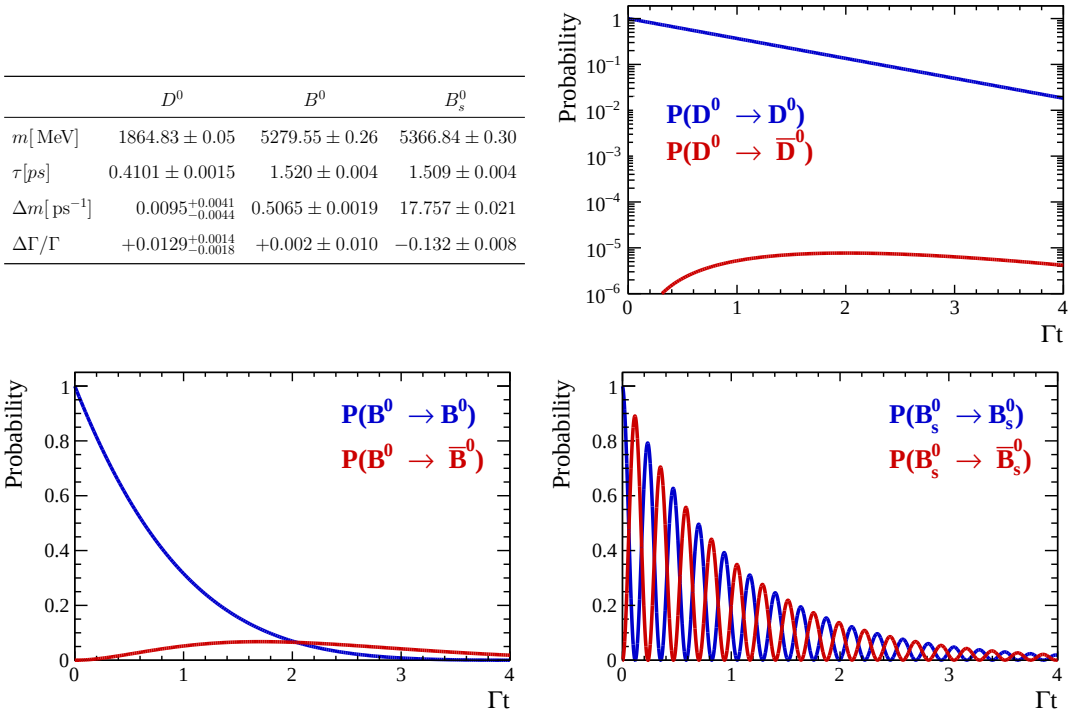

Figure 1.3: Probability to observe an initially pure D^0, B^0 or B_s^0 meson in a mixed (red) or unmixed (blue) state assuming $|q/p| = 1$. The mixing parameters, shown on the top left, are taken from Reference [35] and the mass values from Reference [10].

mass nor width difference and hence have hardly any chance to mix before they decay. In contrast, almost one quarter of neutral B^0 mesons change their flavor within their mean lifetime thanks to a large mass splitting. The B_s^0 meson exhibits not only the fastest oscillation frequency, more than 30 times larger than for B^0 mesons, but also a considerable decay width difference.

Without going into too much detail, the hierarchy of the mixing frequencies can be understood, qualitatively, by identifying the dominant contribution to the box-diagram transitions. The contributions of 'light' quarks, $q = \{u, d, c, s, b\}$, to loop processes are typically suppressed by a factor $\frac{m_q^2}{m_W^2} \ll 1\%$ [36], while top quark exchanges are enhanced with $\frac{m_t^2}{m_W^2} \approx 4.5$. These kinematic loop factors concur with the suppression due to the involved off-diagonal CKM matrix elements, in the following referred to as *Cabibbo suppression*. In case of charm mesons, only down-type quarks (d, s, b) can be exchanged in the loop. The contributions from down and strange quarks approximately cancel each other, historically known as the *Glashow-Iliopoulos-Maiani* (GIM) mechanism [37], and the mass of the beauty quark is not large enough to compensate its strong Cabibbo suppression. Box-diagram transitions of neutral beauty-flavored mesons are dominated by top

quark exchanges such that the mixing frequencies of the B^0 meson and B_s mesons are proportional to $\Delta m_d \propto |V_{td}V_{tb}|^2$ and $\Delta m_s \propto |V_{ts}V_{tb}|^2$, respectively. The ratio of the CKM elements gives $|V_{td}V_{tb}|^2/|V_{ts}V_{tb}|^2 \approx 22$ what corresponds roughly to the experimentally observed ratio, $\Delta m_s/\Delta m_d \approx 35$. A proper theory prediction gives the values [38]:

$$\Delta m_d^{\text{Theo}} = (0.528 \pm 0.078)\ \text{ps}^{-1}, \qquad \Delta m_s^{\text{Theo}} = (18.3 \pm 2.7)\ \text{ps}^{-1}, \tag{1.9}$$

in good agreement with the measured values given in Figure 1.3. The large theory uncertainties are dominated by non-perturbative QCD effects [38–40]. Unless these improve significantly, one cannot draw conclusions about the validity of the Standard Model from this comparison. Nevertheless, the experimental values of the mixing frequencies put tight constraints on various theories extending the Standard Model that typically include new heavy particles altering the loop-level transitions [41–44].

1.4 Manifestations of *CP* violation

The phenomenon of *CP* violation is intimately related to complex phases [45, 46]. Consider the decay of a (charged or neutral) particle P to the final state f and the *CP* conjugate process $\bar{P} \to \bar{f}$. The corresponding quantum-mechanical decay amplitudes can be written as [47, 48]:

$$A_f = A(P \to f) = |A|e^{i(\delta+\varphi)}, \qquad \bar{A}_{\bar{f}} = A(\bar{P} \to \bar{f}) = |A|e^{i(\delta-\varphi)}, \tag{1.10}$$

where the *CP*-odd (*weak*) phase φ originates from the complex CKM elements associated to the underlying quark-level transition and the *CP*-even (*strong*) phase δ results from gluon exchanges during the hadronization process. In multi-body decays, the strong phase is not constant but depends on the kinematic configuration of the final state particles (*phase space*) as detailed in the next chapter. All measurable quantities are proportional to the expectation values, $|A_f|^2$ and $|A_{\bar{f}}|^2$. This implies that there must be at least two decay paths to the same final state in order to generate *CP* violation. The total amplitude is then given by the coherent sum over the decay channels:

$$A_f = |A_1|e^{i(\delta_1+\varphi_1)} + |A_2|e^{i(\delta_2+\varphi_2)}, \quad \bar{A}_{\bar{f}} = |A_1|e^{i(\delta_1-\varphi_1)} + |A_2|e^{i(\delta_2-\varphi_2)}. \tag{1.11}$$

If both the weak phases, φ_1 and φ_2, and the strong phases, δ_1 and δ_2, are different, the interference between the decay channels leads to a *CP* asymmetry:

$$|A_f|^2 - |A_{\bar{f}}|^2 = -4\,|A_1|\,|A_2|\,\sin(\delta_1 - \delta_2)\sin(\varphi_1 - \varphi_2)\,. \tag{1.12}$$

A non-zero weak phase difference requires decay paths with a distinct flavor structure. For instance, both $b \to c$ and $b \to u$ quark-level transitions may lead to the same final state, in which case the weak phase difference is given by: $\varphi_1 - \varphi_2 = \arg(V_{cb}\, V_{ub}) \approx -\gamma$. The *CP* conjugate process has the weak phase difference $\arg(V_{cb}^*\, V_{ub}^*) \approx +\gamma$. Hence, measured *CP* asymmetries can be related to the CKM angles, provided that the strong and weak phases can be disentangled. The procedure is concretized in Chapter 3, after discussing the phenomenology of the strong phase contribution in Chapter 2.

The condition $|A_f|^2 \neq |A_{\bar{f}}|^2$ is also known as *CP* violation *in decay* or *direct CP* violation [46, 49]. For neutral particles, two additional mechanisms leading to *CP* symmetry breaking are accessible. These are collectively referred to as *mixing-induced* or *indirect CP* violation [19, 50–52]. The first kind is called *CP* violation *in mixing* and leads to different $P^0 \to \bar{P}^0$ and $\bar{P}^0 \to P^0$ mixing probabilities (independent of the final state). As evident from Equation 1.8, this requires $|q/p| \neq 1$. If the final state f can be reached by both P^0 and $\bar{P}^0$ flavor states, another type of *CP* violation can arise through the interference between the direct decay $P^0 \to f$ and the decay after mixing $P^0 \to \bar{P}^0 \to f$. A weak phase can be introduced by the mixing process, $\arg(q/p) \neq 0$, or via a *CP*-odd phase between the decay amplitudes $A_f = A(P \to f)$ and $\bar{A}_f = A(\bar{P} \to f)$. The condition for *CP* violation in the *interference of mixing and decay* can be summarized to $\arg(q/p\, A_f/\bar{A}_f) \neq 0$. This is the most complex case and is further clarified in Chapter 3 with a concrete example.

Phenomenology of hadronic multi-body decays

2

This chapter develops the formalism necessary to investigate hadronic interactions occurring in the multi-body decays under study, $D \to \pi\pi\pi\pi$ and $B_s \to D_s K\pi\pi$. First, general considerations on the decay rates and phase-space observables are discussed. It is then outlined how the numerous short-lived resonances contributing as intermediate states to the visible phase-space distribution can be distinguished based on the characteristic angular distributions of the final-state particles. For simplicity the formalism is introduced for three-body decays and generalizations to four-body final states are indicated where necessary.

2.1 Decay rates and phase space

Consider the generic case of an initial particle with mass m_0 and four-momentum p_0 which decays into n particles with masses m_i and four momenta $p_i = (E_i, \vec{p}_i)$, $(i = 1, 2, \ldots, n)$. The rate Γ at which this transition proceeds follows from Fermi's golden rule [4, 53]:

$$\Gamma = \frac{1}{2m_0} \int |A|^2 \, \mathrm{d}\phi_n, \tag{2.1}$$

where the quantum-mechanical amplitude, A, describes the interaction dynamics. The n-body phase-space element, defined as [54]:

$$\mathrm{d}\phi_n = (2\pi)^{4-3n} \, \delta^4 \left(p_0 - \sum_{i=1}^{n} p_i \right) \prod_{i=1}^{n} \mathrm{d}^4 p_i \, \delta(p_i^2 - m_i^2) \,, \tag{2.2}$$

is a measure of how many distinct final-state configurations are kinematically possible. Equation 2.2 indicates that there are $4n$ possible degrees of freedom, manifested in the four-momenta of the final-state particles. They are not independent and must obey four-momentum conservation that removes four redundant degrees of freedom. Knowledge of the final-state particle rest masses removes one additional degree of freedom per particle. In the context of this thesis, only decays of a pseudoscalar particle to an all pseudoscalar final state are relevant. Absence

of spin in both initial and final state implies that there is no preferred direction in space such that the superfluous overall orientation of the system (three degrees of freedom) can be integrated out. The remaining set of $3n-7$ independent phase-space observables, $\mathbf{x}$, unambiguously describe the kinematics of the decay. It is instructive to rewrite the phase-space element, in terms of these observables, as $\mathrm{d}\phi_n = \phi_n(\mathbf{x})\,\mathrm{d}\mathbf{x}$ [54]. Here, the phase-space density, $\phi_n(\mathbf{x})$, results from the integration over the delta functions in Equation 2.2. It expresses, pictorially, the fact that some regions of the phase space might be favored (or disfavored) due to kinematic constrains. Convenient choices for the phase-space observables are the invariant mass combinations of the final-state particles, $m^2_{ij} = (p_i + p_j)^2$ and $m^2_{ijk} = (p_i + p_j + p_k)^2$. In contrast to the full four-momenta used in Equation 2.2, these observables provide a more intuitive description of the decay as illustrated in the following.

Dalitz plots

Let the decay $D^0 \to \pi^+\pi^-\pi^0$ serve as a vivid example of a three-body decay. Two invariant mass (squared) combinations, *e.g.* $\mathbf{x} = (m^2_{\pi^+\pi^-}, m^2_{\pi^+\pi^0})$, are sufficient to describe the phase space fully. The phase-space density is constant in terms of these phase-space observables such that the differential decay rate takes the simple form [54]:

$$\mathrm{d}\Gamma \propto |\mathcal{A}(m^2_{\pi^+\pi^-}, m^2_{\pi^+\pi^0})|^2\,\mathrm{d}m^2_{\pi^+\pi^-}\,\mathrm{d}m^2_{\pi^+\pi^0}\,. \tag{2.3}$$

This expression suggests to visualize the decay dynamics in a scatter plot spanned by the two invariant mass combinations, commonly referred to as a *Dalitz* plot [55, 56]. In case of a constant amplitude, one would observe a uniform event distribution within the kinematic boundaries. Any deviation from a uniform distribution reveals information on the dynamics of the interaction, *i.e.* the norm of the transition amplitude. Figure 2.1(a) illustrates this with a pedagogical example Dalitz plot.

A vertical band of high event accumulation is observed which indicates that the decay $D^0 \to \pi^+\pi^-\pi^0$ proceeds via an intermediate resonance, R, as the chain transition $D^0 \to (R \to \pi^+\pi^-)\pi^0$. The resonance band appears around the nominal mass of the resonance. Such intermediate states decay quasi-instantaneously with a typical lifetime, τ, in the order of $10^{-23}\,\mathrm{s}$. The spread of the resonance band is determined by the inverse of the lifetime; the decay width $\Gamma = 1/\tau$ (*cf.* Equation 2.1) is ordinarily around 100 MeV (for strongly decaying particles). The characteristic peak structure along the horizontal axis ($m^2_{\pi^+\pi^-}$) is referred to as the resonance's *lineshape*. Also the vertical intensity distribution along the resonance band is not constant. Most notably, there is a region of low event population in the center. As discussed in more detail in the next section, this is a direct consequence

of the resonance's spin introducing an angular correlation of the decay products due to total angular momentum conservation. The projection of the Dalitz plot to the vertical axis ($m^2_{\pi^+\pi^0}$) shows a peculiar feature of peaking structures which are not associated to any resonance. Inspection of the two-dimensional Dalitz plane allows to discriminate genuine resonance contributions from such effects known as *kinematic reflections*. In that sense, a spectroscopic analysis of the Dalitz plot, providing crucial insights on the spin of the resonance as well as protection against false peak identification, is clearly superior to simple bump hunting in an (one-dimensional) invariant-mass distribution.

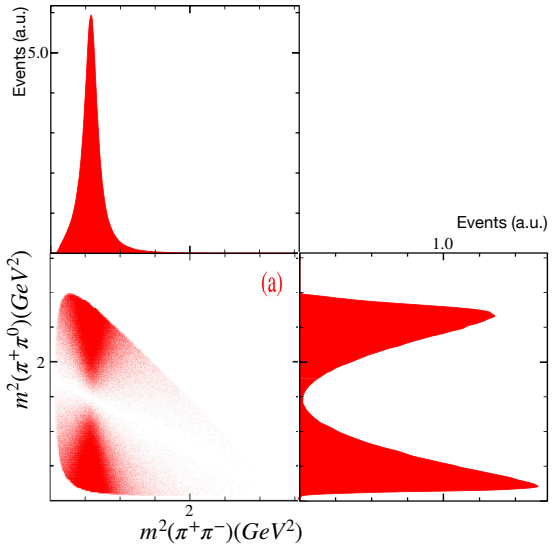

(a) Decay via a vector resonance $R \to \pi^+\pi^-$.

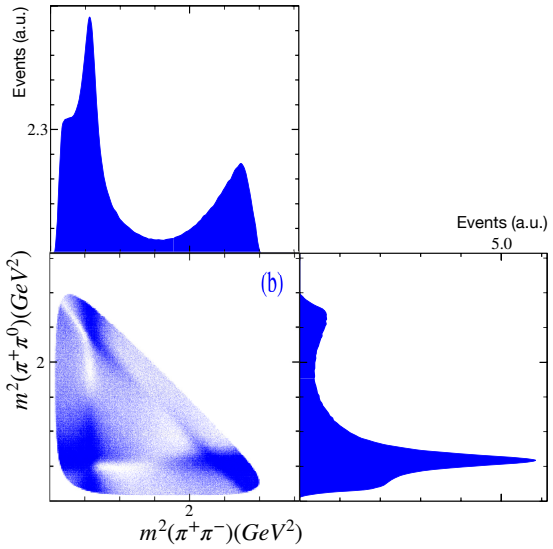

(b) Realistic decay involving multiple resonances reproduced from the results in [57].

Figure 2.1: Dalitz plot and its projection on the squared invariant masses for simulated $D^0 \to \pi^+\pi^-\pi^0$ decays.

In contrast to the simple example above, not only one, but many intermediate resonances may contribute to a common final state. Figure 2.1(b) shows a realistic Dalitz plot for the $D^0 \to \pi^+\pi^-\pi^0$ decay, simulated according to the model developed in Reference [57]. It includes, in addition to a non-resonant $D^0 \to \pi^+\pi^-\pi^0$ component, contributions from the vector mesons $\rho(770)^0$ and $\rho(770)^\pm$ in the decay modes $D^0 \to (\rho(770)^0 \to \pi^+\pi^-)\pi^0$, $D^0 \to (\rho(770)^+ \to \pi^+\pi^0)\pi^-$ and $D^0 \to (\rho(770)^- \to \pi^-\pi^0)\pi^+$ resulting in vertical, horizontal and diagonal resonance bands, respectively. Similar to Young's double slit experiment where photons with multiple (indistinguishable) paths to the same point on a screen interfere quantum-mechanically, multiple decay channels produce interference patterns on the Dalitz plot. These interference effects are generally largest in regions where resonance bands overlap, especially visible by the strong destructive interference in the upper-left corner of the Dalitz plot in Figure 2.1(b). The total amplitude is given by the coherent sum over the intermediate-state amplitudes, $A_i(\mathbf{x}) = |A_i(\mathbf{x})|e^{i\phi_i(\mathbf{x})}$, each of which describes the transition via a specific decay channel,

$$\begin{aligned} |A(\mathbf{x})|^2 &= \left|\sum_i a_i\, A_i(\mathbf{x})\right|^2 \\ &= |a_1 A_1(\mathbf{x})|^2 + |a_2 A_2(\mathbf{x})|^2 + 2\,|a_1 A_1(\mathbf{x})||a_2\, A_2(\mathbf{x})|\cos(\phi_1(\mathbf{x}) - \phi_2(\mathbf{x}) + \delta_1 - \delta_2) + \cdots . \end{aligned} \tag{2.4}$$

The complex coefficients $a_i = |a_i|e^{i\delta_i}$ describe the relative strength and constant phase differences between the amplitudes. In the above mentioned analogy of the double slit experiment, they represent polarization filters in front of the slits leading to a phase shift and relative intensity variation. While a global phase of the total amplitude is unobservable, it is evident, from Equation 2.4, that the intensity distribution over the Dalitz plot comprises vital information about the phase difference among amplitudes. This intrinsic sensitivity to phases is the key aspect of why Dalitz plot (or more formally amplitude) analyses are of particular interest for a broad range of applications, including studies of *CP* violation. Interference effects also provide an opportunity to investigate rare processes. The incoherent contribution of a decay mode with amplitude coefficient $|a_1| \ll 1$ is strongly suppressed ($\propto |a_1|^2$), whereas the interference with a known reference process can be sizable ($\propto |a_1|$).

2.2 Constructing intermediate-state amplitudes

The hadronic transition amplitudes cannot be calculated from perturbative QCD. Instead, a phenomenological model is employed to construct the intermediate-state amplitudes in a way that they are conform with the fundamental symmetries, conservation laws and Lorentz invariance. The *isobar* approach decomposes a multi-body decay into sequential two-body processes [58–60]. As depicted in Figure 2.2 for a generic three-body decay, the initial state progresses into a composite two-body system exhibiting definite quantum numbers, referred to as isobar state [59], and a recoil system. The isobar state, typically associated to an intermediate resonance, further decays into the (stable) final-state particles. It is assumed that the recoil system decouples from the isobar decay. This means that higher order topologies, referred to as *rescattering* processes, where the bachelor particle interacts with the particles originating from the isobar state, are excluded. Within this approximation, the amplitude for *e.g.* the decay channel $i = \{D^0 \to (\rho(770)^0 \to \pi^+\pi^-)\pi^0\}$ can be written as:

$$A_i = \sum_{\lambda} F(D)\,\langle D|\rho_\lambda\pi^0\rangle\,F(\rho)\,T(\rho)\,\langle\rho_\lambda|\pi^+\,\pi^-\rangle \equiv F(D)\,F(\rho)\,T(\rho)\,\mathcal{S}_i, \qquad (2.5)$$

where the *propagator*, $T(\rho)$, describes the dynamics of the resonance production and the vertex functions (or *form factors*), $F(D)$ and $F(\rho)$, account for deviations from a point-like interaction. The two-body isobar amplitudes $\langle D|\rho_\lambda\pi^0\rangle$ and $\langle\rho_\lambda|\pi^+\,\pi^-\rangle$ describe the production and decay of the $\rho(770)^0$ resonance. They are connected by the polarization state, λ, of the intermediate resonance. After performing a coherent sum over the (unobservable) intermediate-state polarizations, the isobar amplitudes are combined into an overall *spin factor*, $\mathcal{S}_i$, for a given decay channel i. It describes the angular correlation of the final-state particles subject to total angular momentum conservation. General physics considerations for the spin factors, form factors and resonance propagators are motivated in the next sections and specific choices for their parameterization are discussed.

It is straightforward to extend the isobar formalism to four-body decays by converting one of the final-state particles to an isobar state. As sketched in Figures 2.2(b) and 2.2(c), this gives rise to two distinct decay topologies. The *quasi two-body* topology denotes the decay of the initial state to two isobar states, each of which in turn decays to two final-state particles. In the *cascade* topology, on the other hand, the initial state first decays into an isobar state and a final-state particle, where the isobar state then decays via a second isobar state and a stable particle.

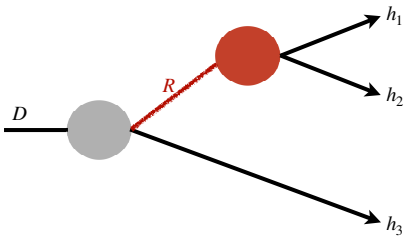

(a) Topology of a three-body decay.

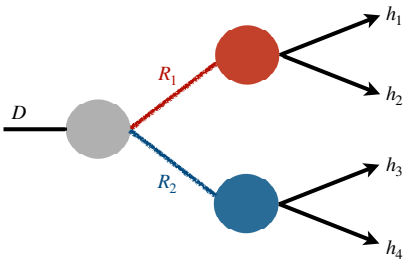

(b) Quasi two-body topology of a four-body decay.

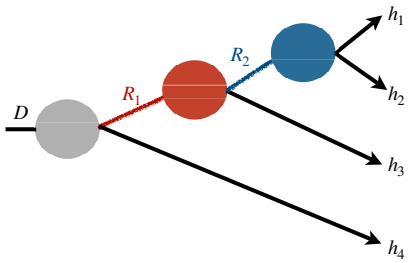

(c) Cascade topology of a four-body decay.

Figure 2.2: Pictorial representation of the isobar model description of an initial state, D, decaying to three or four final-state hadrons, h_i.

Spin factors

To motivate the general features of the expected angular distributions, consider the decay of a spin-S resonance, R, in two pseudoscalar particles. In case of a spinless resonance, the decay system can be arbitrary rotated and an isotropic angular distribution of the final-state particles is observed. A spin-1 resonance, on the other hand, can be in a transverse ($\lambda = \pm 1$) or longitudinal ($\lambda = 0$) polarization state with respect to a chosen quantization axis. To conserve total angular momentum, the two spin-0 decay products must have a relative orbital angular momentum equal to the resonance's spin. They can be considered to be in an angular momentum state $|l\, l_z\rangle = |1\lambda\rangle$, where l and l_z are the eigenvalues of the angular momentum operators $\hat{L}^2$ and $\hat{L}_z$, respectively. The respective eigenfunctions are given by the spherical harmonics $Y_{l l_z}(\theta, \phi)$, where θ is the polar angle with respect to the quantization axis and ϕ the azimuthal angle. For the angular distribution in the resonance's rest frame follows: $Y_{1\pm1}(\theta, \phi) \propto \mp \sin(\theta) e^{\pm i\phi}$ for the transverse and $Y_{10}(\theta, \phi) \propto \mp \cos(\theta)$ for the longitudinal polarization states. This means that, in a semiclassical picture with $\vec{L} = \vec{r} \times \vec{p}$, the movement of the daughter particles, separated by a distance $\vec{r}$, in

direction of the resonance's spin is dynamically suppressed as in this case it is not possible for them to generate an angular momentum in the same direction. If one of the outgoing particles has non-zero spin, possible in the cascade topology, the calculation of the angular distribution is considerably more complex as spin-orbit couplings need to be taken into account. Moreover, multiple sub-processes have to be combined properly in order to compute the spin factor in Equation 2.5. Hence, two-body isobar amplitudes need to be evaluated in a common frame which requires a careful alignment of the isobar rest frames. Similarly, to calculate the interference effects of two decay channels, a common frame for the corresponding spin factors has to be defined. This becomes increasingly complicated the more decay topologies are possible and requires a large amount of bookkeeping. It is therefore desirable to calculate the angular distributions in a frame independent way. To that end, a manifestly Lorentz invariant approach, the covariant *Zemach* (*Rarita-Schwinger*) tensor formalism [61–64], is applied which connects the only final-state observables, the particle's four-momenta, to the spin dynamics of the reaction. It reproduces the above mentioned results when evaluated in the rest frame of the resonance.

From the discussion above it is clear that a spin-1 state has three independent degrees of freedom corresponding to its polarization states. These can be embedded in a higher dimensional object, the *polarization vector* ε^μ. The benefit of which is that it is now straightforward to obtain explicitly covariant expressions by contracting the polarization vector with other Lorentz vectors such as the four-momentum of the final-state particles. However, supplementary constraints are needed in order to reduce the *a priori* four degrees of freedom to the three physical ones. These are know as *Rarita-Schwinger* conditions which read for a spin-1 state with four-momentum p and spin projection λ [65]:

$$p_\mu \, \varepsilon^\mu(p, \lambda) = 0 \, . \tag{2.6}$$

It implies that the time component of $\varepsilon^\mu(p, \lambda)$ must vanish in the particle's rest frame (**RF**) . The remaining spatial components can then be chosen as follows:

$$\varepsilon^\mu(p, \lambda = \pm 1) \overset{\mathbf{RF}}{=} \mp \frac{1}{\sqrt{2}} \, (0, 1, \pm i, 0) \, , \quad \varepsilon^\mu(p, \lambda = 0) \overset{\mathbf{RF}}{=} (0, 0, 0, 1) \, . \tag{2.7}$$

The polarization vectors in an arbitrary frame are computed performing a Lorentz transformation from the rest frame to the desired frame. Now, a *projection operator* on the spin-1 subspace spanned by the three polarization vectors is constructed [63]:

$$P^{\mu\nu}_{(1)}(p) = \sum_\lambda \varepsilon^\mu(p, \lambda) \, \varepsilon^{*\nu}(p, \lambda) = - \, g^{\mu\nu} + \frac{p^\mu \, p^\nu}{p^2} \overset{\mathbf{RF}}{=} \mathrm{diag}(0, -1, -1, -1), \tag{2.8}$$

where $g^{\mu\nu} = \text{diag}(+1, -1, -1, -1)$ is the Minkowski metric and the last term gives the explicit expression in the rest frame of the particle. The contraction of the spin-1 projection operator with an arbitrary four-vector, a^μ, is orthogonal to the momentum, *i.e.* $a'^\mu p_\mu = 0$ with $a'^\mu = P^{\mu\nu}_{(1)}(p) a_\nu$. For example, $P^{\mu\nu}_{(1)}(p) p_\nu = 0$ and $P^{\mu\nu}_{(1)}(p) \varepsilon(p,\lambda)_\nu = -\varepsilon(p,\lambda)^\mu$. Hence, the spin projection operator selects that part of a^μ which satisfies the necessary condition of a spin-1 state given by Equation 2.6.

With these considerations, the original example decay process ($R \to a\, b$) can be reexamined. The decaying resonance is represented by its polarization vector, $\varepsilon(p_R, \lambda)^\mu$. The final-state observables are given by the four-momenta of particle a and b, p_a and p_b. Equivalently, one can define their total $p_R = p_a + p_b$ and relative momentum $q_R = p_a - p_b$. A state of pure angular momentum, $L = 1$, for the two particle system can now be created with the help of the projection operator defined above. To conserve total angular momentum, the spin-1 subspace projected into should exactly be the one defined by the decaying resonance. For that reason, the projection operator $P_{(1)\mu\nu}(p_R)$ is contracted with the final-state momenta. Only the relative momentum is relevant since $P_{(1)\mu\nu}(p_R) p^\nu_R = 0$. The resulting object is called *orbital angular momentum tensor*,

$$L_{(1)\mu}(p_R, q_R) = -P_{(1)\mu\nu}(p_R)\, q^\nu_R. \tag{2.9}$$

It fulfills, by construction, the spin-1 Rarita-Schwinger condition (*cf.* Equation 2.6) and thus has three independent elements in accordance with the number of degrees of freedom for a state with said angular momentum. The equivalent projection and orbital angular momentum tensors for higher (integer) spin states are given in Appendix A.

Altogether, the Lorentz-invariant isobar amplitude is calculated by contracting the polarization vector of the decaying resonance with the orbital angular momentum tensor of the decay products:

$$\langle R_\lambda | a\, b \rangle = \varepsilon(p_R, \lambda)_\mu\, L^\mu_{(1)}(p_R, q_R) \overset{\mathbf{RF}}{=} |\vec{q}|\, Y_{1\lambda}(\theta, \phi), \tag{2.10}$$

where the last expression is evaluated in the rest frame of the resonance and $\vec{q}$ is the relative three-momentum of the daughter particles in that frame. Indeed, the result agrees, up to an energy dependent factor, with the one motivated at the beginning. As the quantum mechanical angular momentum operator acts only on the angular part but not on the radial component of the wave function, the latter does not specify an energy dependence and the results are, in fact, fully consistent. The energy dependent factor appearing naturally in the covariant formalism is discussed in more detail later in combination with the form factors.

The construction of the spin factor for a given decay channel proceeds in two steps: first, the individual two-body amplitudes for each node of the decay tree are calculated by appropriately combining polarization, spin projection and angular momentum tensors into Lorentz scalars. Afterwards, the isobar amplitudes are combined and a sum over the polarization states is performed. This procedure is elucidated on the basis of the example decay channel $D^0 \to (\rho(770)^0 \to \pi^+\pi^-)\pi^0$ in the following. A general recipe to construct spin factors for arbitrary topologies and the explicit expressions for the four-body decay modes relevant for this thesis are given in Appendix A.

The decay chain starts with the transition from the charm meson to a vector resonance and a bachelor pion. A complex conjugate polarization vector is assigned to the resonance to signify its production rather than its decay. As the initial state has spin zero, the decay products must have a relative orbital angular momentum $L = 1$ in order to compensate the resonance's spin. Hence, the isobar amplitude is given by:

$$\langle D|\rho_\lambda\,\pi^0\rangle = L^\mu_{(1)}(p_D, q_D)\,\varepsilon^*_\mu(p_\rho, \lambda). \tag{2.11}$$

The produced spin-1 resonance decays via two pseudoscalars. The corresponding two-body amplitude has already been discussed and follows from Equation 2.10:

$$\langle \rho_\lambda|\pi^+\,\pi^-\rangle = \varepsilon_\nu(p_\rho, \lambda)\,L^\nu_{(1)}(p_\rho, q_\rho). \tag{2.12}$$

Now, everything is in place for the final spin factor calculation:

$$\begin{aligned}\mathcal{S}_i &= \sum_\lambda \langle D|\rho_\lambda\,\pi^0\rangle\langle\rho_\lambda|\pi^+\,\pi^-\rangle = \sum_\lambda L^\mu_{(1)}(p_D, q_D)\,\varepsilon^*_\mu(p_\rho, \lambda)\,\varepsilon_\nu(p_\rho, \lambda)\,L^\nu_{(1)}(p_\rho, q_\rho)\\ &= L^\mu_{(1)}(p_D, q_D)\,L_{(1)\mu}(p_\rho, q_\rho) \overset{\text{RF}}{=} -|\vec{p}_D||\vec{q}_\rho|\cos(\theta_\mathrm{H})\,\beta_\mathrm{H},\end{aligned} \tag{2.13}$$

where the first step inserts Equations 2.11 and 2.12 and the second step uses the definition of the spin projection operator, $P_{(1)\mu\nu}(p_\rho) = \varepsilon^*_\mu(p_\rho, \lambda)\,\varepsilon_\nu(p_\rho, \lambda)$, and the fact that the orbital angular momentum tensor $L_{(1)\nu}(p_\rho, q_\rho)$ is already projected into the spin-1 subspace of the resonance, $P^{\mu\nu}_{(1)}(p_\rho)\,L_{(1)\nu}(p_\rho, q_\rho) = L_{(1)\mu}(p_\rho, q_\rho)$. The last step evaluates the expression in the rest frame of the resonance. In this frame, the angle between one of the resonance's daughters and the D meson is referred to as the *helicity angle* of the resonance, θ_H. The condition for a vanishing transition amplitude, $\cos(\theta_\mathrm{H}) = 0$, corresponds to a diagonal line in the Dalitz plot shown in Figure 2.1(a) cutting through the middle of the resonance band. The additional factor $\beta_\mathrm{H} = \left(\frac{m_D^2 + m^2(\pi^+\pi^-) - m^2_{\pi^0}}{m_D^2}\right)$ comes from the Lorentz boost from the rest frame of the initial state to the resonance's rest frame. In practice, no explicit expression in a certain reference frame is derived but the full tensor algebra (in form of the second to last step in Equation 2.13) is computed.

Form factors

To motivate the nature of the form factors, it is instructive to consider the radial part, $\psi(r)$, of a total wave function $\psi(r,\theta,\phi) = \psi(r) \cdot \psi(\theta,\phi)$ describing the two-body daughter system in a decay $R \to ab$. The angular distribution, $\psi(\theta,\phi) = Y_{l l_z}(\theta,\phi)$, was discussed in context of the spin factors. The Schrödinger equation for the radial wave function in a central field is given by:

$$\left[-\frac{1}{2\mu}(\partial_r^2 + \frac{2}{r}\partial_r) + \frac{L(L+1)}{2\mu r^2} + V(r)\right]\psi(r) = E\,\psi(r), \tag{2.14}$$

where r is the separation between the daughter particles, μ is the reduced mass of the two-body system, L is the orbital angular momentum and $V(r)$ is the interaction potential. The daughter particles might be pictured to be bound within the effective radius, r_{BW}, of the resonance. They have to tunnel through the centrifugal barrier in order to leave the system, *i.e.* for the resonance to decay. A higher angular momentum creates a stronger centrifugal barrier and decreases the transition probability. This effect can be quantified by assuming a square well interaction potential (with radius r_{BW}) resulting in the *Blatt-Weisskopf barrier factors*, B_L [66]. They express the transmission probability in terms of the angular momentum and the *breakup momentum*, q, which is defined as the magnitude of the three-momentum of daughter particle a (or b) in the rest frame of the decaying particle R:

$$q^2 = \frac{[m^2(a\,b) - (m(a)+m(b))^2]\,[m^2(a\,b) - (m(a)-m(b))^2]}{4\,m^2(a\,b)}\,. \tag{2.15}$$

With the definition $B_L(q) = q^L\,F_L(q)$, the explicit expressions for an angular momentum $L = \{0,1,2\}$ are:

$$\begin{aligned} F_0(q) &= 1, \\ F_1(q) &= r_{BW}/\sqrt{1+(q\,r_{BW})^2}, \\ F_2(q) &= r_{BW}^2/\sqrt{9+3\,(q\,r_{BW})^2+(q\,r_{BW})^4}. \end{aligned} \tag{2.16}$$

The factor q^L is separated as it is inherently included in the spin factors, compare Equation 2.10. Hence, the form factors, F_L, as in Equation 2.16 are included for each isobar vertex to calculate the amplitude of a given decay channel. Note that this choice is entirely heuristic as the true interaction potential is unknown and other parameterizations exist [67]. The Blatt-Weisskopf barrier factors are the ones most commonly used. In particular, they ensure the correct behavior of the amplitudes at the threshold $q = 0$, where the daughter particles are produced at rest (in the rest frame of the resonance). In this extreme case, it is not possible

at all for the daughter particles to have a non-zero orbital angular momentum and the amplitude should vanish. More generally, the fact that it is difficult for slowly moving particles to generate enough angular momentum to account for the resonance spin is reflected in the asymptotic behavior of the barrier factors near the threshold, $B_L(q) \propto q^L \,(\text{for}\, q \to 0)$. As a consequence, one generally expects that the decay of charm or beauty mesons via higher spin resonances is suppressed. For example, the lowest lying vector (tensor) resonance contributing to $D \to \pi^+\pi^-\pi^0$ decays is the $\rho(770)^0$ ($f_2^0(1270)$) meson which gives a breakup momentum of $q_1 = 765\,\text{MeV}$ ($q_2 = 480\,\text{MeV}$) if it is produced on-shell. A naive estimate of the relative branching fraction results in $(B_2(q_2)/B_1(q_1))^2 \approx 3\%$.

The q^L dependence of the spin factors can be interpreted as centrifugal barrier effect, in the sense of its threshold behavior discussed above. The additional $F_L(q)$ term appearing in the barrier factors damps the amplitude at high momentum transfers and might be considered as correction due to the finite extend of the resonance. On a more technical level, it keeps the amplitudes finite in the limit $q \to \infty$ where q^L is clearly diverging but $q^L F_L(q)$ has the asymptotic limit $q^L F_L(q) \to 1$. This is of minor relevance for most practical applications since the break-up momentum is limited by the mass of the decaying resonance.

Resonance lineshapes

General features of the resonance lineshapes can be depicted, in simplified terms, by considering the time development of a quantum-mechanical wave function, $\psi(r,\theta,\phi,t) = \psi(r,\theta,\phi)\, e^{-i\,E\,t}$, where E is the eigenvalue of the Hamiltonian describing the system. The probability to observe an unstable particle (somewhere) decreases, according to Fermi's Golden rule (Equation 2.2), as $\mathrm{P}(t) = \int |\psi(r,\theta,\phi,t)|^2 \mathrm{d}r\mathrm{d}\Omega \propto e^{-\Gamma t}$, which in turn implies that the energy acquires an imaginary part, $E = E_0 - i\,\Gamma/2$. By transforming from the time into the energy space via a Fourier transformation the characteristic resonance distribution, known as *Breit-Wigner* [68,69] lineshape, is revealed:

$$\tilde{\psi}(E) = \int \psi(t) e^{i\,E\,t} \mathrm{d}t \propto \frac{1}{(E - E_0) + i\frac{\Gamma}{2}}. \tag{2.17}$$

The energy distribution shows a peak around the characteristic energy of the resonance, E_0, whose spread is determined by the decay width. In this form, the Breit-Wigner function is non-relativistic. Its covariant counterpart arises from quantum field theory as propagator of an unstable particle [70–72]:

$$T_{\mathrm{BW}}(s) = \frac{1}{M^2(s) - s - i\,\sqrt{s}\,\Gamma(s)}\,, \tag{2.18}$$

where $s = p^2$ is the square of the center-of-mass energy. The energy-dependent (*running*) mass $M(s)$ and width $\Gamma(s)$ are normalized to give the nominal mass[1], m_R, and width, Γ_R, when evaluated at the nominal mass, $M^2(s = m_R^2) = m_R^2$ and $\Gamma(s = m_R^2) = \Gamma_R$. They can be identified as the real and imaginary part of the so-called *self-energy*, which describes loop corrections to the bare propagator arising from the Lagrangian. An example of a mesonic quantum fluctuation contributing to the propagator of the $\rho(770)^0$ resonance would be the loop process $\rho(770)^0 \to \pi^+\pi^- \to \rho(770)^0$, where a virtual pion pair is emitted and reabsorbed (or higher orders thereof). For small center-of-mass energies (momentum flowing through the propagator) only off-shell particles can be created in the loop and the entire self-energy is contained in the real part, $M^2(s)$. As soon as the energy reaches a certain kinematic threshold, $\sqrt{s} = 2m_\pi$, the loop receives on-shell contributions. This happens exactly when the (real) decay $\rho(770)^0 \to \pi^+\pi^-$ becomes kinematically possible which in turn implies that the self-energy develops an imaginary part, *i.e.* a non-zero decay rate $\Gamma(s)$. A more detailed discussion of the self-energy is beyond the scope of this thesis but can be found in most quantum field theory textbooks, *e.g.* in Reference [4]. The implications of the energy dependence of both $M^2(s)$ and $\Gamma(s)$ relevant for the presented analyses are discussed in the following paragraphs. It is important to note that Equation 2.18 is strictly valid only for fundamental particles like the Z^0 boson and cannot be derived from first principles for hadronic states. It should therefore be considered as an effective model, inspired by quantum field theory, which has been empirically found to well describe experimental data.

For reasonably narrow resonances, far away from the kinematic threshold, the running mass and width might be approximated as being constant, in which case a simple Breit-Wigner form is obtained, $T(s)^{-1} = m_R^2 - s - i\, m_R\, \Gamma_R$. For broad resonances this is not appropriate. The energy dependence of the running width can be computed from Equation 2.1, provided that the amplitude describing the transition is know. For a decay in two stable particles, $R \to ab$, the amplitude in the rest frame of the resonance is given by $A_{R\to ab} = B_L(q)\, Y_{L\lambda}(\theta, \phi)$ and the calculation yields:

$$\begin{aligned}\sqrt{s}\,\Gamma_{R\to ab}(s) &= \int |A_{R\to ab}|^2 \,\mathrm{d}\Phi_2 \\ &= m_R\,\Gamma_R \left(\frac{q}{q_R}\right) \frac{m_r}{\sqrt{s}} \frac{B_L(q)^2}{B_L(q_R)^2}\,. \end{aligned} \tag{2.19}$$

[1]Note that m_R is indeed the physical (renormalized) mass and not the bare mass appearing in the Lagrangian [4].

The additional factor $q/\sqrt{s}$ comes from the integration over the phase space and the normalization of the spherical harmonics is used, $\int |Y_{lm}|^2 \mathrm{d}\Omega = 1$. The expression is explicitly normalized to give the nominal width at the nominal mass, where the break-up momentum evaluated at the nominal mass is denoted as q_R. The lineshape obtained when inserting Equation 2.19 into Equation 2.18 with $M^2(s) = m_R^2$ is know as the *relativistic* (two-body) Breit-Wigner function [72]. Figure 2.3 shows the running width, $\Gamma_{f^0\to\pi\pi}(s)$, for the scalar resonance $f^0(980)$ decaying in two pions as well as the intensity, $|T_{\mathrm{BW}}(s)|^2$, and phase, $\theta_{\mathrm{BW}}(s) = \arg(T_{\mathrm{BW}}(s)) = \arctan(\frac{\sqrt{s}\Gamma(s)}{m_R^2 - s})$, distribution of its relativistic Breit-Wigner lineshape. Besides the peak in the invariant-mass distribution, a rapid phase variation when approaching the propagator pole, where the real part vanishes, is a characteristic feature of a resonance and determines how it interferes with other processes. Equivalently, a (counter-clockwise) circular trajectory in the complex (*Argand* [73]) plane spanned by the real and imaginary part of the Breit-Wigner distribution, is observed. For the scalar resonances $K_0^*(1430)$, σ and the vector resonance $\rho(770)$ more sophisticated (empirical) lineshape parameterizations exist, which can be found in Appendix B. Isobar states are not necessarily associated with intermediate resonances. Such non-resonant states are denoted by surrounding the daughter particle system with brackets and indicate their orbital angular momentum configuration (in spectroscopic notation) with an subscript; for example $(\pi^+\pi^-)_S$ refers to a non-resonant di-pion S-wave state. The lineshape for non-resonant states is set to unity.

In fact, Equation 2.19 gives only the *partial* width for the decay into a specific final state. Even if only a single final state is of interest, as is usually the case, the total decay width, given by the sum over all partial widths,

$$\Gamma(s) = \sum_i g_i \, \Gamma_i(s), \tag{2.20}$$

is to be used in the propagator imposing a major challenge. While the energy dependence of each partial width can, in principle, be computed with similar considerations as discussed above, it requires, in most cases, information from external measurements to infer the coupling strengths to the different final states, g_i. These can be related to the branching fractions, $\mathcal{B}_i$, by folding the corresponding partial width with the lineshape of the resonance [10]:

$$\mathcal{B}_i = \int_{s_{min}}^{\infty} \frac{g_i \, m_R \, \Gamma_i(s)}{|m_R^2 - s - i \, m_R \, \sum_j g_j \, \Gamma_j(s)|^2} \, \mathrm{d}s. \tag{2.21}$$

This definition accounts for the fact that channels opening far above the resonance pole can only contribute to the right tail of the lineshape. Especially the proximity

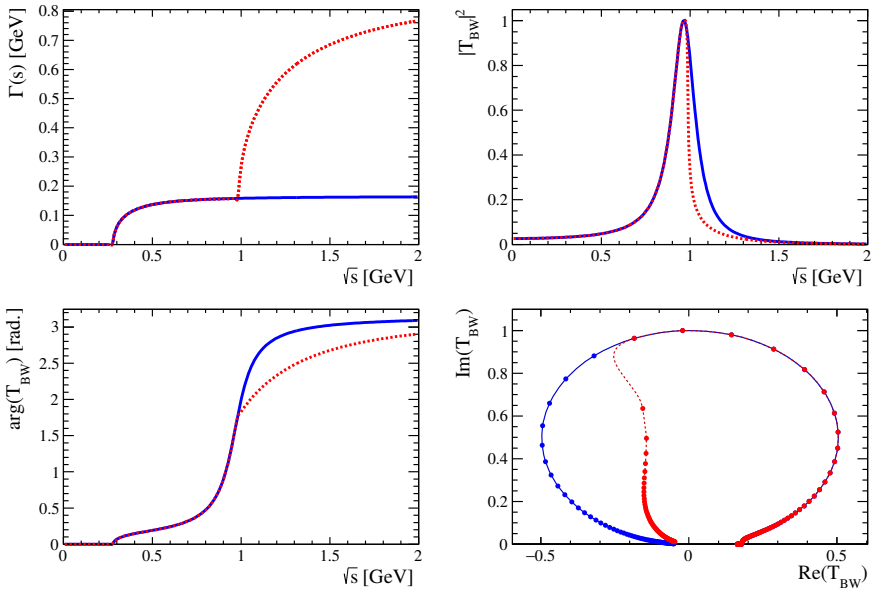

Figure 2.3: Running width (top-left), intensity (top-right) and phase (bottom-left) of the Breit-Wigner lineshape as function of the center-of-mass energy ($\sqrt{s}$) for the $f_0(980)$ meson with resonance parameters taken from Reference [74]. The counter-clockwise trajectory on the Argand plane is shown in steps of 10 MeV (bottom-right). The distributions are plotted for both: taking only the partial width into the $\pi\pi$ channel into account (blue), and using the total decay width into the $\pi\pi$ and KK channels (red).

to the kinematic threshold of an additional decay channel can significantly deform the observed lineshape, as displayed in Figure 2.3. The $f_0(980)$ resonance is close to the KK threshold ($m_{f_0(980)} = 965\,\text{MeV} \approx 2 \cdot m_{K^\pm}$ [10]) above which it decays to this final state with a branching ratio of $\mathcal{B}_{f^0\to KK}/\mathcal{B}_{f^0\to\pi\pi} \approx 43\%$ [74]. The sudden increase of the total decay width, $\Gamma_{f_0(980)}(s) = g_{\pi\pi}\,\Gamma_{f_0(980)\to\pi\pi}(s) + g_{KK}\,\Gamma_{f_0(980)\to KK}(s)$, above the KK threshold leads to a sharpening of the resonance peak and an immanent phase distortion.

The partial width for a three-body final state, $R \to abc$, is considerably more complicated than the two-body case. In a cascade decay such as $a_1(1260)^+ \to (\rho(770)^0 \to \pi^+\pi^-)\,\pi^+$, the finite width of the intermediate resonance must be taken into account. The situation is aggregated in presence of multiple sub-decay modes, *e.g.* $a_1(1260)^+ \to (f^0(980) \to \pi^+\pi^-)\,\pi^+$, in which case not only their relative contribution but also their interference pattern has to be known. Again, this might be parameterized employing the isobar model including form factors, the lineshape of the intermediate resonance and the spin factor of the decay. However, the integration over the phase space,

$$\sqrt{s}\,\Gamma_{R\to abc}(s) = \int |A_{R\to abc}|^2\,\mathrm{d}\Phi_3 = \int |\sum_i a_i\,A_i|^2\,\mathrm{d}\Phi_3, \tag{2.22}$$

has no analytic expression in general. It can be evaluated numerically by scanning over the center-of-mass energy as illustrated in Figure 2.4. Here, the evolution of

the $a_1(1260)^+ \to \pi^+\pi^-\pi^+$ Dalitz plot is demonstrated for increasing values of the center-of-mass energy. The phase-space volume generally scales with the available center-of-mass energy and more and more structures emerge as soon as the decay via a specific resonance becomes kinematically possible. Figure 2.5(left) shows the corresponding running-width distribution computed by integrating over the Dalitz plot at a fixed set of grid-points, s_i. The result for arbitrary center-of-mass energies is then obtained by a linear interpolation in-between two consecutive grid points. The running width slowly starts to rise above the $\pi\pi\pi$ threshold. It ascends steeply above $\sqrt{s} \approx 0.9\,\text{GeV}$ where the invariant mass of the $\pi^+\,\pi^-$ subsystem is sufficient for an on-shell $\rho(770)^0$ resonance production, before it saturates at high center-of-mass energies where the di-pion invariant mass predominantly falls on the high-mass tail of the resonance. Similar features develop if either new intermediate resonance contributions or additional final states, such as $KK\pi$, open up. Note that Figure 2.4 and Figure 2.5 are only illustrative examples as the precise substructure of the $a_1(1260)^+$ meson is yet to be determined. This means that the lineshape and the underlying resonance composition must be studied simultaneously as each one of them requires knowledge of the other. A method how to efficiently resolve their inherent co-dependency is presented in context of the analysis of $D \to \pi\pi\pi\pi$ decays, in Section 6.4, where the axial-vector meson $a_1(1260)^+$ contributes in the cascade topology, $D^0 \to (a_1(1260)^+ \to \pi^+\pi^-\pi^+)\,\pi^-$.

The energy-dependent mass is fundamentally connected to the decay width via the *Kramers-Kronig dispersion* relation [75, 76]:

$$M^2(s) = m_R^2 + \frac{m_R}{\pi} \int_{s_{min}}^{\infty} \left(\frac{\Gamma(s')}{s - s'} - \frac{\Gamma(s')}{m_R^2 - s'} \right) \mathrm{d}s'. \tag{2.23}$$

Its calculation requires a detailed understanding of the decay width for arbitrarily large center-of-mass energies which is arguably hardly possible with a sufficient level of confidence. The center-of-mass energy range in which the running width can be studied is typically restricted by the production process of the resonance (and its intrinsic width, Γ_R). For example, the accessible center-of-mass energy for the $a_1(1260)^+$ meson originating from $D^0 \to a_1(1260)^+\,\pi^-$ decays is limited by $m_D - m_\pi \approx 1.7\,\text{GeV}$. The running mass can obtain sizable contributions from decay channels which open far beyond that. Moreover, the integral in Equation 2.23 is highly sensitive to the choice of form factors which are, in fact, needed to ensure the convergency, *i.e.* to keep $\Gamma(s)$ finite in the limit $s \to \infty$. The calculation of the running mass should therefore be considered to be substantially less reliable than the decay width. Rare attempts, primarily for the broad $\rho(770)^0$ and $a_1(1260)^+$ resonance [67, 75, 77, 78], have been made to study its features in more detail. In practice, the energy-dependent mass is often approximated as being constant.

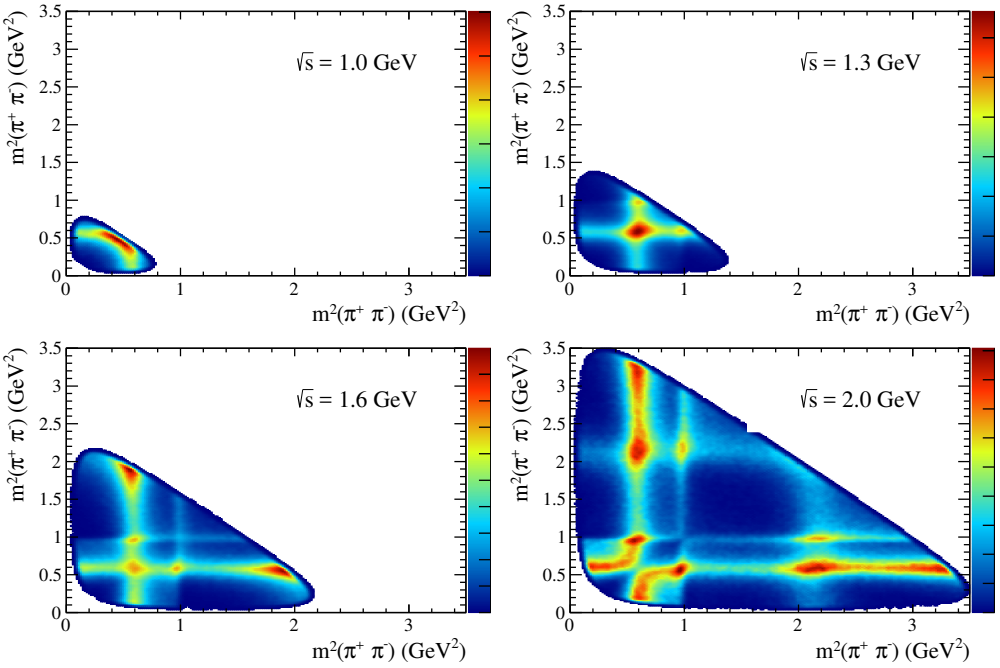

Figure 2.4: Simulated evolution of the $a_1(1260)^+ \to \pi^+\pi^-\pi^+$ Dalitz plot with the center-of-mass energy. Decay modes via the intermediate resonances $\rho(770)^0$, $f_0(980)^0$ and $\rho(1450)^0$ decaying to $\pi^+\pi^-$ are considered. Their relative transition rates and phases are chosen arbitrarily, for illustration purposes only. The Dalitz plots are symmetric as the like-sign pions are indistinguishable.

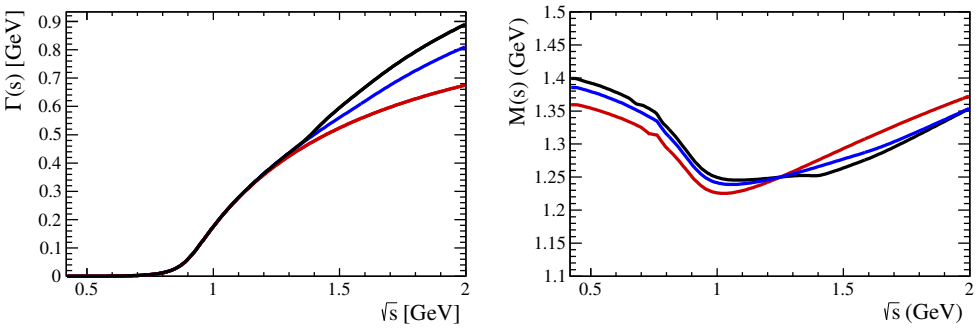

Figure 2.5: Running width (left) and running mass (right) of the $a_1(1260)^+$ meson. Decay channels are added successively: first only decays into the tri-pion final state via the $\rho(770)^0$ resonance are considered (red), then decay modes via the $f_0(980)^0$ and $\rho(1450)^0$ resonances are included (blue) and finally also the partial width into the $KK\pi$ final state via the decay channel $a_1(1260)^+ \to (\bar{K}^*(892) \to K^-\pi^+)K^+$ is added (black). Their relative contributions are chosen arbitrarily, for illustration purposes only.

Figure 2.5(right) shows the running-mass distribution for the $a_1(1260)^+$ meson when successively adding additional decay channels. Starting with only considering the decay mode $a_1(1260)^+ \to (\rho(770)^0 \to \pi^+\pi^-)\,\pi^+$, a dip develops in the region where the on-shell $\rho(770)^0$ resonance production is maximal and the $a_1(1260)^+$ meson effectively becomes less massive. It is observed that the inclusion of additional intermediate resonances or final states quite generally leads to a leveling of the running-mass distribution far away from the three-pion threshold ($\sqrt{s} > 1\,\text{GeV}$) such that $M^2(s)$ is, indeed, approximately constant near the nominal resonance mass ($1\,\text{GeV} < \sqrt{s} < 1.5\,\text{GeV}$). This is in agreement with other similar studies in References [67, 75, 78]. In a way, this justifies the common practice of setting the running mass constant and larger dispersive effects are only expected for either broad resonances or resonances close to the kinematic threshold.

2.3 Amplitude decomposition

An amplitude analysis aims to identify the contributing decay channels and to measure their relative magnitudes and phases. First, a set of intermediate-state amplitudes (*amplitude model*) is hypothesized. Given a dataset of N measured observables, $\{\mathbf{x}_1, \mathbf{x}_2, ..., \mathbf{x}_N\}$, the *maximum likelihood technique* [79, 80] is used to estimate (*fit*) the amplitude coefficients and additional lineshape parameters, collectively denoted as θ. Normalizing the differential decay rate to yield a *probability density function* (PDF):

$$\mathcal{P}(\mathbf{x}|\theta) = \frac{\left|\sum_i a_i\, A_i(\mathbf{x})\right|^2\, \phi_4(\mathbf{x})}{\int \left|\sum_i a_i\, A_i(\mathbf{x})\right|^2 \mathrm{d}\Phi_4}, \tag{2.24}$$

the likelihood function is defined as the joint density of the data sample considered as a function of θ, $\mathcal{L}(\theta) = \prod_{i=1}^{N} \mathcal{P}(\mathbf{x}_i|\theta)$. The likelihood estimator $\hat{\theta}$ is given by the particular parameter set that maximizes $\mathcal{L}(\theta)$. For numerical reasons, the negative logarithm of the likelihood function, $-\ln \mathcal{L}(\theta) = -\sum_{i=1}^{N} \ln \mathcal{P}(\mathbf{x}_i|\theta)$, is minimized with the routine implemented in the MINUIT [81] package. The precision of the estimated parameters and their correlations are computed from the second derivatives:

$$\mathrm{cov}(\theta_i, \theta_j) = -\left(\frac{\partial^2}{\partial\theta_i\, \partial\theta_j} \ln \mathcal{L}\,\bigg|_{\theta=\hat{\theta}}\right)^{-1}, \tag{2.25}$$

where the statistical uncertainty on parameter θ_i is given by $\sigma_i = \sqrt{\mathrm{cov}(\theta_i, \theta_i)}$. Information from external measurements can be incorporated in the likelihood procedure by means of so-called *Gaussian constraints*. Say the parameter θ_k has been (independently) determined to be $\mu_k \pm \sigma_k$, the following extension accounts for this prior knowledge: $-\ln \mathcal{L}(\theta) \to -\ln \mathcal{L}(\theta) + \frac{(\theta_k - \mu_k)^2}{2\sigma_k^2}$. In doing so, the uncertainty on the constrained parameter (θ_k) is correctly propagated to the statistical uncertainty of the other (unconstrained) parameters determined from the likelihood fit procedure.

The PDF in Equation 2.24 is invariant under a simultaneous transformation of all amplitude coefficients: $a_i \to c \cdot a_i$, with a complex number c. Thus, one of the amplitude coefficients can be fixed to unity. After the optimal amplitude model parameters have been determined, convention-independent quantities are derived:

$$F_i \equiv \frac{\int \left|a_i\, A_i(\mathbf{x})\right|^2 \mathrm{d}\Phi_4}{\int \left|\sum_i a_i\, A_i(\mathbf{x})\right|^2 \mathrm{d}\Phi_4}, \qquad I_{ij} \equiv \frac{\int 2\,\mathrm{Re}[a_i a_j^*\, A_i(\mathbf{x}) A_j^*(\mathbf{x})]\, \mathrm{d}\Phi_4}{\int \left|\sum_i a_i\, A_i(\mathbf{x})\right|^2 \mathrm{d}\Phi_4}, \tag{2.26}$$

where the *decay fractions* F_i are a measure of the relative strength between the different transitions and the *interference fractions* I_{ij} measure the interference effects between amplitude pairs. Constructive and destructive interference lead to $I_{ij} > 0$ and $I_{ij} < 0$, respectively. Note that $\sum_i F_i + \sum_{j<k} I_{jk} = 1$.

Measurement of CKM matrix elements

3

A key consistency test of the Standard Model is to verify the unitarity conditions by over-constraining the CKM matrix with independent measurements sensitive to various distinct combinations of matrix elements. A non-closed Unitarity Triangle, *i.e.* $\alpha + \beta + \gamma \neq 180°$ or too short (long) sides, would be a striking sign of physics beyond the Standard Model. Theories modifying the flavor structure of the Standard Model include, amongst others, a forth fermion generation in combination with an extended Higgs sector [82, 82, 83], a small right-handed coupling of the W-boson [84,85], a flavor changing neutral current (Z') [41,86,87] or a new particle species (*leptoquarks*) allowing transitions from quarks to leptons [41, 88, 89]. This chapter first summarizes the current experimental status of the CKM matrix. Two methods to improve the present knowledge of the CKM angle γ are presented afterwards.

3.1 Experimental status

The magnitudes of the CKM matrix elements can be determined from the decay rates of respective flavor-changing transitions which are proportional to the coupling strength $|V_{ij}|^2$. Inputs from non-perturbative QCD calculations [11,90] are required to relate the decay rates (or branching fractions) to the CKM parameters. As an example, the magnitude of the CKM matrix element V_{ub} is measured via semileptonic $b \to u\, l^-\, \bar{\nu}_l$ quark-level transitions leading to $\bar{B}^0 \to \pi^+ l^- \bar{\nu}_l$ and $B^- \to \pi^0 l^- \bar{\nu}_l$ [91,92] (with $l^- = \{e^-, \mu^-\}$) or $\Lambda_b \to p\mu^-\bar{\nu}_\mu$ [93] decays. The current world-average value is $|V_{ub}| = (3.50 \pm 0.13) \cdot 10^{-3}$ [35], where the precision is limited by the calculation of the hadronic form factors [94, 95]. As the B^0 meson mixing frequency is proportional to $\Delta m_d \propto |V_{td}|^2$ (*cf.* Section 1.3), its measurement allows constraining one side of the Unitarity Triangle, which again requires knowledge of non-perturbative QCD effects. The influence of those can be reduced by relating the B^0 and B_s meson mixing frequencies via $\Delta m_d = \frac{\Delta m_d^{\text{Theo}}}{\Delta m_s^{\text{Theo}}} \cdot \Delta m_s$ [30]. The ratio of the mixing frequencies can be more reliably extracted from the theory,

with a relative uncertainty of approximately 3% [96] in contrast to the individual uncertainties which are around 14% [38]. A new measurement of the B_s meson mixing frequency is presented in Part III based on $B_s \to D_s\pi\pi\pi$ decays. It is also an essential ingredient to study *CP* violation in the beauty-strange system.

As reasoned in Section 1.4, measurements of *CP* asymmetries generally permit determining the CKM phases. The current world-average values of those are given in Table 3.1. The precision on the CKM angles α and β are driven by measurements of *CP* violation in the B^0 meson system. These include $B^0 \to \pi\pi$ [97, 98] and $B^0 \to J/\psi K^0_s$ [99, 100] decays which are sensitive to the CKM angle α and β, respectively. While a detailed discussion of those measurements would go beyond the scope of this thesis (excellent reviews can be found in References [30, 101]), it is worth noting that the definition of the angles α and β contain CKM matrix elements involving the top quark. This implies that they cannot be accessed in tree-level transitions of the b quark. In that sense, the CKM angle γ, the least well constrained *CP*-violating parameter of the Unitarity Triangle, is unique as it can be accessed by both tree-level and loop-level transitions. New physics phenomena beyond the Standard Model are expected to manifest in loop processes, whereas tree-level decays are unaltered. A precise determination of the CKM angle γ from tree-level processes is therefore an important benchmark of the Standard Model, to be compared with loop-level measurements. The world-average value given in Table 3.1 includes only tree-level measurements. These generally exploit the interference between $b \to u$ and $b \to c$ quark-level transitions. As the interference effect are typically suppressed by the small magnitude of the V_{ub} matrix element, the statistical power of a single decay channel is rather limited. The LHCb collaboration alone has performed 15 (tree-level) measurements sensitive to the CKM angle γ [102], where the most stringent constraints come from measurements of direct *CP* violation in $B^+ \to DK^+$ decays. Their combination gives a value of $\gamma = \left(74.0^{+5.0}_{-5.8}\right)^\circ$ [103] and thus dominates the world-average [30]. The LHCb collaboration has also performed a loop-level measurement based on the charmless $B^0 \to \pi^+\pi^-$ and $B^0_s \to K^+K^-$ decay modes [104–106]. Here, the sensitivity to the CKM angle γ originates from the interference of the $b \to u$ tree-level with the $b \to d$ or $b \to s$ loop-level transitions [107]. The result, $\gamma = \left(63.5^{+7.2}_{-6.7}\right)^\circ$ [104], is in good agreement with the tree-level determination. By imposing the unitarity condition, tighter constraints can be derived from the knowledge of all other CKM parameters. The CKMfitter [30] group performed such a global parameter estimation in order to infer the apex of the Unitarity Triangle as displayed in Figure 3.1. Measurements of the CKM angles (only tree-level measurements of the CKM angle γ are considered) as well as measurements related to the sides of the triangle such as the magnitude of V_{ub}, the mixing frequencies Δm_d and Δm_s

and a measure of *CP* violation in the neutral kaon system, ϵ_K, are incorporated. Within the current precision, the result is consistent with a closed triangle. Under the assumption that the Standard Model holds, this global fit procedure also allows to infer the value of the CKM angle γ *indirectly*, *i.e.* excluding its *direct* measurement, from measurements of all other CKM parameters. The result yields a value of $\gamma = \left(65.64^{+0.97}_{-3.42}\right)^\circ$ [30]. For a meaningful comparison the precision of the direct measurement needs to be improved. There are two complementary ways to increase the accuracy even further, besides collecting more data. One can either attempt to maximize the statistical power of a given measurement by developing more sophisticated analysis techniques or add completely new decay channels to the world-average. Both approaches are investigated in this thesis: the former is discussed in Section 3.2 in context of $B^+ \to DK^+$ decays, while Section 3.3 deals with the yet unexplored opportunity to measure the CKM angle γ from mixing-induced *CP* violation in $B_s \to D_s K\pi\pi$ decays. Experimental aspects and the sensitivity of these analyses are then discussed in Part II and Part III, respectively.

Table 3.1: World-average values for the CKM phases taken from Reference [30].

CKM angle	World average[°]
α	$86.4^{+4.5}_{-4.3}$
β	$22.1^{+0.7}_{-0.7}$
γ	$72.1^{+5.4}_{-5.7}$
β_s	$1.056^{+0.028}_{-0.020}$

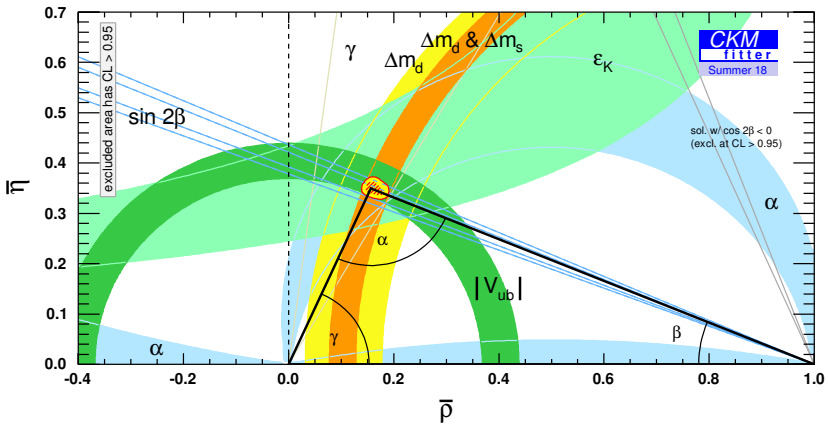

Figure 3.1: Current constraints on the CKM Unitarity Triangle [30]. The side $V_{cd}V_{cb}^*$ is normalized to unit length. Constraints from the CKM angles α, β and γ as wells as from Δm_d and Δm_s and ϵ_K are displayed (shaded areas). The red (yellow) area indicates the 68% (95%) confidence level region of the apex of the triangle.

3.2 Measurement of the CKM angle γ from $B^{\pm} \to DK^{\pm}$ decays

Decays of charged beauty mesons to a neutral charm meson and a bachelor kaon can proceed via $b \to c$ or $b \to u$ quark-level transitions leading to the processes $B^- \to D^0 K^-$ or $B^- \to \bar{D}^0 K^-$, respectively, as depicted in Figure 3.2. The associated CKM matrix elements introduce a relative *CP*-violating weak phase difference of $\arg(V_{ub}V_{cs}^*/(V_{cb}V_{us}^*)) = -\gamma + \mathcal{O}(\lambda^4)$ between the tree-level diagrams. The difference between the weak phase and the CKM angle γ is tiny with respect to the current experimental precision and is ignored in the following. The $B^- \to \bar{D}^0 K^-$ transition is disfavored with respect to the $B^- \to D^0 K^-$ transition due to the involved CKM matrix elements, $|V_{ub}V_{cs}|/|V_{cb}V_{us}| \approx 0.4$, and color suppressed by a factor of three. A naive estimate of the relative magnitude r_B of the $B^- \to \bar{D}^0 K^-$ and $B^- \to D^0 K^-$ decay amplitudes is thus given by $r_B \approx 0.1$. The relative transition rates might be altered by additional QCD effects which also introduce a *CP*-conserving strong phase difference, δ_B, between the two B meson decay processes [108]. Assuming tree-level dominance [109], the ratio of transition amplitudes contributing to $B^- \to DK^-$ and $B^+ \to DK^+$ decays, where D refers to either D^0 or $\bar{D}^0$, can be written as [108, 110, 111]:

$$\frac{A_{B^- \to \bar{D}^0 K^-}}{A_{B^- \to D^0 K^-}} \equiv r_B \, e^{i(\delta_B - \gamma)}, \qquad \frac{A_{B^+ \to D^0 K^+}}{A_{B^+ \to \bar{D}^0 K^+}} \equiv r_B \, e^{i(\delta_B + \gamma)}, \tag{3.1}$$

as illustrated in Figure 3.2. Provided that the charm meson decays into a final state, f, which is accessible for both D^0 and $\bar{D}^0$ flavor states, *e.g.* $f = \{\pi^+\pi^-, \pi^+\pi^-\pi^0, \pi^+\pi^-\pi^+\pi^-, \dots\}$, the superposition of the different decay paths leads to observable *CP* asymmetries and enables access to the CKM angle γ. Following the formalism described in Chapter 2, the $D^0 \to f$ and $\bar{D}^0 \to f$ decay amplitudes are given by the coherent sum over intermediate-state amplitudes,

$$A_D(\mathbf{x}) = \sum_i a_i \, A_i(\mathbf{x}), \qquad A_{\bar{D}}(\mathbf{x}) = \sum_i \bar{a}_i \, \bar{A}_i(\mathbf{x}) = \sum_i \bar{a}_i \, A_i(\overline{\mathbf{x}}), \tag{3.2}$$

where the *CP*-conjugate phase-space point $\overline{\mathbf{x}}$ is defined such that it is mapped onto $\mathbf{x}$ by the interchange of final-state charges and the reversal of three-momenta; for example, $\mathbf{x} = (m^2(\pi^+\pi^0), m^2(\pi^-\pi^0))$ and $\overline{\mathbf{x}} = (m^2(\pi^-\pi^0), m^2(\pi^+\pi^0))$ in case of $f = \pi^+\pi^-\pi^0$. The *CP*-conjugate of a given intermediate-state amplitude, $A_i(\mathbf{x})$, is then defined as $\bar{A}_i(\mathbf{x}) \equiv A_i(\overline{\mathbf{x}})$. Neglecting mixing and assuming no direct *CP* violation in the charm system[1] ($a_i = \bar{a}_i$), the total decay amplitudes are obtained

[1] The small effects of *CP* violation and mixing in the charm system can be straightforward implemented in the formalism, see *e.g.* References [112, 113], but are ignored here for the sake of simplicity.

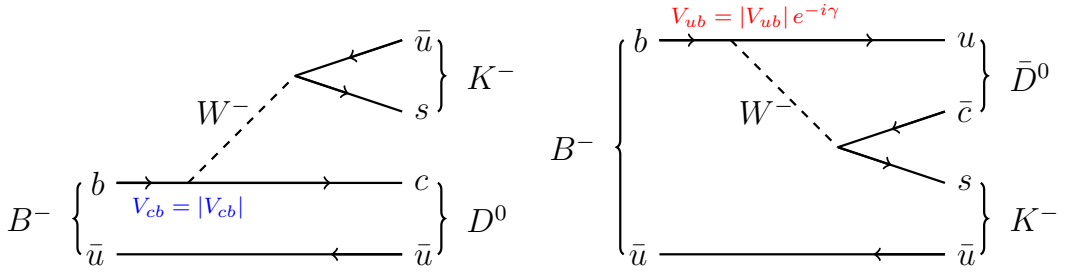

Figure 3.2: Tree-level Feynman diagrams for $B^- \to D^0 K^-$ (left) and $B^- \to \bar{D}^0 K^-$ (right) decays.

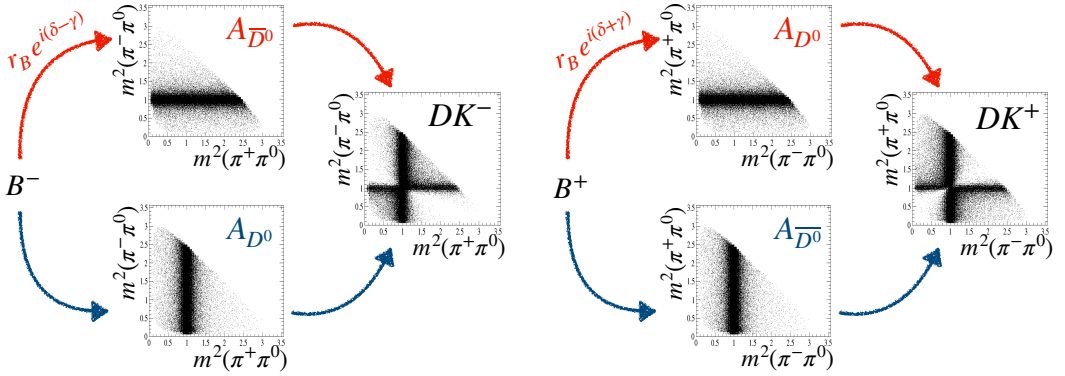

(a) $A_{B^-} = A_{D^0} + r_B\, e^{i(\delta_B - \gamma)} A_{\bar{D}^0}$ **(b)** $A_{B^+} = A_{\bar{D}^0} + r_B\, e^{i(\delta_B + \gamma)} A_{D^0}$

Figure 3.3: Superposition of decays paths contributing to the $B^- \to DK^-$ (left) and $B^+ \to DK^+$ (right) processes with $D \to \pi^+\pi^-\pi^0$. The contribution of a single scalar resonance, $R^{\pm}$, is show: $D^0 \to (R^+ \to \pi^+\pi^0)\pi^-$ and $\bar{D}^0 \to (R^- \to \pi^-\pi^0)\pi^+$. The weak phase difference introduces an asymmetric interference pattern for the B^- and B^+ Dalitz plots. The values $r_B = 0.5$, $\delta_B = 70°$ and $\gamma = 70°$ are chosen. Note that the axes on the B^+ Dalitz plots are flipped, *i.e.* *CP*-conjugated, with respect to the B^- Dalitz plot. In that case the visible phase-space structure of both coincides in case of no *CP* violation ($\gamma = 0$).

by combining the beauty and charm sub-processes [114–116]:

$$\begin{aligned} A_{B^-}(\mathbf{x}) &\propto A_D(\mathbf{x}) + r_B\, e^{i(\delta_B - \gamma)}\, A_{\bar{D}}(\mathbf{x}), \\ A_{B^+}(\mathbf{x}) &\propto A_{\bar{D}}(\mathbf{x}) + r_B\, e^{i(\delta_B + \gamma)}\, A_D(\mathbf{x}). \end{aligned} \tag{3.3}$$

Note that the total decay amplitudes are evaluated in terms of the $D^0 \to f$ phase space point, $\mathbf{x}$. In general, they depend on the higher dimensional phase space of the beauty meson decay. However, the process $B^\pm \to DK^\pm$ is isotropic such that there are effectively no relevant degrees of freedom. Due to the large lifetime of the charm meson it is well justified to consider $B^\pm \to DK^\pm$ and $D \to f$ as isolated processes and factorize the respective decay amplitudes [117]. The lineshape of the charm meson can be written as delta-function (narrow width approximation [118]), $A_{B^\pm \to DK^\pm} \propto \delta(s - m_D^2)$, and the phase space decomposed as [54]: $\mathrm{d}\Phi(B^\pm \to (D \to f)K^\pm) = \mathrm{d}\Phi(B^\pm \to DK^\pm)\,\mathrm{d}\Phi(D \to f)\,\mathrm{d}s$. The former introduces an error of the order $\Gamma_D/m_D \approx 10^{-15}$, the latter is strictly valid. After performing the integral over the D meson invariant mass squared, s, and the trivial solid angle in $\mathrm{d}\Phi(B^\pm \to DK^\pm)$, only the $D \to f$ phase space, $\mathrm{d}\Phi(D \to f)$, with on-shell D mass remains. This implies that the $D^0 \to f$ and $\bar{D}^0 \to f$ Dalitz plots interfere, as depicted in Figure 3.3 for a simple example. The phases δ_B and γ rotate the Dalitz plots with respect to each other, where the weak phase γ introduces an asymmetric interference pattern for B^- and B^+ meson decays:

$$\begin{aligned} |A_{B^-}(\mathbf{x})|^2 &\propto |A_D(\mathbf{x})|^2 + r_B^2 |A_{\bar{D}}(\mathbf{x})|^2 + 2r_B |A_D(\mathbf{x})||A_{\bar{D}}(\mathbf{x})| \cos(\delta_B + \Delta\phi_D(\mathbf{x}) - \gamma), \\ |A_{B^+}(\mathbf{x})|^2 &\propto |A_{\bar{D}}(\mathbf{x})|^2 + r_B^2 |A_D(\mathbf{x})|^2 + 2r_B |A_D(\mathbf{x})||A_{\bar{D}}(\mathbf{x})| \cos(\delta_B + \Delta\phi_D(\mathbf{x}) + \gamma), \end{aligned} \tag{3.4}$$

where the strong phase difference $\Delta\phi_D(\mathbf{x}) \equiv \arg(A_D(\mathbf{x})) - \arg(A_{\bar{D}}(\mathbf{x}))$ between D^0 and $\bar{D}^0$ decays is introduced. Due to the small branching fraction of the total decay chain, $\mathcal{B}(B^\pm \to (D \to f)K^\pm) \approx 10^{-7}$ [10], and the small interference effect, proportional to $r_B \approx 0.1$, it proves elusive to determine the hadronic parameters of the charm decay and the physical observables of the beauty decay simultaneously. Fortunately, the charm decay amplitudes can also be determined exploiting other production mechanisms providing more abundant data samples, such as the direct production in proton-proton or electron-positron collisions. With these as input, the phases δ_B and γ as well as the parameter r_B can be extracted from B^- and B^+ decays by comparing their phase-space distributions.

The total yields of B^- ($N(B^-)$) and B^+ ($N(B^+)$) decays are given by the integral of Equation 3.4 over the entire phase space [119]:

$$N(B^{\pm}) \propto 1 + r_B^2 + 2\, r_B\, (2F_+ - 1)\, \cos(\delta_B \pm \gamma). \tag{3.5}$$

They provide sensitivity to the CKM angle γ which is however diluted by the factor $(2F_+ - 1) \in [-1, 1]$ arising from the integration over the interfering amplitudes. The parameter F_+ can be physically interpreted as the average *CP*-even fraction of the D meson decay. For this, it is instructive to consider the decay in terms of the *CP* eigenstates $|D_{CP\pm}\rangle = (|D^0\rangle \pm |\bar{D}^0\rangle)/\sqrt{2}$ (which are approximately equal to the mass eigenstates [35] D_L and D_H defined in Equation 1.5) with the corresponding amplitudes $A_{CP\pm}(\mathbf{x}) = (A_D(\mathbf{x}) \pm A_{\bar{D}}(\mathbf{x}))/\sqrt{2}$. The *CP*-even fraction is then defined as [119, 120]:

$$\begin{aligned} F_+ &\equiv \frac{\int |A_{CP+}(\mathbf{x})|^2 \, \mathrm{d}\Phi}{\int |A_{CP+}(\mathbf{x})|^2 + |A_{CP-}(\mathbf{x})|^2 \, \mathrm{d}\Phi} \\ &= \frac{\int |A_D(\mathbf{x})|^2 + |A_{\bar{D}}(\mathbf{x})|^2 + 2|A_D(\mathbf{x})||A_{\bar{D}}(\mathbf{x})| \, \cos(\Delta\phi_D(\mathbf{x})) \, \mathrm{d}\Phi}{2 \int |A_D(\mathbf{x})|^2 + |A_{\bar{D}}(\mathbf{x})|^2 \, \mathrm{d}\Phi}. \end{aligned} \tag{3.6}$$

Figure 3.4 compares the $B^{\pm} \to (D \to \pi^+\pi^-\pi^+\pi^-)K^{\pm}$ yields measured by the LHCb collaboration [121], where a *CP* asymmetry,

$$A_{CP} = \frac{N(B^-) - N(B^+)}{N(B^-) + N(B^+)} = (10.0 \pm 3.4\,(\text{stat}) \pm 1.8\,(\text{syst}))\%, \tag{3.7}$$

is perceivable by eye. To interpret the result in terms of the observables r_B, δ_B and γ, knowledge of the *CP*-even fraction is required. For D meson decays into *CP* eigenstates, it is trivially known, *e.g.* $F_+ = 1$ for $f = \pi^+\pi^-$ (*CP*-even) or $F_+ = 0$ for $f = K^0_s\pi^0$ (*CP*-odd). For more complicated cases, such as $f = \pi^+\pi^-\pi^+\pi^-$, it can either be derived from the decay amplitudes or directly measured from quantum entangled $D\bar{D}$ pairs as explained later.

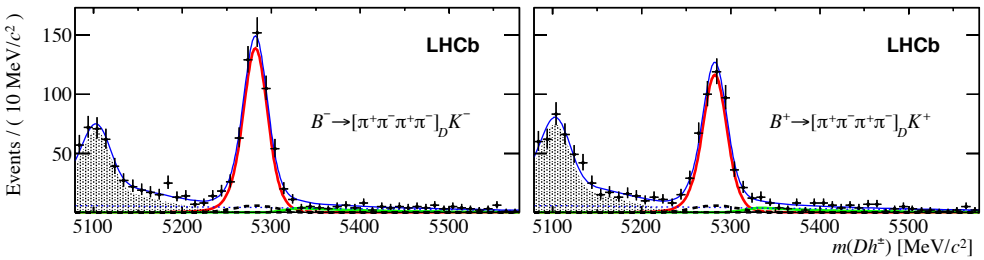

Figure 3.4: Invariant mass distributions of $B^- \to DK^-$ (left) and $B^+ \to DK^+$ (right) candidates with $D \to \pi^+\pi^-\pi^+\pi^-$. Modified from [121].

Model-unbiased measurement of the CKM angle γ

There are essentially two alternative approaches to determine the CKM angle γ from $B^{\pm} \to DK^{\pm}$ decays: a *model-dependent* method based on Equation 3.4 which relies on a parameterization of the decay amplitudes [114–116]; and a *model-independent* one which uses the total event yields and requires only the *CP*-even fraction of the decay as input [119,120]. For charm decays to two-body final-states, solely the latter approach is possible. The model-independent approach is also the only method which has so far been explored for the four-body $f = \pi^+\pi^-\pi^+\pi^-$ final state [121]. Besides the dilution of the sensitivity with the factor $(2F_+ - 1)$, there are several disadvantages of this method. First, the total yields provide just two measurable quantities, $N(B^-) - N(B^+) \propto 2r_B\,(2F_+ - 1)\sin(\delta_B)\sin(\gamma)$ and $N(B^-) + N(B^+) \propto 1 + r_B^2 + 2r_B\,(2F_+ - 1)\cos(\delta_B)\cos(\gamma)$, while there are three unknowns, r_B, δ_B and γ. Therefore several such measurements in different final states, $f = \{\pi^+\pi^-, K^+K^-, K^0_s\pi^0, \dots\}$, need to be combined to provide sufficient constraints. Still, the CKM angle γ can only be determined up to an eight-fold discrete ambiguity. The model-dependent method overcomes these drawbacks. It compares the event density at each infinitesimal phase-space point providing sufficient information to extract all physical observables and the strong-phase variation resolves discrete phase ambiguities. Hence, a stand-alone measurement of the CKM angle γ in a single decay channel with only a two-fold ambiguity ($\gamma \to \gamma + 180°$, $\delta_B \to \delta_B + 180°$), *i.e.* a single solution in the interval $[0°, 180°]$, is feasible. This is the best way to exploit the available statistics, in principle. On the downside, the model uncertainty of the amplitude description is hard to quantify with a sufficient level of confidence and introduces an irreducible systematic uncertainty on the extraction of the CKM angle γ; particularly relevant for future high precision measurements.

A hybrid approach improves the model-independent method by measuring the yields in several disjoint hyper-volumes (*bins*) of the phase space [114, 122, 123]. Consider, for example, a final state with *CP*-even fraction $F_+ = 50\%$. In that case, the *CP*-even and *CP*-odd contributions would cancel each other and no total yield asymmetry would be observable, see Equation 3.5. By separating the Dalitz plot into (predominantly) *CP*-even and *CP*-odd regions, an optimal sensitivity to the CKM angle γ can be reached. Even though an amplitude model is indispensable to identify such regions, the results obtained are model independent, in the sense that an inaccurate amplitude description results only in an increased statistical uncertainty but does not bias the measurement. In particular, one expects that the binning scheme inspired by any reasonable amplitude model gives a better

sensitivity than choosing bins randomly. This approach will be referred to as *model-unbiased* method in the following. Figure 3.5 shows an example for an amplitude-model inspired Dalitz-plot binning for the $D^0 \to K^0_s\pi^+\pi^-$ decay. Here, the regions of phase space are chosen such that the strong phase difference $\Delta\phi_D(\mathbf{x})$ is approximately equal in each bin. Other possible metrics optimizing the sensitivity for a measurement of the CKM angle γ are discussed *e.g.* in Reference [124].

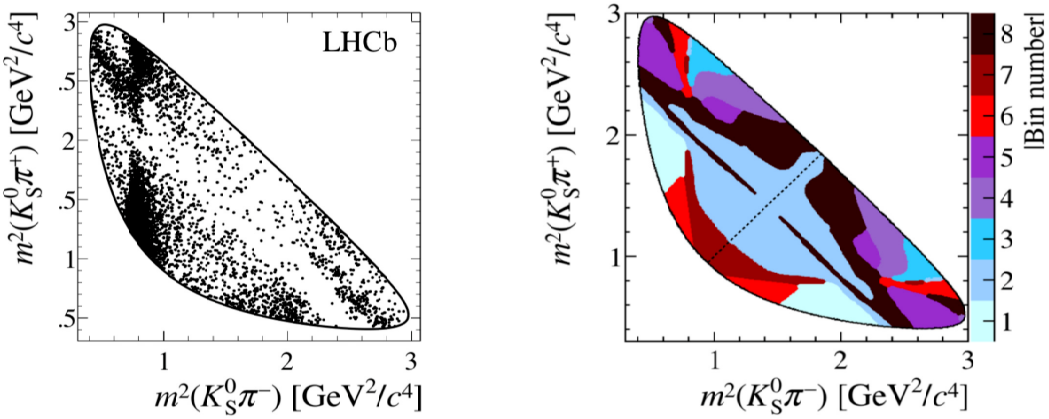

Figure 3.5: Dalitz plot distribution of $D^0 \to K^0_s\pi^+\pi^-$ decays (left), modified from Reference [125], and model inspired binning of the phase space (right), where the Figure is taken from Reference [126] and the amplitude model has been determined in Reference [127].

Model-independent measurement of strong phases

The yield of B^- and B^+ decays in a given phase-space bin, i, are determined by:

$$N_i(B^+) \propto T_i + r_B^2\,\bar{T}_i + 2\,r_B\,\sqrt{T_i\,\bar{T}_i}\,\left(c_i\,\cos(\delta_B-\gamma) + s_i\,\sin(\delta_B-\gamma)\right),$$
$$N_i(B^-) \propto \bar{T}_i + r_B^2\,T_i + 2\,r_B\,\sqrt{T_i\,\bar{T}_i}\,\left(c_i\,\cos(\delta_B+\gamma) + s_i\,\sin(\delta_B+\gamma)\right), \quad (3.8)$$

where the fraction of $D^0 \to f$ and $\bar{D}^0 \to f$ decays that populate this bin are denoted as $T_i \equiv K_i/\sum_i K_i$ and $\bar{T}_i \equiv \bar{K}_i/\sum_i \bar{K}_i$ with $K_i \equiv \int_{\text{Bin}\,i} |A_D|^2 \mathrm{d}\Phi$ and $\bar{K}_i \equiv \int_{\text{Bin}\,i} |A_{\bar{D}}|^2 \mathrm{d}\Phi$ [114]. The average strong phase difference is quantified by the parameters:

$$c_i \equiv \frac{\int_{\text{Bin}\,i} |A_D|\,|A_{\bar{D}}|\cos(\Delta\Phi_D)\mathrm{d}\Phi}{\sqrt{K_i\,\bar{K}_i}}, \quad s_i \equiv \frac{\int_{\text{Bin}\,i} |A_D|\,|A_{\bar{D}}|\sin(\Delta\Phi_D)\mathrm{d}\Phi}{\sqrt{K_i\,\bar{K}_i}}. \quad (3.9)$$

Noting that $\sum_i T_i = 1$, $\sum_i \bar{T}_i = 1$, $\sum_i c_i = 2F_+ - 1$ and $\sum_i s_i = 0$ (due to the symmetry of the Dalitz plot), Equation 3.8 is retained by summing over all bins,

$N(B^\pm) = \sum_i N_i(B^\pm)$. All of these hadronic parameters (T_i, $\bar{T}_i$, c_i and s_i) can be measured from $D \to f$ decays, provided that the charm meson is produced in a well-known superposition of D and $\bar{D}$ states [128, 129]. Such well-defined superposition states are prepared in decays of the $\psi(3770)$ charmonium resonance, which can be efficiently produced in electron-positron collider experiments, for example at CLEO-c (or BES-III) as discussed in Chapter 5. The $\psi(3770)$ meson has quantum numbers $J^{PC} = 1^{--}$ which are conserved in its strong decay to a charm meson pair, $\psi(3770) \to D_a \bar{D}_b$. Hence, the quantum numbers, in particular the flavor and *CP* content, of the combined $D_a \bar{D}_b$ system are known such that the charm mesons propagate in a quantum entangled state. The charge conjugation eigenvalue of the $\psi(3770)$ meson implies an asymmetric wave function of the entangled system, $|D_a^0 \bar{D}_b^0\rangle - |\bar{D}_a^0 D_b^0\rangle$. For the entangled decay amplitude follows: $A_{D_a\, D_b}(\mathbf{x}, \mathbf{x}') \equiv A_{D_a^0}(\mathbf{x}) A_{\bar{D}_b^0}(\mathbf{x}') - A_{\bar{D}_a^0}(\mathbf{x}) A_{D_b^0}(\mathbf{x}')$, where $\mathbf{x}$ ($\mathbf{x}'$) refers to the phase space of the $D_a \to f_a$ ($D_b \to f_b$) decay. This implies that as soon as the wave function of one of the charm mesons, D_b, collapses, *i.e.* it is reconstructed in a decay to a final state f_b, the quantum state of the other charm meson, D_a, is fixed. Now, let particle D_a decay into the final state of interest, $f_a = \pi^+\pi^-\pi^+\pi^-$. If particle D_b is reconstructed in a *CP*-even (*CP*-odd) eigenstate, $f_b = \{\pi^+\pi^-, K^+K^-, \dots\}$ ($f_b = \{K_s^0\pi^0, K_s^0\eta, \dots\}$), then the D_a meson is know to be in a *CP*-odd (*CP*-even) state[2] and decays with the amplitude $A_{CP-}(\mathbf{x})$ ($A_{CP+}(\mathbf{x})$). Equivalently, if D_b is in a flavor eigenstate, $D_b = D^0$ or $D_b = \bar{D}^0$, the flavor of D_a has to be the opposite, $D_a = \bar{D}^0$ or $D_a = D^0$. As a result, the phase-space distribution of the $D_a \to f_a$ decay differs depending on the final state of the other charm meson and the following yields are observed in a given ($D_a \to f_a$) phase-space bin (note the striking resemblance to Equation 3.8):

$$\begin{aligned}
D_a = D^0 : &\qquad N_i(D^0) \propto T_i \\
D_a = \bar{D}^0 : &\qquad N_i(\bar{D}^0) \propto \bar{T}_i \\
D_a = D_{CP+} : &\qquad N_i(D_{CP+}) \propto T_i + \bar{T}_i + 2\sqrt{T_i\,\bar{T}_i}\,c_i \\
D_a = D_{CP-} : &\qquad N_i(D_{CP-}) \propto T_i + \bar{T}_i - 2\sqrt{T_i\,\bar{T}_i}\,c_i.
\end{aligned} \tag{3.10}$$

By measuring these yields, the hadronic parameters T_i, $\bar{T}_i$ and c_i can be determined.

[2] The $\psi(3770)$ meson has the *CP* eigenvalue +1. This implies that the two charm mesons have opposite *CP* content, $CP|D_a\rangle = -CP|D_b\rangle$, since $CP|\psi\rangle = 1 \stackrel{!}{=} CP|D_a\rangle CP|D_b\rangle(-1)^L$, where $L = 1$ is the relative orbital angular momentum between the two charm mesons conserving the resonance's spin.

The measurement of s_i is more involved and requires to reconstruct the other charm meson in a mixed-*CP* state such as $f_b = K^0_s\pi^+\pi^-$ or $f_b = f_a = \pi^+\pi^-\pi^+\pi^-$ [124, 130]. In that case, also the phase space ($\mathbf{x}'$) of the $D_b \to f_b$ decay has to be divided in bins. The number of cases in which the D_a decay is reconstructed in the $D_a \to f_a$ phase-space bin i and (at the same time) the D_b decay is reconstructed in the $D_b \to f_b$ phase-space bin j is denoted as $N_{ij}(D_a, D_b)$. It is calculated by integrating the absolute square of the entangled decay amplitude ($|A_{D_a\,D_b}(\mathbf{x}, \mathbf{x}')|^2$) in regions of the $D_a \to f_a$ and $D_b \to f_b$ phase spaces:

$$N_{ij}(D_a, D_b) \propto T_i\,\bar{T}'_j + \bar{T}_i\,T'_j - 2\sqrt{T_i\,\bar{T}'_j\,\bar{T}_i\,T'_j}(c_i\,c'_j + s_i\,s'_j), \tag{3.11}$$

where the hadronic parameters of the $D_b \to f_b$ decay (T'_i, $\bar{T}'_i$, c'_i and s'_i) are equivalently defined as for the $D_a \to f_a$ decay. The hadronic parameters for $f_b = K^0_s\pi^+\pi^-$ have been measured in Reference [128]. For $f_b = f_a = \pi^+\pi^-\pi^+\pi^-$, they are identical to the to be determined $D_a \to f_a$ parameters.

3.3 Extracting the CKM angle γ from $B_s \to D_s K\pi\pi$ decays

Decays of B_s^0 mesons to the $D_s^- K^+\pi^+\pi^-$ final state proceed via $\bar{b} \to \bar{c}$ quark-level transitions as depicted in Figure 3.6(left). Sensitivity to the CKM angle γ originates from the interference with $b \to u$ quark-level transitions leading to $\overline{B}_s^0 \to D_s^- K^+\pi^+\pi^-$ decays as shown in Figure 3.6(right) [131–135]. This is achieved through a foregone B_s^0 to $\overline{B}_s^0$ mixing process as illustrated in Figure 3.7. Due to the involved CKM matrix elements, the $\overline{B}_s^0 \to D_s^- K^+\pi^+\pi^-$ decay is suppressed relative to the (direct) $B_s^0 \to D_s^- K^+\pi^+\pi^-$ decay by a factor of $r \approx |V_{ub}\,V_{cs}|/|V_{bc}\,V_{us}| \approx 0.4$, altered by additional strong interaction effects. The weak phase difference is, again to a good approximation, given by the CKM angle γ [131, 135], *i.e.* $\arg(V_{ub}\,V_{cs}^*/(V_{bc}^*\,V_{us})) \approx -\gamma$.

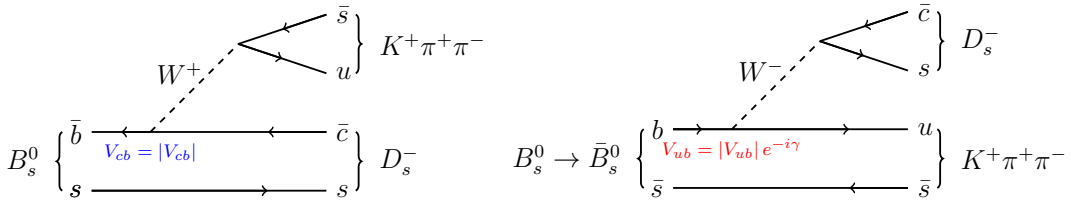

Figure 3.6: Leading order Feynman diagrams for $B_s^0 \to D_s^- K^+\pi^+\pi^-$ (left) and $\overline{B}_s^0 \to D_s^- K^+\pi^+\pi^-$ (right) decays.

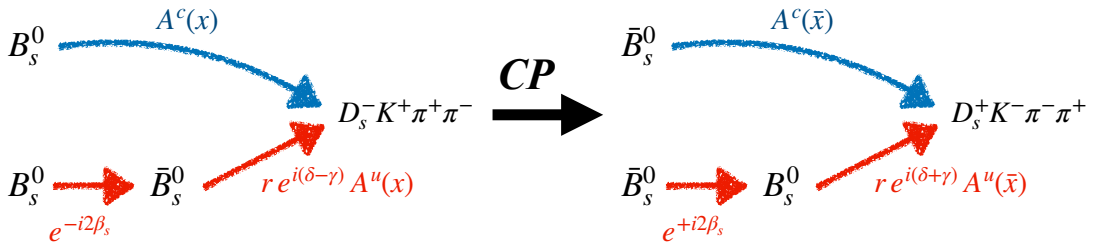

Figure 3.7: Possible decay paths of an initial B_s ($\overline{B}_s^0$) meson to reach the final state $D_s^- K^+\pi^+\pi^-$ ($D_s^+ K^-\pi^-\pi^+$) are illustrated on the left (right).

Differential decay rate

To derive the resulting decay rate, the mixing formalism introduced in Section 1.3 needs to be extended. Instead of the probability to observe an initially produced B_s^0 meson in a certain flavor eigenstate, *e.g.* $|\langle B_s^0|B_s^0(t)\rangle|^2$, the probability to observe a decay to the final state $f = D_s^- K^+\pi^+\pi^-$, $|\langle f|B_s^0(t)\rangle|^2$, is of interest. The static decay amplitudes of the flavor eigenstates are denoted as:

$$\langle f|B_s^0\rangle \equiv A^c(\mathbf{x}), \qquad \langle f|\overline{B}_s^0\rangle \equiv r\, e^{i(\delta-\gamma)}\, A^u(\mathbf{x}), \tag{3.12}$$

with the relative magnitude r and the (constant) strong and weak phase differences δ and γ, respectively. The dynamical part is described by the hadronic amplitudes $A^c(\mathbf{x})$ and $A^u(\mathbf{x})$, where the superscript c (u) refers to a $b \to c$ ($b \to u$) quark-level transition. These are parameterized in terms of a coherent sum over intermediate-state amplitudes:

$$A^c(\mathbf{x}) = \sum_i a_i^c\, A_i(\mathbf{x}), \qquad A^u(\mathbf{x}) = \sum_i a_i^u\, A_i(\mathbf{x}). \tag{3.13}$$

While $B_s^0 \to f$ and $\overline{B}_s^0 \to f$ decays share the same set of possible intermediate-state amplitudes, $A_i(\mathbf{x})$, their hadronization process is different leading to distinct amplitude coefficients, $a_i^c \neq a_i^u$. The magnitude squared of the hadronic amplitudes is normalized to unity when integrated over the entire phase space, $\int |A^c(\mathbf{x})|^2\, \mathrm{d}\Phi_4(\mathbf{x}) = \int |A^u(\mathbf{x})|^2\, \mathrm{d}\Phi_4(\mathbf{x}) = 1$. Similarly, the overall strong phase difference between $A^c(\mathbf{x})$ and $A^u(\mathbf{x})$ is normalized to zero, $\arg\left(\int A^c(\mathbf{x})^*\, A^u(\mathbf{x})\, \mathrm{d}\Phi_4(\mathbf{x})\right) = 0$. This ensures that the parameters r and δ do not depend on the convention employed for the amplitude coefficients. The D_s meson is considered as a stable particle due to its large lifetime (narrow decay width) with respect to the strongly decaying intermediate resonances contributing to the $K\pi\pi$ sub-system. Since the D_s meson is a pseudoscalar particle, no relevant polarization information is lost by not considering its sub-decay modes. These only play a role for experimental aspects of the analysis discussed later. With these considerations, the differential decay rates for initial B_s^0 or $\overline{B}_s^0$ mesons follow from their time development in

Equation 1.7 [34, 38, 135]:

$$\begin{aligned}
\frac{d\Gamma(B_s^0 \to f)}{dt\, \mathrm{d}\Phi_4(\mathbf{x})} = |\langle f|B_s^0(t)\rangle|^2 \propto e^{-\Gamma_s t}\Bigg[&\left(|A^c(\mathbf{x})|^2 + r^2\,|A^u(\mathbf{x})|^2\right)\cosh\left(\frac{\Delta\Gamma_s\, t}{2}\right)\\
&+\left(|A^c(\mathbf{x})|^2 - r^2\,|A^u(\mathbf{x})|^2\right)\cos\left(\Delta m_s\, t\right)\\
&-2\,r\,\mathrm{Re}\left(A^c(\mathbf{x})^*\,A^u(\mathbf{x})\,e^{i(\delta-(\gamma-2\beta_s))}\right)\sinh\left(\frac{\Delta\Gamma_s\, t}{2}\right)\\
&-2\,r\,\mathrm{Im}\left(A^c(\mathbf{x})^*\,A^u(\mathbf{x})\,e^{i(\delta-(\gamma-2\beta_s))}\right)\sin\left(\Delta m_s\, t\right)\Bigg],\\
\frac{d\Gamma(\overline{B}_s^0 \to f)}{dt\, \mathrm{d}\Phi_4(\mathbf{x})} = |\langle f|\overline{B}_s^0(t)\rangle|^2 \propto e^{-\Gamma_s t}\Bigg[&\left(|A^c(\mathbf{x})|^2 + r^2\,|A^u(\mathbf{x})|^2\right)\cosh\left(\frac{\Delta\Gamma_s\, t}{2}\right)\\
&-\left(|A^c(\mathbf{x})|^2 - r^2\,|A^u(\mathbf{x})|^2\right)\cos\left(\Delta m_s\, t\right)\\
&-2\,r\,\mathrm{Re}\left(A^c(\mathbf{x})^*\,A^u(\mathbf{x})\,e^{i(\delta-(\gamma-2\beta_s))}\right)\sinh\left(\frac{\Delta\Gamma_s\, t}{2}\right)\\
&+2\,r\,\mathrm{Im}\left(A^c(\mathbf{x})^*\,A^u(\mathbf{x})\,e^{i(\delta-(\gamma-2\beta_s))}\right)\sin\left(\Delta m_s\, t\right)\Bigg].
\end{aligned} \tag{3.14}$$

Here, the mixing process introduces an additional weak phase difference, equivalent to the phase between the complex coefficients q and p which relate the B_s meson mass eigenstates to the flavor eigenstates as described in Section 1.3. To leading order, this phase originates from the top quark contribution to the box-diagram (shown in Figure 1.2) mediating the mixing process such that it can be related to the CKM angle β_s, $\arg(q/p) \approx 2\arg(V_{tb}\,V_{ts}^*) \approx -2\beta_s$ [38, 135]. Assuming the Standard Model, the phase $-2\beta_s$ is approximately equal to the weak phase measured in $B_s \to J/\psi\,\phi$ [136] and related decays [137–139], referred to as ϕ_s in the literature [38]. This phase is experimentally well constrained to be $\phi_s = (-1.20 \pm 1.78)^\circ$ [35], consistent with zero. By taking ϕ_s as external input, the presented analysis of $B_s \to D_s K\pi\pi$ decays can be considered as a measurement of the CKM angle γ. The magnitude of q/p is assumed to be unity (no *CP* violation in mixing), as determined experimentally with very high precision ($|q/p| = 1.0003 \pm 0.0014$ [35, 140]). The decay rates to the *CP*-onjugate final state $\bar{f} = D_s^+ K^-\pi^-\pi^+$ (with phase-space point $\overline{\mathbf{x}}$), $d\Gamma(\overline{B}_s^0 \to \bar{f})$ and $d\Gamma(B_s^0 \to \bar{f})$, follow from the expressions for $d\Gamma(B_s^0 \to f)$ and $d\Gamma(B_s^0 \to f)$ in Equation 3.14 by replacing $A^c(\mathbf{x}) \to A^c(\overline{\mathbf{x}})$, $A^u(\mathbf{x}) \to A^u(\overline{\mathbf{x}})$ and $-(\gamma - 2\beta_s) \to +(\gamma - 2\beta_s)$, as illustrated in Figure 3.7. This assumes no direct *CP* violation in the hadronic

amplitudes (*i.e.* $a_i^c = \bar{a}_i^c$ and $a_i^u = \bar{a}_i^u$), as expected for tree-level dominated decays. The four decay rates are collectively described by the following PDF:

$$\begin{aligned}\mathcal{P}(\mathbf{x}_{q_f}, t, q_i, q_f) \propto e^{-\Gamma_s t}\Bigg[&\left(|A^c(\mathbf{x}_{q_f})|^2 + r^2\,|A^u(\mathbf{x}_{q_f})|^2\right)\cosh\left(\frac{\Delta\Gamma_s\, t}{2}\right)\\ &+ q_i\, q_f\left(|A^c(\mathbf{x}_{q_f})|^2 - r^2\,|A^u(\mathbf{x}_{q_f})|^2\right)\cos\left(\Delta m_s\, t\right)\\ &- 2\,r\,\mathrm{Re}\left(A^c(\mathbf{x}_{q_f})^*\,A^u(\mathbf{x}_{q_f})\,e^{i\left(\delta - q_f(\gamma-2\beta_s)\right)}\right)\sinh\left(\frac{\Delta\Gamma_s\, t}{2}\right)\\ &- 2\,q_i\,q_f\,r\,\mathrm{Im}\left(A^c(\mathbf{x}_{q_f})^*\,A^u(\mathbf{x}_{q_f})\,e^{i\left(\delta - q_f(\gamma-2\beta_s)\right)}\right)\sin\left(\Delta m_s\, t\right)\Bigg],\end{aligned} \tag{3.15}$$

where the discrete observables $q_i = \{+1, -1\}$ and $q_f = \{+1, -1\}$ refer to the initial flavor state $(B_s^0, \overline{B}_s^0)$ and the final state $(f, \bar{f})$, respectively. The phase-space point, $\mathbf{x}_{q_f}$, depends on the final state. For $q_f = +1$ (-1), it is $\mathbf{x}_{q_f} = \mathbf{x}$ $(\overline{\mathbf{x}})$. The sensitivity to the weak phase $\gamma - 2\beta_s$ stems from the interference terms, given by the third and fourth term in Equation 3.15. These introduce a time-dependent asymmetry between decay rates which are related by a *CP* transformation as displayed in Figure 3.8. Simulated phase-space distributions for initial B_s^0 and $\overline{B}_s^0$ mesons decaying to the final states f and $\bar{f}$ are compared. At different decay-times, distinct local asymmetries are observed, most notably in regions where a resonance contributes to both $b \to c$ and $b \to u$ quark-level transitions.

Decay-time distribution

It is also instructive to examine the decay rates as function of the decay-time only, by integrating over the phase-space:

$$\begin{aligned}\int \mathcal{P}(\mathbf{x}_{q_f}, t, q_i, q_f)\,\mathrm{d}\Phi_4(\mathbf{x}_{q_f}) &\equiv \mathcal{P}(t, q_i, q_f)\\ &\propto \Bigg[\cosh\left(\frac{\Delta\Gamma_s\, t}{2}\right) + q_i\, q_f\, C\cos\left(\Delta m_s\, t\right)\\ &\quad + D_{q_f}\sinh\left(\frac{\Delta\Gamma_s\, t}{2}\right) - \, q_i\; S_{q_f}\sin\left(\Delta m_s\, t\right)\Bigg]e^{-\Gamma_s t},\end{aligned} \tag{3.16}$$

where the five *CP coefficients* $C, D \equiv D_{q_f=+1}, \bar{D} \equiv D_{q_f=-1}, S \equiv S_{q_f=+1}$ and $\bar{S} \equiv S_{q_f=-1}$ are defined as [141]:

$$C = \frac{1-r^2}{1+r^2}, \quad D_{q_f} = -\frac{2\,r\,\kappa\cos\left(\delta - q_f\left(\gamma - 2\beta_s\right)\right)}{1+r^2}, \quad S_{q_f} = \, q_f\,\frac{2\,r\,\kappa\sin\left(\delta - q_f\left(\gamma - 2\beta_s\right)\right)}{1+r^2}. \tag{3.17}$$

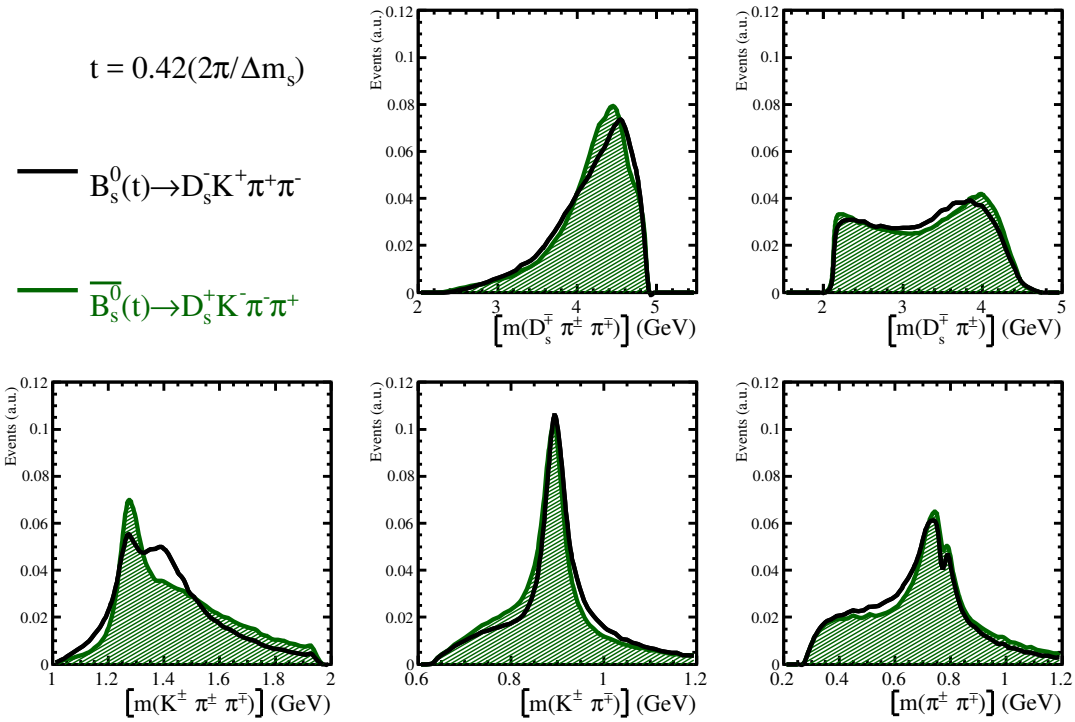

(a) Phase-space projections at decay time $t = 0.42(2\pi/\Delta m_s)$.

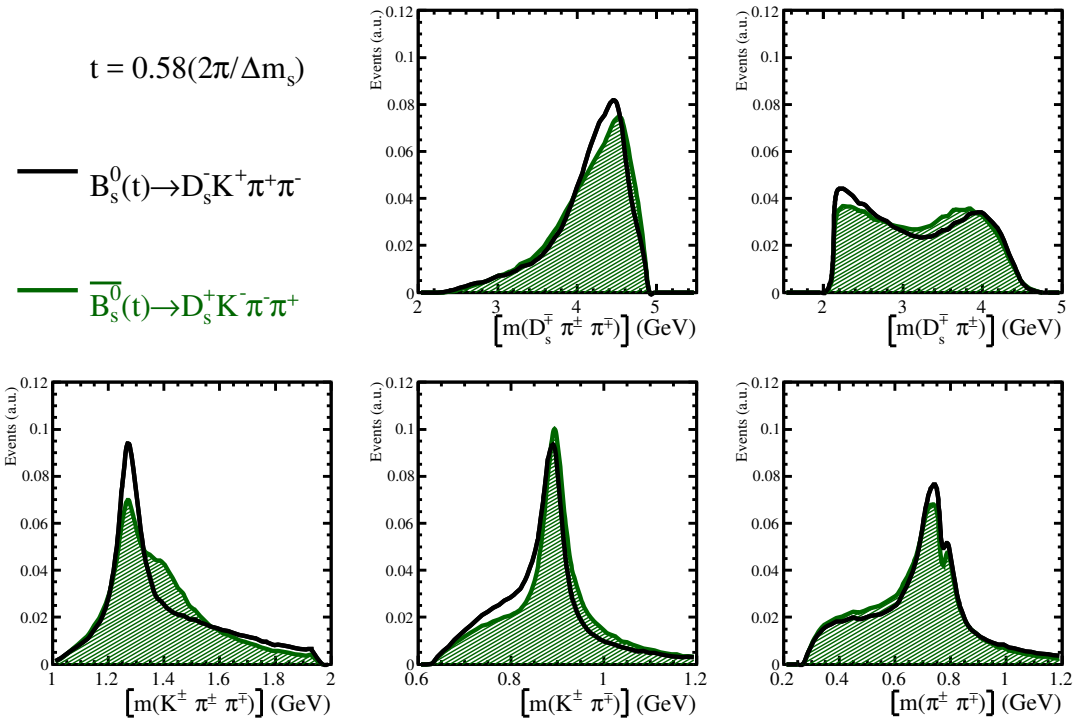

(b) Phase-space projections at decay time $t = 0.58(2\pi/\Delta m_s)$.

Figure 3.8: Simulated phase-space distributions for initial B_s^0 (black) and $\overline{B}_s^0$ (green) mesons decaying to the final states f and $\bar{f}$, respectively. Several resonances decaying into $K^+\pi^+\pi^-$, $K^+\pi^-$ and $\pi^+\pi^-$ are included with different relative magnitudes and phases for $b \to c$ and $b \to u$ quark-level transitions. The values $r = 0.4$, $\delta = 10°$ and $\gamma - 2\beta_s = 70°$ are assumed.

Henceforth, the terminology *sinusoidal* (*hyperbolic*) coefficients is used to refer to the parameters C, S and $\bar{S}$ (D and $\bar{D}$). The *coherence factor* κ results from the integration over the interfering amplitudes across the phase space,

$$\kappa \equiv \int A^c(\mathbf{x})^* \, A^u(\mathbf{x}) \, \mathrm{d}\Phi_4, \tag{3.18}$$

and is bounded between zero and unity. It is $\kappa \approx 1$ for $A^c(\mathbf{x}) \approx A^u(\mathbf{x})$, whereas $B_s^0 \to f$ and $\overline{B}_s^0 \to f$ decays that populate separate regions of the phase space would lead to $\kappa = 0$. Figure 3.9(left) compares simulated decay-time distributions for initial B_s^0 and $\overline{B}_s^0$ mesons decaying into the $D_s^- K^+\pi^+\pi^-$ and $D_s^-\pi^+\pi^+\pi^-$ final states. The latter is a *flavor-specific* decay mode, meaning that the direct decay $B_s^0 \to f$ ($\overline{B}_s^0 \to \bar{f}$) is possible, while $B_s^0 \to \bar{f}$ ($\overline{B}_s^0 \to f$) decays are not permitted (or strongly suppressed). This implies $r = \kappa = 0$ ($C = 1$ and $D = \bar{D} = S = \bar{S} = 0$) simplifying the decay-time PDF in Equation 3.16 substantially. Figure 3.9(right) compares the corresponding *mixing asymmetries*, defined as [131, 132]:

$$\begin{aligned} A^f_{\mathrm{mix}}(t) &= \frac{N_f(t) - \bar{N}_f(t)}{N_f(t) + \bar{N}_f(t)} = \frac{C\cos\left(\Delta m_s\, t\right) - S\sin\left(\Delta m_s\, t\right)}{\cosh\left(\frac{\Delta\Gamma_s\, t}{2}\right) + D\sinh\left(\frac{\Delta\Gamma_s\, t}{2}\right)}, \\ A^{\bar{f}}_{\mathrm{mix}}(t) &= \frac{\bar{N}_{\bar{f}}(t) - N_{\bar{f}}(t)}{\bar{N}_{\bar{f}}(t) + N_{\bar{f}}(t)} = \frac{C\cos\left(\Delta m_s\, t\right) + \bar{S}\sin\left(\Delta m_s\, t\right)}{\cosh\left(\frac{\Delta\Gamma_s\, t}{2}\right) + \bar{D}\sinh\left(\frac{\Delta\Gamma_s\, t}{2}\right)}, \end{aligned} \tag{3.19}$$

where $N_f(t)$ ($\bar{N}_f(t)$) and $N_{\bar{f}}(t)$ ($\bar{N}_{\bar{f}}(t)$) denote the number of initially produced B_s ($\overline{B}_s^0$) mesons decaying at proper-time t to the final states f and $\bar{f}$, respectively. For flavor-specific final states, both mixing asymmetries are equal, $A^f_{\mathrm{mix}}(t) = A^{\bar{f}}_{\mathrm{mix}}(t) = \cos\left(\Delta m_s\, t\right) / \cosh\left(\frac{\Delta\Gamma_s\, t}{2}\right)$, and have the largest possible oscillation amplitude allowing to measure the mixing frequency Δm_s with high precision [142]. An observation of $A^f_{\mathrm{mix}}(t) \neq A^{\bar{f}}_{\mathrm{mix}}(t)$ would signal *CP* violation, as expected for the $D_s^- K^+\pi^+\pi^-$ final state. Equivalently, one can construct two *time-dependent CP asymmetries* as follows:

$$\begin{aligned} A^{\langle f\rangle}_{CP}(t) &= \frac{\left(N_f(t) + N_{\bar{f}}(t)\right) - \left(\bar{N}_{\bar{f}}(t) + \bar{N}_f(t)\right)}{\left(N_f(t) + N_{\bar{f}}(t)\right) + \left(\bar{N}_{\bar{f}}(t) + \bar{N}_f(t)\right)} = \frac{-\left(S + \bar{S}\right)\sin\left(\Delta m_s\, t\right)}{2\cosh\left(\frac{\Delta\Gamma_s\, t}{2}\right) + \left(D + \bar{D}\right)\sinh\left(\frac{\Delta\Gamma_s\, t}{2}\right)}, \\ A^{\langle i\rangle}_{CP}(t) &= \frac{\left(N_f(t) + \bar{N}_f(t)\right) - \left(\bar{N}_{\bar{f}}(t) + N_{\bar{f}}(t)\right)}{\left(N_f(t) + \bar{N}_f(t)\right) + \left(\bar{N}_{\bar{f}}(t) + N_{\bar{f}}(t)\right)} = \frac{\left(D - \bar{D}\right)\sinh\left(\frac{\Delta\Gamma_s\, t}{2}\right)}{2\cosh\left(\frac{\Delta\Gamma_s\, t}{2}\right) + \left(D + \bar{D}\right)\sinh\left(\frac{\Delta\Gamma_s\, t}{2}\right)}. \end{aligned} \tag{3.20}$$

These *CP* asymmetries are displayed in Figure 3.10 for simulated $B_s \to D_s K\pi\pi$ decays. The *CP* asymmetry $A^{\langle f\rangle}_{CP}(t)$ compares the inclusive decay rate of an initial B_s^0 meson (to either f or $\bar{f}$) with the *CP*-conjugate process. It is sensitive to *CP* violation from the sinusoidal coefficients S and $\bar{S}$. For $S \neq -\bar{S}$, $A^{\langle f\rangle}_{CP}(t)$ oscillates

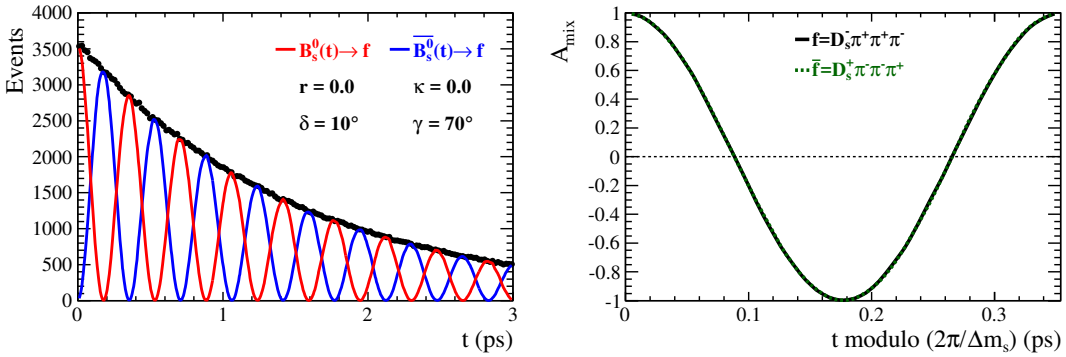

(a) Flavor-specific $B_s \to D_s\pi\pi\pi$ decays.

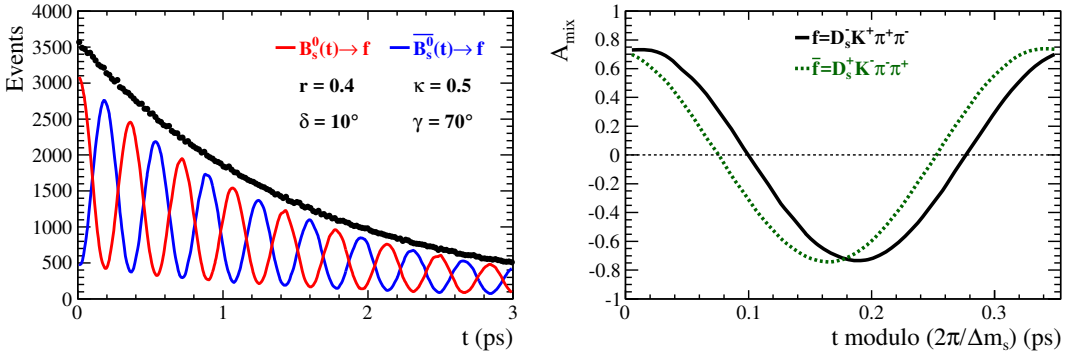

(b) $B_s \to D_sK\pi\pi$ decays.

Figure 3.9: *Left:* Simulated decay-time distributions for decays into the final state f, provided that an initial B_s^0 (red) or $\overline{B}_s^0$ (blue) meson is produced and their superposition (black). *Right:* Mixing asymmetries for decays into the final states f (black) and $\bar{f}$ (green) folded into one oscillation period.

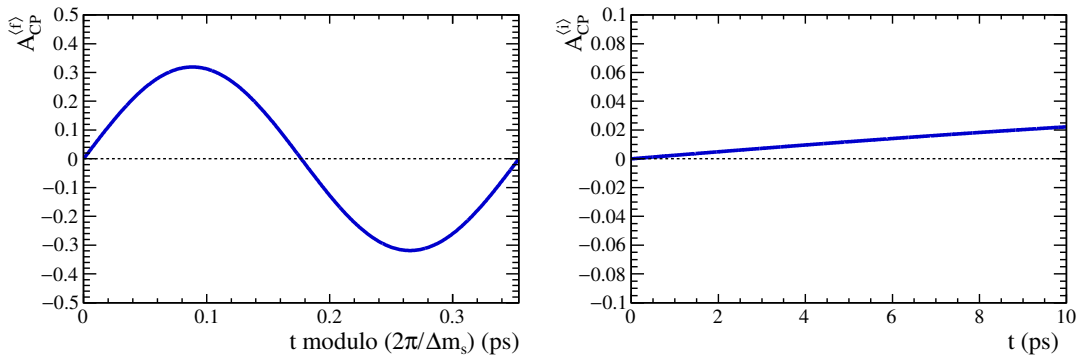

Figure 3.10: Time-dependent *CP* asymmetries $A_{CP}^{\langle f \rangle}(t)$ (left) and $A_{CP}^{\langle i \rangle}(t)$ (right) for simulated $B_s \to D_sK\pi\pi$ decays assuming the values $r = 0.4$, $\kappa = 0.5$, $\delta = 10°$ and $\gamma - 2\beta_s = 70°$.

with the frequency Δm_s. Similarly, the *CP* asymmetry $A_{CP}^{\langle i \rangle}(t)$ compares the decay rates into the final states f and $\bar{f}$ averaged over the initial flavor of the B_s meson and is sensitive to *CP* violation from the hyperbolic coefficients. It increases almost linearly with the proper time. Thus, a significant *CP* asymmetry can only be observed at high proper times, where the statistics is low (due to the exponential decay). On the plus side, the measurement of $A_{CP}^{\langle i \rangle}(t)$ does not require to determine the initial flavor of the B_s meson, an experimentally challenging task as discussed in more detail later.

Similar to the factor $2F_+ - 1$ in $B^\pm \to DK^\pm$ decays (see Equation 3.5), the coherence factor dilutes the observable *CP* asymmetries because constructive and destructive interference effects cancel each other when integrated over the entire phase space. Nevertheless, the (phase-space integrated) decay-time distribution provides enough measurable quantities, in form of the five *CP* coefficients, to extract the four physical parameters r, κ, δ and $\gamma - 2\beta_s$. Such an analysis has been performed for $B_s \to D_s K$ decays in Reference [143], superseded by Reference [141]. For this two-body decay, the coherence factor is $\kappa = 1$ and the remaining parameters are measured to be $r = 0.37^{+0.10}_{-0.09}$, $\delta = (358^{+13}_{-14})^\circ$ and $\gamma = (128^{+17}_{-22})^\circ$ [141]. The four-body decay $B_s \to D_s K\pi\pi$ can be studied analogously, with the complication that the coherence factor needs to be determined additionally. Hence, the sensitivity is expected to be lower than for $B_s \to D_s K$ decays. On the other hand, if the full PDF in Equation 3.15 is used, the precision with which the CKM angle γ can be determined could also be enhanced in case of large interference effects in some regions of the phase space. As this requires a parameterization of the decay amplitudes, this model-dependent method leads to the same disadvantages as discussed in the previous section. Both approaches (phase-space integrated and model-dependent) are investigated in this thesis.

Part II

STRONG PHASES IN $D \to \pi\pi\pi\pi$ DECAYS

A portal to *CP* violation in the charm and beauty systems

4

Thanks to its rich resonance structure, the decay $D \to \pi\pi\pi\pi$ provides an excellent laboratory to study light mesons contributing as intermediate states thereby shedding light on the behavior of strong interactions at low energies. To disentangle the various components, an amplitude analysis is performed. Knowledge of the strong phase variation also allows to examine the whole phase space for potential *CP* violating effects eventually identifying regions of enhanced sensitivity.

Phenomenology of the decay

The only previous analysis of the $D \to \pi\pi\pi\pi$ amplitude structure was performed by the FOCUS collaboration [144]. The dominant resonant component was identified to be the $a_1(1260)^{\pm}$ resonance contributing via the decay process $D \to a_1(1260)^{\pm}\pi^{\mp}$. As a ground state of the axial-vector meson system, the properties of the $a_1(1260)^{\pm}$ meson are an important benchmark for phenomenological approaches describing the non-perturbative regime of the strong interaction [145, 146] or lattice QCD calculations. While the latter approach so far mainly focussed on the pseudoscalar and vector ground-states [147, 148], the mass and width of the $a_1(1260)^{\pm}$ meson were recently computed, based on simplified assumptions [149], to be $m_{a_1}^{\text{Lattice}} = (1435^{+53}_{-162})\,\text{MeV}$ and $\Gamma_{a_1}^{\text{Lattice}} = (680 \pm 310)\,\text{MeV}$. Despite of large effort, the properties of the $a_1(1260)^{\pm}$ meson are also not well understood experimentally. The *Particle Data Group* (PDG) listed 30 different measurements in their 2016 review edition [150]. Most measurements agree on the mass, leading to a PDG average of $m_{a_1}^{\text{PDG(16)}} = (1230 \pm 40)\,\text{MeV}$. The width, however, remains an unresolved question[1], estimated to be in the range from 250 MeV to 600 MeV [150]. In $D \to \pi\pi\pi\pi$ decays, the $a_1(1260)$ resonance is produced in an *external W* boson emission process, as shown in Figure 4.1(left), and subsequently decays strongly via multiple sub-decay modes into the tri-pion final state. If the

[1] Including the results presented in this thesis, the PDG provided for the first time (since decades) an average value of the width in their 2018 review edition, $m_{a_1}^{\text{PDG(18)}} = (1245^{+10}_{-16})\,\text{GeV}$ and $\Gamma_{a_1}^{\text{PDG(18)}} = (389 \pm 29)\,\text{GeV}$.

$a_1(1260)$ meson couples to the weak charged current, it is produced with positive charge (for an initial D^0 state), otherwise it emerges with opposite charge from the spectator-quark interaction. Such processes are collectively referred to as *non-self-conjugate* or *flavor-non-specific* since both intermediates states $a_1(1260)^+\pi^-$ and $a_1(1260)^-\pi^+$ can arise from D^0 or $\bar{D}^0$ meson decays. In contrast, the *internal* W boson emission diagram, shown in Figure 4.1(right), results in *self-conjugate* intermediate states such as $\rho(770)^0\rho(770)^0$ which can be decomposed into *CP* eigenstates depending on the relative orbital angular momentum of the quasi-two body resonance system.

Beyond light hadron spectroscopy, studies of multi-body charm decays are well motivated by the search for potential new sources of *CP* violation. The Standard Model predicts minute *CP* asymmetries in the charm system ($\mathcal{O}(10^{-4} - 10^{-3})$ [151, 152]). This is due to the fact that tree-level decays of charm hadrons involve only the first two quark generations, where no weak phases contribute, see Equation 1.3. Hence, loop processes are required to access *CP*-violating phases via the coupling to a virtual b quark. These are strongly suppressed in the charm system by the same mechanism that leads to a negligible mixing, compare Section 1.3. This implies that any observation of a sizable *CP* violation, $\mathcal{O}(1\%)$, would be a clear indication of physics beyond the Standard Model. Recently, the LHCb collaboration reported the first observation of *CP* violation in the charm system; the difference in *CP* asymmetries between $D \to K^-K^+$ and $D \to \pi^+\pi^-$ decays was measured to be $A_{CP}(K^-K^+) - A_{CP}(\pi^+\pi^-) = (-15.4 \pm 2.9) \cdot 10^{-4}$ [153], in agreement with the Standard Model expectation. Contributions from new physics phenomena beyond the Standard Model might be enhanced in multi-body decays through interference effects with the multifarious resonance spectrum. These decays also provide additional observables such as angular asymmetries to identify new sources of *CP* violation. The LHCb collaboration conducted a search for *CP* violation in the decay $D \to \pi\pi\pi\pi$ by comparing the relative density of D^0 and $\bar{D}^0$ decays in multi-dimensional bins of phase space and excluded *CP*-violating effects at the 10% level [154]. More recently, also an unbinned technique, called the energy test [155], which compares average distances of events in phase space has been applied[2] (to a larger data set) [156]. A significance for *CP* non-conservation of 2.7σ was found. Even if this deviation can be established with more data and eventually a *CP*-violating effect above the level expected from the Standard Model is observed, the employed model-independent approach does not yield information about the underlying mechanism. With a search for *CP* violation in the amplitude components of the decay, potential sources might be uncovered. This

[2]The search for *CP* violation in the decay $D \to \pi\pi\pi\pi$ with the energy test used the amplitude model presented in this thesis for sensitivity and optimization studies.

complementary approach is explored, for the first time in $D \to \pi\pi\pi\pi$ decays, in this thesis. The amplitude analysis of the FOCUS collaboration did not distinguish whether the initial state was a D^0 or $\bar{D}^0$ meson. It was thus not possible to study *CP*-violating processes. Moreover, the strong phase difference between D^0 and $\bar{D}^0$ decays is *the* essential ingredient permitting to extract the CKM angle γ from $B^\pm \to DK^\pm$ decays, as discussed Section 3.2.

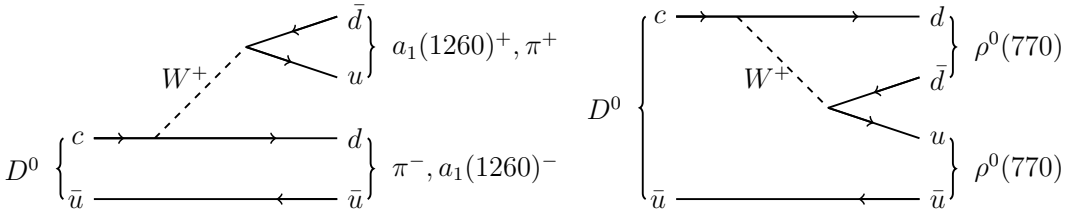

Figure 4.1: Leading order Feynman diagrams for color-favored (left) and color-suppressed (right) decays that contribute towards the resonant structure in $D^0 \to \pi^+\pi^-\pi^+\pi^-$ decays.

Analysis overview

This part focusses on the amplitude analysis of $D \to \pi\pi\pi\pi$ decays. The CLEO-c legacy data set is used for this study motivated by the fact that the model-independent measurement of the $D^0 \to \pi^+\pi^-\pi^+\pi^-$ and $\bar{D}^0 \to \pi^+\pi^-\pi^+\pi^-$ strong phase difference progressed in parallel. The latter was carried out by a physicist at the University of Bristol, Dr. Samuel Harnew [124], and relied on the amplitude model developed in this thesis to define an optimal binning scheme[3]. The results of this measurement are also concisely summarized as they provide an important cross-check of the validity of the amplitude description and represent, historically, the main motivation to come up with such an amplitude model.

The experimental apparatus is briefly introduced in Chapter 5. It is then outlined how suitable $D \to \pi\pi\pi\pi$ candidates are reconstructed and selected. The results of the amplitude analysis are presented in Chapter 6 including a detailed study of the $a_1(1260)$ resonance lineshape and a search for *CP* violation in the intermediate-state components. Chapter 7 compares the predictions of the amplitude model with the model-independent measurement of the strong phase difference between D^0 and $\bar{D}^0$ decays. Finally, the expected sensitivity for a future measurement of the CKM angle γ from $B^\pm \to (D \to \pi\pi\pi\pi)K^\pm$ decays at the LHCb experiment is discussed.

[3]The author of this thesis provided the amplitude model including its implementation in software and acted as a reviewer for the model-independent strong phase measurement and in that sense significantly contributed to the quality of the analysis despite not being co-author of the resulting publication [124].

Event selection at the CLEO-c detector

5

This chapter briefly introduces the CLEO-c experiment focussing on the detector components that are relevant for the presented analysis. It is then explained how the measured detector signatures allow to reconstruct $D \to \pi\pi\pi\pi$ signal candidates. Afterwards, the composition of the selected data sample is discussed and the signal yield is determined.

5.1 Experimental setup

The *Cornell Electron Storage Ring* (CESR) [157] is a particle accelerator with a circumference of 768 m located at the Cornell University in Ithaca, New York. It produces symmetric electron-positron collisions with centre-of-mass energies ranging from 3 GeV to 12 GeV, depending on the operation mode. The electrons and positrons either scatter or, more interestingly, annihilate producing new leptons or hadrons, which in turn rapidly decay into long-lived or stable particles. These collision products are reconstructed with the *CLEO* [158] detector surrounding the interaction region. First commissioned in 1979, this general purpose detector underwent several major upgrades [159–165] in order to improve the performance and to account for a shifting main focus of the physics program. The CLEO detector was originally designed to study bottomonium resonances (bound states of b and $\bar{b}$ quarks) and decays of B mesons, what requires center-of-mass energies above 10 GeV. Its final incarnation, called the *CLEO-c* detector [157], is optimized for the operation at center-of-mass energies around 4 GeV allowing for a copious production of charmonium resonances such as the J/ψ or $\psi(3770)$ mesons. Figure 5.1 shows a schematic view of the CLEO-c detector, which is almost hermetic covering 93% of the solid angle around the interaction point. The detector components serve three main purposes: the reconstruction of charged particle trajectories, measuring the energy of neutral particles and the identification of the particle species.

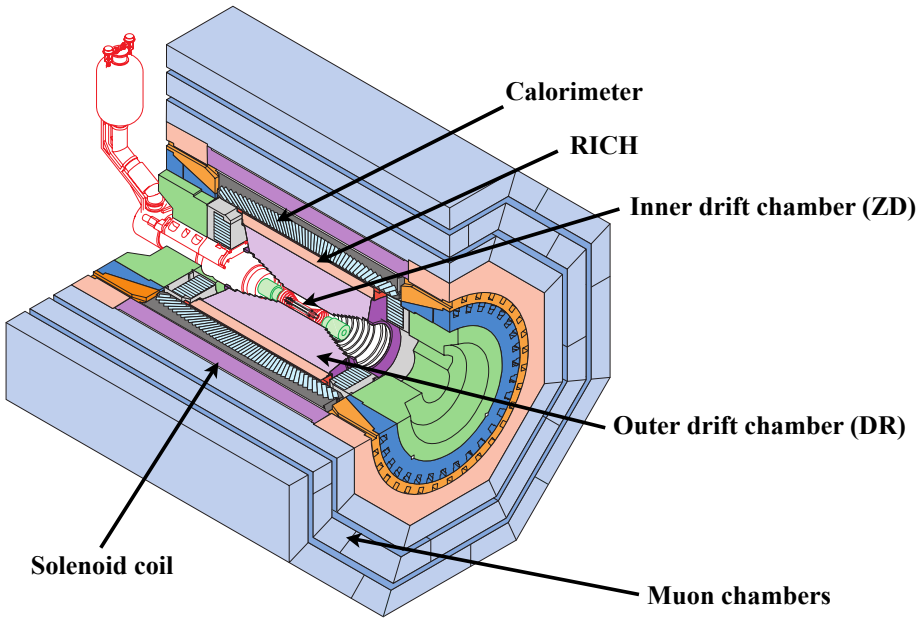

Figure 5.1: Schematic view of the CLEO-c detector. Modified from [166].

Track reconstruction

The reconstruction of the trajectories of charged particles (*tracks*), also referred to as *tracking*, permits determining their electric charge and momentum. This is accomplished by exploiting the curvature of the tracks in a magnetic field. The tracking system of the CLEO-c detector comprises two cylindrical drift chambers inside a uniform magnetic field parallel to the beam direction. A magnetic field strength of 1 T is provided by a superconducting solenoid coil encompassing the tracking system. The inner drift chamber, called the *ZD* detector [157], covers the radial region between 4 cm and 12 cm from the interaction point. It is composed of 300 drift cells, which have square profiles measuring 10 mm across, arranged in six layers. Each cell consists of an anode wire running approximately parallel to the beam pipe which is surrounded by eight field wires held at a constant potential difference. When a charged particle passes through a cell, it ionizes the gas filled into the drift chamber and the resulting electrons are attracted to the anode wire. The timing information of the induced current with respect to the beam interaction allows to measure the distance of closest approach between the track and the anode wire (*hit position*) with a spatial resolution around 100 µm. The layers of the ZD detector are arranged at small alternating stereo angles (between 4.4° and 5.8°) with respect to the beam axis to allow for the reconstruction of the track momentum component in beam (longitudinal) direction.

The main drift chamber, refereed to as the *DR* detector [163], covers the radial region between 12 cm and 82 cm. It is build technologically similar than the ZD detector and is arranged in 47 layers with 9796 cells in total. The drift cells have slightly larger profiles measuring 14 mm across. The 16 innermost layers are a parallel to the beam pipe, while the remaining ones have stereo angles between 1.3° and 1.7°. The outer wall of the DR detector is lined with cathode strips improving the longitudinal position measurement. By combining the information of both drift chambers, a relative momentum resolution less than 0.5% for tracks with momenta below 2 GeV is achieved [157].

Particle identification and calorimetry

Identifying the particle species is essential to correctly reconstruct charm meson decays. Particularly relevant to this analysis is the separation of charged pions and kaons in order to discriminate $D \to \pi^+\pi^-\pi^+\pi^-$ decays from topologically and kinematically similar decays such as $D \to K^\pm\pi^\mp\pi^+\pi^-$.

The CLEO-c detector uses two complementary methods for charged particle identification (PID). First, the drift chambers measure the relative strength of the charge deposits along the particle's trajectory. The energy loss (per unit length), dE/dx, due to electromagnetic interactions with the detector material depends on the particle's velocity, as described by the Bethe-Bloch formula [167, 168]. Combined with the momentum determination, the mass of the particle can be inferred from the measured energy loss. Figure 5.2(left) shows the dE/dx distribution as function of momentum where different particle species (pions, kaons and protons) appear as shifted bands. A good separation between pions and kaons is observed for momenta below 700 MeV. Discrimination power for high momentum tracks is provided by a *Ring-Imaging-CHerenkov* (RICH) detector [164, 165] which is positioned outside of the tracking system and covers 83% of the solid angle. The RICH detector exploits the fact that charged particles emit photons in a cone around their trajectory when transversing a dielectric medium at a velocity greater than the speed of light in that medium, a phenomenon called Cherenkov effect. The opening angle of the light cone, $\cos\theta_C = 1/(n\beta)$, is a function of the particle's velocity, β, and depends on the refractive index of the radiator material, n. Lithium fluoride crystals are used as radiator with $n = 1.5$. The produced ring of Cherenkov photons propagates through an expansion volume filled with nitrogen allowing for a more precise determination of the opening angle. The Cherenkov photons are detected via the photoelectric effect with multi-wire proportional chambers. Figure 5.2(right) shows the opening angle as function of

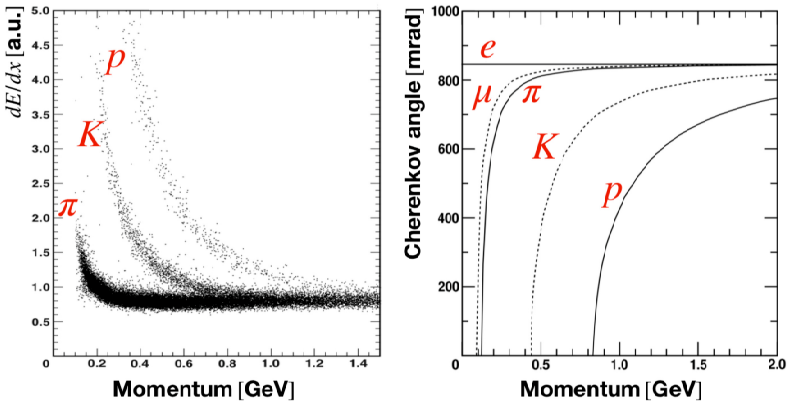

Figure 5.2: Energy loss per unit length (left) and Cherenkov angle (right) as function of momentum for different particle species. Figures modified from [157].

momentum for different particle species demonstrating a good separation between kaons and pions in the relevant momentum range ($0.7 - 2\,\text{GeV}$). The information of the RICH detector is combined with the energy loss measurement to compute a so-called delta log-likelihood variable $\Delta\mathcal{L}_{ij}$ comparing two different particle hypothesis, i and j, for a given track. For example, $\Delta\mathcal{L}_{K\pi} < 0$ indicates that the track is more likely a pion than a kaon. This requirement identifies charged pions having momenta below 1 GeV with an efficiency above 95% and keeps the rate of kaons misclassified as pions below 1% [169].

The CLEO-c calorimeter [157] provides particle identification for neutral particles, such as photons or π^0 mesons decaying (predominantly) into two photons, and measures their energies. It is also used to identify electrons. The calorimeter consists of 7800 scintillating cesium iodide crystals of dimension $5\,\text{cm} \times 5\,\text{cm} \times 30\,\text{cm}$ covering 93% of the solid angle. Incoming electrons or photons electromagnetically interact with the calorimeter triggering cascades of photons and electron-positron pair, known as *electromagnetic showers*. These showers induce scintillation light in the crystals which is detected by silicon photo-diodes located on the back of each crystal. This allows to measure the total energy of the shower.

Three muon tracking chambers separated by iron layers build the outermost part of the CLEO-c detector. With typical momenta below 1 GeV, not even muons, which experience a minimal interaction with the detector material, can penetrate them. Thus, the muon chambers are essentially obsolete for the CLEO-c experiment.

5.2 Event topology

The presented analysis exploits the full CLEO-c data sample taken at a center-of-mass energy of $\sqrt{s} = 3.7\,\text{GeV}$. The data set was recorded between the years 2003 and 2007 and corresponds to a total integrated luminosity of $818\,\text{pb}^{-1}$. At the operated collider energy, the incident electron and positron annihilate into a virtual photon creating a $\psi(3770)$ charmonium resonance with a high production cross-section of 6.3 nb [157]. The mass of the $\psi(3770)$ meson is just above the kinematic threshold for open-charm pair production. Approximately half of the $\psi(3770)$ mesons decay to a neutral charm meson pair, with the other half predominantly decaying into their charged counterparts. Altogether this amounts to roughly five million neutral charm meson pairs created during the CLEO-c running period. However, only one in around a hundred D^0 mesons decays to the four pion final state under study [10]. Due to the threshold production, no additional fragmentation particles can be produced resulting in low charged and neutral particle multiplicities of 5.0 and 2.4 on average [157].

The event reconstruction starts with a standardized track selection as described in more detail in Reference [169]. First, particle trajectories are determined based on their measured detector hits. Weak criteria on the track fit quality are imposed. Track candidates are further required to be in the fiducial region of the detector and to have a momentum between 50 MeV and 2 GeV. The $\psi(3770)$ resonance is produced (almost) at rest and so are the subsequently created charm mesons due to the proximity to the kinematic threshold. Thus decay vertices of the charm mesons cannot be resolved and track candidates must be consistent with the beam collision region. Four charged tracks consistent with the pion hypothesis, compare Section 5.1, are combined to build a signal candidate. The flavor of which, *i.e.* D^0 or $\bar{D}^0$ meson, is inferred (*tagged*) from the *other* charm meson in the event as illustrated in Figure 5.3. This is achieved by requiring that a single kaon track can be associated to the other D meson decay. A positively charged kaon indicates a $\bar{c} \to \bar{s}$ transition, or equivalent a $\bar{D}^0$ decay, on the tag side. As the initial state contains a $c\bar{c}$ quark pair and decays strongly, this unambiguously determines the flavor eigenstate of the signal $D \to \pi^+\pi^-\pi^+\pi^-$ decay to be the opposite. However, not only flavor specific decays such as $\bar{D}^0 \to K^+e^-\bar{\nu}_e$ but also quasi-flavor specific decays such as $\bar{D}^0 \to K^+\pi^-$ are reconstructed. In the later case, there is a small probability to misidentify the flavor content due to strongly Cabibbo suppressed $D^0 \to K^+\pi^-$ decays. In addition, decay modes with multiple charged kaons, misidentified kaons or charm mixing can lead to a wrong tag decision. The fraction of wrong tags has been measured from flavor specific charm decays on the signal side to be $\omega = 4.5 \pm 0.5\%$ [170]. Analogously, *CP*-even, *CP*-odd and mixed-*CP* tags are derived from a variety of decay modes as explained in Section 3.2. The

following discussion concentrates on the flavor-tagged candidates, which make up approximately 90% of the full data sample, as only those are used for the amplitude analysis. The model-independent measurement of the hadronic parameters uses a combination of all tags, where the sensitivity is driven by the *CP*-even, *CP*-odd and mixed-*CP* tags [124]. This procedure ensures that the results of both methods are (quasi-)independent as detailed in Chapter 7.

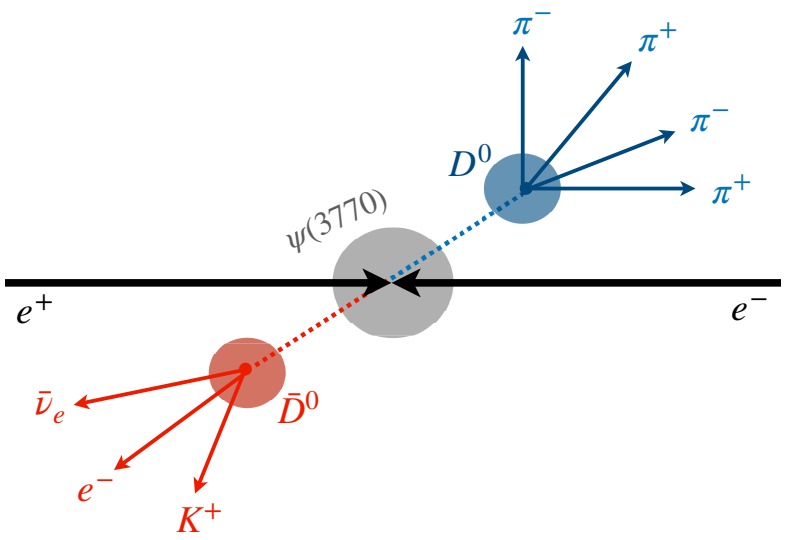

Figure 5.3: Schematic topology of the $e^+e^- \to \psi(3770) \to D\bar{D}$ reaction. The signal charm meson decays into four pions, while the other charm meson can be used to tag the flavor if it decays flavor specific. The flight distance of the charm mesons cannot be resolved experimentally.

5.3 Data sample composition

The main background source originates from candidates made of unrelated hadrons created from the underlying continuum reaction ($e^+e^- \to q\bar{q}$) which, by chance, pass the selection. The cross section for the continuum background is approximately equal to the signal $e^+e^- \to \psi(3770) \to D\bar{D}$ interaction [157]. Apart from this combinatorial background, there is a peaking background arising from real $D \to (K^0_S \to \pi^+\pi^-)\,\pi^+\,\pi^-$ decays. Even though the final state is common to the signal decay mode, it is an incoherent process since the K^0_S lifetime is much longer than those of any other possible intermediate resonance. The $K^0_S \to \pi^+\pi^-$ candidates are suppressed by the track selection since the pions originate from a displaced vertex. Nonetheless, a significant fraction of them reside. Hence, signal candidates are rejected if the invariant mass of any $\pi^+\,\pi^-$ combination is within 7.5 MeV (corresponding to three standard deviations of detector resolution) of the world-average K^0_S mass [10].

Valid signal candidates are identified based on their kinematic properties. Here, the fact that the entire beam energy is converted to the charm meson pair allows to define two powerful variables reflecting energy and momentum conservation. First, the beam-constrained mass,

$$m_{bc} \equiv \sqrt{\left(\frac{\sqrt{s}}{2}\right)^2 - \vec{p}_D{}^2}, \tag{5.1}$$

is constructed from the three-momentum of the D candidate, $\vec{p}_D$, and substitutes the reconstructed energy of the D candidate, E_D, with (half of) the center-of-mass energy, $\sqrt{s}$. The latter is determined from accelerator parameters to a much higher precision ($\sigma(\sqrt{s}) = 2\,\text{MeV}$ [169]). Second, the missing energy ΔE is defined as

$$\Delta E \equiv E_D - \frac{\sqrt{s}}{2}. \tag{5.2}$$

These variables are (nearly) uncorrelated. Fully reconstructed signal events should have missing energy close to zero and a beam-constrained mass consistent with the nominal D^0 mass. In general, the m_{bc} signal width is a measure of the beam-energy spread while the ΔE signal width is dominated by the detector resolution. Candidates that satisfy $m_{bc} > 1.83$ GeV and $|\Delta E| < 0.05$ GeV are considered further.

Yield estimation

To estimate the number of signal events contained in the data sample, a two-dimensional extended maximum likelihood fit[1] to the plane spanned by the beam-constrained mass and missing energy is performed. Figure 5.4(left) shows the event distribution in this plane. The shape of the signal peak depends not only on the beam-energy spread and the detector resolution but also on the intrinsic resonance lineshape of the $\psi(3770)$ meson. In addition, the missing-energy distribution of the signal component is affected by initial state radiation where the incident electron or positron emits a low energetic photon before annihilation. The radiative tail is towards higher m_{bc} values as in case of significant initial state radiation the reconstructed three-momentum of the D candidate is lower. In contrast, there is a bremsstrahlung tail due to final state radiation to the left side in the missing energy dimension. Rather than attempting to describe this complicated interplay of

[1] An extended likelihood fit takes into account that the sample size is a poisson distributed random number by normalizing the PDF to the observed yield.

effects, an effective empirical model is employed. The sum of three (two) Gaussian functions with common mean but different widths are used to describe the signal component in the m_{bc} (ΔE) dimension which is displayed in Figure 5.5. The width of each Gaussian is allowed to differ left and right of the mean (bifurcated Gaussian) to account for the radiative tails. The combinatorial background distribution in the beam-constrained mass dimension is linear below the signal peak region and shows a smooth kinematic cut-off above it. The endpoint is given by the beam energy. An ARGUS [171] function, see Appendix C, is used to parameterize these features. A linear function is sufficient to describe the missing-energy distribution of the background component. The signal yield is determined from the fit, displayed in Figure 5.5, to be 7250 ± 56 (stat) ± 46 (syst), where the first uncertainty is statistical and second is systematic. The systematic uncertainty is estimated by repeating the fit with different appropriate PDF hypotheses.

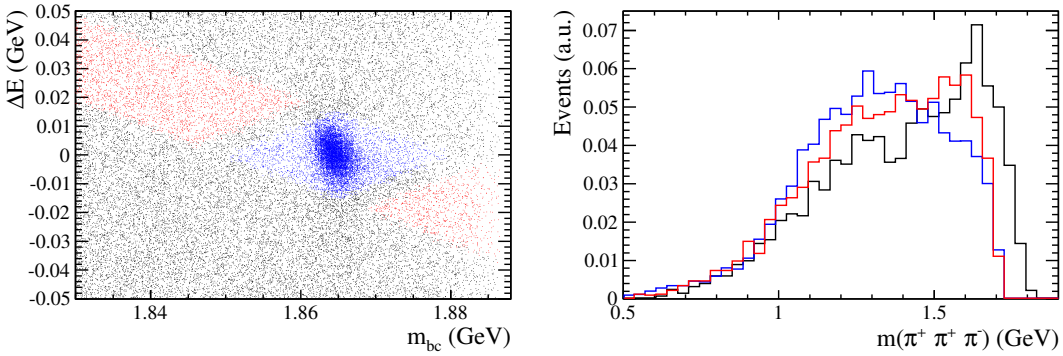

Figure 5.4: *Left:* Distribution of $D \to \pi\pi\pi\pi$ candidates in the m_{bc} and ΔE plane. The central region (blue) is defined as the signal region, with sideband regions (red) providing background samples. *Right:* Invariant-mass distribution of the $\pi^+\pi^+\pi^-$ system for candidates in the signal (blue) and sideband (red) region. The kinematic boundary for candidates with $m_{bc} - m_D > 15\,\text{MeV}$ (black) is shifted towards higher values such that the phase-space distribution of these candidates is not representative for the background contribution inside the signal region. Analog arguments hold for other invariant-mass combinations.

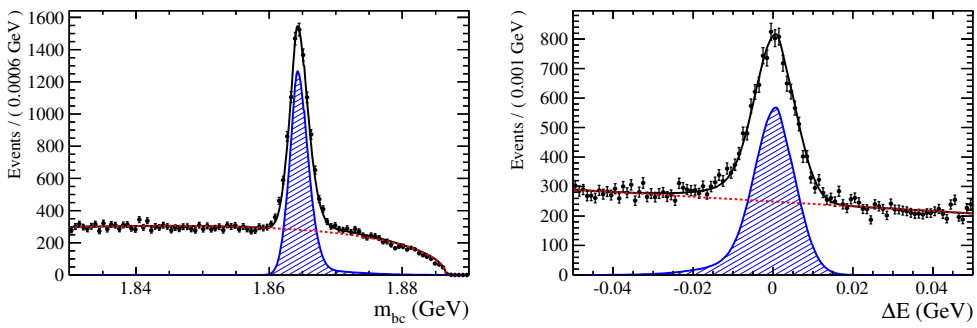

Figure 5.5: Beam-constrained mass (left) and missing energy (right) distribution of $D \to \pi\pi\pi\pi$ candidates, overlaid with the projections of the fitted PDF (solid black line). The signal component is shown in blue (solid) and the background component in red (dashed).

Signal and background regions

A signal region for the candidates used in the amplitude fit described in Chapter 6 is defined in the plane spanned by the beam-constrained mass and missing energy. To accurately model the remaining background within that region, a suitable sideband region needs to be defined. The phase-space distribution of the candidates in this sideband region is studied and assumed to be the same in the signal region as discussed in more detail in Section 6.2. It is therefore indispensable to select signal and sideband regions with equivalent kinematic properties. In particular, they should preserve the range of the reconstructed D candidate mass. The four-pion invariant mass can be expressed in terms of m_{bc} and ΔE as follows:

$$m(\pi\pi\pi\pi) = \sqrt{E_D^2 - \vec{p}_D{}^2} = \sqrt{\Delta E^2 + \Delta E\sqrt{s} + m_{bc}^2}. \tag{5.3}$$

Now, a region in which the D candidate mass is consistent with the nominal D meson mass (within some margin) can be obtained by selecting candidates with $|m(\pi\pi\pi\pi) - m_D| < 15\,\text{MeV}$. This relation describes an annulus in the m_{bc} and ΔE plane. The annulus appears as a diagonal band in the considered region of the m_{bc} and ΔE plane, see Figure 5.4(left). Lines normal to the annulus have an angle of inclination $\vartheta = \arctan\left(\frac{\sqrt{s}+2\,\Delta E}{2\,m_{bc}}\right)$ about the center of the annulus. The signal region is defined by requiring $|\vartheta - \vartheta_D| < 0.004$, where $m_{bc} = m_D$ and $\Delta E = 0\,\text{GeV}$ at ϑ_D, as shown in Figure 5.4(left). This choice retains more than 95% of the signal events[2]. The signal fraction in this region is $f_\text{S} = (78.4 \pm 0.6\ (\text{stat}) \pm 0.5\ (\text{syst}))\%$. Similarly, sideband regions are defined with $|\vartheta - \vartheta_D| > 0.006$. To illustrate how the choice of sideband region impacts the phase-space distribution of the final-state particles, Figure 5.4(right) shows exemplary the tri-pion invariant-mass distribution for D candidates in the signal and sideband region. By construction, their kinematic ranges coincide. This is not the case for candidates outside the annulus of constant invariant mass. They show an excess above $m_D - m_\pi \approx 1.73\,\text{GeV}$ which is kinematically not accessible for candidates inside the signal region. Candidates outside the annulus of constant invariant mass are thus not representative for the residual background contribution within the signal region.

[2] A tighter signal window could be chosen with *e.g.* $|m_{bc} - m_D| < 5\,\text{MeV}$ instead of $|\vartheta - \vartheta_D| < 0.004$ enhancing the signal purity. However, the latter choice is slightly more efficient in collecting the radiative tails of the signal component. As the combinatorial background is well understood, a decision in favor of signal retention over signal purity is made.

6 Amplitude Analysis

The phase space of the four-body decay $D^0 \to \pi^+\pi^-\pi^+\pi^-$ is five-dimensional as argued in Chapter 2. Figure 6.1 displays projections to the invariant mass combinations $m(\pi^+\pi^-), m(\pi^+\pi^+), \min[(\pi^+\pi^+\pi^-)], \max[m(\pi^+\pi^+\pi^-)]$ and $m(\pi^+\pi^-\pi^-)$ for charm meson candidates in the signal region. The $\min[m(\pi^+\pi^\pm\pi^-)]$ ($\max[m(\pi^+\pi^\pm\pi^-)]$) distribution shows the $\pi^+\pi^\pm\pi^-$ combination with the lowest (highest) invariant mass, while $m(\pi^+\pi^-)$ ($m(\pi^+\pi^-\pi^-)$) shows a random $\pi^+\pi^-$ ($\pi^+\pi^-\pi^-$) invariant mass combination. To describe this complicated phase-space distribution, an amplitude analysis is performed which decomposes the various intermediate-state contributions. As the flavor of the signal candidates is inferred from the other charm meson in the event, there are two independent data sets available which either contain $D^0 \to \pi\pi\pi\pi$ or $\bar{D}^0 \to \pi\pi\pi\pi$ decays described by the total amplitudes $A_{D^0}(\mathbf{x})$ and $A_{\bar{D}^0}(\mathbf{x})$, respectively, as defined in Equation 3.2. Each data sample contains a small fraction of misidentified flavor eigenstates, $\omega = 4.5 \pm 0.5\%$ (see Section 5.2). The signal PDF[1] for candidates tagged as D^0 mesons is thus given by:

$$\mathcal{P}_{\mathrm{S}}(\mathbf{x}|\theta_{\mathrm{S}}) = \frac{\left[(1-\omega)\,|A_{D^0}(\mathbf{x})|^2 + \omega\;|A_{\bar{D}^0}(\mathbf{x})|^2\right]\,\epsilon(\mathbf{x})\,\phi_4(\mathbf{x})}{\int\left[|A_{D^0}(\mathbf{x})|^2 + |A_{\bar{D}^0}(\mathbf{x})|^2\right]\,\epsilon(\mathbf{x})\,\mathrm{d}\Phi_4}, \tag{6.1}$$

and similar for the opposite tag. The set of parameters to be determined, θ_{S}, are the complex coefficients of the intermediate-state amplitudes and several poorly known resonance masses and widths. Distinct phase-space regions are populated by events with characteristic kinematic properties such that the selection efficiency is not necessarily uniform over the entire phase space. The signal PDF takes this explicitly into account by including an acceptance function $\epsilon(\mathbf{x})$, defined as the fraction of signal decays that are reconstructible at a given phase-space position, which is determined in Section 6.1. The small residual contamination of combinatorial background is studied in Section 6.2. The construction of the signal amplitude model is discussed afterwards, before the results of the amplitude analysis are presented and interpreted. Initially it is assumed that *CP* symmetry is conserved in the charm decay ($a_i = \bar{a}_i$). This assumption is tested in Sec. 6.5.

[1] The effect of charm mixing is negligible for the given data set.

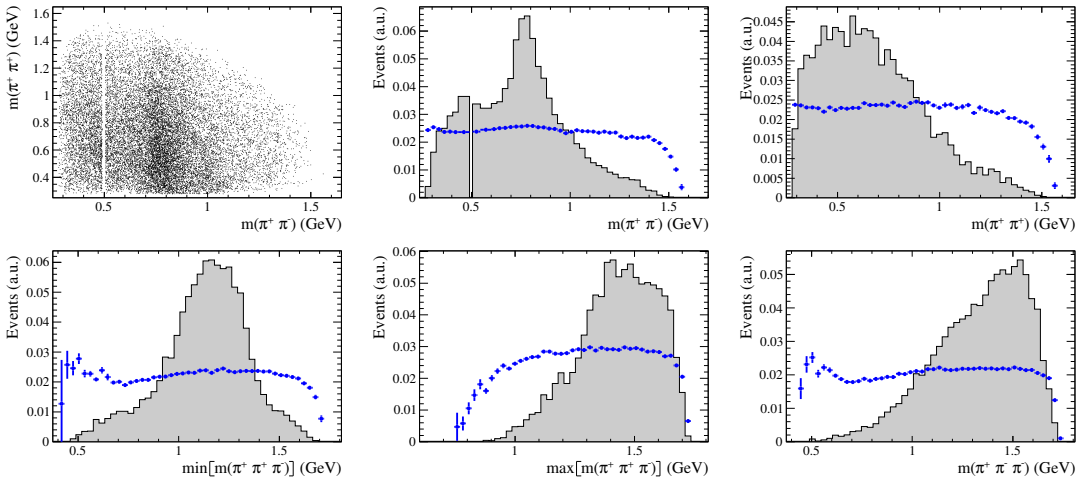

Figure 6.1: Invariant-mass projections for $D^0 \to \pi^+\pi^-\pi^+\pi^-$ candidates in the signal region. The effect of the K^0_S veto can clearly be seen in the projections to the $\pi^+\pi^-$ invariant mass. Efficiency variations (blue data points) in arbitrary scale as function of the phase-space variables are overlaid (for the one-dimensional projections).

6.1 Phase-space acceptance

The influence of the reconstruction and selection process on the phase-space distribution is investigated using large samples of simulated events, also referred to as *Monte-Carlo (MC)* events. The MC event generator EvtGen [172] is employed to simulate both the initial electron-positron collision and the decays of the thereby created particles. Hadronic and electromagnetic interactions of those particles with the detector material and the resulting detector response are evaluated with the Geant [173,174] package. Afterwards, the identical reconstruction and selection procedure is applied to the MC events as for real data events. The number of selected MC events is approximately 100 times larger than the signal yield observed on data. The phase-space acceptance, $\epsilon(\mathbf{x})$, can be obtained by measuring the ratio of selected to generated MC events in several bins of phase space. Figure 6.1 shows the efficiency variation as function of the phase-space variables. The overall scale of the selection efficiency is irrelevant since it is absorbed by the normalization of the signal PDF in Equation 6.1. A rather constant distribution is observed in the central regions, whereas the efficiency variation towards the kinematic boundaries is more pronounced. The regions close to the kinematic boundaries are typically populated by decays in which at least one of the final-state particles is at rest (in the center-of-mass frame) such that the selection efficiency is lower due to requirements on the minimum track momentum. In contrast to these one-dimensional projections which are for visualization purposes only, a five-dimensional binning is needed to describe the actual acceptance function, $\epsilon(\mathbf{x})$, to account for the correlation of the phase-space observables. In this case, the

finite statistics of the simulated data sample prevents to resolve fine structures. An alternative approach would be to parameterize the efficiency variation over the phase space by a sum of polynomials which is again complicated due to the high dimensionality [175]. Instead, a method is chosen which includes the phase-space acceptance in the normalization of the likelihood function, avoiding the need to explicitly model it or to bin the phase space [144, 170, 176].

The logarithmic likelihood function constructed from the efficiency corrected signal PDF in Equation 6.1 contains terms of the following kind:

$$\begin{aligned} &\ln\left(\frac{|A_{D^0}(\mathbf{x}|\theta_S)|^2\,\epsilon(\mathbf{x})\,\phi_4(\mathbf{x})}{\int |A_{D^0}(\mathbf{x}|\theta_S)|^2\,\epsilon(\mathbf{x})\,\phi_4(\mathbf{x})\,\mathrm{d}\mathbf{x}}\right) \\ &= \ln\left(\epsilon(\mathbf{x})\,\phi_4(\mathbf{x})\right) + \ln(|A_{D^0}(\mathbf{x}|\theta_S)|^2) - \ln\left(\int |A_{D^0}(\mathbf{x}|\theta_S)|^2\,\epsilon(\mathbf{x})\,\phi_4(\mathbf{x})\,\mathrm{d}\mathbf{x}\right). \end{aligned} \tag{6.2}$$

The first term is independent of the parameters of interest, θ_S, such that it does not influence the minimum of the logarithmic likelihood function and can be dropped. The phase-space acceptance still enters via the normalization integral, the last term in Equation 6.2. Given a set of MC events distributed according to the PDF $g(\mathbf{x})$, this normalization term can be computed numerically using the *Monte-Carlo integration* technique [177, 178]:

$$\int |A_{D^0}(\mathbf{x})|^2\,\epsilon(\mathbf{x})\,\phi_4(\mathbf{x})\,\mathrm{d}\mathbf{x} \approx \frac{V}{N_{\mathrm{Gen}}}\sum_k^{N_{\mathrm{Gen}}} \frac{\epsilon(\mathbf{x}_k)\,\phi_4(\mathbf{x}_k)}{g(\mathbf{x}_k)}\,|A_{D^0}(\mathbf{x}_k)|^2, \tag{6.3}$$

where $V = \int \mathrm{d}\mathbf{x}$ is the phase-space volume, $\mathbf{x}_k$ is the k-th event of the MC sample and N_{Gen} is the number of generated events. The explicit dependence on the efficiency variation can be canceled by using the above-mentioned simulated data sample propagated through the entire reconstruction chain. These MC events can be interpreted as being generated according to the PDF $g(\mathbf{x}) \propto \epsilon(\mathbf{x})\,\phi_4(\mathbf{x})\,|A^{\mathrm{Gen}}_{D^0}(\mathbf{x})|^2$, where $A^{\mathrm{Gen}}_{D^0}(\mathbf{x})$ denotes a preliminary amplitude model used to simulate the D meson decay. For Equation 6.3 follows:

$$\int |A_{D^0}(\mathbf{x})|^2\,\epsilon(\mathbf{x})\,\phi_4(\mathbf{x})\,\mathrm{d}\mathbf{x} \approx \frac{V}{N_{\mathrm{Gen}}}\sum_k^{N_{\mathrm{Sel}}} \frac{|A_{D^0}(\mathbf{x}_k)|^2}{|A^{\mathrm{Gen}}_{D^0}(\mathbf{x}_k)|^2}, \tag{6.4}$$

where N_{Sel} is the number of selected events. While basically every choice for the generator PDF is valid (also $A^{\mathrm{Gen}}_{D^0}(\mathbf{x}) = \text{const.}$), the precision of the MC integration is greatly improved if it resembles the distribution observed in data ($A^{\mathrm{Gen}}_{D^0}(\mathbf{x}) \approx A_{D^0}(\mathbf{x})$), a technique known as *importance sampling* [179]. With the chosen preliminary amplitude model (inspired by the amplitude analysis of the FOCUS collaboration [144]) and a sample size of $N_{\mathrm{Sel}} \approx 600\,\mathrm{k}$, the uncertainty of the MC integral is of the order 0.1%, negligible with respect to other systematic uncertainties.

6.2 Background model

Candidates in the sideband region are used to constrain the parameters, θ_{B}, of the background PDF,

$$\mathcal{P}_{\mathrm{B}}(\mathbf{x}|\theta_{\mathrm{B}}) = \frac{\epsilon(\mathbf{x})\, B(\mathbf{x}|\theta_{\mathrm{B}})\, \phi_4(\mathbf{x})}{\int \epsilon(\mathbf{x})\, B(\mathbf{x}|\theta_{\mathrm{B}})\, \mathrm{d}\Phi_4}, \tag{6.5}$$

where the background function $B(\mathbf{x}|\theta_{\mathrm{B}})$ describes the distribution in phase space. These candidates are a result of randomly combined particles originating from various different processes, some of which may contain resonances. Hence, the chosen background function considers contributions from the resonances $\sigma^0, \rho(770)^0, f_0(980)^0$ and several ad-hoc scalar resonances with free masses and widths. They are added incoherently on top of non-resonant components, where several exponential and polynomial functions are included to allow for more flexibility: $B(\mathbf{x}|\theta_{\mathrm{B}}) = \sum_{i=1}^{7} b_i\, |B_i(\mathbf{x}|\theta_{\mathrm{B}})|^2$, where b_i are (real) fit parameters. The explicit parameterization[2] of the seven background components $B_i(\mathbf{x}|\theta_{\mathrm{B}})$ is given in Appendix D. A maximum likelihood fit determines the 23 free parameters (θ_{B}) of the background model. Figure 6.2 displays the fit result.

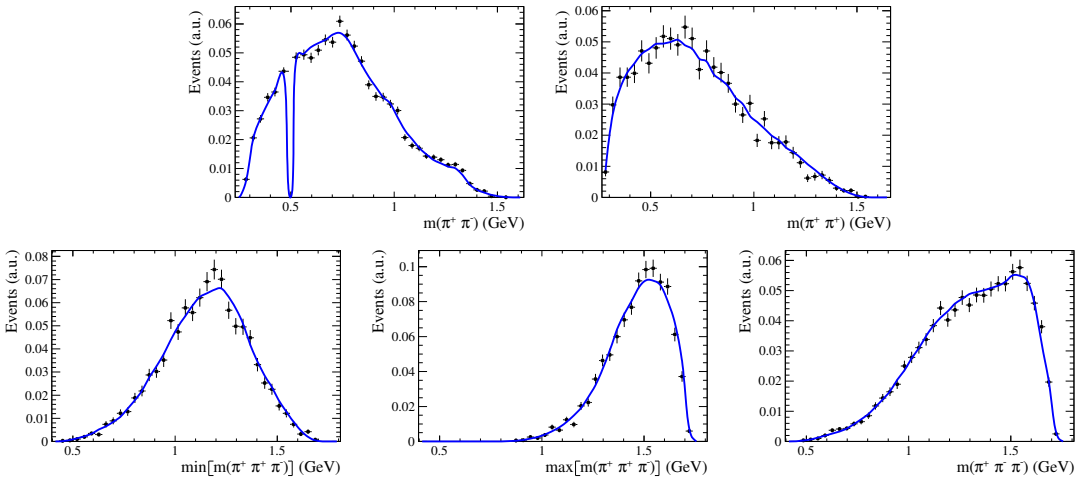

Figure 6.2: Invariant-mass distributions of $D^0 \to \pi^+\pi^-\pi^+\pi^-$ candidates in the sideband region (points with error bars) and fit projections (solid line).

[2]The chosen parameterization has the advantage that the same framework used to describe the signal contribution can be used but has no physical meaning and could be arbitrarily interchanged by any other suitable functional form.

6.3 Signal model construction

The total PDF describing the phase-space distribution of the candidates in the signal regions is constructed from the signal PDF and the background PDF,

$$\mathcal{P}(\mathbf{x}|\theta) = f_{\mathrm{S}}\,\mathcal{P}_{\mathrm{S}}(\mathbf{x}|\theta_{\mathrm{S}}) + (1 - f_{\mathrm{S}})\,\mathcal{P}_{\mathrm{B}}(\mathbf{x}|\theta_{\mathrm{B}}), \tag{6.6}$$

where f_{S} is the signal fraction as determined in Section 5.3 and $\theta = (\theta_{\mathrm{S}}, \theta_{\mathrm{B}})$ is the total set of fit parameters. The parameters of the background PDF are fixed to those determined in Section 6.2. The construction of the signal amplitude model poses a major challenge as discussed in the following.

Resonance spectrum

The light meson spectrum comprises a cornucopia of resonances potentially contributing to the $D \to \pi\pi\pi\pi$ decay. By inspecting the invariant-mass projections displayed in Figure 6.1, a large contribution from the vector resonance $\rho(770)$ to the $\pi^+\pi^-$ subsystem is revealed. As the exited pion spectrum generally involves broad resonances, it is impossible to clearly identify any other structures. The amplitude model provided by the FOCUS collaboration [144] provides more insight. As mentioned in Chapter 4, the dominant contribution was identified to be the $a_1(1260)$ meson decaying via $\rho(770)\pi$ or $\sigma^0\pi$ in three pions. The former decay mode can proceed in two distinct angular momentum configurations: $a_1(1260)[\mathrm{S}] \to \rho(770)\pi$ and $a_1(1260)[\mathrm{D}] \to \rho(770)\pi$, where the letters in square brackets refer to the relative orbital angular momentum of the decay products in spectroscopic notation. The P-wave decay, $a_1(1260)[\mathrm{P}] \to \rho(770)\pi$, is forbidden by parity conservation of the strong interaction. The sub-leading contribution was found to be the quasi-two-body decay $D[\mathrm{S},\mathrm{P},\mathrm{D}] \to \rho(770)\rho(770)$, where three different angular momentum couplings are possible. Further contributions from the decay channels $D \to R\,(\pi^+\pi^-)_{\mathrm{S}}$, with $R = \sigma^0, f_0(980)^0, f_2(1270)^0$, were considered. An amplitude fit with this model to the (flavor-tagged) CLEO-c data set does not give a satisfactory result, see Appendix D. In fact, the underlying physics permits a much larger number of possible decay channels. This analysis considers in addition contributions from the $\pi(1300), a_1(1420), a_2(1320), \pi_1(1600), a_1(1640)$ and $\pi_2(1670)$ mesons decaying in the cascade topology via various sub-decay modes to the three-pion final state. As the initial state of the charm meson is known, related non-self-conjugate decay modes, *e.g.* $D^0 \to a_1(1260)^+\pi^-$ and $D^0 \to a_1(1260)^-\pi^+$, can and need to be resolved, effectively doubling the number of possible cascade decay channels. As the strong interaction is *CP* symmetric, the

sub-decay modes of three-body resonances and their conjugates are constrained to be the same. This implies for example that the relative magnitude and phase between $a_1(1260)^+ \to \rho^0(770)\pi^+$ and $a_1(1260)^+ \to \sigma^0\pi^+$ decays are the same as for the conjugate modes, $a_1(1260)^- \to \rho^0(770)\pi^-$ and $a_1(1260)^- \to \sigma^0\pi^-$. However, the weak production processes $D^0 \to a_1(1260)^+\pi^-$ and $D^0 \to a_1(1260)^-\pi^+$ are different requiring one additional complex fit parameter. On top of that, the resonance $f_0(1370)^0$ decaying into two pions, additional quasi-two-body states, $\{\sigma^0\sigma^0, \sigma^0\rho(770), f_2(1270)^0\rho(770), \dots\}$ and several non-resonant amplitudes are taken into account. The complete list of considered amplitudes amounts to 83 and can be found in Table 6.1.

Table 6.1: Intermediate-state components considered for the $D^0 \to \pi^+\pi^-\pi^+\pi^-$ LASSO model building procedure. For cascade (non-self-conjugate) decay channels, the conjugate partner is implied. If no angular momentum is specified, the lowest angular momentum state compatible with angular momentum conservation and, where appropriate, parity conservation, is used.

(a) Cascade decays

$D^0 \to \pi^- \; [a_1(1260)^+ \to \pi^+ \sigma^0]$
$D^0 \to \pi^- \; [a_1(1260)^+[S,D] \to \pi^+ \rho(770)^0]$
$D^0 \to \pi^- \; [a_1(1260)^+ \to \pi^+ f_0(980)^0]$
$D^0 \to \pi^- \; [a_1(1260)^+ \to \pi^+ f_2(1270)^0]$
$D^0 \to \pi^- \; [a_1(1260)^+ \to \pi^+ f_0(1370)^0]$
$D^0 \to \pi^- \; [a_1(1260)^+[S,D] \to \pi^+ \rho(1450)^0]$
$D^0 \to \pi^- \; [\pi(1300)^+ \to \pi^+ \sigma^0]$
$D^0 \to \pi^- \; [\pi(1300)^+ \to \pi^+ \rho(770)^0]$
$D^0 \to \pi^- \; [\pi(1300)^+ \to \pi^+ (\pi^+\pi^-)_P]$
$D^0 \to \pi^- \; [a_2(1320)^+ \to \pi^+ \rho(770)^0]$
$D^0 \to \pi^- \; [a_2(1320)^+ \to \pi^+ f_2(1270)^0]$
$D^0 \to \pi^- \; [a_1(1420)^+ \to \pi^+ f_0(980)^0]$
$D^0 \to \pi^- \; [\pi_1(1600)^+ \to \pi^+ \rho(770)^0]$
$D^0 \to \pi^- \; [a_1(1640)^+ \to \pi^+ \sigma^0]$
$D^0 \to \pi^- \; [a_1(1640)^+[S,D] \to \pi^+ \rho(770)^0]$
$D^0 \to \pi^- \; [a_1(1640)^+ \to \pi^+ f_2(1270)^0]$
$D^0 \to \pi^- \; [\pi_2(1670)^+ \to \pi^+ \sigma^0]$
$D^0 \to \pi^- \; [\pi_2(1670)^+ \to \pi^+ \rho(770)^0]$
$D^0 \to \pi^- \; [\pi_2(1670)^+ \to \pi^+ f_2(1270)^0]$

(b) Quasi two-body decays

$D^0 \to (\pi\,\pi)_S \, (\pi\,\pi)_S$
$D^0 \to \sigma^0 \, (\pi\,\pi)_S$
$D^0 \to \sigma^0 \, \sigma^0$
$D^0 \to \sigma^0 \, f_0(980)^0$
$D^0 \to \sigma^0 \, f_0(1370)^0$
$D^0 \to f_0(980)^0 \, f_0(980)^0$
$D^0 \to f_0(1370)^0 \, f_0(1370)^0$
$D^0 \to \rho(770)^0 \, \sigma^0$
$D^0 \to \rho(770)^0 \, f_0(980)^0$
$D^0 \to \rho(770)^0 \, f_0(1370)^0$
$D^0 \to \rho(1450)^0 \, \sigma^0$
$D^0[S,P,D] \to (\pi\,\pi)_P \, (\pi\,\pi)_P$
$D^0[S,P,D] \to \rho(770)^0 \, (\pi\,\pi)_P$
$D^0[S,P,D] \to \rho(770)^0 \, \rho(770)^0$
$D^0[S,P,D] \to \rho(770)^0 \, \omega(782)^0$
$D^0[S,P,D] \to \omega(782)^0 \, \omega(782)^0$
$D^0[S,P,D] \to \rho(1450)^0 \, (\pi\,\pi)_P$
$D^0[S,P,D] \to \rho(1450)^0 \, \rho(1450)^0$
$D^0 \to f_2(1270)^0 \, \sigma^0$
$D^0 \to f_2(1270)^0 \, f_0(980)^0$
$D^0[P,D] \to f_2(1270)^0 \, \rho(770)^0$
$D^0[S,P,D] \to f_2(1270)^0 \, f_2(1270)^0$

Model building

Every single decay channel consistent with conservation laws also contributes to $D \to \pi\pi\pi\pi$ decays, albeit most of them on a negligible level given the finite data statistics. Therefore a model building procedure is applied with the goal to identify the most significant contributions. An optimal model provides a good description of the observed phase-space distribution while keeping the number of included amplitudes as small as possible. The amount of possible amplitude combinations is way beyond what can be tested by a brute-force approach. A typical algorithmic model building procedure starts with a small set of amplitudes, which are known or believed to contribute, and successively adds amplitudes on top of one another, keeping those which improve the fit result by a pre-defined metric (*e.g.* a certain change in the likelihood or χ^2 values) [170]. Such a stepwise approach risks that certain combinations of amplitudes are never considered together, particularly relevant for strongly interfering resonance contributions, and tends to produce overly simplistic models [180, 181]. It also requires enormous CPU resources, depending on how fast the algorithm is converging. In lieu of this, the *Least Absolute Shrinkage and Selection Operator* (LASSO) [180, 182] approach is applied which starts the other way around and considers, initially, the entire pool of amplitudes. With so many free fit parameters it is inevitable that some amplitudes receive a non-zero contribution only to describe statistical fluctuations of the given data sample rather than real physical features, an issue known as *overfitting*. Thus the model complexity is limited by adding a penalty term to the likelihood function:

$$-2\,\log\mathcal{L} \to -2\,\log\mathcal{L}' = -2\,\log\mathcal{L} + \lambda \sum_i \sqrt{\int |a_i\,A_i(\mathbf{x})|^2\,\mathrm{d}\Phi_4}, \tag{6.7}$$

which generally shrinks the amplitude coefficients towards zero. The general suppression of all intermediate-state amplitudes (due to the penalty term) concurs with the goodness of the fit represented by the (plain) likelihood function ($-2\,\log\mathcal{L}$). Therefore, the LASSO penalty term (predominantly) reduces contributions from intermediate-state components which do not notably improve the fit quality. The LASSO parameter λ controls the amount of shrinkage and has to be tuned on data. For this purpose, Equation 6.7 is minimized for various choices of λ. Figure 6.3(left) shows the resulting negative logarithmic likelihood values ($-2\,\log\mathcal{L}$) as function of the regularization parameter λ. The likelihood value stays approximately constant until $\lambda \approx 10$, above which the level of agreement between the fit result and the data starts to decline. At the same time, the number of amplitudes with a sizable decay fraction is consecutively reduced. This can

be seen in Figure 6.3(middle), which shows how many amplitudes with a decay fraction above 0.5% remain for a given value of λ. The *Bayesian information criteria* [183] (BIC) is used to balance the fit quality against the model complexity:

$$\mathrm{BIC}(\lambda) = -2 \log \mathcal{L} + r \log N_{\mathrm{S}}, \tag{6.8}$$

where N_{S} is the number of signal events and r is the number of amplitudes with a decay fraction above a chosen threshold (0.5%). Figure 6.3(right) shows the obtained BIC values scanning over the λ parameter, where an optimal value of $\lambda = 28$ is observed. At this working point 16 amplitudes have a decay fraction above the chosen threshold. All others are considered to be identical to zero and are removed. The remaining set of amplitudes is henceforth referred to as the LASSO model.

More than half of the considered amplitudes fall below the threshold already at the starting point[3], $\lambda = 0.1$. The LASSO procedure removes another eight amplitudes (or 16 fit parameters) having significant decay fractions with only a minor decrease in fit quality. Reasonable adjustments of the decay-fraction threshold to values in the range from 0.05% to 2% result in either the same or marginal different models containing one amplitude more or less. These models, see Appendix D, are considered as alternatives to the baseline LASSO model for systematic studies. Further alternative models are constructed by excluding the amplitudes selected under nominal conditions one-by-one from the set of all amplitudes considered and repeating the model finding procedure.

It is important to note that a few resonance contributions are identified in preliminary studies to be strongly disfavored by the data and are removed from the pool of amplitudes in order to stabilize the fit procedure. Moreover, there are certain groups of amplitudes with the same angular distribution that are prone to produce artificially high interference effects. This may result in fine-tuned models including, for example, two similar amplitudes with high decay fractions which are effectively canceled by their large negative interference. Even though the LASSO procedure is, in principle, able to remove such fine-tuned amplitude combinations, some obvious cases are avoided in order to reduce the parameter space. Amongst them are for example the di-scalar amplitudes: $D \to (\pi\,\pi)_S\,(\pi\,\pi)_S$, $D \to (\pi\,\pi)_S\,\sigma^0$, $D \to \sigma^0\,\sigma^0$, $D \to \sigma^0\,f_0(1370)^0$ and $D \to f_0(1370)^0\,f_0(1370)^0$. Only one amplitude of these groups is included at a time and the model selection is performed for each choice. The model with the lowest optimal BIC value is chosen as baseline, others are considered as alternative models.

[3]For $\lambda = 0$, the fit has problems to converge properly due to the large amount of redundant fit parameters. It is observed that a small non-zero value for λ stabilizes the fit significantly.

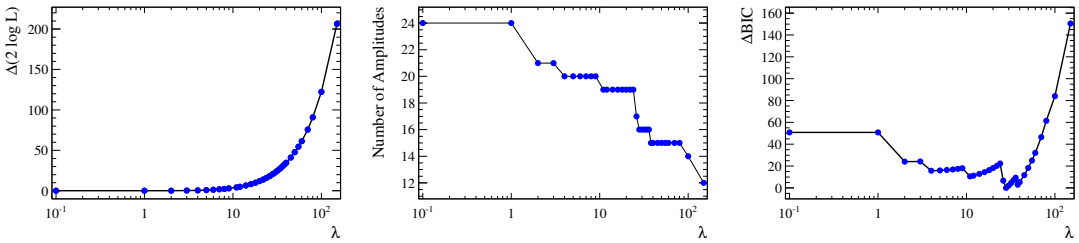

Figure 6.3: Difference in the negative logarithmic likelihood value from its minimum (left), number of amplitude with a decay fraction above 0.5% (middle) and difference in the BIC value from its minimum (right) as function of the LASSO parameter λ.

6.4 Resonance composition

Table 6.3 lists the real and imaginary part of the complex amplitude coefficients a_i, obtained by fitting the LASSO model to the data, along with the corresponding decay fractions. The fit model projected to invariant mass combinations shows reasonable agreement with the data, as demonstrated in Figure 6.4. The quality of the fit in the five-dimensional phase space is quantified by binning the data and calculating the metric:

$$\chi^2 = \sum_{i=1}^{N_{\text{bins}}} \frac{(N_i - N_i^{\text{pred}})^2}{N_i^{\text{pred}}}, \tag{6.9}$$

where N_i is the number of signal candidates in a given bin, N_i^{pred} is the event count predicted by the fitted amplitude model and N_{bins} is the number of bins. A robust χ^2 calculation is ensured by employing an adaptive binning algorithm [170]. The phase space is divided such that each bin is populated by at least 25 signal candidates leading to smaller hyper-volumes in regions of high event density. Ideally, the χ^2 value divided by the number of degrees of freedom[4], $\nu = N_{\text{bins}} - 1 - N_{\text{par}}$ where N_{par} is the number of free fit parameters, should be close to unity. For the LASSO model it amounts to $\chi^2/\nu = 1.4$ indicating a decent fit quality given that the metric accounts only for statistical uncertainties and systematic uncertainties are of similar magnitude as discussed in Section 6.6.

The LASSO model is significantly more complex than the FOCUS amplitude model [144]. Most notably, additional cascade decays via the $\pi(1300)$, $a_1(1640)$ and $\pi_2(1670)$ resonances are included. The $a_1(1260)$ meson is confirmed as the prominent resonance contribution. It is observed that the decay $D^0 \to a_1(1260)^+\pi^-$

[4]The number of effective degrees of freedom in an unbinned fit is bounded by $N_{\text{bins}} - 1$ and $(N_{\text{bins}} - 1) - N_{par}$. The latter is used as a conservative estimate.

Table 6.3: Real and imaginary part of the complex amplitude coefficients and fractional contribution of each component of the LASSO model. The first quoted uncertainty is statistical, while the second arises from systematic sources (discussed in Section 6.6). The third uncertainty in the fit fraction arises from the alternative models considered.

Decay channel	$\mathrm{Re}(a_i)$	$\mathrm{Im}(a_i)$	$F_i\,(\%)$
$D^0 \to \pi^-\,[a_1(1260)^+ \to \pi^+\,\rho(770)^0]$	100.0 (fixed)	0.0 (fixed)	$38.1 \pm 2.3 \pm 3.2 \pm 1.7$
$D^0 \to \pi^-\,[a_1(1260)^+ \to \pi^+\,\sigma^0]$	$16.5 \pm 4.1 \pm 4.3$	$49.2 \pm 4.3 \pm 5.7$	$10.2 \pm 1.4 \pm 2.1 \pm 2.5$
$D^0 \to \pi^+\,a_1(1260)^-$	$21.8 \pm 2.8 \pm 3.6$	$18.0 \pm 2.4 \pm 1.7$	-
$D^0 \to \pi^+\,[a_1(1260)^- \to \pi^-\,\rho(770)^0]$	-	-	$3.1 \pm 0.6 \pm 0.5 \pm 0.9$
$D^0 \to \pi^+\,[a_1(1260)^- \to \pi^-\,\sigma^0]$	-	-	$0.8 \pm 0.2 \pm 0.1 \pm 0.4$
$D^0 \to \pi^-\,[\pi(1300)^+ \to \pi^+\,\sigma^0]$	$-25.6 \pm 5.2 \pm 16.0$	$33.6 \pm 6.0 \pm 10.0$	$6.8 \pm 0.9 \pm 1.5 \pm 3.1$
$D^0 \to \pi^+\,[\pi(1300)^- \to \pi^-\,\sigma^0]$	$-11.0 \pm 4.1 \pm 10.3$	$25.8 \pm 4.6 \pm 12.7$	$3.0 \pm 0.6 \pm 2.0 \pm 2.0$
$D^0 \to \pi^-\,[a_1(1640)^+[D] \to \pi^+\,\rho(770)^0]$	$-33.0 \pm 5.4 \pm 7.5$	$-2.9 \pm 4.0 \pm 3.6$	$4.2 \pm 0.6 \pm 0.9 \pm 1.8$
$D^0 \to \pi^-\,[a_1(1640)^+ \to \pi^+\,\sigma^0]$	$16.0 \pm 4.5 \pm 6.4$	$-19.6 \pm 4.4 \pm 7.11$	$2.4 \pm 0.7 \pm 1.1 \pm 1.3$
$D^0 \to \pi^-\,[\pi_2(1670)^+ \to \pi^+\,f_2(1270)^0]$	$-3.8 \pm 3.2 \pm 5.9$	$26.3 \pm 3.1 \pm 3.2$	$2.7 \pm 0.6 \pm 0.7 \pm 0.9$
$D^0 \to \pi^-\,[\pi_2(1670)^+ \to \pi^+\,\sigma^0]$	$-7.2 \pm 3.1 \pm 2.1$	$-29.2 \pm 3.1 \pm 5.8$	$3.5 \pm 0.6 \pm 0.8 \pm 0.9$
$D^0 \to \sigma^0\,f_0(1370)^0$	$26.8 \pm 6.6 \pm 18.4$	$69.5 \pm 6.2 \pm 16.8$	$21.2 \pm 1.8 \pm 4.2 \pm 5.2$
$D^0 \to \sigma^0\,\rho(770)^0$	$35.9 \pm 3.6 \pm 3.8$	$-21.7 \pm 3.1 \pm 5.6$	$6.6 \pm 1.0 \pm 1.2 \pm 3.0$
$D^0 \to \rho(770)^0\,\rho(770)^0$	$6.5 \pm 3.4 \pm 5.5$	$24.3 \pm 3.7 \pm 5.0$	$2.4 \pm 0.7 \pm 1.1 \pm 1.0$
$D^0[P] \to \rho(770)^0\,\rho(770)^0$	$-5.1 \pm 2.7 \pm 3.0$	$-42.2 \pm 3.0 \pm 7.5$	$7.0 \pm 0.5 \pm 1.6 \pm 0.3$
$D^0[D] \to \rho(770)^0\,\rho(770)^0$	$-45.2 \pm 4.5 \pm 6.8$	$-10.2 \pm 3.5 \pm 6.4$	$8.2 \pm 1.0 \pm 1.7 \pm 3.5$
$D^0 \to f_2(1270)^0\,f_2(1270)^0$	$-4.6 \pm 2.9 \pm 3.0$	$-23.1 \pm 2.9 \pm 3.6$	$2.1 \pm 0.5 \pm 0.3 \pm 2.3$
Sum			$122.0 \pm 4.0 \pm 6.4 \pm 7.6$

dominates over the conjugate mode $D^0 \to a_1(1260)^-\pi^+$. This implies that the $a_1(1260)$ meson is preferentially produced via its coupling to the W boson rather than originating from the spectator-quark interaction, *cf.* Figure 4.1. The decay $D^0 \to K^+K^-\pi^+\pi^-$ shows a consistent structure as the decay mode $D^0 \to K_1(1270)^+K^-$ is favored with respect to $D^0 \to K_1(1270)^-K^+$ [1, 184]. A similar pattern is also seen in the beauty system, where $B^0 \to a_1(1260)^+\pi^-$ transitions are preferred over $B^0 \to a_1(1260)^-\pi^+$ [185,186]. Except for the scalar $\pi(1300)$ meson, all other resonances decaying into three pions are exclusively observed with the same charge as the W boson. The $a_1(1640)$ meson was previously reported in Reference [187] decaying to $\sigma^0\pi$ and $f_2(1270)^0\pi$, and in Reference [188] decaying to $\rho(770)^0\pi$, though confirmation of this hadronic state is still needed [150]. The model building procedure identifies the decay modes $a_1(1640)[D] \to \rho(770)^0\pi$ and $a_1(1640) \to \sigma^0\pi$ with a combined decay fraction of 6.6%. The S-wave and D-wave dominance of the $a_1(1260) \to \rho(770)^0\pi$ and $a_1(1640) \to \rho(770)^0\pi$ decay channels, respectively, is qualitatively consistent with the prediction of the *vacuum quark-pair-creation model* [15, 189] and points towards the interpretation of the $a_1(1640)$ meson as the first radial radial excitation of the $a_1(1260)$ meson [190].

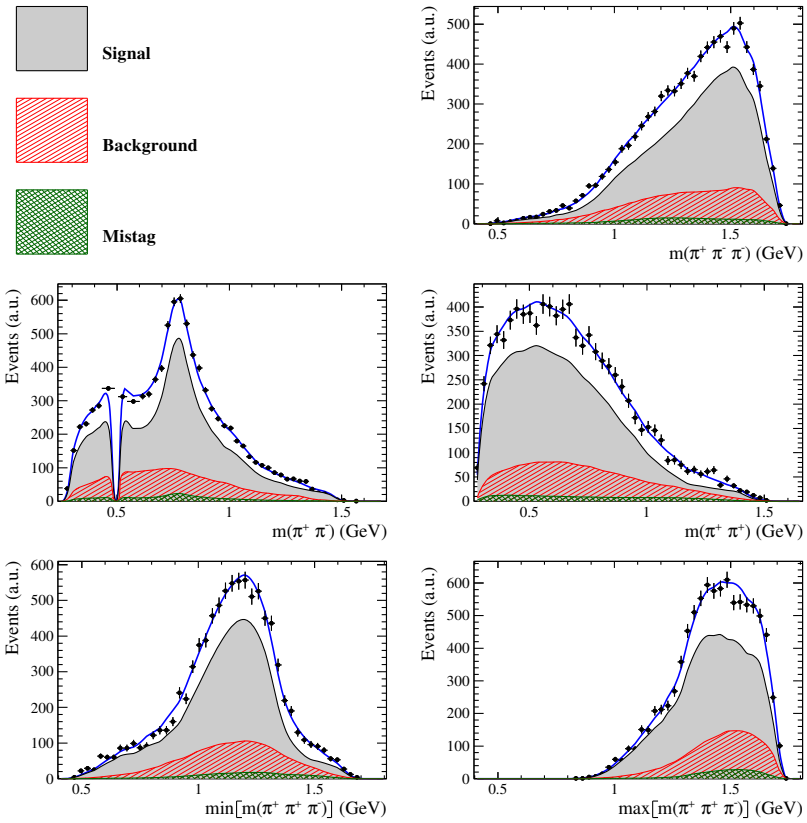

(a) Signal, background and wrongly tagged contributions are overlaid.

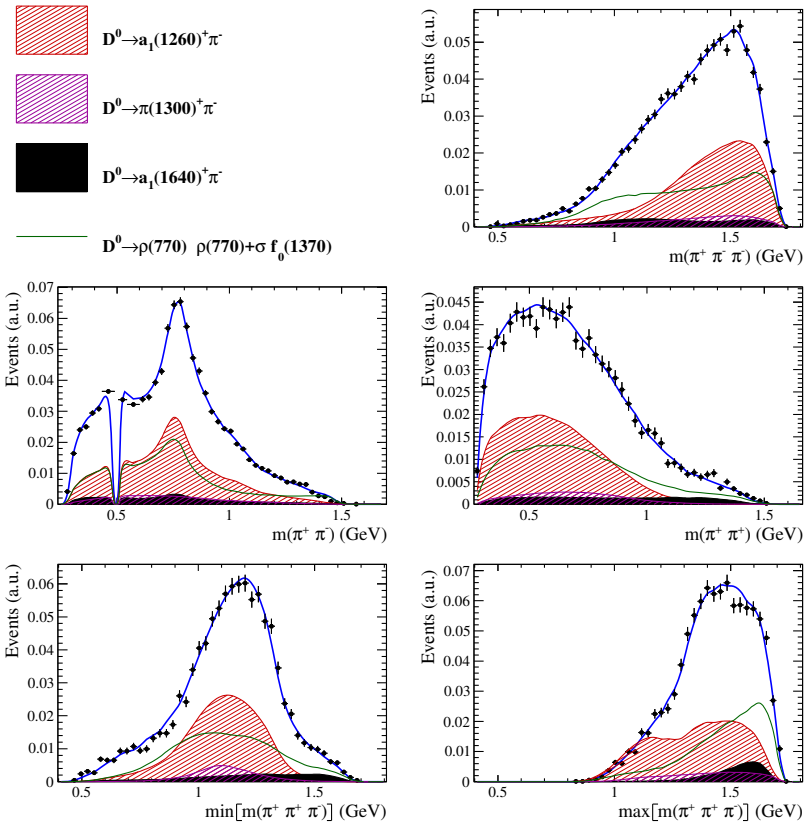

(b) Incoherent contributions from the dominant intermediate-state components are overlaid.

Figure 6.4: Invariant-mass distributions of $D^0 \to \pi^+\pi^-\pi^+\pi^-$ signal candidates (points with error bars) and fit projections (blue solid line).

There are also large contributions from several quasi two-body modes lead by $D^0 \to \sigma^0 f_0(1370)^0$ and $D^0 \to \rho(770)^0 \rho(770)^0$ decays. The latter shows an interesting polarization structure contradicting the naive expectation of S-wave dominance. Due to the large width of the $\rho(770)$ meson, this decay can proceed with a sizable energy release such that the centrifugal-barrier suppression is relatively mild. Consistent patterns are found in $D^0 \to \rho(770)^0 K^*(892)^0$ [191] and $D^0 \to K^*(892)^0 \bar{K}^*(892)^0$ [1, 184] decays with large P- and D-wave contributions. Still, the underlying mechanism which enhances higher angular momentum configurations in these decay modes is puzzling and requires further studies to understand its origin. A possible explanation are final-state rescattering effects [192, 193].

The interference fractions (I_{ij} defined in Equation 2.26) are given in Table D.1. Large interference effects between the decay channels $D^0 \to \pi^- [a_1(1260)^+ \to \pi^+ \rho(770)^0]$ and $D^0 \to \pi^- [a_1(1260)^+ \to \pi^+ \sigma^0]$ ($I_{ij} \approx +20\%$) as well as between $D^0 \to \pi^- [\pi(1300)^+ \to \pi^+ \sigma^0]$ and $D^0 \to \sigma^0 f_0(1370)^0$ ($I_{ij} \approx -10\%$) are observed. This is expected as those components have a significant overlap in phase space. The sum of all 120 interference fractions results in a net destructive interference around -22%.

Study of resonance lineshapes

As discussed in Section 2.2, the lineshape calculation for mesons decaying via the cascade topology is more involved since the partial decay width depends on their resonant substructure studied in parallel. The numerical computation of Equation 2.22 is CPU intensive and thus impractical to repeat each time the resonance composition is adjusted during the likelihood optimization. As a solution, an iterative approach is followed. First, the energy-dependent width distribution is derived assuming a uniform phase space population. With that as input, an initial amplitude fit is performed. Thereafter, the running decay width is recalculated with the acquired knowledge about the resonant substructure and the amplitude fit is repeated using the updated resonance propagator. It is observed that the partial decay width is not highly sensitive to the details of substructure analysis such that this procedure converges already after a few iterations, as demonstrated in Figure 6.5(left) for the $a_1(1260)$ meson. The running-width distributions for other resonances are shown in Figure B.1. The energy-dependent mass of the $a_1(1260)$ meson is calculated from Equation 2.23 using the final decay width iteration. The result is displayed in Figure 6.5(right) and shows a plateau around the nominal mass, as argued in Section 2.2. For all other resonances, a constant mass is used.

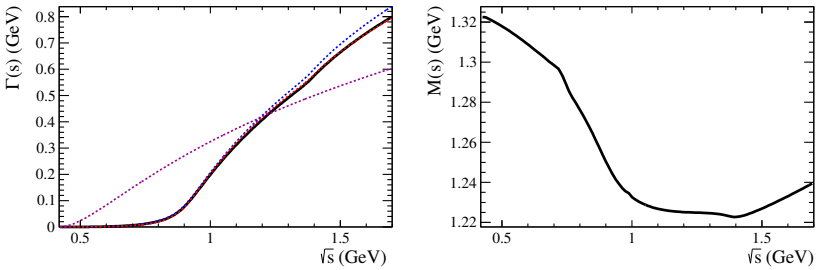

Figure 6.5: Energy-dependent decay width (left) of the $a_1(1260)$ meson after the first (magenta), second (blue), third (red) and the final, fifth, (black) iteration. The running-mass distribution is shown on the right.

Table 6.4 lists the resonance properties extracted from the amplitude fit. All measured masses and widths are in good agreement with the PDG estimates. The determined $a_1(1260)$ resonance parameters are compatible with the values obtained from an amplitude analysis of $D^0 \to K^-\pi^+\pi^-\pi^+$ decays performed by the LHCb collaboration: $m_{a_1(1260)} = (1195.05 \pm 1.05\,(\text{stat}) \pm 6.33\,(\text{syst}))\,\text{MeV}$ and $\Gamma_{a_1(1260)} = (422.01 \pm 2.10\,(\text{stat}) \pm 12.72\,(\text{syst}))\,\text{MeV}$ [191]. The results of the FOCUS $D \to \pi\pi\pi\pi$ amplitude analysis are $m_{a_1(1260)} = (1240^{+30}_{-10})\,\text{MeV}$ and $\Gamma_{a_1(1260)} = (560^{+120}_{-40})\,\text{MeV}$ [144]. As discussed above, no resonance contributions to the three-pion system apart from the $a_1(1260)$ meson have been considered providing a conclusive argument for the measurement of a larger decay width. The COMPASS collaboration has studied the $a_1(1260)$ meson via its production in the $p+\pi \to p+\pi\pi\pi$ scattering process and found the values: $m_{a_1(1260)} = (1255 \pm 6\,(\text{stat})^{+7}_{-17}\,(\text{syst}))\,\text{MeV}$ and $\Gamma_{a_1(1260)} = (367 \pm 9\,(\text{stat})^{+28}_{-25}\,(\text{syst}))\,\text{MeV}$ [194]. As a simplified lineshape description was used, these results cannot be straightforward compared to the values in Table 6.4. To illustrate the impact of the lineshape parameterization, additional amplitude fits using a relativistic Breit-Wigner (Equation 2.19) or a constant width Breit-Wigner function for the $a_1(1260)$ propagator are performed. The results are: $m_{a_1(1260)} = (1221 \pm 8\,(\text{stat}))\,\text{MeV}$ and $\Gamma_{a_1(1260)} = (387 \pm 18\,(\text{stat}))\,\text{MeV}$; or

Table 6.4: Resonance parameters determined from the fit to $D \to \pi\pi\pi\pi$ candidates. The uncertainties are statistical, systematic and model-dependent, respectively. The PDG estimates are given as comparison [10].

Parameter	Fit value [MeV]	PDG value [MeV]
$m_{a_1(1260)}$	$1225 \pm 9 \pm 17 \pm 10$	1230 ± 40
$\Gamma_{a_1(1260)}$	$430 \pm 24 \pm 25 \pm 18$	$250 - 600$
$m_{\pi(1300)}$	$1128 \pm 26 \pm 59 \pm 37$	1300 ± 100
$\Gamma_{\pi(1300)}$	$314 \pm 39 \pm 61 \pm 26$	$200 - 600$
$m_{a_1(1640)}$	$1691 \pm 18 \pm 16 \pm 25$	1647 ± 22
$\Gamma_{a_1(1640)}$	$171 \pm 33 \pm 20 \pm 35$	254 ± 27

$m_{a_1(1260)} = (1134 \pm 8\ (\text{stat}))\,\text{MeV}$ and $\Gamma_{a_1(1260)} = (367 \pm 15\ (\text{stat}))\,\text{MeV}$. The nominal lineshape model is preferred over the relativistic Breit-Wigner (constant width Breit-Wigner) with a significance of 10σ (7σ), determined from the log-likelihood difference between the two fit results, $\sigma = \sqrt{\Delta(-2\log\mathcal{L})}$, assuming *Wilk's* theorem [79,195]. The $a_1(1260)$ lineshape parameters have also been measured in decays of the τ lepton to the $\pi\pi\pi\nu_\tau$ final state. For example, the CLEO collaboration determined the mass and width to be $m_{a_1(1260)} = (1331 \pm 10\,(\text{stat}) \pm 3\,(\text{syst}))\,\text{MeV}$ and $\Gamma_{a_1(1260)} = (814 \pm 36\,(\text{stat}) \pm 13\,(\text{syst}))\,\text{MeV}$ [67]. The unusually large value for the decay width might again be related to the specific choice of lineshape parametrization. In particular, a large dependency on the form factor was observed. This might be related to the fact that the three-pion spectrum is completely dominated by the $a_1(1260)$ meson due to the limited phase space of the τ lepton decay. As, in this case, there is no second interfering process, no phase information can be extracted and the mass and width can only be constrained from the observed intensity distribution. The three-pion spectrum in τ lepton decays was later reanalyzed combining the CLEO data sample [67] with ALEPH [196], ARGUS [197] and OPAL [198] data. In this study, a similar lineshape parameterization was used as in the $D \to \pi\pi\pi\pi$ amplitude analysis presented here. The following results were obtained: $m_{a_1(1260)} = (1233 \pm 18)\,\text{MeV}$ and $\Gamma_{a_1(1260)} = (431 \pm 20)\,\text{MeV}$ [76], in excellent agreement with the amplitude fit.

Quasi-model-independent lineshapes

The discussion of the $a_1(1260)$ lineshape highlights the fact that measurements of the mass and width of hadronic states are highly model-dependent. Hence, the chosen lineshape parameterization is verified in a quasi-model-independent way as pioneered in References [199,200]. The procedure tests the implicit assumption that hadronic resonances can be described with a Breit-Wigner function, $T_{\text{BW}}(s)$, by replacing the nominal lineshape of a given resonance with a generic complex-valued function, $f(s)$. This function is constructed as follows: first, several knot-points, s_i (i=$\{1,2,\ldots,6\}$) are chosen in the invariant mass region around the nominal mass of the resonance. The magnitudes and phases of the function at these knot positions, *i.e.* $\text{Re}[f(s_i)]$ and $\text{Im}[f(s_i)]$, are then directly determined from a fit to the data. While doing so, the function values for invariant masses in-between two consecutive knot positions are interpolated with a cubic spline in order to obtain a smooth function [201]. The location of the knots is chosen ad-hoc. It is verified with simulated pseudo-experiments that a Breit-Wigner lineshape can be properly described with this configuration. Figure 6.6 shows the determined quasi-model-independent lineshapes for the $a_1(1260)$, $\pi(1300)$ and $a_1(1640)$ resonances, where the expectations from a Breit-Wigner propagator with the mass and width

from the nominal fit are superimposed. The general features of the respective Breit-Wigner functions are reproduced by the interpolated splines. The Argand diagrams show clear circular, counter-clockwise trajectories; the expected behavior of resonant states as discussed in Section 2.2. This is a solid indication that these resonances are indeed real features of the data and not the result of overfitting or similar artifacts of the amplitude model. Note that the high-mass tail of the $a_1(1640)$ meson is outside of the phase-space boundary such that the full phase motion cannot be investigated. As the investigated resonances have large decay widths and the interpolated spline function requires an extensive amount of free fit parameters (eight more than the Breit-Wigner function), the quasi-model-independent approach is fairly sensitive to statistical fluctuations in the data. With this in mind, the agreement with the Breit-Wigner expectation can be considered as reasonable in all cases. The quasi-model-independent results provide a straightforward way to test alternative parameterizations (as used in other measurements), albeit the discriminating power is limited by the large statistical uncertainty.

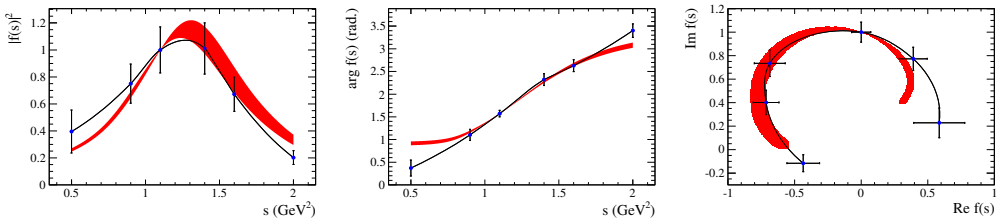

(a) Lineshape of the $a_1(1260)$ resonance.

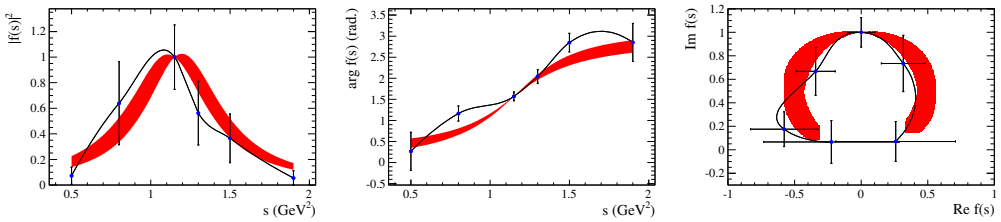

(b) Lineshape of the $\pi(1300)$ resonance.

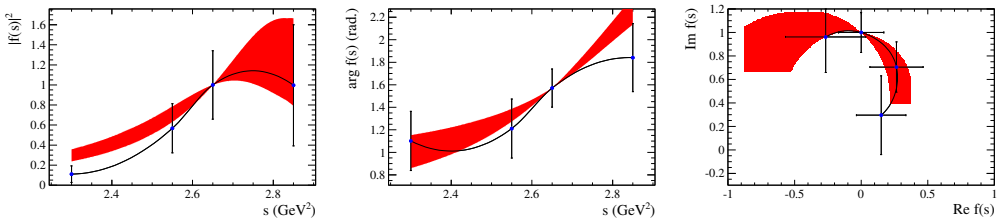

(c) Lineshape of the $a_1(1640)$ resonance.

Figure 6.6: Magnitude-squared (left), phase (middle) and Argand (right) diagram of the quasi-model-independent lineshape. The fitted knots are displayed as points with error bars and the black line shows the interpolated spline. The Breit-Wigner lineshape with the mass and width from the nominal fit is superimposed (red area). The latter is chosen to agree with the interpolated spline at the point $\mathrm{Re}\, f(s) = 0$, $\mathrm{Im}\, f(s) = 0$.

6.5 Search for *CP* violation

A search for *CP* violation is conducted by fitting the LASSO model to the flavor-tagged D^0 and $\overline{D}^0$ data samples allowing the respective amplitude coefficients to differ. These are expressed in terms of *CP*-conserving, c_i, and *CP*-violating, Δc_i, complex parameters,

$$a_i \equiv c_i\,(1 + \Delta c_i), \qquad \bar{a}_i \equiv c_i\,(1 - \Delta c_i), \tag{6.10}$$

such that for $\Delta c_i = 0$ there is no *CP* violation between the corresponding D^0 and $\overline{D}^0$ intermediate-state amplitudes. More specifically, the *CP*-violating parameters are included for each distinct weak decay processes, while the strong interaction is assumed to be *CP*-conserving. This implies, for example, that the amplitudes for the processes $D^0 \to \pi^-\,[a_1(1260)^+ \to \pi^+\,\rho(770)^0]$ and $D^0 \to \pi^-\,[a_1(1260)^+ \to \pi^+\,\sigma^0]$ have different c_i parameters but share a common *CP*-violating parameter Δc_i. A measure of *CP* violation in each amplitude component is then derived from the decay-fraction asymmetry,

$$\mathcal{A}^i_{CP} \equiv \frac{\int |a_i\,A_i(\mathbf{x})|^2\,\mathrm{d}\Phi_4 - \int |\bar{a}_i\,\bar{A}_i(\mathbf{x})|^2\,\mathrm{d}\Phi_4}{\int |a_i\,A_i(\mathbf{x})|^2\,\mathrm{d}\Phi_4 + \int |\bar{a}_i\,\bar{A}_i(\mathbf{x})|^2\,\mathrm{d}\Phi_4}. \tag{6.11}$$

The results are listed in Table 6.5. No significant *CP* asymmetry is observed for any of the intermediate-state amplitudes, with sensitivities ranging from 4% to 22%. Similarly, the global decay-rate asymmetry is calculated from the amplitude model to be:

$$\mathcal{A}_{CP} \equiv \frac{\int |A_{D^0}(\mathbf{x})|^2\,\mathrm{d}\Phi_4 - \int |A_{\overline{D}^0}(\mathbf{x})|^2\,\mathrm{d}\Phi_4}{\int |A_{D^0}(\mathbf{x})|^2\,\mathrm{d}\Phi_4 + \int |A_{\overline{D}^0}(\mathbf{x})|^2\,\mathrm{d}\Phi_4} = [+0.60 \pm 0.56\ (\mathrm{stat})]\%. \tag{6.12}$$

To avoid the systematic uncertainty arising from the amplitude model, this quantity can also be determined from the observed yield asymmetry,

$$\mathcal{A}_{CP} = \frac{N_{D^0}/\varepsilon_{D^0} - N_{\overline{D}^0}/\varepsilon_{\overline{D}^0}}{N_{D^0}/\varepsilon_{D^0} + N_{\overline{D}^0}/\varepsilon_{\overline{D}^0}} = [+0.54 \pm 1.04\,(\mathrm{stat}) \pm 0.51\,(\mathrm{syst})]\%, \tag{6.13}$$

where N_{D^0} ($N_{\overline{D}^0}$) denotes the the number of identified D^0 ($\overline{D}^0$) mesons. The systematic uncertainty originates from alternative parameterizations of the signal and background PDFs used to estimate the signal yields, *cf.* Section 5.3, and a potential difference in selection efficiencies between D^0 and $\bar{D}^0$ decays, ε_{D^0} and $\varepsilon_{\overline{D}^0}$. Due to the charge symmetric final state, the reconstruction efficiency of $D^0 \to \pi^+\pi^-\pi^+\pi^-$ and $\bar{D}^0 \to \pi^+\pi^-\pi^+\pi^-$ decays is, in principle, identical.

However, the decay of the other charm meson in the event used to tag the signal flavor state involves asymmetric[5] final states, *e.g.* in $D \to K\pi$ decays. The reconstruction efficiencies of these tag side decay modes have been determined by the CLEO collaboration in context of their branching fraction measurement [202] and translate to a relative efficiency[6] for detecting a $\overline{D}^0$ with respect to a D^0 signal decay of $\varepsilon_{\overline{D}^0}/\varepsilon_{D^0} = 0.9899 \pm 0.0015$. The results in Equation 6.12 and Equation 6.13 are consistent with each other and with *CP* conservation.

Table 6.5: Decay-fraction asymmetry and significance for each component of the LASSO model. The first uncertainty is statistical, the second systematic and the third due to alternative models.

Decay channel	$\mathcal{A}^i_{CP}$ (%)	Significance (σ)
$D^0 \to \pi^- a_1(1260)^+$	$+4.7 \pm 2.6 \pm 4.3 \pm 2.4$	0.9
$D^0 \to \pi^+ a_1(1260)^-$	$+13.7 \pm 13.8 \pm 9.8 \pm 5.8$	0.8
$D^0 \to \pi^- \pi(1300)^+$	$-1.6 \pm 12.9 \pm 5.0 \pm 4.4$	0.1
$D^0 \to \pi^+ \pi(1300)^-$	$-5.6 \pm 11.9 \pm 25.6 \pm 10.3$	0.2
$D^0 \to \pi^- a_1(1640)^+$	$+8.6 \pm 17.8 \pm 16.0 \pm 10.8$	0.3
$D^0 \to \pi^- \pi_2(1670)^+$	$+7.3 \pm 15.1 \pm 8.0 \pm 6.6$	0.4
$D^0 \to \sigma^0 f_0(1370)^0$	$-14.6 \pm 16.5 \pm 9.3 \pm 1.3$	0.8
$D^0 \to \sigma^0 \rho(770)^0$	$+2.5 \pm 16.8 \pm 13.8 \pm 14.6$	0.1
$D^0 \to \rho(770)^0 \rho(770)^0$	$-5.6 \pm 5.0 \pm 2.2 \pm 1.9$	1.0
$D^0 \to f_2(1270)^0 f_2(1270)^0$	$-28.3 \pm 12.3 \pm 18.5 \pm 9.7$	1.2

[5] Detector induced effects responsible for charge asymmetric reconstruction efficiencies are discussed in context of the $B_s \to D_s K\pi\pi$ analysis in Section 10.4, where they are studied in more detail.

[6] The amplitude fit also accounts for the small difference in D^0 and $\bar{D}^0$ reconstruction efficiencies by setting the phase-space acceptances to $\epsilon(\mathbf{x})$ and $\frac{\varepsilon_{\bar{D}^0}}{\varepsilon_{D^0}}\,\epsilon(\mathbf{x})$, respectively.

6.6 Systematic uncertainties

The considered systematic uncertainties on the fit parameters can be categorized into three main sources: an intrinsic fit bias, several experimental issues and uncertainties related to the amplitude model. The latter is generally the dominant systematic effect. All systematic uncertainties are added in quadrature and summarized in Table 6.6. The total systematic errors are in the range from 50% to three times the statistical uncertainty, depending on the parameter. The following section details how the individual uncertainties are estimated.

Fit bias

A large ensemble of pseudo-experiments is generated from the nominal LASSO model. The obtained MC samples are then fitted with the same PDF in order to verify that the input parameters can be retrieved. For each pseudo-experiment, a *pull* value for a given parameter is computed as: $\text{Pull}(\theta_i) = (\theta_i^{\text{Fit}} - \theta_i^{\text{Gen}})/\sigma_{\theta_i}$, where the input value is denoted as θ_i^{Gen} and the fit returns the value θ_i^{Fit} with statistical uncertainty σ_{θ_i}. The width of the pull distributions are compatible with unity demonstrating a consistent error calculation. Small biases of the mean of the pull distributions (around 0.1 times the statistical uncertainty σ_{θ_i}, see Table 6.6) are assigned as systematic uncertainty.

Experimental uncertainties

Experimental systematic uncertainties occur due to imperfect knowledge of the yield of background candidates in the signal region and their distribution in phase space. The former is studied by repeating the amplitude fit allowing the signal fraction, f_{S}, to vary under Gaussian constraints. In this way, the statistical error of the fit parameters of interest increases by an amount reflecting the uncertainty on the signal fraction. Thus, the shift of the statistical uncertainties, σ_{θ_i}, and the biases of the central values with respect to the nominal fit result are computed and added in quadrature to obtain the corresponding systematic uncertainty for each fit parameter. The same procedure is applied to assess the systematic uncertainty related to the background PDF, whose parameters are fixed in the nominal fit to the ones obtained from sideband data. Aside from this, several alternative background models are tested whereby each of the background components, described in Appendix D, is replaced, one at a time, by a function which is constant over the entire phase space. The largest deviations from the nominal fit parameter values are taken as systematic uncertainties. The systematic uncertainty due to the wrong tag rate, ω, is estimated in the same manner as for the signal fraction.

The determination of the phase-space acceptance relies on simulated data. To evaluate the uncertainty due to possible data-simulation differences arising from the track reconstruction or particle identification, momentum-dependent correction factors obtained from independent internal studies of the CLEO collaboration [203, 204] are used to re-weight the simulated events separately for each effect. The amplitude fit is repeated and the resulting shift of the fit parameters is assigned as systematic uncertainty.

The systematic uncertainties from experimental sources are consistently small. They range from 0.1 to at most 0.5 times the statistical uncertainty (depending on the parameter), see Table 6.6.

Model-dependent uncertainties

Several poorly known lineshape parameters are determined in the nominal amplitude fit, so that their uncertainties are already included in the statistical error of the fit parameters. To account for the uncertainties of the other resonance masses and widths which are fixed to the values reported in Appendix B, these are varied one-by-one within their quoted errors and the related shift of the fit parameters is included as systematic uncertainty. These systematic uncertainties are sizable (up to two times the statistical uncertainty for some parameters) and are dominated by the limited knowledge of the resonance parameters of the scalar σ^0 and $f_0(1370)$ mesons.

The default value of the Blatt-Weisskopf radial parameter is set to $r_{\mathrm{BW}} = 1.5\,\mathrm{GeV}^{-1}$, in accordance with similar analyses (*e.g.* those in References [170, 184, 191]). It is changed to $r_{\mathrm{BW}} = 0.0\,\mathrm{GeV}^{-1}$ or $r_{\mathrm{BW}} = 3.0\,\mathrm{GeV}^{-1}$ to study the impact of this choice. The largest shift of the fit parameters is taken as systematic error. In particular, the determined resonance masses are affected, where shifts at the same order as the statistical uncertainty are observed.

The energy dependence of the partial widths into the three pion channel are calculated employing an iterative procedure, as described in Section 6.4. Here, the lineshape iteration previous to the final is used to estimate the systematic error of this approach. The calculation of the total decay width also requires, in some cases, input from external measurements of branching fractions to other final states. As a systematic check, only the partial width into the final state under study is considered. In a similar fashion, the energy-dependent mass of the $a_1(1260)$ meson is approximated by a constant. The deviations from the nominal fit result for each above-mentioned lineshape variation is added in quadrature to obtain a total systematic uncertainty (which is up to two times the statistical uncertainty for some parameters).

The signal PDF in Equation 6.1 ignores a small interference effect between the quantum-correlated signal and tag-side decays. Recapitulating the discussion in Section 3.2, the quantum-entangled system can be described by the antisymmetric total amplitude, $A_{D_a^0}(\mathbf{x})A_{\bar{D}_b^0}(\mathbf{x}') - A_{\bar{D}_a^0}(\mathbf{x})A_{D_b^0}(\mathbf{x}')$. Now, let the tagging particle be reconstructed in the decay $D_b \to K^+X$ (with $K^+X = \{K^+e^-\bar{\nu}_e, K^+\pi^-, ...\}$) and define $K_t \equiv \int A_{\bar{D}_b^0}(\mathbf{x}')\,\mathrm{d}\phi(\mathbf{x}')$ and $K_t\, k_t e^{i\delta_t} \equiv \int A_{D_b^0}(\mathbf{x}')\,\mathrm{d}\phi(\mathbf{x}')$, where k_t and δ_t are the relative magnitude and phase between $\bar{D}_b^0 \to K^+X$ and $D_b^0 \to K^+X$ decays. The relative magnitude is zero for the flavor-specific decay $D_b \to K^+e^-\bar{\nu}_e$ and small for the other tag decay modes, $k_t \approx 5\%$ [170]. The decay rate of the signal decay $D_a \to \pi\pi\pi\pi$ is then given by:

$$\Gamma(\mathbf{x}) \propto |A_{D_a^0}(\mathbf{x})|^2 + k_t^2\,|A_{\bar{D}_a^0}(\mathbf{x})|^2 + 2k_t\left(\mathrm{Re}(A_{D_a^0}(\mathbf{x})A^*_{\bar{D}_a^0}(\mathbf{x}))\cos(\delta_t) + \mathrm{Im}(A_{D_a^0}(\mathbf{x})A^*_{\bar{D}_a^0}(\mathbf{x}))\sin(\delta_t)\right),$$

based on which an alternative signal PDF is defined. The term proportional to k_t^2 is tiny and thus neglected. The values for $k_t\cos(\delta_t)$ and $k_t\sin(\delta_t)$ averaged over all tag-side decay modes are taken from Reference [170], $\langle k_t\cos(\delta_t)\rangle = 0.061 \pm 0.042$ and $\langle k_t\sin(\delta_t)\rangle = 0.029 \pm 0.007$. The shifts of the fit parameters with respect to the nominal approach are assigned as systematic uncertainty (which are at the same order as the statistical uncertainty for some parameters).

Alternative amplitude models

The baseline LASSO model is in no way unique. Slightly modified configurations of the model finding procedure may lead to a different set of selected amplitudes with similar complexity and fit quality. An ensemble of alternative models is obtained from variations of the nominal approach as discussed in Section 6.3. Seven models providing a similar fit quality as the LASSO model are predestined for systematic studies. In addition, an *extended* amplitude model is constructed by including all conjugate partners of the non-self-conjugate intermediate states selected by the nominal LASSO procedure. For example, the $D^0 \to \pi^+\,[a_1(1640)^- \to \pi^-\,\sigma^0]$ amplitude is added since the baseline model contains the $D^0 \to \pi^-\,[a_1(1640)^+ \to \pi^+\,\sigma^0]$ amplitude. From the fit results using these alternative models, see Tables D.2-D.3, an additional model-dependent error is derived from their sample variance. The amplitude coefficients are, by definition, parameters of a given model. Hence, the systematic uncertainty due to the choice of amplitude components is only calculated for the convention-independent decay fractions and resonance parameters. Here, the decay fraction is set to zero if a nominal amplitude is not included in an alternative model. The model-dependent uncertainty is at the same order as the statistical uncertainty for the resonance parameters (see Table 6.4) and up to three times the statistical uncertainty for the decay fractions (see Table 6.3).

Table 6.6: Systematic uncertainties on the fit parameters of the LASSO model in units of statistical standard deviations, σ. The different contributions are: 1) Blatt-Weisskopf barrier factors, 2) Masses and widths of resonances, 3) Background model, 4) Signal fraction, 5) Wrong tag fractions, 6) Tag-side interference, 7) Efficiency, 8) Fit bias, 9) Energy-dependent masses and widths.

Fit parameter	1	2	3	4	5	6	7	8	9	Total
$D^0 \to \pi^- \left[a_1(1260)^+ \to \pi^+ \sigma^0\right]$ Re(a_i)	0.55	0.11	0.16	0.09	0.20	0.78	0.17	0.22	0.14	1.05
$D^0 \to \pi^- \left[a_1(1260)^+ \to \pi^+ \sigma^0\right]$ Im(a_i)	1.20	0.19	0.28	0.16	0.19	0.28	0.11	0.14	0.18	1.33
$D^0 \to \pi^+ a_1(1260)^-$ Re(a_i)	0.43	1.13	0.24	0.11	0.22	0.16	0.18	0.09	0.11	1.29
$D^0 \to \pi^+ a_1(1260)^-$ Im(a_i)	0.56	0.35	0.10	0.12	0.10	0.04	0.15	0.07	0.09	0.71
$D^0 \to \pi^- \left[\pi(1300)^+ \to \pi^+ \sigma^0\right]$ Re(a_i)	1.32	1.72	0.06	0.19	0.29	0.22	0.54	0.28	2.07	3.08
$D^0 \to \pi^- \left[\pi(1300)^+ \to \pi^+ \sigma^0\right]$ Im(a_i)	0.12	0.53	0.20	0.17	0.25	0.22	0.08	0.09	1.51	1.67
$D^0 \to \pi^+ \left[\pi(1300)^- \to \pi^- \sigma^0\right]$ Re(a_i)	0.74	1.83	0.17	0.03	0.10	0.45	0.33	0.03	1.39	2.51
$D^0 \to \pi^+ \left[\pi(1300)^- \to \pi^- \sigma^0\right]$ Im(a_i)	0.01	1.01	0.23	0.08	0.40	0.33	0.10	0.17	2.50	2.76
$D^0 \to \pi^- \left[a_1(1640)^+[D] \to \pi^+ \rho(770)^0\right]$ Re(a_i)	0.85	0.44	0.09	0.11	0.06	0.90	0.14	0.34	0.33	1.39
$D^0 \to \pi^- \left[a_1(1640)^+[D] \to \pi^+ \rho(770)^0\right]$ Im(a_i)	0.53	0.26	0.39	0.08	0.03	0.38	0.05	0.17	0.40	0.90
$D^0 \to \pi^- \left[a_1(1640)^+ \to \pi^+ \sigma^0\right]$ Re(a_i)	0.97	0.44	0.37	0.15	0.03	0.69	0.08	0.17	0.42	1.42
$D^0 \to \pi^- \left[a_1(1640)^+ \to \pi^+ \sigma^0\right]$ Im(a_i)	0.45	1.23	0.19	0.13	0.23	0.80	0.12	0.01	0.35	1.61
$D^0 \to \pi^- \left[\pi_2(1670)^+ \to \pi^+ f_2(1270)^0\right]$ Re(a_i)	0.70	1.57	0.44	0.02	0.16	0.24	0.11	0.13	0.41	1.84
$D^0 \to \pi^- \left[\pi_2(1670)^+ \to \pi^+ f_2(1270)^0\right]$ Im(a_i)	0.21	0.38	0.14	0.08	0.06	0.89	0.15	0.07	0.16	1.03
$D^0 \to \pi^- \left[\pi_2(1670)^+ \to \pi^+ \sigma^0\right]$ Re(a_i)	0.47	0.05	0.03	0.08	0.15	0.26	0.02	0.19	0.32	0.68
$D^0 \to \pi^- \left[\pi_2(1670)^+ \to \pi^+ \sigma^0\right]$ Im(a_i)	0.07	1.82	0.16	0.11	0.11	0.29	0.10	0.03	0.24	1.87
$D^0 \to \sigma^0 f_0(1370)^0$ Re(a_i)	0.37	0.71	0.29	0.04	0.25	0.26	0.11	0.01	2.62	2.79
$D^0 \to \sigma^0 f_0(1370)^0$ Im(a_i)	0.85	2.24	0.15	0.04	0.18	0.28	0.53	0.10	1.09	2.71
$D^0 \to \sigma^0 \rho(770)^0$ Re(a_i)	0.01	0.86	0.22	0.07	0.07	0.49	0.07	0.20	0.24	1.06
$D^0 \to \sigma^0 \rho(770)^0$ Im(a_i)	0.81	0.99	0.18	0.09	0.11	1.05	0.19	0.05	0.66	1.81
$D^0[S] \to \rho(770)^0 \rho(770)^0$ Re(a_i)	0.25	1.05	0.06	0.07	0.13	1.11	0.13	0.15	0.40	1.62
$D^0[S] \to \rho(770)^0 \rho(770)^0$ Im(a_i)	1.24	0.35	0.25	0.05	0.08	0.26	0.13	0.05	0.03	1.35
$D^0[P] \to \rho(770)^0 \rho(770)^0$ Re(a_i)	0.17	0.97	0.16	0.08	0.18	0.31	0.02	0.11	0.32	1.11
$D^0[P] \to \rho(770)^0 \rho(770)^0$ Im(a_i)	0.18	2.08	0.10	0.11	0.20	1.32	0.09	0.17	0.15	2.50
$D^0[D] \to \rho(770)^0 \rho(770)^0$ Re(a_i)	0.45	1.33	0.05	0.08	0.09	0.43	0.04	0.01	0.31	1.51
$D^0[D] \to \rho(770)^0 \rho(770)^0$ Im(a_i)	0.05	1.60	0.34	0.07	0.03	0.78	0.19	0.20	0.05	1.83
$D^0 \to f_2(1270)^0 f_2(1270)^0$ Re(a_i)	0.67	0.52	0.23	0.10	0.22	0.37	0.10	0.24	0.17	1.03
$D^0 \to f_2(1270)^0 f_2(1270)^0$ Im(a_i)	0.50	1.11	0.19	0.02	0.07	0.02	0.06	0.04	0.15	1.24
$m_{a_1(1260)}$	1.31	1.15	0.14	0.04	0.14	0.10	0.13	0.15	0.52	1.85
$\Gamma_{a_1(1260)}$	0.10	0.48	0.04	0.04	0.01	0.04	0.13	0.03	0.88	1.03
$m_{\pi(1300)}$	0.75	0.78	0.19	0.15	0.36	0.10	0.39	0.12	1.90	2.26
$\Gamma_{\pi(1300)}$	0.11	0.82	0.06	0.02	0.25	0.05	0.16	0.17	1.27	1.55
$m_{a_1(1640)}$	0.64	0.45	0.06	0.05	0.13	0.03	0.07	0.22	0.37	0.89
$\Gamma_{a_1(1640)}$	0.54	0.21	0.12	0.09	0.05	0.04	0.05	0.38	0.07	0.61

Sensitivity to the CKM angle γ with $B^{\pm} \to DK^{\pm}$ decays

7

The $D \to \pi\pi\pi\pi$ amplitude model developed in Chapter 6 provides not only valuable insights into the decay dynamics but is also an important input for a future determination of the CKM angle γ in $B^{\pm} \to (D \to \pi\pi\pi\pi)K^{\pm}$ decays. Here, knowledge of the strong phase difference between $D^0 \to \pi^+\pi^-\pi^+\pi^-$ and $\bar{D}^0 \to \pi^+\pi^-\pi^+\pi^-$ decays allows the measurement of the weak phase difference (γ) from the observed *CP* asymmetry between $B^- \to DK^-$ and $B^+ \to DK^+$ decays (*cf.* Equation 3.4). Thanks to the unique properties of the quantum-entangled $D\bar{D}$ pairs collected by the CLEO-c detector, several hadronic parameters of the charm decay can also be measured in a model-independent way as discussed in detail in Section 3.2. This is useful for two reasons: first, the model-independent measurement of the hadronic parameters can be compared to the predictions of the amplitude model which is an invaluable cross-check of the amplitude parameterization. Second, a model-unbiased measurement of the CKM angle γ from $B^{\pm} \to (D \to \pi\pi\pi\pi)K^{\pm}$ decays is enabled.

A model-independent measurement of the $D \to \pi\pi\pi\pi$ hadronic parameters is performed in Reference [124] using the CLEO-c legacy data set. More specifically, the fractional *CP*-even content F_+ (defined in Equation 3.6) is determined and the hadronic parameters T_i, $\bar{T}_i$, c_i and s_i (defined in Equation 3.9) are measured which represent the fractional contribution from $D^0 \to \pi\pi\pi\pi$ (T_i) and $\bar{D}^0 \to \pi\pi\pi\pi$ ($\bar{T}_i$) decays as well as the sine (s_i) and cosine (c_i) of the strong phase difference between D^0 and $\bar{D}^0$ decays in a given phase-space bin i. The abstract five-dimensional binning scheme (with five bins) is defined based on the phase-space description of the (LASSO) amplitude model developed in this thesis (see Section 6.4) maximizing the sensitivity to a future measurement of the CKM angle γ with $B^{\pm} \to D(\to \pi\pi\pi\pi)K^{\pm}$ decays [124]. The yield of flavor-tagged ($N_i(D^0)$ and $N_i(\bar{D}^0)$), *CP*-tagged ($N_i(D_{CP+})$ and $N_i(D_{CP-})$) and

mixed *CP*-tagged ($N_{ij}(D_a, D_b)$) signal decays is measured in these bins. This allows to infer the hadronic parameters T_i, $\bar{T}_i$, c_i and s_i from Equations 3.10 and 3.11. The determined values for the five bins are displayed in Figure 7.1. Predictions from the amplitude model developed in this thesis are overlaid. These are computed numerically from the integrals in Equations 3.6 and 3.9. The uncertainties are calculated by randomly varying the fit parameters of the LASSO model within their statistical and systematic uncertainties taking their correlation into account. An additional systematic uncertainty is assigned by computing the hadronic parameters for each of the alternative amplitude models (given in Tables D.2 and D.3). The standard deviation of the obtained values is taken as model uncertainty. The hadronic parameters T_i and $\bar{T}_i$ are in reasonable agreement with their predicted values. A hypothesis test of their consistency results in a p-value[1] of 0.05 [124]. One generally expects a decent conformity for these parameters since the sensitivity of their model-independent measurement is driven by the flavor-tagged data sample, which is used in the amplitude fit as well. The measured values of the c_i and s_i parameters also follow the same general trend as projected from the LASSO model resulting in a p-value of 0.19 [124]. As the sensitivity to the strong-phase difference originates (almost) entirely from the *CP*- and mixed *CP*-tagged data samples, this provides a crucial independent cross-check of the amplitude parameterization. Such consistency tests are rarely possible as they require a coherent admixture of flavor eigenstates as discussed in Section 3.2. This is just the second cross-check of this kind [128]. Several alternative binning schemes are investigated with p-values ranging from 0.03 to 0.19 for the c_i and s_i parameters, from 0.05 to 0.59 for the T_i and $\bar{T}_i$ parameters or from 0.05 to 0.10 for their combination [124]. Similarly, the model-independent measurement of the fractional *CP*-even content, $F_+ = (76.9 \pm 2.1\,(\text{stat}) \pm 1.0\,(\text{syst}))\%$ [124], agrees within 0.9σ with the prediction of the amplitude model: $F_+^{\text{model}} = (72.9 \pm 0.9\,(\text{stat}) \pm 1.5\,(\text{syst}) \pm 1.0(\text{model}))\%$. Altogether, one can conclude that the statistically limited model-independent measurement of the hadronic parameters confirms the general features described by the amplitude model developed in this thesis. Potential model deficiencies could be investigated more precisely with currently existing or future BES-III datasets corresponding to approximately 3.5 and 12 times the statistics accumulated at the CLEO-c experiment.

[1] The p-value quantifies the probability, under a certain hypothesis, that an outcome as likely or less likely as the observed one is realized.

Sensitivity studies performed in Reference [124] show that the measured hadronic parameters will allow for a model-unbiased extraction of the CKM angle γ from $B^{\pm} \to D(\to \pi\pi\pi\pi)K^{\pm}$ decays using the currently available LHCb dataset ($9\,\text{fb}^{-1}$) with a precision of $\sigma(\gamma) = (10\,(\text{stat}) + 7\,(\text{syst}))^{\circ}$, competitive with the current most precise single measurement from $B^{\pm} \to D(\to K^0_S\pi^+\pi^-)K^{\pm}$ decays [205]. The first uncertainty is due to the limited statistics of the beauty meson decay and the second due to the limited knowledge of the $D \to \pi\pi\pi\pi$ hadronic parameters. With additional input from currently existing and future BES-III datasets and the expected statistics after the phase-1 upgrade of the LHCb experiment ($50\,\text{fb}^{-1}$ [206]), the uncertainties could be further reduced to $\sigma(\gamma) = (2.5\,(\text{stat}) + 1.2\,(\text{syst}))^{\circ}$.

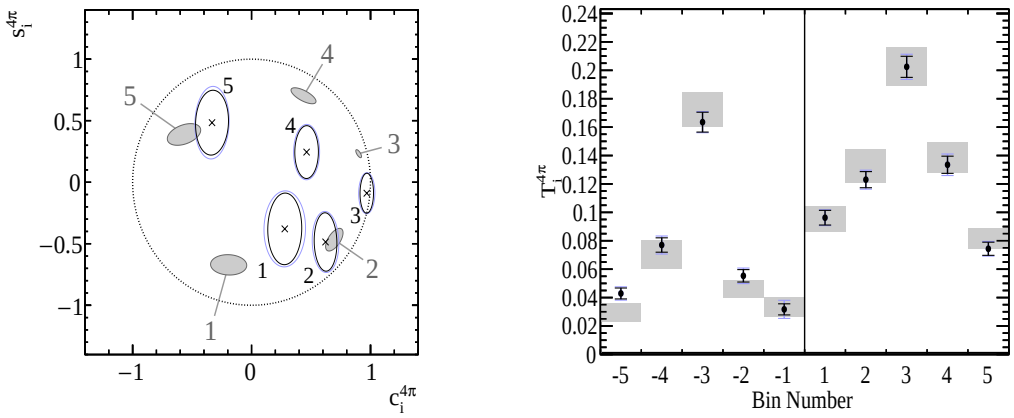

Figure 7.1: Hadronic parameters of the $D \to \pi\pi\pi\pi$ decay measured in an amplitude-model inspired binning scheme with five bins. Model-independent measurements of the c_i and s_i parameters (black ellipses for statistical, blue ellipses for total uncertainty) and the predictions of the amplitude model developed in this thesis (grey shaded ellipses) are compared on the left. All ellipses show the 39.3% confidence region. Model-independent measurements of the T_i (positive bin numbers) and $\bar{T}_i$ (negative bin numbers) parameters (black error bars for statistical, blue error bar for total uncertainty) and the predictions of the amplitude model developed in this thesis (grey bands) are compared on the right. Figures are taken from Reference [124].

Part III

MIXING-INDUCED CP VIOLATION IN $B_s \to D_s K\pi\pi$ DECAYS

8 Analysis strategy

This part investigates mixing-induced *CP* violation in $B_s \to D_s K\pi\pi$ decays following the formalism outlined in Section 3.3. In contrast to $B^\pm \to DK^\pm$ decays, where the charm decay amplitude can be factorized and measured externally, the full phase space of the beauty meson decay is relevant. The suppression due to the involved CKM matrix elements is on a comparable scale for $B_s^0 \to D_s^- K^+\pi^+\pi^-$ and $\overline{B}_s^0 \to D_s^- K^+\pi^+\pi^-$ decays ($r \approx 40\%$) such that interference effects are expected to be sizable and, in particular, much larger than for $B^\pm \to DK^\pm$ decays (with $r_B \approx 10\%$). This fact combined with the additional decay-time information allows to extract hadronic parameters directly from data, thereby enabling a stand-alone measurement of the *CP*-violating weak phase. The kinematically and topologically similar yet flavour specific decay $B_s \to D_s\pi\pi\pi$ is used as calibration channel, not only to study several experimental aspects of the decay-time dependent analysis but also to constrain the $B_s^0 - \overline{B}_s^0$ mixing frequency. The relative branching fraction of these decay modes was measured to be [207]:

$$\frac{\mathcal{B}(B_s \to D_s K\pi\pi)}{\mathcal{B}(B_s \to D_s\pi\pi\pi)} = (5.2 \pm 0.5(\text{stat}) \pm 0.3(\text{syst}))\,\% \tag{8.1}$$

using proton-proton collision data recorded by LHCb detector in 2011. The analysis in Reference [207] observed the decay $B_s \to D_s K\pi\pi$ for the first time but the low signal yield of 216 ± 22 events prevented further studies of *CP* asymmetries. The analysis presented in this thesis exploits the significantly larger currently available LHCb data set and improves the selection efficiency substantially. The reconstruction and selection for the signal and calibration channel are outlined in Chapter 9, followed by the determination of the signal and background yields. Experimental challenges of the analysis are discussed in Chapter 10. In Chapter 11, the CKM angle γ is extracted from the $B_s \to D_s K\pi\pi$ data sample using two different approaches: the (model-independent) phase-space integrated fit is presented first, followed by the significantly more complex full time-dependent amplitude fit which trades a better statistical precision against an additional model uncertainty. The systematic uncertainties of both methods are determined afterwards, before the results are compared.

Event selection at the LHCb detector

9

In contrast to the clean environment at electron-positron colliders, see Chapter 5, there are around one hundred particles originating from a proton-proton interaction. This chapter outlines how these intricate event signatures are reconstructed with the LHCb detector. The technical implementation of the detector components is briefly discussed in Section 9.1. The LHCb detector has collected the world's largest sample of beauty meson decays. However, only one of 50 thousand produced B_s mesons decays into the final state of interest. How to reconstruct and isolate potential signal candidates is discussed in Section 9.2 followed by a determination of the signal yield.

9.1 Experimental apparatus

The *Large Hadron Collider* (LHC) [208] is a particle accelerator with a circumference of 27 km located at the *European Organization of Nuclear Research* (CERN), near Geneva. It has been designed to collide proton or heavy ion beams at a center-of-mass energy of 14 TeV and a frequency of 40 MHz. During the first period of data-taking (*Run-I*), the center-of-mass energy was set to 7 TeV in 2011 and 8 TeV in 2012. It was then increased to 13 TeV for the second period of operations (*Run-2*) which ran from 2015 to 2018. The main operation mode of the LHC was to produce proton-proton collisions relevant for the presented analysis, but also proton-lead and lead-lead collisions have been recored. After an upgrade phase, data-taking will resume in 2020 with the design center-of-mass energy of 14 TeV.

The *Large Hadron Collider beauty* (LHCb) detector [209] is dedicated to study the interactions of hadrons containing beauty or charm quarks. At the LHC, such heavy hadrons predominantly emerge from quark-antiquark pair production via gluon-gluon fusion. As the interacting gluons carry, in general, significantly different momentum fractions of the proton, the $q\bar{q}$ pairs are largely boosted along the beam axis. Hence, approximately a quarter of the heavy quarks are produced

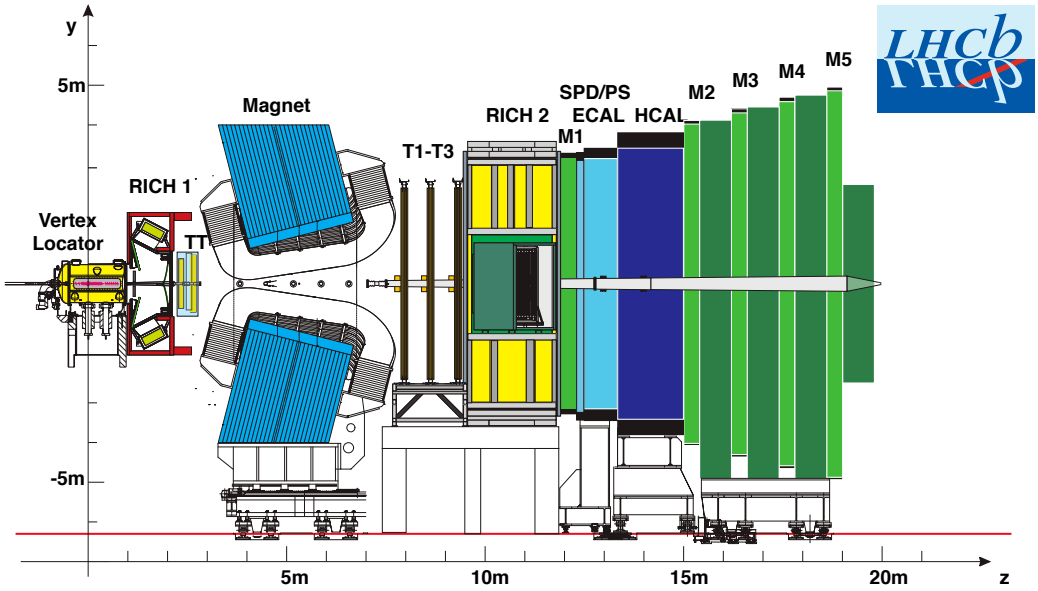

Figure 9.1: Schematic view of the LHCb detector in the y-z plane. Figure modified from Reference [209].

within the acceptance of the LHCb detector [209] although it covers only 4% of the solid angle around the interaction point. The forward geometry is evident from Figure 9.1 which shows a schematic view of the LHCb detector. A cartesian coordinate system is defined where the z-axis is aligned with the beam direction and the y-axis points vertically upwards. A dipole magnet [210] provides an integrated magnetic field strength of 4 Tm bending tracks in the x-z plane. Several tracking systems are placed before and after the magnet to allow for measurements of charged particles momenta with relative uncertainties ranging from 0.4% at 5 GeV to 0.6% at 100 GeV [209]. Additional sub-detectors are installed for particle identification and calorimetry of neutral particles, conceptually similar as for the CLEO-c detector.

Vertexing and tracking

The *Vertex Locator* (VELO) [211, 212] surrounds the primary interaction region. It precisely reconstructs both the position of the proton-proton interaction, the so-called *primary vertex* (PV), and displaced *secondary vertices* (SV) originating from the decays of long-lived hadrons. The ability to accurately resolve primary and secondary vertices is critical for time-dependent analyses. In particular, studies of B_s meson mixing require an excellent decay vertex resolution as discussed in Chapter 10. The VELO is composed of 21 modules placed along the beam axis, each equipped with two different types of half-disc shaped silicon strip detectors.

The *r-sensors* have circular-shaped strips and measure the radial distance to the z-axis, while the azimuthal angle is measured with *ϕ-sensors* which have strips in radial direction. As charged particles pass through these strips, they create electron-hole pairs leading to measurable pulses at the electrodes. Position information in z-direction is provided by the spacing of the modules. The performance of the VELO depends on the number of tracks associated to a vertex as shown in Figure 9.2(left). For 10 (50) reconstructed tracks, a resolution of approximately 200 µm (50 µm) in z-direction and of 25 µm (10 µm) in the transverse plane is achieved [213]. The *Tracker Turicensis* (TT) is located directly in front of the magnet. It consists of four layers of silicon strip sensors. The outer layers are aligned with the y-axis, whereas the inner layers are tilted by small stereo angles of $\pm 5°$. This allows for a three dimensional positions measurement with a single hit resolution of approximately 50 µm. The TT enables to reconstruct low-momentum tracks ($\sim 2\,\text{GeV}$) which are bent out of the spectrometer by the magnetic field and long-lived particles that decay outside of the VELO such as the K_s^0 meson.

The tracking system is completed by three tree tracking stations installed behind the magnet. Each station consists of four layers arranged in the same geometry as the layers of the TT. The innermost part of each layer is covered by the *Inner Tracker* (IT) [214] which uses the same technology as the TT. The *Outer Tracker* (OT) [3, 215, 216] covers the around eight times larger outer area of the tracking stations where the particle flux is lower. It is a drift chamber composed of thin straw tubes with diameters of 4.9 mm. Charged particles transversing the OT ionize the gas within the straw-tubes. The drift time of the resulting ionization cluster is measured allowing for a spatial resolution around 200 µm.

Particle identification and calorimetry

Two RICH detectors [217, 218] are installed to provide charged particle identification. One is placed in front of the magnet, the other after. Their setup is conceptually similar to the RICH detector used at the CLEO-c experiment. Different radiators are used to cover a large momentum range ($2\,\text{GeV} < p < 100\,\text{GeV}$). A mirror system guides the emitted Cherenkov light to photon detectors located outside of the LHCb detector acceptance.

A complex calorimeter system is used to identify electrons, photons and hadrons and to measure their energies [219, 220]. Incoming particles first pass through the *Scintillator Pad Detector* (SPD) which consists of scintillating layers. The SPD allows to discriminate electrons and photons as only the former produce scintillating light. The *PreShower* (PS) detector is located behind the SPD,

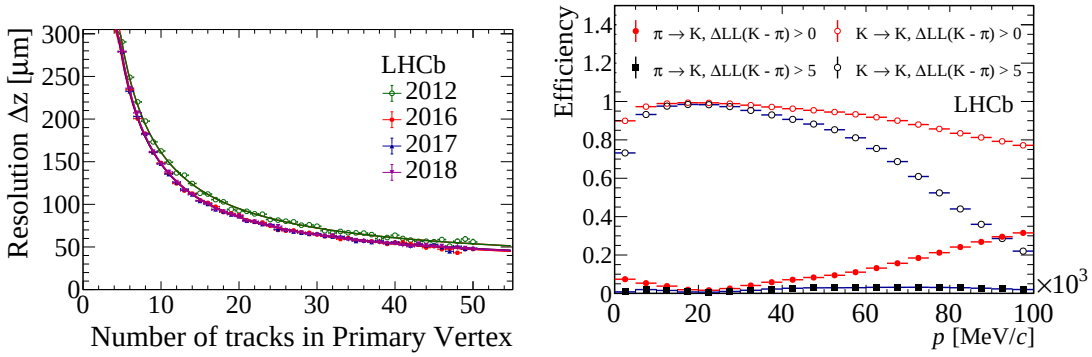

Figure 9.2: *Left:* Resolution of the PV reconstruction in z-direction. *Right:* Efficiency to select kaons and rate of pions misclassified as kaons for different PID requirements, with $\Delta\mathrm{LL}(\mathrm{K}-\pi) = \Delta \ln \mathcal{L}_{K\pi}$. Figures taken from [213].

separated by a lead plate. It detects the electromagnetic showers induced by the absorber material. The PS helps to separate electrons and charged pions based on their energy deposit. Similarly, the *Electromagnetic CALorimeter* (ECAL) and the *Hadronic CALorimeter* (HCAL) are composed of alternating layers of absorber and scintillating material. The ECAL uses lead absorbers to measure the energy of photons and electrons, while the energy of hadrons is measured by the HCAL using iron absorbers to induce hadronic showers.

Muons are identified by a system of five muon stations [221, 222]. One of them (M1) is positioned before the calorimeter system. The muon stations M2-M5 are separated by iron plates and build the last part of the detector. Only muons acting as minimum ionizing particles can penetrate them. Multiwire proportional chambers are used to collect the detector hits, with the exception of the inner part of the station M1 which uses gas electron multiplier detectors instead to account for the higher particle flux.

The information of all sub-detectors is combined to compute a (logarithmic) likelihood value for a particle hypothesis x with respect to the pion hypothesis (representing the most abundant particle species), $\Delta \ln \mathcal{L}_{x\pi}$ [223, 224]. Figure 9.2(right) shows the performance of the particle identification (PID) requirement $\Delta \ln \mathcal{L}_{K\pi} > 0$ to select kaon candidates, particularly relevant for the presented analysis. The selection efficiency for kaons is above 90% for momenta in the range $10 - 90\,\mathrm{GeV}$, while the rate of pions misclassified as kaons varies from a few percent at low momenta to more than 20% above a momentum of $80\,\mathrm{GeV}$ [213]. A tighter PID requirement (*e.g.* $\Delta \ln \mathcal{L}_{K\pi} > 5$) can reduce the pion misclassification rate but also decreases the kaon selection efficiency significantly.

Trigger system

It is not possible to record data at the (nominal) collision rate of 40 MHz. The LHCb trigger system [213, 225–228] decides, in real-time, whether an event is deemed interesting for the core physics program or can be discarded. It consists of three levels which subsequently reduce the output rate allowing for a more sophisticated event reconstructions at each step. The first trigger stage, called *Level-Zero* (L0) trigger, is entirely hardware based. It uses information from the calorimeters and the muon chambers, which can be read out at the full collision rate, to filter the events. The L0 trigger reduces the rate to approximately 1 MHz at which the full detector can be read out. Selected events are further processed by the *High-Level-Trigger* (HLT) which is implemented in software and runs on a large computing farm. The HLT is further divided into two stages. The first level, HLT1, performs a partial event reconstruction and reduces the event rate to around 100 kHz (depending on the data-taking period). This allows for a more advanced event reconstruction at the second stage, called HLT2. The final event rate is about 10 kHz (depending on the data-taking period) with which the data is recorded. More details on the selection criteria imposed at the different trigger stages are given in Section 9.2.

Recorded data samples and simulation

This analysis uses proton-proton collision data corresponding to $1\,\text{fb}^{-1}$, $2\,\text{fb}^{-1}$ and $4\,\text{fb}^{-1}$ of integrated luminosities collected in 2011, 2012 and between 2015 and 2017, respectively. Simulated samples for $B_s \to D_s K\pi\pi$ and $B_s \to D_s\pi\pi\pi$ decays are generated for each data-taking condition [229]. These are needed to study reconstruction and selection efficiencies as detailed later in this thesis. Proton-proton collisions and hadronization of the resulting quarks are simulated using PYTHIA [230, 231]. Decays of the produced B_s meson are simulated with the EVTGEN [172] package assuming a preliminary amplitude model, as done for the amplitude analysis of $D \to \pi\pi\pi\pi$ decays. The detector response is evaluated with the GEANT4 [173, 174] package. Simulated events are then reconstructed and selected in the same way as the real data [232, 233].

9.2 Event reconstruction and selection

Figure 9.3 schematically sketches the characteristic decay topology. Created promptly at the primary vertex, the long-lived B_s meson flies on average a distance of one centimeter before it decays, at the secondary vertex, into a D_s meson, a kaon and two oppositely charged pions. After typically traveling a few millimeters, the D_s meson further decays at the tertiary vertex. Three decay modes of the D_s meson are considered due to their (comparable) large branching fractions and all charged final states: $D_s^- \to K^-K^+\pi^-$, ${D_s}^- \to \pi^-\pi^+\pi^-$ and ${D_s}^- \to K^-\pi^+\pi^-$. Of those, the decay $D_s^- \to K^-K^+\pi^-$ is the most prominent one ($\mathcal{B}(D_s^- \to K^-K^+\pi^-) = 5.45 \pm 0.17\%$ [10]), while the branching fractions of the decays modes ${D_s}^- \to \pi^-\pi^+\pi^-$ and ${D_s}^- \to K^-\pi^+\pi^-$ are approximately a factor five and ten lower. The sequential selection strategy exploits the specific decay structure combined with particle identification information to discriminate signal decays from several background processes leaving similar signatures. These include random combinations of tracks accidentally fulfilling all imposed selection criteria. Apart from this purely combinatorial background, also true b-hadron decays in which either the particle species of daughter particles is misclassified or parts of the decay chain, for example a neutral daughter particle, are not reconstructed could impersonate signal candidates.

Assembling signal candidates

The reconstruction of the signal decay chain $B_s \to D_sK\pi\pi$ starts with forming a D_s candidate. First, particle trajectories are interpolated by fitting tracks to the detector hits. Only high quality tracks, defined by a small track fit χ^2 (per degree of freedom), are considered. A particle hypothesis is assigned to each track as described in Section 9.1. The actual particle identification selection requirements depend on the D_s decay mode and are given in Appendix E. As the daughter particles of the D_s meson come from a detached vertex they are expected to have, on average, a large impact parameter (IP) which is defined as the minimum distance of a track to the primary vertex as sketched in Figure 9.3. Originating from heavy meson decays, the final-state particles have, on average, a harder momentum distribution than combinatorial background. The requirements on the (transverse) momentum are kept loose in order to avoid biases on the decay kinematics. If three appropriate tracks are found, the reconstruction algorithm attempts to backtrace them to a common origin, the supposed D_s decay vertex. It is considered to be successful in case the vertex fit has a sufficient quality and the invariant mass of the tri-hadron system is consistent with the nominal D_s

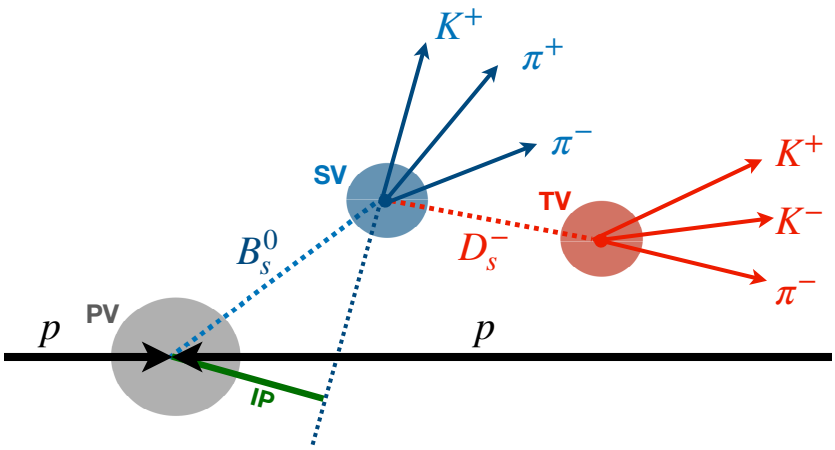

Figure 9.3: Topology of the decay $B_s \to D_s K\pi\pi$. After being produced at the primary vertex (PV), the B_s meson decays at the secondary vertex (SV). The arisen D_s meson decays further at the displaced tertiary vertex (TV). The impact parameter (IP) of the K^+ bachelor track with respect to the PV is exemplarily indicated.

meson mass (within $\pm 25\,\text{MeV}$). The D_s candidate is combined with three hadrons, hereafter referred to as the *companion* particles, to build a B_s candidate. It is identified as either a $B_s \to D_s K\pi\pi$ or a $B_s \to D_s\pi\pi\pi$ candidate depending on the PID information of the companion particles. Since the B_s meson is supposed to originate from the primary vertex, the impact parameter (IP, see Figure 9.3) should be small. Otherwise, the selection criteria for the secondary vertex and the companion tracks are similar to those imposed for the D_s decay vertex and daughter particles. To further suppress combinatorial background, a significant displacement of the secondary vertex from the primary vertex is demanded. This is quantified by the distance between the vertices, the B_s flight distance ($\text{FD}_{\text{PV}}(B_s)$). The decay time, which is calculated from the flight distance in combination with the reconstructed momentum, p_{B_s}, and mass, m_{B_s}, of the B_s candidate,

$$t = \frac{\text{FD}_{\text{PV}}(B_s)}{p_{B_s}}\, m_{B_s}, \tag{9.1}$$

is required to be larger than 0.4 ps. Additionally, a significant separation between the tertiary vertex and the secondary vertex is demanded.

To improve the decay-time and momentum resolution, a global kinematic fit of the decay chain, a so-called decay tree fit (DTF [234]), is performed constraining the B_s candidate to originate from the primary vertex and the B_s and D_s masses to their world-average values [10].

Trigger strategy

For the evaluation of reconstruction effects, it is relevant wether a signal candidate has affected the decision-making process of a specific trigger line (as detailed in the next chapter). For that reason, an algorithm is deployed which matches the online reconstructed trigger objects to the offline reconstructed candidates [235]. Three cases are considered for this analysis: either the matched signal candidate (Triggered On Signal, TOS) or the remaining part of the event is sufficient for a positive trigger decision (Triggered Independent of Signal, TIS); or both are sufficient (TIS and TOS).

The hardware trigger searches for events containing a hadron (L0Hadron), photon (L0Photon) or electron (L0Electron) with high transverse energy in the calorimeters or at least one muon candidate with high transverse momentum (L0Muon and L0DiMuon). The signal candidates are required to be TOS on the L0Hadron trigger line. Events failing this requirement are retained if any of the L0 trigger lines gave a positive decision independent of the signal candidate. These disjoint trigger categories are denoted as L0-TOS and L0-TIS in the following. Candidates in the L0-TIS trigger category have a much softer momentum spectrum which influences several experimental aspects of the analysis discussed in Chapter 10.

The software trigger searches for at least one displaced track with high transverse momentum. After that, two-, three- or four-track secondary vertices are inclusively reconstructed and required to be well separated from any primary vertex. Signal candidates are required to be TOS on the respective HLT trigger lines. As the offline selection criteria are typically tighter than the trigger selection cuts, it is referred to References [213, 236–238] for more details on the trigger lines.

Phase-space region

Due to the comparably low masses of the final-state particles with respect to the B_s meson mass, there is a huge phase space available for the $B_s \to D_s K\pi\pi$ decay. The invariant mass of the $K\pi\pi$ subsystem extends up to approximately 3.4 GeV. It has however been observed that the decay proceeds predominantly through the low lying axial vector states $K_1(1270)$ and $K_1(1400)$ [207], while the combinatorial background is concentrated at high $K\pi\pi$ invariant masses ($m(K\pi\pi) > 2\,\text{GeV}$) as illustrated in Figure 9.4. Moreover, the excited kaon spectrum above 2 GeV is poorly understood experimentally [10] such that a reliable extraction of the strong-phase variation in that region is not feasible. The phase-space region is thus limited to the range $m(K\pi\pi) < 1.95\,\text{GeV}$, which is right below the charm-strange threshold ($B_s^0 \to D_s^+ D_s^-$). This selection requirement has a signal efficiency of 85% and rejects approximately 80% of the combinatorial background.

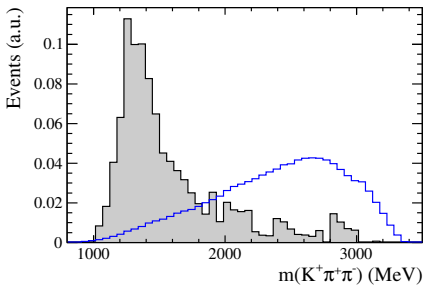

Figure 9.4: Invariant-mass distribution of the $K\pi\pi$ system for background-subtracted (as explained in Section 9.3) $B_s \to D_s K\pi\pi$ candidates (filled gray histogram) and for candidates from the high-mass sideband region defined as $m(D_s K\pi\pi) > 5500\,\text{MeV}$ (blue histogram) normalized to the same area.

Physical background sources

Misreconstructed decays of charm mesons, abundantly created in $B^0 \to D^-\pi^+$ or similar transitions, can be mistaken as D_s candidates. As an example, a $D^- \to K^+\pi^-\pi^-$ decay can pass the $D_s^- \to K^+K^-\pi^-$ candidate selection if one of the pion daughter particles is misidentified as kaon. To identify such cases, the invariant mass of the tri-hadron system is recomputed assigning a pion mass hypothesis to the ambiguous kaon candidate. Figure 9.5(left) shows a clear peak at the nominal D^- meson mass. Candidates within that peak region are rejected unless they fulfill tight PID requirements. In a similar manner, background contributions from Λ_c^- baryons decaying into the $K^+\bar{p}\pi^-$ final state are vetoed as shown in Figure 9.5(right). Here, the anti-proton might be misidentified as kaon. An additional background source arises from two-body charm decays, *e.g.* a $D^0 \to K^+K^-$ decay combined with a random pion track can be misinterpreted as a $D_s^- \to K^+K^-\pi^-$ candidate. The di-kaon invariant mass is thus required to be sufficiently lower than the nominal D^0 meson mass. Similar veto cuts are implemented for the other D_s decay modes.

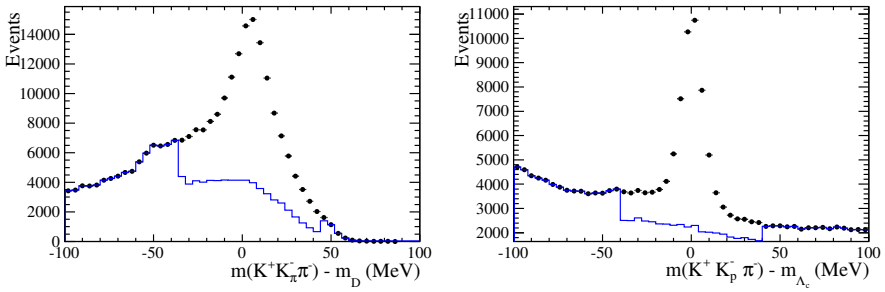

Figure 9.5: Background contributions to $B_s \to \left(D_s^- \to K^+K^-\pi^-\right)\pi\pi\pi$ candidates originating from D^- decays where the π^- is misidentified as K^- (left) or from Λ_c decays where the $\bar{p}$ is misidentified as K^- (right). The D_s invariant mass is recomputed applying a different mass hypothesis to the K^- candidate. The distributions are shown without (black) and with (blue) the veto cuts applied.

Multivariate classification

Signal candidates passing the afore-mentioned selection criteria are still swamped by random track combinations. A multivariate classification [239,240] is performed to further suppress the combinatorial background. Provided with clean signal and background proxies (training samples), a supervised machine learning algorithm combines the information of several input variables, including their correlation, into one powerful discriminator. The chosen feature space involves not only topological variables related to the vertex separation, such as the impact parameters of the B_s candidate and final-state particles or the flight distance of the D_s candidate with respect to the secondary vertex, but also several quality criteria of the track and vertex reconstruction. As combinatorial background candidates are typically accompanied by several additional tracks, two more variables are included which are a measure of the isolation of the B_s candidate from other tracks in the event. These are the asymmetry between the transverse momentum of the B_s candidate and the sum of transverse momenta of all tracks (that are not part of the signal candidate) reconstructed within a cone around the B_s candidate (A_{pT}^{cone}) and the smallest change in secondary vertex fit quality when adding one extra track ($\Delta\chi^2_{add-track}$). The classifier training uses background subtracted[1] $B_s \to D_s\pi\pi\pi$ data as representation of the signal and $B_s \to D_sK\pi\pi$ candidates from the high-mass sideband ($m(D_sK\pi\pi) > 5500\,\text{MeV}$) for the background. Afterwards, the trained classifier is applied to the (whole) $B_s \to D_sK\pi\pi$ data sample. A requirement on the classifier response is chosen such that it maximizes the signal significance $N_s/\sqrt{N_s + N_b}$, where N_s and N_b are the signal and background yield inside the signal region ($m(D_sK\pi\pi) = m_{B_s} \pm 60\,\text{MeV}$). This working point corresponds to a signal efficiency of approximately 90% and a background rejection of approximately 85%. The estimation of the event yields is discussed in the next section. More details on the training and optimization of the multivariate classifier are given in Appendix E.

[1] Throughout the thesis, the terminology *background subtracted* refers to the application of the *sPlot* technique [241] which is discussed in Section 9.3.

9.3 Yields determination

After the selection, the $B_s \to D_s K\pi\pi$ and $B_s \to D_s\pi\pi\pi$ data samples contain not only true signal decays and random track combinations but also an irreducible background component from partially reconstructed b-hadron decays as well as a residual contamination from misidentified decays. These contributions can be disentangled on a statistical basis by means of an extended maximum likelihood fit to the reconstructed B_s mass shown in Figure 9.6. The general features of the signal and background shapes are motivated in the following, while details on their functional form are given in Appendix C.

Signal model

With an intrinsic decay width way below one meV, the shape of the signal mass peak is driven by the detector resolution. It is approximately Gaussian, typically with a slightly larger tail towards low masses due to the energy loss by bremsstrahlung in the detector. The Johnson's SU function [242] provides a reasonable flexible parameterization to cope with this demands. The shape parameters are determined from the $B_s \to D_s\pi\pi\pi$ sample and thereafter fixed to these values when fitting $B_s \to D_s K\pi\pi$ candidates. Decays of B_d mesons are described by the same PDF shifted by the known mass difference between B_s and B_d mesons of $87.42 \pm 0.24\,\text{MeV}$ [10].

Combinatorial background

The combinatorial background contribution is expected to be well described by a smooth, non-peaking function. A second order polynomial is chosen, whose parameters are determined directly in the fit to data.

Partially reconstructed background

For the $B_s \to D_s\pi\pi\pi$ data sample, there is a sizable contribution from partially reconstructed $B_s \to D_s^*\pi\pi\pi$ decays, where the D_s^* meson decays to $D_s\gamma$ or $D_s\pi^0$. Due to the momentum carried away by the non-reconstructed neutral pion or photon, one expects a broad invariant-mass distribution concentrated at low values with a tail extending into the signal region. An empirical description for the shape of this contribution is derived from simulated $B_s \to D_s^*\pi\pi\pi$ decays subject to the nominal $B_s \to D_s\pi\pi\pi$ candidate selection. Figure 9.7(left) shows the respective reconstructed B_s mass distribution. A sum of several Gaussian(-like) functions is used to describe it. The same shape is assumed for the analogous $B_s \to D_s^* K\pi\pi$ and $B_d \to D_s^* K\pi\pi$ components contributing to the $B_s \to D_s K\pi\pi$ data sample, where the latter is shifted by the mass difference between B_d and B_s mesons.

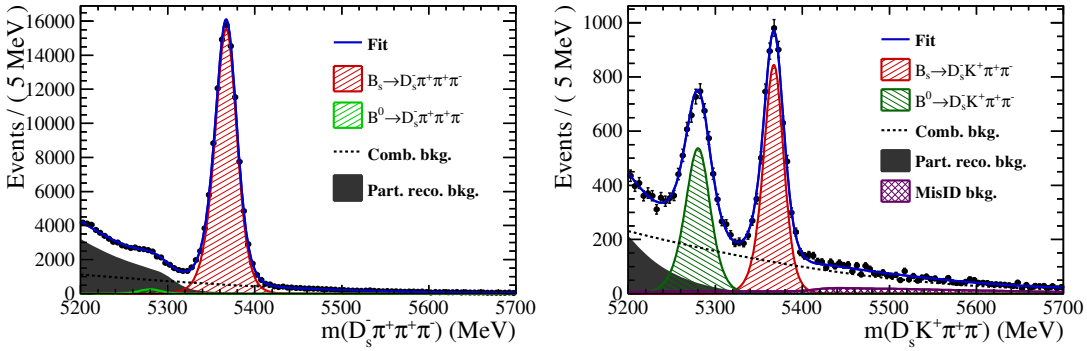

Figure 9.6: Invariant-mass distribution of $B_s \to D_s\pi\pi\pi$ (left) and $B_s \to D_sK\pi\pi$ (right) candidates.

Misidentified background

Despite stringent PID requirements are imposed on the companion kaon track, a small fraction of $B_s \to D_s\pi\pi\pi$ and $B_s \to D_s^*\pi\pi\pi$ decays, where one of the pions is misidentified as a kaon, contaminates the $B_s \to D_sK\pi\pi$ sample. To determine the corresponding background shapes, these decay modes are simulated and reconstructed as $B_s \to D_sK\pi\pi$ candidates. Since the wrong particle hypothesis is assigned to the pion, the background distributions peak above the signal region as shown in Figure 9.7(middle, right). They are modeled by the sum of several Gaussian(-like) functions. The expected yield of this *cross-feed* background is derived from a control sample of $D^{*+} \to (D^0 \to K^-\pi^+)\,\pi^+$ decays which can be cleanly reconstructed without particle identification criteria. First, the probability of a pion to pass the PID requirement imposed on the kaon candidate is determined in bins of transverse momentum and pseudo-rapidity[2] to account for the dependence of the selection criterium on the track kinematic. Provided with the pion kinematics from the simulated sample, the rate of misidentified pions in $B_s \to D_s\pi\pi\pi$ ($B_s \to D_s^*\pi\pi\pi$) decays is estimated to be 0.6% (0.5%) for Run-I and 0.3% (0.2%) for Run-II data. Together with the $B_s \to D_s\pi\pi\pi$ and $B_s \to D_s^*\pi\pi\pi$ (signal) yields determined from the the fit to the $B_s \to D_s\pi\pi\pi$ candidates, the cross-feed yield from these decay modes to the $B_s \to D_sK\pi\pi$ sample is computed.

The cross-feed contamination from $B_s \to D_sK\pi\pi$ and $B_s \to D_s^*K\pi\pi$ decays to the $B_s^0 \to D_s\pi\pi\pi$ data sample is considered to be negligible due to the low branching fractions and the tight PID requirements on the companion pions.

[2]The pseudo-rapidity is defined as $\eta = -\ln\theta/2$, where θ is the angle with respect to the beam direction.

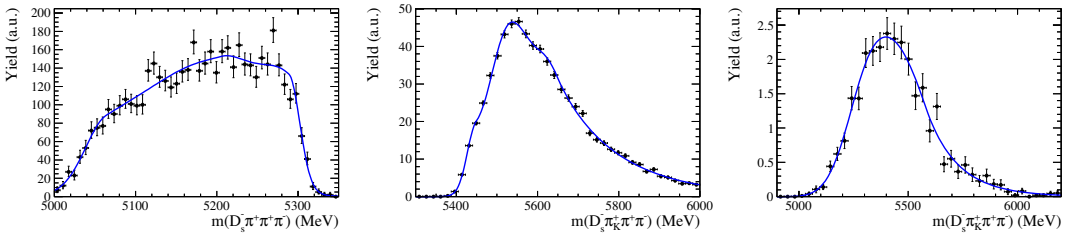

Figure 9.7: *Left:* Invariant-mass distribution of simulated $B_s^0 \to D_s^* \pi\pi\pi$ decays, where the γ/π^0 from the D_s^* decay is excluded from the reconstruction. *Middle:* Invariant-mass distribution of simulated $B_s^0 \to D_s \pi\pi\pi$ decays, where one of the pions is reconstructed as a kaon. *Right:* Invariant-mass distribution of simulated $B_s^0 \to D_s^* \pi\pi\pi$ decays, where the γ/π^0 from the D_s^* decay is excluded from reconstruction and one of the pions is reconstructed as a kaon. Empirical models describing the shapes are shown in blue.

Background subtraction

Figure 9.6 shows the reconstructed B_s mass distribution for $B_s \to D_s \pi\pi\pi$ and $B_s \to D_s K\pi\pi$ candidates passing all selection criteria along with the fit projections. All signal and background yields, except for the cross-feed yields which are fixed to their estimated values, are determined by the likelihood fit[3] and are listed in Table 9.1. For further analysis of the data samples, the background contributions are subtracted on a statistical basis by employing the *sPlot* [241] technique, a more advanced sideband subtraction method. The information from the likelihood fit to the discriminating variable (the reconstructed B_s mass in this case) is used to compute a weight ω_i, called *sWeight*, for each candidate. The signal distribution in a control variable, say the proper time t, is then unfolded by applying these sWeights to the candidates, provided that control and discriminating variables are uncorrelated. For parameter estimation, a weighted likelihood function is constructed from the signal PDF ($\mathcal{P}_\mathrm{S}(t_i|\theta)$) in the control variable t [243]: $-\ln \mathcal{L}(\theta) = -\sum_{i=1}^{N} \omega_i \ln \mathcal{P}_\mathrm{S}(t_i|\theta)$. No explicit modeling of the background contribution in the control variable is needed. This is particularly useful for high-dimensional problems or complicated physical background sources.

Table 9.1: Determined yields for the $B_s \to D_s \pi\pi\pi$ (left) and $B_s \to D_s K\pi\pi$ (right) data samples.

Component	Yield
$B_s \to D_s \pi\pi\pi$	104176 ± 356
$B^0 \to D_s \pi\pi\pi$	1742 ± 363
Partially reco. bkg.	43157 ± 407
Combinatorial bkg.	40992 ± 455

Component	Yield
$B_s \to D_s K\pi\pi$	5172 ± 88
$B^0 \to D_s K\pi\pi$	4109 ± 100
Partially reco. bkg.	1825 ± 204
Misidentified bkg.	1186 (fixed)
Combinatorial bkg.	9172 ± 221

[3] The likelihood fit is performed simultaneously in several data categories split by the data-taking period and L0 trigger category to account for slightly different mass resolutions and by the D_s decay mode to account for different signal purities.

Experimental aspects of decay-time dependent measurements

10

In an ideal measurement, the decay-time spectrum of neutral B_s meson decays into a flavor eigenstate f is described by the decay rate introduced in Section 3.3. However, there are several difficulties emerging in a real-life experiment as illustrated in Figure 10.1. First, the proper time can only be measured with a finite precision such that the actually observed distribution is smeared out. Section 10.1 details the implications of the decay-time resolution on the analysis of B_s meson decays. The geometrical acceptance of the LHCb detector along with the reconstruction and selection process inevitably distorts the measured decay-time spectrum from the theoretically expected one. How to account for this effect is discussed in Section 10.2. The experimental challenges related to the identification of the flavor state of neutral mesons are outlined in Section 10.3, followed by a discussion of physical and detector induced effects which could mimic a *CP* asymmetry. For the sake of simplicity, the following discussion is on the basis of the phase-space integrated (theoretical) decay rate (*cf.* Equation 3.16) denoted as $\mathrm{d}\Gamma_{\mathrm{theo}}(t)/\mathrm{d}t$. All implications are equally valid for the phase-space dependent decay rate.

10.1 Decay-time resolution

An excellent decay-time resolution is essential in order to resolve the fast $B_s^0 - \overline{B}_s^0$ mixing with an oscillation period of approximately 350 fs [10]. A finite decay-time resolution damps the measured $B_s^0 - \overline{B}_s^0$ oscillation amplitude as illustrated in Figure 10.1b. The smearing of the decay-time distribution can be described by a convolution of the theoretical decay rate with a Gaussian resolution model

$$\frac{\mathrm{d}\Gamma_{\mathrm{exp}}(t)}{\mathrm{d}t} = \int \frac{\mathrm{d}\Gamma_{\mathrm{theo}}(t')}{\mathrm{d}t'} R(t-t'|\mu_t, \sigma_t)\,\mathrm{d}t' \equiv \frac{\mathrm{d}\Gamma_{\mathrm{theo}}(t')}{\mathrm{d}t'} \otimes R(t-t'|\mu_t, \sigma_t), \quad (10.1)$$

which converts the true decay time, t', into the reconstructed decay time, t. The mean of the Gaussian function, μ_t, represents a potential bias in the decay-time

measurement and the width is equivalent to the decay-time resolution σ_t. Assuming a sufficient detector resolution ($\sigma_t \ll \tau$ and $\sigma_t \ll 1/\Delta m_s$), the convolution of the oscillating terms in the decay rate,

$$e^{-\Gamma t}\cos(\Delta m_s t) \otimes R(t-t'|\mu_t = 0, \sigma_t) \propto \mathcal{D}_{\text{res}}\, e^{-\Gamma t}\cos(\Delta m_s t), \tag{10.2}$$

leads to a dilution of the oscillation amplitude by a factor $\mathcal{D}_{\text{res}} = e^{-\frac{\Delta m_s^2 \sigma_t^2}{2}}$; for example $\mathcal{D}_{\text{res}} = 0.73$ with a decay-time resolution of $\sigma_t = 45\,\text{fs}$. The impact on the hyperbolic terms of the decay rate is negligible.

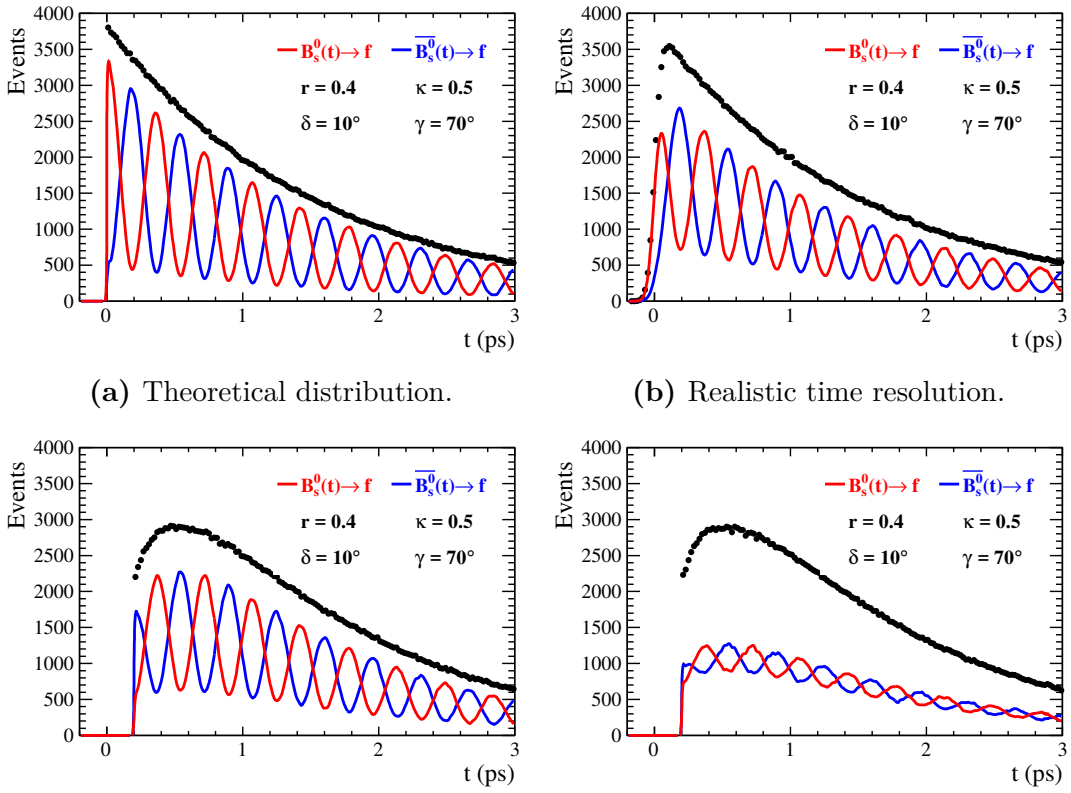

(a) Theoretical distribution.

(b) Realistic time resolution.

(c) Realistic time resolution and acceptance.

(d) Realistic time resolution, acceptance and flavor tagging.

Figure 10.1: Illustration of various experimental effects on the decay rate.

Per-event decay-time resolution

The decay-time is determined from the measured flight distance and the reconstructed three-momentum of the b-hadron, both of which are suffering from experimental uncertainties. The uncertainty on the decay length, σ_l, is dominated by the secondary-vertex resolution (approximately 200 µm in z-direction) since the number of tracks used to reconstruct the decay vertex (six for the studied decay mode) is much smaller than for the primary vertex (100 tracks on average). The momentum resolution, σ_p, is limited by multiple scattering with the detector material ($\frac{\sigma_p}{p} \approx 0.5\%$). For the decay-time uncertainty follows:

$$\sigma_t^2 = \left(\frac{m}{p}\right)^2 \sigma_l^2 + \left(\frac{t}{p}\right)^2 \sigma_p^2 \tag{10.3}$$

revealing that the decay-time resolution depends on the particular event, especially on the decay time itself. Due to the exponential decay, the majority of candidates have a small proper time in which case the contribution from the flight-distance uncertainty to the time resolution outweighs the momentum resolution by an order of magnitude. It is only at very large proper times, that the contribution from the momentum resolution becomes competitive.

The global kinematic fit to the decay topology (DTF, *cf.* Section 9.2) provides an estimate of the decay-time resolution for each event. Even though the per-event decay-time error estimate, δ_t, takes both the uncertainties on the particle momenta and the vertex positions into account, it is not necessarily representative of the true resolution σ_t. It omits additional effects such as imperfect detector alignment and uncertainties on the material budget or magnetic field of the detector. Therefore, the raw decay-time error has to be calibrated.

Principles of calibration method

To gauge the time-resolution scale requires a reference process with known (true) proper-time. One option would be to analyze the differences between the generated and reconstructed decay-times using simulated data. However, especially the effects not taken into account by the DTF error estimate are also not expected to be perfectly modeled by the simulation. Real data, on the other hand, is unavoidably affected by the imperfect measurement and thus, in general, lacks information about the true decay-time. A method to circumvent this restriction on real data is not to use true b-hadron decays but to reconstruct artificial B_s candidates out of tracks originating directly form the primary vertex. These *fake* B_s candidates have a known true decay-time of $t = 0$ since, by construction, the apparent secondary

vertex position coincides with the primary interaction point. The difference of the measured decay time of these candidates with respect to the true decay time is attributed to the decay-time resolution. More specifically, the PDF describing the reconstructed decay-time distribution of the fake B_s candidates,

$$\mathcal{P}_{\text{fake}}(t) = \delta(t') \otimes R(t - t') = R(t), \tag{10.4}$$

correspond exactly to the sought resolution function.

The selection of the fake B_s candidates[1] is kept as similar as possible to the one for true B_s decays with the important difference that the D_s candidate and the companion tracks are required to come from the primary vertex. More detail are given in Appendix E. Figure 10.2(left) shows the decay-time distributions for fake B_s candidates. Since some D_s candidates might actually be fragments of true b-hadron decays, the decay-time distribution of the fake B_s candidates is potentially biased towards positive decay times. Therefore, the decay-time resolution is determined from the negative decay-time distribution only. The sum of two Gaussian functions with common mean but different widths is chosen as resolution model acknowledging two (almost) independent sources of uncertainty (momentum and vertex position determination). A measure of the effective resolution is derived from the damping of the $B_s^0 - \overline{B}_s^0$ oscillation amplitude as: $\sigma_t = \sqrt{(-2/{\Delta m_s}^2)\ln \mathcal{D}_{\text{res}}}$, where the dilution is given by [141]: $\mathcal{D}_{\text{res}} = f_1 e^{-\sigma_1^2 {\Delta m_s}^2/2} + (1 - f_1) e^{-\sigma_2^2 {\Delta m_s}^2/2}$, and σ_1 and σ_2 are the widths of the Gaussian functions and f_1 is their relative fraction.

To analyze the relation between the per-event decay time error δ_t and the actual resolution σ_t, the fake B_s sample is divided into equal-statistics slices of δ_t. For each slice, the effective resolution is determined as described above. Figure 10.2(right) shows the obtained values for σ_t as a function of the per-event decay time error δ_t. To account for the variable binning, the bin values are not placed at the bin center but at the weighted mean of the respective per-event-error bin. A linear calibration function:

$$\sigma_t(\delta_t) = s_0 + s_1 \cdot \delta_t \tag{10.5}$$

is used to parametrize the observed distribution. For a perfectly calibrated detector one would expect $s_0 = 0$ and $s_1 = 1$. A non-zero offset seems implausible at first glance supposing that $\sigma_t \to 0$ for $\delta_t \to 0$. However, there are no events with estimated decay-time errors smaller than 0.01 ps. It is hence neither possible nor needed to specify the limit $\delta_t \to 0$ and Equation 10.5 provides a sufficient characterization in the region of interest.

[1] Only 4% of the total available luminosity is used for the prompt data sample due to CPU and memory constraints imposed by the central data processing.

There have been major improvements to the detector alignment for the Run-II data-taking period [213]. In particular, new tunings in the track-pattern recognition and vertex reconstruction have been implemented which impact the estimated decay-time uncertainty. It is thus necessary to perform separate calibrations for the Run-I and Run-II data samples. The VELO track reconstruction has been further improved for the data-taking in 2017 such that the calibration for Run-II data needs to be portioned additionally into two categories: data taken in 2015/2016 and 2017. Table 10.1 summarizes the calibration results. The average resolution obtained by summing over the calibrated per-candidate decay-time errors amounts to $\langle \sigma_t \rangle = 37.2 \pm 0.4\,\text{fs}$.

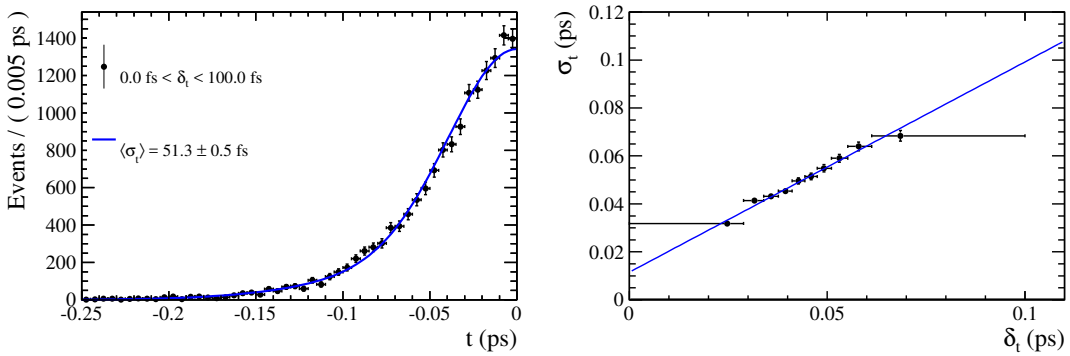

Figure 10.2: Decay-time distribution of fake B_s candidates (left) and measured resolution σ_t as function of the per-event decay time error estimate δ_t for fake B_s candidates (right) using data recorded in 2016.

Table 10.1: Time-resolution calibration parameters obtained for various prompt data samples.

Data-taking period	s_0 [fs]	s_1
Run-I	10.3 ± 1.5	1.280 ± 0.042
2015/2016	11.6 ± 1.6	0.877 ± 0.040
2017	6.5 ± 1.4	0.961 ± 0.036

10.2 Decay-time acceptance

There are several reconstruction and selection effects which artificially alter the decay-time distribution. Most notably are requirements on a significant displacement of the b-hadron candidates from the primary vertex imposed primarily by the high-level trigger lines to cope with the high abundancy of prompt tracks (*cf.* Section 9.2). This translates into a low selection efficiency at small decay times leading to a typical steep turn-on shape of the selection efficiency growing rapidly with the decay time until reaching a plateau at intermediate decay times (as illustrated in Figure 10.1c). At high decay times the selection efficiency drops again almost linearly due to peculiarities of the VELO track reconstruction[2]. The non-uniformity of the detection efficiency needs to be considered when interpreting the measured decay-time spectrum:

$$\frac{\mathrm{d}\Gamma_{\mathrm{exp}}(t)}{\mathrm{d}t} = \left[\frac{\mathrm{d}\Gamma_{\mathrm{theo}}(t')}{\mathrm{d}t} \otimes R(t-t'|\mu_t,\sigma_t)\right] \epsilon(t), \tag{10.6}$$

where the acceptance function, $\epsilon(t)$, describes the probability to reconstruct a signal candidate with reconstructed proper time t and t' signifies the true proper time of the candidate.

Parametrization of the time-acceptance

The decay-time acceptance is analytically described by a *B-spline* curve [245, 246]:

$$\epsilon(t) = \sum_{i=0}^{N} v_i\, b_i(t). \tag{10.7}$$

The cubic basis polynomials $b_i(t)$ are uniquely defined by a set of so-called knots $(t_0, t_1, \ldots, t_N)$ which are placed across the considered decay-time range to account for local variations. At least $N = 6$ knots are necessary for a sufficient description of the decay-time acceptance. Two knots are located by default at the lower and upper edge of the decay-time interval, the remaining ones are chosen such that there is an approximately equal amount of data in-between two consecutive knots. The polynomial coefficients, v_i, are adjusted such that the B-spline curve matches the actual acceptance shape. This parameterization is very flexible and allows for an analytical computation of the decay-time integrals appearing in the normalization of the PDF boosting significantly the CPU performance [247].

[2]The VELO track finding algorithm assumes that the tracks are not too far displaced from the primary vertex (for performance reasons as it is run in the software trigger) introducing a small degradation of reconstruction efficiency for long-lived b-hadron candidates [244].

Extraction of the time-acceptance from control modes

Since the CP coefficients describing the theoretical decay-time distribution of $B_s \to D_s K\pi\pi$ decays are unknown and yet to be determined, it is not feasible to extract them together with the decay-time acceptance shape from the same data sample. In particular, the hyperbolic CP coefficients modify the exponential decay-time distribution and are therefore highly correlated with the acceptance shape. The decay-time distribution of flavor specific decays such as $B_s \to D_s\pi\pi\pi$ or $B_d \to D_s K\pi\pi$, on the contrary, are well understood as discussed in Section 3.3.

With an (almost) identical decay-topology and very high statistics (20 times higher than for $B_s \to D_s K\pi\pi$ decays), the $B_s \to D_s\pi\pi\pi$ sample provides the ideal control mode to study the decay-time acceptance. A likelihood fit to the (flavor-averaged and background-subtracted) proper-time spectrum, shown in Figure 10.3 (top-left), is performed using a PDF based on Equation 10.6 (and the well known theoretical decay-time distribution) where the resolution model determined in Section 10.1 is employed. The B_s meson lifetime and decay-width difference are fixed to their world-average values [35] leaving the B-spline coefficients (*cf.* Equation 10.7) as only free fit parameters. Due to small differences in the selection and decay kinematics, the acceptance function obtained in this way ($\epsilon_{D_s\pi\pi\pi}(t)$) is not exactly equal to the desired one for $B_s \to D_s K\pi\pi$ decays ($\epsilon_{D_s K\pi\pi}(t)$); they differ by a small, decay-time dependent correction factor $R(t)$:

$$\epsilon_{D_s\pi\pi\pi}(t) = \epsilon_{D_s K\pi\pi}(t) \cdot R(t). \tag{10.8}$$

At first order, the correction factor is expected to be $R(t) \approx 1$. It is determined using simulated samples of $B_s \to D_s\pi\pi\pi$ and $B_s \to D_s K\pi\pi$ decays, where kinematic differences between the decay modes are well described [2]. Two distinct B-splines curves are introduced to describe the corresponding decay-time distributions shown in Figure 10.3 (top-right) for $B_s \to D_s\pi\pi\pi$ and in Figure 10.3 (bottom-right) for $B_s \to D_s\pi\pi\pi$ decays: one represents the acceptance shape for simulated $B_s \to D_s K\pi\pi$ candidates ($\epsilon^{MC}_{D_s K\pi\pi}(t)$); the other parameterizes the correction factor $R(t)$. For the decay-time acceptance of simulated $B_s \to D_s\pi\pi\pi$ decays follows:

$$\epsilon^{MC}_{D_s\pi\pi\pi}(t) = \epsilon^{MC}_{D_s K\pi\pi}(t) \cdot R(t). \tag{10.9}$$

Note that the correction factor represents the ratio of two acceptances and as such can be more reliably extracted from the simulation than the individual acceptances since many systematic effects arising from potential simulation

mismodeling cancel. The control mode $B_d \to D_s K\pi\pi$ adds additional sensitivity to the acceptance determination. The low yield (approximately 90% of the $B_s \to D_s K\pi\pi$ yield, see Section 9.3) is compensated by the advantage of being subject to exactly the same selection as the signal decay. It can safely be assumed that no correction factor is needed in that case. Hence, the PDF describing the $B_d \to D_s K\pi\pi$ proper-time distribution, shown in Figure 10.3 (bottom-left), uses the $B_s \to D_s K\pi\pi$ acceptance introduced in Equation 10.8.

A simultaneous likelihood fit to the four datasets ($B_s \to D_s\pi\pi\pi$ data, $B_d \to D_s K\pi\pi$ data, $B_s \to D_s K\pi\pi$ simulation and $B_s \to D_s\pi\pi\pi$ simulation) is performed to allow for a straightforward propagation of uncertainties. Figure 10.3 displays the fit result together with the extracted acceptance shapes. The general trend of the observed efficiency variation is as expected qualitatively. A good agreement between the acceptance shapes extracted from data and simulation is observed and the correction function is nearly flat across the whole range. The decay-time acceptance is determined separately for each data-taking period and each trigger category. This is discussed in more detail in Appendix E, where also the numerical values of the fitted parameters are given.

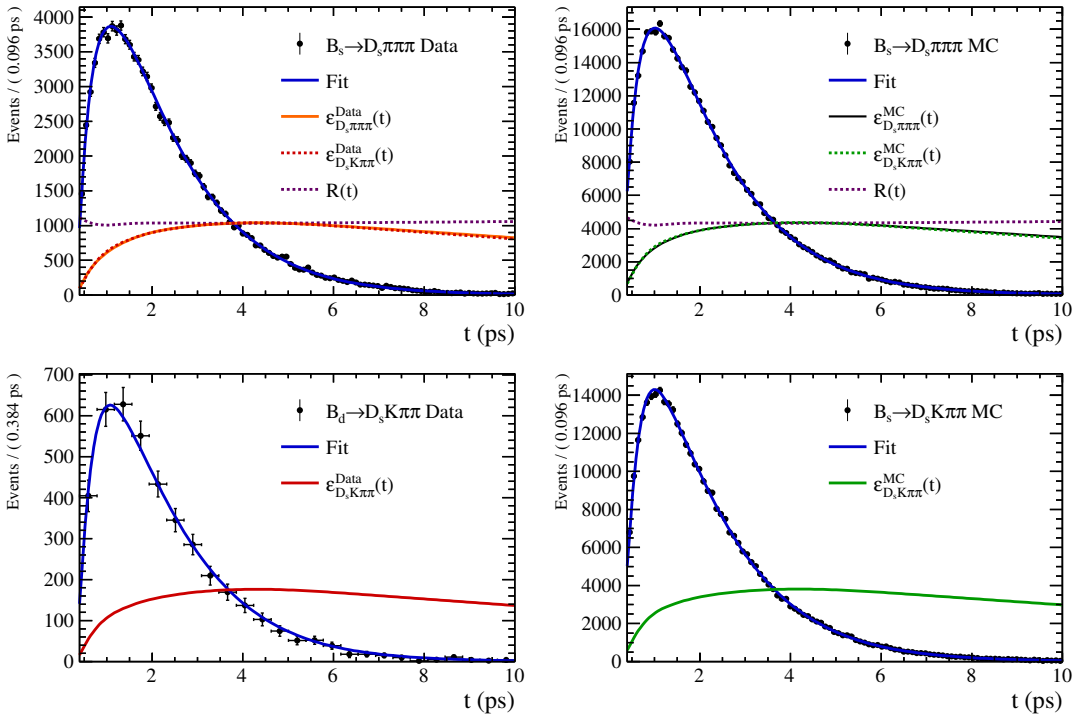

Figure 10.3: Decay-time fit projections for $B_s \to D_s\pi\pi\pi$ data (top-left), $B_s \to D_s\pi\pi\pi$ MC (top-right), $B_d \to D_s K\pi\pi$ data (bottom-left) and $B_s \to D_s K\pi\pi$ MC (bottom-right). All data categories are combined. The respective acceptance functions are overlaid in an arbitrary scale.

10.3 Identifying the neutral meson production flavor

Measurements of neutral meson mixing or *CP* asymmetries necessitate knowledge about the initially created flavor eigenstate. Given the busy environment at hadron colliders, this is a delicate task. Methods which challenge that problem, typically by exploiting peculiar features of the b-hadron production process, are collectively referred to as *flavor taggers*.

Flavor-tagging algorithms

In proton-proton collisions, b-quarks are predominantly produced in quark-antiquark pairs. Each b-quark hadronizes independently giving rise to two hadrons of opposing bottom flavor. Provided that one of them is the signal B_s meson, its flavor can be inferred indirectly from the other b-hadron in the event. This is only possible if the tagging hadron, also called *opposite side* (OS) hadron, decays flavor specific [248, 249]. An example is the decay $B^- \to D^0 \mu^- \bar{\nu}_\mu$, where the (negative) charge of the muon originating from the tagging B^- hadron indicates a signal B_s^0 meson as illustrated in Figure 10.4. More generally, the OS lepton taggers search for muons or electrons from semileptonic decays via $b \to c\, l^- \bar{\nu}_l$ transitions. Another algorithm reconstructs charm meson candidates produced in $b \to c$ transitions (OS charm tagger). A D^0, D^+ or Λ_c^+ hadron on the tag side corresponds to a B_s^0 meson on the signal side. This method is not only sensitive to (certain) semileptonic decays, see the example mentioned above, but also to fully hadronic decays such as $B^- \to D^0 \pi^-$. The charm meson decays preferably into a kaon; the charge of which provides evidence for the b-hadron production flavor on its own, *i.e.* the K^- originating from a $b \to c \to s$ cascade transition corresponds to a signal B_s^0 meson. This signature is exploited by the OS kaon tagger. A conceptually different flavor tagging algorithm does not search for specific decay products but inclusively reconstructs the vertex of the OS hadron (OS vertex-charge tagger). An effective charge is assigned to this vertex based on the charges of the associated tracks. Since each single OS tagger has limited predictive power, their information is combined into a common response [248].

A complementary approach deduces the b-hadron production flavor of the signal B_s meson from its fragmentation. For a bottom quark to hadronize to a B_s meson, a $s\bar{s}$ quark pair needs to be created out of the vacuum. The additional strange quark forms, together with an up quark, a charged kaon in about 50% of the cases. A kaon with negative (positive) charge corresponds to a $\bar{B}_s^0$ (B_s^0) meson produced alongside it. Thus the *same side* (SS) tagger searches for a kaon track in proximity of the reconstructed B_s signal candidate [250].

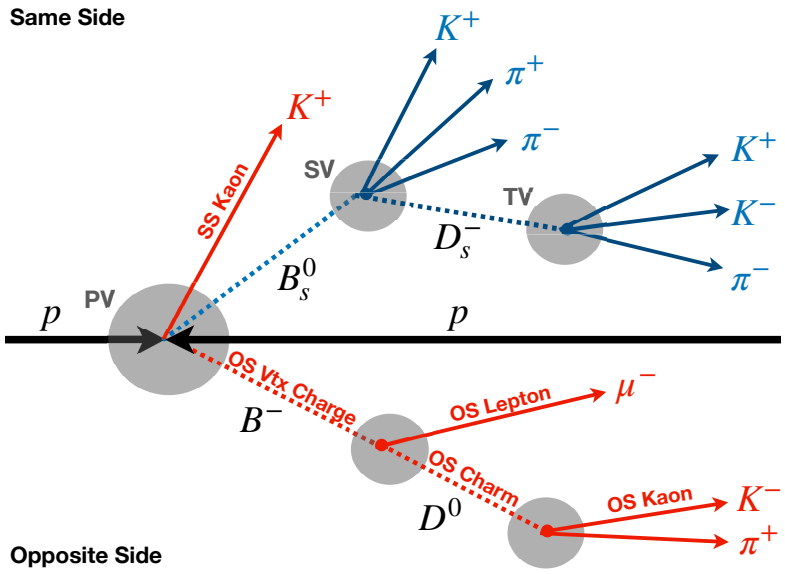

Figure 10.4: Typical event topology exploited by the SS and OS taggers to identify the initially produced flavor eigenstate. Signal tracks are drawn in blue, while particles used by the tagging algorithms are drawn in red.

Tagging dilution

Depending on the properties of the event, each flavor tagger predicts the bottomness of the signal B_s meson at production time. The tagging decision, q, is defined as $q = +1$ for an initial B_s^0 meson and $q = -1$ for an initial $\bar{B}_s^0$ meson. Unfortunately, it is not always possible to provide a decision. This might be due to the fact that the tagging particle, *e.g.* the kaon in case of the SS kaon tagger, cannot be reconstructed or is discarded by the imposed selection criteria. In this case, the flavor tag takes the value $q = 0$. The fraction of events for which a given algorithm delivers a tag decision, the tagging efficiency ϵ_{tag}, is an important benchmark.

Even though a flavor tagger gives a decision, it might not be correct. Instead of tagging particles correlated with the flavor of the b-hadron, the algorithms can select a random track from the underlying event. In addition, the OS algorithms assume that the flavor of the tagging hadron at decay is the same as at production. While this is justified for charged b-hadrons, neutral ones might change their flavor via mixing. In case of B^0 mesons, some predictive power is retained since only 19% change their flavor before the decay [10]. As consequence of the fast oscillation, all information about the initial flavor state are lost for OS tagging B_s mesons. The fraction of incorrectly assigned tags, the mistag rate ω, is typically between 30% and 40% at the LHCb experiment [248–250].

In light of potentially wrong tagging decisions, the measured $B_s^0 \to f$ ($N_f^{\text{meas}}(t)$) and $\bar{B}_s^0 \to f$ ($\bar{N}_f^{\text{meas}}(t)$) yields contain a wrong flavor component:

$$N_f^{\text{meas}}(t) = (1-\omega)\, N_f(t) + \omega\, \bar{N}_f(t), \qquad \bar{N}_f^{\text{meas}}(t) = (1-\omega)\, \bar{N}_f(t) + \omega\, N_f(t),$$

where $N_f(t)$ and $\bar{N}_f(t)$ are the true yields. This dilutes the oscillation amplitude as illustrated in Figure 10.1d. For the measured mixing asymmetry follows:

$$A_{\text{mix}}^{\text{meas}}(t) = \frac{N_f^{\text{meas}}(t) - \bar{N}_f^{\text{meas}}(t)}{N_f^{\text{meas}}(t) + \bar{N}_f^{\text{meas}}(t)} = (1-2\omega)\, A_{\text{mix}}(t). \tag{10.10}$$

Here, $A_{\text{mix}}(t)$ is the true (physical) mixing asymmetry, defined in Equation 3.19, and the tagging dilution, $\mathcal{D}_{\text{tag}} = 1 - 2\omega$, expresses the loss of sensitivity due to imperfect knowledge of the b-hadron production flavor. More specifically, the statistical uncertainty on the physical asymmetry, given N measured events, amounts to:

$$\sigma_{A_{\text{mix}}} = \sqrt{\frac{1 - (A_{\text{mix}}^{\text{meas}})^2}{N\, \epsilon_{\text{tag}}\, \mathcal{D}_{\text{tag}}^2}}. \tag{10.11}$$

The precision obtained with a data sample containing N events and effective tagging power, $\epsilon_{eff} = \epsilon_{\text{tag}}\, \mathcal{D}_{\text{tag}}^2$, is equivalent to a data sample with $\epsilon_{eff} \cdot N$ events and perfect flavor tagging. Hence, flavor-tagging algorithms are generally tuned to maximize the effective tagging power. Depending on the decay mode, effective tagging powers from 2% [251] to 8% [252] have been achieved at the LHCb experiment.

Per-event mistag probability

It requires precise knowledge of the mistag rate in order to interpret a measured flavor or *CP* asymmetry in terms of the physical observables. In fact, the flavor-tagging algorithms do not only provide a flavor tag but also express their confidence in this decision, in terms of an estimated mistag probability η (which approximates the true mistag rate ω), based on the output of a multivariate classifier. These are trained on flavor specific control channels ($B^+ \to J/\psi\, K^+$ decays for the OS algorithms and $B_s^0 \to D_s^- \pi^+$ for the SS kaon tagger) and are fed with kinematic and geometric properties of the tagging particle(s) as well as variables related to the event topology and the signal b-hadron [248–250]. The mistag estimate differs for each event. For example, the SS kaon tagger decision is more reliable if there is only one kaon candidate in vicinity of the signal B_s meson compared to

cases with multiple random tracks from the underlying event close by. Figure 10.5 shows the estimated mistag distributions obtained applying the OS combination (left) and SS kaon (right) algorithm to tag $B_s \to D_s K\pi\pi$ and $B_s \to D_s\pi\pi\pi$ signal candidates.

In principle, an average value for the mistag rate could be used. However, it is beneficial to consider the mistag probability as per-event observable (as detailed in the next chapter) acknowledging the fact that the tagging information for certain candidates is more trustworthy. In doing so, the effective tagging power increases by an amount proportional to the variance of the mistag distribution (σ_ω^2):

$$\epsilon_{eff} = \langle \mathcal{D}_{\text{tag}}^2 \rangle = \frac{1}{N}\sum_i (1-2\omega_i)^2 = \langle \mathcal{D}_{\text{tag}} \rangle^2 + 4\,\sigma_\omega^2 \geq \langle \mathcal{D}_{\text{tag}} \rangle^2 \tag{10.12}$$

where ω_i is the (true) per-event mistag probability and a value of $\omega_i = 0.5$ is assigned to untagged events. As a simple example, consider a tagger with an average mistag rate of $\langle\omega\rangle = 40\%$ and a standard variation of $\sigma_\omega = 10\%$. In this case, the effective tagging power increases by 100% if the per-event mistag probability is used instead of the average value; equivalent to twice the amount of data.

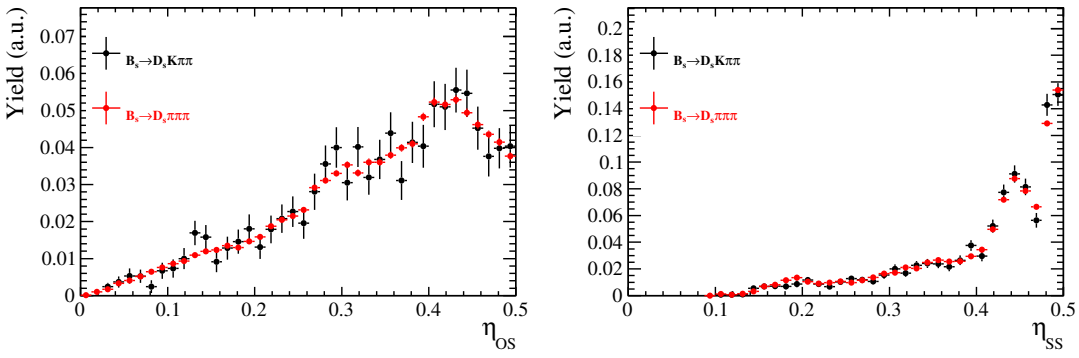

Figure 10.5: Distributions of the predicted mistag η for the OS combination (left) and the SS kaon tagger (right) for $B_s \to D_s K\pi\pi$ (black) and $B_s \to D_s\pi\pi\pi$ (red) signal candidates. Only candidates with non-zero tag decision are show.

Calibration of flavor tagging algorithms

The output of a given multivariate classifier does not necessarily represent the actual (physical) mistag probability. In particular, the algorithm might perform differently on the signal decay $B_s \to D_s K\pi\pi$ than on the decay modes used for the training, *e.g.* due to differences in the kinematics of the tagging or signal candidates. Moreover, the combination of the individual OS taggers into a single response assumes that they are uncorrelated. Indeed, they have a sizable overlap such that the performance of the OS tagger combination is overestimated in general. The tagger responses are thus calibrated on the flavor specific control mode $B_s \to D_s\pi\pi\pi$, which is kinematically and topologically similar to the signal decay. The idea of the calibration method is illustrated in Figure 10.6 for the SS tagger. It shows the measured mixing asymmetry, given by

$$A_{\text{mix}}^{\text{meas}}(t) = \mathcal{D}_{\text{res}}\,\mathcal{D}_{\text{tag}}\,A_{\text{mix}}(t) \tag{10.13}$$

taking also the decay-time resolution into account, in bins of the mistag probability η estimated by the tagging algorithm. The measured oscillation amplitude, clearly declines with increasing values of η. Since the true flavor asymmetry is know for the control mode, and so is the decay-time resolution (see Section 10.1), the tagging dilution can be extracted, in each η bin, from the measured asymmetry. In agreement with other decay-time dependent analyses performed at the LHCb experiment (*e.g.* those in References [136, 141, 142, 251, 252]) and confirmed with a finer binning in η and on simulated data [2], a linear calibration function is found to be sufficient to map the estimated to the true mistag rate as measured in data, see Figure 10.7:

$$\omega(\eta) = p_0 + p_1 \cdot (\eta - \langle\eta\rangle), \tag{10.14}$$

where p_0 and p_1 are the tagging calibration parameters.

The binned approach outlined above is only used to motivate the general relation between estimated and true mistag rate. Instead, the actual tagger calibration performs an unbinned likelihood fit to the decay-time distribution of $B_s \to D_s\pi\pi\pi$ candidates taking the tagging information into account. This makes optimal use of the available statistics and allows to calibrate the OS combination and SS kaon taggers simultaneously. Further technical details of the fit implementation and the results are discussed in the next chapter.

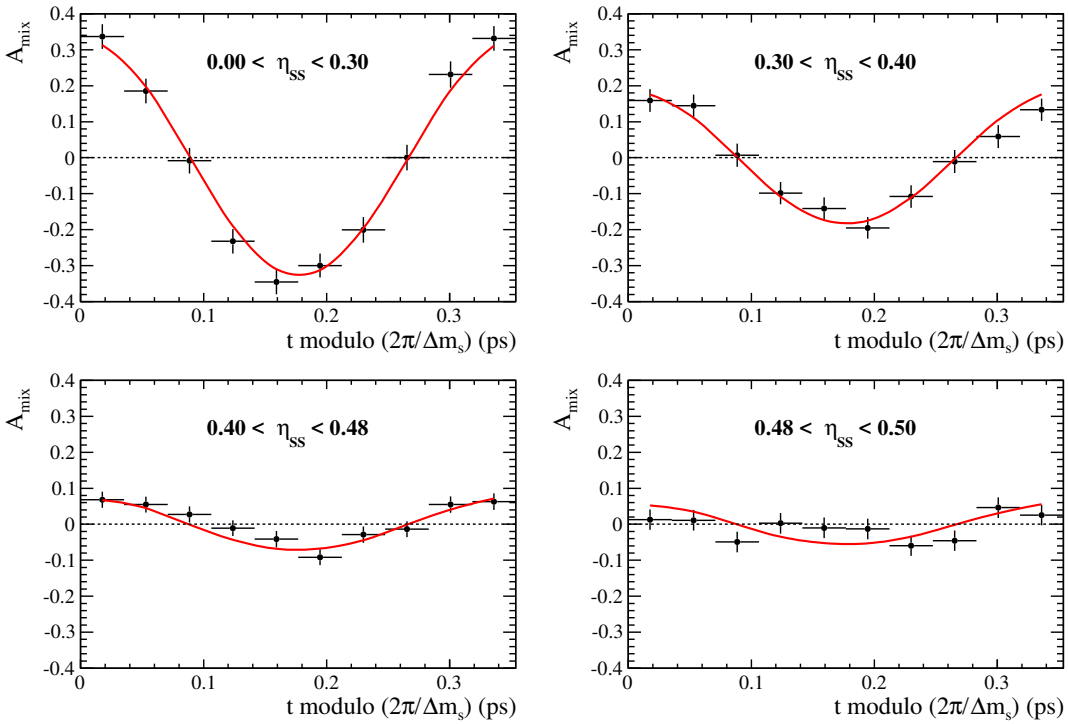

Figure 10.6: Mixing asymmetry in bins of the predicted mistag rate for the SS kaon tagger. The actual mistag rate is extracted in each bin by means of a time-dependent fit displayed in red.

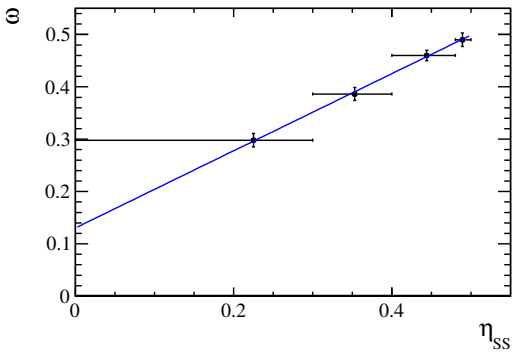

Figure 10.7: Measured (true) mistag rate in bins of the predicted mistag rate for the SS kaon tagger. A linear calibration function is overlaid in blue.

10.4 Nuisance asymmetries

Production asymmetry

Given that two proton beams are colliding at the LHCb experiment, there is a slight excess of particles, in form of the beam remnants, over antiparticles available for the hadronization process. As an example, a produced b quark might coalesce with light valence quarks of the proton remnants to form a Λ_b (bud) baryon, while the equivalent process for $\bar{b}$ quarks is not possible. Instead, a $\bar{b}$ quark needs to combine with quarks from the fragmentation process to produce an anti-baryon. This implies that Λ_b baryons are more abundantly created than $\bar{\Lambda}_b$ baryons. Similar arguments hold for other b-hadron species. For LHC energies, the production asymmetries, defined as

$$A_p(X) = \frac{N(\bar{X}) - N(X)}{N(\bar{X}) + N(X)}, \tag{10.15}$$

are predicted to be at most at the 1% level depending on the b-hadron kinematics [253, 254]. Here $N(X)$ and $N(\bar{X})$ denote the number of produced particles and antiparticles of a given b-hadron species X. The presence of an initial flavor asymmetry modifies the measured time-dependent CP asymmetries $A_{CP}^{\langle f \rangle}(t)$ and $A_{CP}^{\langle i \rangle}(t)$ (defined in Equation 3.20), which are sensitive to CP violation from the sinusoidal and hyperbolic CP coefficients, in non-trivial ways:

$$\begin{aligned} A_{\text{raw}}^{\langle f \rangle}(t) &\approx A_{CP}^{\langle f \rangle}(t) - A_P \\ A_{\text{raw}}^{\langle i \rangle}(t) &\approx A_{CP}^{\langle i \rangle}(t) - \left(\frac{2\,C\cos(\Delta m_s\, t)}{2\cosh(\Delta\Gamma/2t) + (D + \bar{D})\sinh(\Delta\Gamma/2t)} \right) A_P, \end{aligned} \tag{10.16}$$

which need to be disentangled from genuine CP violating effects. As depicted in Figure 10.8, the impact on $A_{\text{raw}}^{\langle i \rangle}(t)$ is particularly striking since an oscillating feature develops, whereas $A_{\text{raw}}^{\langle f \rangle}(t)$ is shifted by a constant offset. The production asymmetry can be measured from flavor specific B_s meson decays, for which $A_{CP}^{\langle f \rangle}(t) = A_{CP}^{\langle i \rangle}(t) = 0$. Here, the flavor-averaged CP asymmetry ($A_{\text{raw}}^{\langle i \rangle}(t)$) is experimentally easier to access since it does not require flavor tagging. Such an analysis has been performed by the LHCb collaboration in proton-proton collisions at center-of-mass energies of 7 TeV and 8 TeV using $B_s \to D_s\pi$ decays [255], where the production asymmetry was measured in bins of p_T and η of the B_s meson. To correct for the different kinematics, the production asymmetries measured in $B_s \to D_s\pi$ decays are folded with the background subtracted p_T, η distribution of $B_s \to D_s K\pi\pi$ decays. The resulting effective production asymmetry amounts to $A_P^{\text{Run-I}}(B_s^0) = (-0.045 \pm 1.04)\%$. As for center-of-mass energies of $\sqrt{s} = 13$ TeV no

such measurement has been performed yet, the production asymmetry for Run-II data is extracted from the control mode $B_s \to D_s\pi\pi\pi$ as discussed in more detail in the next chapter.

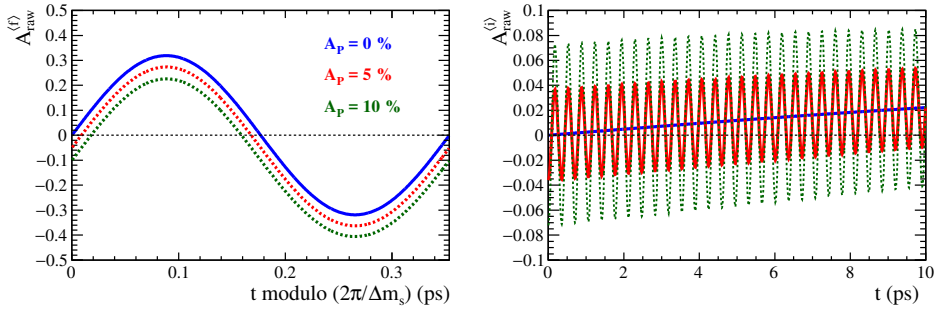

Figure 10.8: Influence of A_P on the time-dependent CP asymmetries $A_{CP}^{\langle f \rangle}(t)$ (left) and $A_{CP}^{\langle i \rangle}(t)$ (right) which are sensitive to CP violation from the sinusoidal and hyperbolic CP coefficients, respectively.

Detection asymmetry

There are two effects responsible for different detection efficiencies of positively and negatively charged particles: their nuclear cross sections might be dissimilar and the performance of the track reconstruction is asymmetric. The latter is mainly due to the fact that particles are preferentially bent in certain regions of the detector depending on their charge. As the magnet polarity is frequently inverted, the tracking asymmetry cancels to a large extend. The residual tracking asymmetry is below 0.1% and can be ignored for this analysis [256]. The material interaction is particularly relevant for kaons as, for example, the $\bar{u}$ valence quark in a K^- meson can annihilate with a u valence quark of the nucleons composing the detector material. In contrast, the u valence quark in a K^+ meson can only annihilate with a $\bar{u}$ sea quark. The kaon detection asymmetry, defined as

$$A_D(K^-) = \frac{\epsilon(K^-) - \epsilon(K^+)}{\epsilon(K^-) + \epsilon(K^+)} \tag{10.17}$$

where $\epsilon(K^\mp)$ denotes the detection efficiencies of a $K^\mp$ meson, is hence negative and expected to be at the 1% level [257]. It is reduced at high kaon momenta for which the inelastic scattering with the valence quarks is less likely. Since the detector contains approximately the same number of protons and neutrons (or u and d quarks), the detection asymmetry for pions is negligible small.

Depending on the reconstructed D_s decay mode, the final state of the signal decay $B_s \to D_sK\pi\pi$ contains in total three ($D_s \to KK\pi$), two ($D_s \to K\pi\pi$) or a single kaon ($D_s \to \pi\pi\pi$). It is assumed that the detection asymmetries of two oppositely charged kaons cancel, given that their kinematic distributions are approximately equal [258]. The remaining single kaon detection asymmetry for the $D_s \to KK\pi$ and $D_s \to \pi\pi\pi$ decay channels is determined from high statistics

charm control modes. As *CP* violation in the charm system is negligible, the yield asymmetry between $D^- \to K^+\pi^-\pi^-$ and $D^+ \to K^-\pi^+\pi^+$ decays (corrected for an additional D^+ production asymmetry) gives an estimate of the kaon detection asymmetry. Such a measurement has been performed in References [257, 259] in bins of the kaon momentum. The effective detection asymmetry (of the LHCb detector) for $B_s \to D_s K\pi\pi$ decays integrated over the signal kaon kinematics amounts to $A_D(K^-) = -0.9 \pm 0.2\%$. Figure 10.9 illustrates the influence on the time-dependent *CP* asymmetries:

$$\begin{aligned} A_{\text{raw}}^{\langle f\rangle}(t) &\approx A_{CP}^{\langle f\rangle}(t) - \left(\frac{2\,C\cos(\Delta m_s\,t) + (\bar{S} - S)\sin(\Delta m_s\,t)}{2\cosh(\Delta\Gamma/2t) + (D + \bar{D})\sinh(\Delta\Gamma/2t)}\right) A_D, \\ A_{\text{raw}}^{\langle i\rangle}(t) &\approx A_{CP}^{\langle i\rangle}(t) - A_D. \end{aligned} \tag{10.18}$$

While the asymmetry $A_{\text{raw}}^{\langle i\rangle}(t)$ is shifted by a constant amount, the oscillation of the asymmetry $A_{\text{raw}}^{\langle f\rangle}(t)$ is modulated.

The detection asymmetry impacts the reconstruction of not only signal candidates but also tagging particles which are often kaons. As a consequence, flavor taggers might perform differently depending on the initial flavor of the B_s meson. This is expressed by the tagging asymmetry parameters $\Delta\epsilon_{\text{tag}}, \Delta p_0$ and Δp_1 as:

$$\begin{aligned} \epsilon_{\text{tag}} &= \langle\epsilon_{\text{tag}}\rangle + \Delta\epsilon_{\text{tag}}, \quad & \omega(\eta) &= (\langle p_0\rangle + \Delta p_0) + (\langle p_1\rangle + \Delta p_1)\cdot(\eta - \langle\eta\rangle), \\ \bar{\epsilon}_{\text{tag}} &= \langle\epsilon_{\text{tag}}\rangle - \Delta\epsilon_{\text{tag}}, \quad & \bar{\omega}(\eta) &= (\langle p_0\rangle - \Delta p_0) + (\langle p_1\rangle - \Delta p_1)\cdot(\eta - \langle\eta\rangle). \end{aligned}$$

Here, ϵ_{tag} ($\bar{\epsilon}_{\text{tag}}$) and $\omega(\eta)$ ($\bar{\omega}(\eta)$) denote the tagging efficiency and mistag rate of an initial B_s^0 ($\overline{B}_s^0$) meson and $\langle\epsilon_{\text{tag}}\rangle$,$\langle p_0\rangle$ and $\langle p_1\rangle$ are the flavor-averaged tagging parameters. A flavor-tagging performance asymmetry is, in principle, similar to a production asymmetry as it leads to an apparent different number of initially created B_s^0 and $\bar{B}_s^0$ mesons. Since the tagging asymmetry depends on the specific algorithm (OS or SS tagger), these two effects can be disentangled albeit a small correlation persists. This is done in fit to the decay-time distribution of $B_s \to D_s\pi\pi\pi$ candidates described in the next chapter.

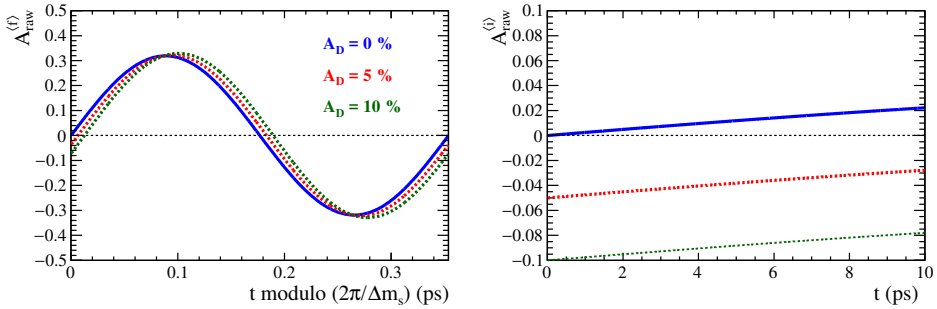

Figure 10.9: Influence of the detection asymmetry on the time-dependent *CP* asymmetries $A_{CP}^{\langle f\rangle}(t)$ (left) and $A_{CP}^{\langle i\rangle}(t)$ (right) which are sensitive to *CP* violation from the sinusoidal and hyperbolic *CP* coefficients, respectively.

Measurement of the $B_s^0 - \overline{B}_s^0$ mixing frequency and the CKM angle γ

11

This chapter covers the (phase-space integrated) decay-time analyses of the reference channel $B_s \to D_s\pi\pi\pi$ and the signal channel $B_s \to D_sK\pi\pi$. The latter allows extracting the CKM angle γ in a *model-independent* way. Afterwards, the resonance spectrum in $B_s \to D_sK\pi\pi$ decays is studied and a full time-dependent amplitude analysis is performed for a *model-dependent* determination of the CKM angle γ. The chapter concludes with comparing the results of both methods.

11.1 Decay-time spectrum of $B_s \to D_s\pi\pi\pi$ decays

A likelihood fit to the (background-subtracted) proper-time spectrum of the $B_s \to D_s\pi\pi\pi$ candidates is performed to determine the tagging calibration parameters and the B_s production asymmetry at center-of-mass energies of 13 TeV. During the measurement it is found out that the analysis of the reference channel also permits setting a powerful new constraint on the $B_s^0 - \overline{B}_s^0$ mixing frequency Δm_s. Due to the flavor-specific nature of the decay, the theoretical decay-time PDF takes on a simple form as discussed in Section 3.3. In light of the experimental effects discussed in the previous chapter, the PDF needs to be modified as follows [141–143]:

$$
\begin{aligned}
\mathcal{P}(t, q_{OS}, q_{SS}, q_f|\delta_t, \eta_{OS}, \eta_{SS}) \propto& \left[(1 + q_f A_D)\, p(t, q_{OS}, q_{SS}, q_f|\delta_t, \eta_{OS}, \eta_{SS})\, e^{-\Gamma_s t} \otimes R(t - t'|\sigma_t(\delta_t))\right] \epsilon(t) \\
p(t, q_{OS}, q_{SS}, q_f|\delta_t, \eta_{OS}, \eta_{SS}) =& \Bigg[(1 + A_P) f(q_{OS}, \eta_{OS}) f(q_{SS}, \eta_{SS}) \left(\cosh\left(\frac{\Delta\Gamma_s\, t}{2}\right) + q_f \cos\left(\Delta m_s\, t\right)\right) \\
&+ (1 - A_P) \bar{f}(q_{OS}, \eta_{OS}) \bar{f}(q_{SS}, \eta_{SS}) \left(\cosh\left(\frac{\Delta\Gamma_s\, t}{2}\right) - q_f \cos\left(\Delta m_s\, t\right)\right)\Bigg] \\
f(q, \eta) =& |q| \left[1 + q\left(1 - 2\, w(\eta)\right)\right] \epsilon_{\text{tag}} + 2\,(1 - |q|)\,(1 - \epsilon_{\text{tag}}) \\
\bar{f}(q, \eta) =& |q| \left[1 + q\left(1 - 2\, \bar{w}(\eta)\right)\right] \bar{\epsilon}_{\text{tag}} + 2\,(1 - |q|)\,(1 - \bar{\epsilon}_{\text{tag}})
\end{aligned}
\tag{11.1}
$$

The signal PDF $\mathcal{P}(t, q_{OS}, q_{SS}, q_f|\delta_t, \eta_{OS}, \eta_{SS})$ is conditional on the per-event observables [260] δ_t, η_{OS} and η_{SS} describing the estimated decay-time error and the estimated mistag rates of the OS (combination) and SS taggers, respectively.

The parameters of the resolution model and the decay-time acceptance function are fixed to the values determined in the dedicated studies in Chapter 10. The decay width and decay width difference are fixed to their world-average values [35]. Both taggers are simultaneously calibrated during the fit as described by the helper functions $f(q,\eta)$ and $\bar{f}(q,\eta)$, which also take tagging asymmetries between initial B_s^0 and $\overline{B}_s^0$ meson into account. Their response is then explicitly combined. The tagging algorithms have been retuned for the Run-II data-taking period to account for the changed conditions, especially the increased centre-of-mass energy of the proton-proton collisions. It is therefore necessary to perform separate calibrations for the two data-taking periods.

Figure 11.1 displays the decay-time distribution and the mixing asymmetry for $B_s \to D_s\pi\pi\pi$ signal candidates. All features are well reproduced by the fit projections which are overlaid. Table 11.1 lists the determined fit parameters. Within uncertainties (systematic uncertainties are discussed in Section 11.4) the measured production asymmetry for Run-II data is consistent with both zero and the production asymmetry for Run-I data determined in Section 10.4. The fit estimate of the mixing frequency agrees well within uncertainties with the world-average value ($\Delta m_s = 17.757 \pm 0.021\,\mathrm{ps}^{-1}$ [35]) and is significantly more precise. Tables 11.2 and 11.3 report the observed tagging performances for Run-I and Run-II data considering three mutually exclusive categories: tagged by the OS combination algorithm only, tagged by the SS kaon algorithm only and tagged by both OS and SS algorithms. While the flavor taggers suffer from the higher track multiplicity during the Run-II data-taking period, they profit from the harder momentum spectrum of the produced $b\bar{b}$ quark pair. Combined, this results in a net (absolute) improvement of almost 1% in effective tagging power.

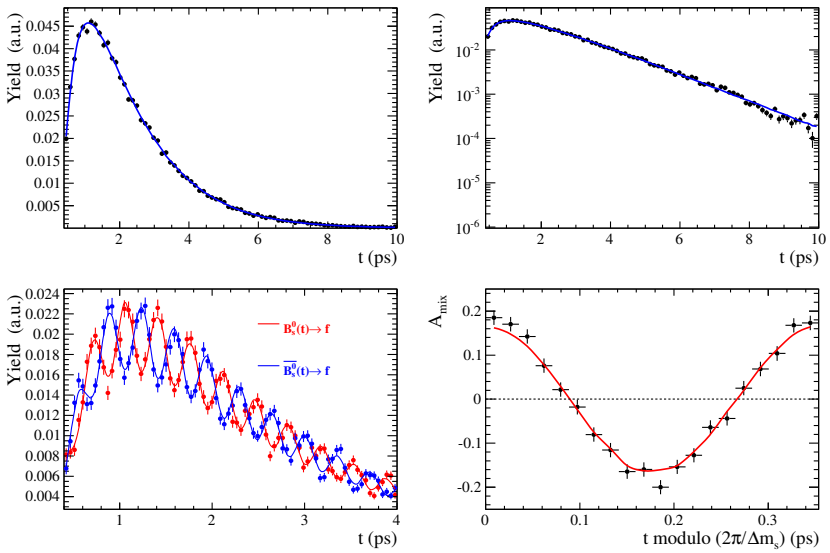

Figure 11.1: Flavour averaged (top) and tagged (bottom-left) decay-time distribution of background-subtracted $B_s \to D_s\pi\pi\pi$ candidates as well as the mixing asymmetry folded into one oscillation period (bottom-right) along with the fit projections (solid lines).

Table 11.1: Parameters determined from the fit to the $B_s \to D_s\pi\pi\pi$ decay-time distribution. The uncertainties are statistical and systematic (discussed in Section 11.4), respectively.

Fit Parameter	Run-I	Run-II
p_0^{OS}	0.398 ± 0.010 ± 0.010	0.372 ± 0.005 ± 0.005
p_1^{OS}	0.895 ± 0.085 ± 0.090	0.788 ± 0.043 ± 0.030
Δp_0^{OS}	0.030 ± 0.011 ± 0.002	0.008 ± 0.006 ± 0.001
Δp_1^{OS}	0.011 ± 0.095 ± 0.017	0.067 ± 0.052 ± 0.002
$\epsilon_{\text{tag}}^{OS}$ [%]	47.775 ± 0.365 ± 0.067	40.399 ± 0.182 ± 0.029
$\Delta\epsilon_{\text{tag}}^{OS}$ [%]	0.016 ± 1.353 ± 0.097	0.316 ± 0.618 ± 0.046
p_0^{SS}	0.444 ± 0.008 ± 0.005	0.428 ± 0.004 ± 0.002
p_1^{SS}	0.949 ± 0.111 ± 0.067	0.787 ± 0.039 ± 0.025
Δp_0^{SS}	-0.019 ± 0.009 ± 0.001	-0.017 ± 0.004 ± 0.000
Δp_1^{SS}	0.064 ± 0.124 ± 0.017	0.028 ± 0.048 ± 0.006
$\epsilon_{\text{tag}}^{SS}$ [%]	68.426 ± 0.340 ± 0.013	69.903 ± 0.170 ± 0.007
$\Delta\epsilon_{\text{tag}}^{SS}$ [%]	-0.046 ± 1.242 ± 0.082	-0.319 ± 0.575 ± 0.062
A_P [%]	-0.045 (fixed)	-0.183 ± 0.642 ± 0.048
Δm_s [ps^{-1}]	17.7651 ± 0.0084 ± 0.0058	

Table 11.2: The flavour tagging performances for only OS tagged, only SS tagged and both OS and SS tagged signal candidates for Run-I data.

$B_s \to D_s\pi\pi\pi$	ϵ_{tag}[%]	$\langle\omega\rangle$[%]	ϵ_{eff}[%]
Only OS	14.74 ± 0.11	39.09 ± 0.80	1.25 ± 0.16
Only SS	35.38 ± 0.18	44.26 ± 0.62	1.05 ± 0.18
Both OS-SS	33.04 ± 0.30	37.33 ± 0.73	3.41 ± 0.33
Combined	83.16 ± 0.37	40.59 ± 0.70	5.71 ± 0.40

Table 11.3: The flavour tagging performances for only OS tagged, only SS tagged and both OS and SS tagged signal candidates for Run-II data.

$B_s \to D_s\pi\pi\pi$	ϵ_{tag}[%]	$\langle\omega\rangle$[%]	ϵ_{eff}[%]
Only OS	11.78 ± 0.05	37.01 ± 0.51	1.15 ± 0.07
Only SS	41.28 ± 0.10	42.65 ± 0.35	1.79 ± 0.12
Both OS-SS	28.62 ± 0.15	35.35 ± 0.40	3.63 ± 0.16
Combined	81.68 ± 0.19	39.28 ± 0.40	6.57 ± 0.21

11.2 Model-independent analysis of $B_s \to D_s K\pi\pi$ decays

The decay-time fit to the $B_s \to D_s K\pi\pi$ candidates uses a signal PDF based on Equation 3.16 with analog modifications accounting for experimental influences as in Equation 11.1. The B_s production asymmetry for Run-II data and the $B_s^0 - \overline{B}_s^0$ mixing frequency are fixed to the values extracted from the $B_s \to D_s\pi\pi\pi$ data sample, whereas the tagging calibration parameters are allowed to vary within Gaussian constraints (taking their correlation into account) considering small kinematic differences between the decay modes. Otherwise, the fit strategy is identical to the one discussed in the previous section. Figure 11.2 shows the decay-time distribution, as well as mixing and time-dependent *CP* asymmetries together with the fit projections. The mixing asymmetries for $D_s^- K^+\pi^+\pi^-$ and $D_s^+ K^-\pi^-\pi^+$ final states are shifted with respect to each other as expected in case of *CP* violation. In particular, the time-dependent asymmetry $A_{CP}^{\langle f\rangle}$ provides a solid evidence for the breaking of *CP* symmetry as an oscillating feature is perceivable. The time-dependent asymmetry $A_{CP}^{\langle i\rangle}$, on the other hand, is not decisively resolvable with the currently available statistics. The *CP* coefficients $C, D, \bar{D}, S$ and $\bar{S}$ determined from the fit are reported in Table 11.4. They are converted to the physical observables r, κ, δ and $\gamma - 2\beta_s$ in Section 11.5, after discussing systematic uncertainties in Section 11.4.

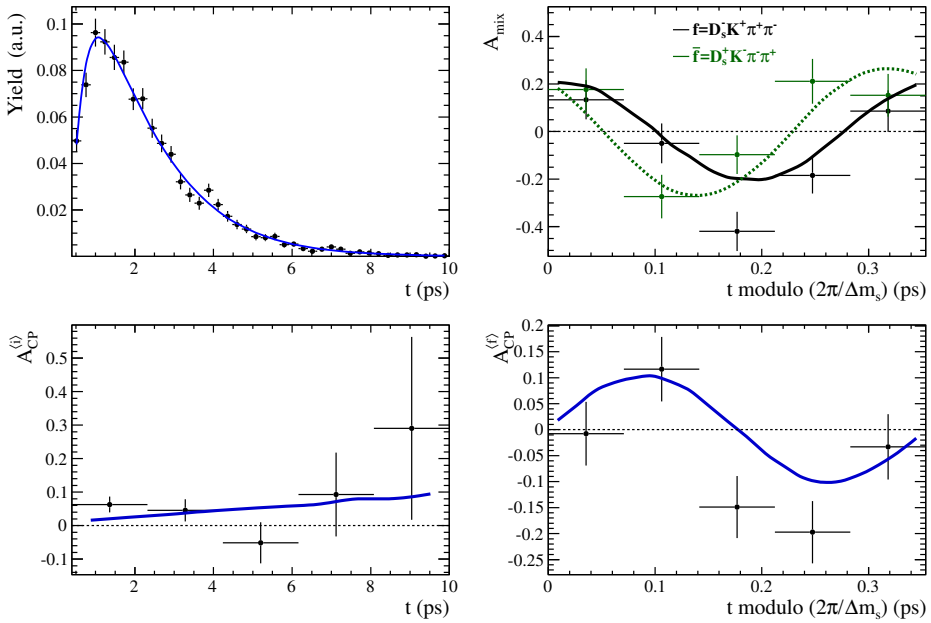

Figure 11.2: Decay-time distribution (top-left), mixing asymmetry (top-right) and time-dependent *CP* asymmetries $A_{CP}^{\langle f\rangle}(t)$ (bottom-left) and $A_{CP}^{\langle i\rangle}(t)$ (bottom-right) of background-subtracted $B_s \to D_s K\pi\pi$ candidates along with the fit projections (solid lines).

Table 11.4: *CP* coefficients determined from the fit to the $B_s \to D_s K\pi\pi$ decay-time distribution. The uncertainties are statistical and systematic (discussed in Section 11.4), respectively.

Fit Parameter	Value
C	0.68 ± 0.12 ± 0.03
D	-0.00 ± 0.32 ± 0.07
$\bar{D}$	0.39 ± 0.30 ± 0.07
S	-0.14 ± 0.17 ± 0.03
$\bar{S}$	-0.54 ± 0.17 ± 0.02

11.3 Time-dependent amplitude analysis

The time-dependent amplitude analysis combines the strategy of the phase-space integrated fit discussed in the previous section with the techniques developed in course of the $D \to \pi\pi\pi\pi$ analysis presented in Part II. The employed signal PDF replaces the phase-space integrated (theoretical) decay rate with the full decay rate given in Equation 3.15 (which includes the total decay amplitudes $A^c(\mathbf{x})$ and $A^u(\mathbf{x})$ describing $b \to c$ and $b \to u$ quark-level transitions) but is otherwise identical to the PDF used in Section 11.2. Variations of the reconstruction and selection efficiency over the phase space are incorporated by evaluating the likelihood normalization integrals with simulated decays as described in Section 6.1. Figure 11.3 shows projections of the phase-space acceptance to several invariant mass combinations, for visualization purposes only. The largest variations of the phase-space efficiency are observed for invariant masses involving the (unstable) D_s meson. Most notably

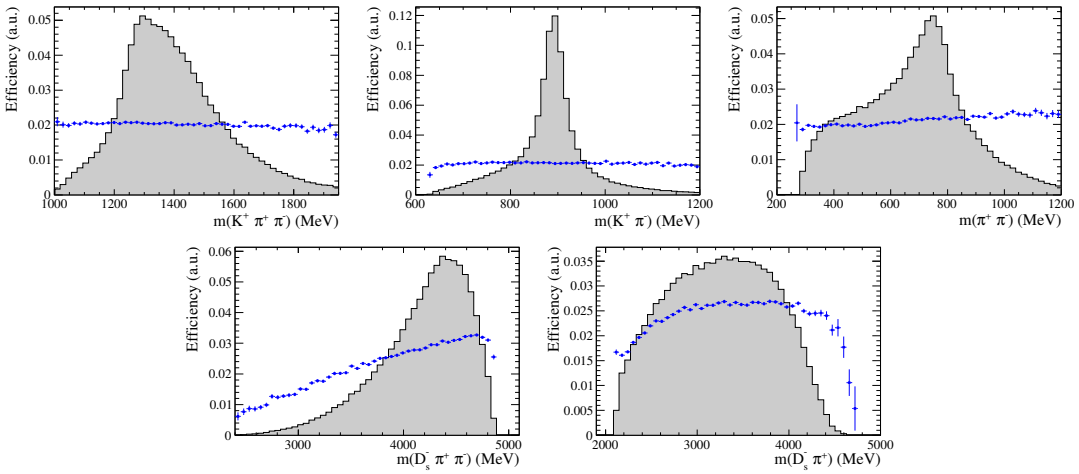

Figure 11.3: Efficiency variation (blue data points) in arbitrary scale as a function of the phase-space variables obtained from the ratio of selected and generated MC events. The overlaid (filled) histograms show the background-subtracted data distributions of $B_s \to D_s K\pi\pi$ candidates.

is the $D_s^-\pi^+\pi^-$ combination, where a low invariant mass implies low (average) momenta of the D_s candidate and the companion pions. A small momentum of the D_s candidate in turn leads to small momenta of its decay products (three hadrons) such that there are in total five low momentum tracks. The probability that at least one of those does not pass the minimum momentum threshold is high. The remaining kaon track has a large momentum, where the performance of the PID requirement decreases (*cf.* Figure 9.2). The combination of these two effects are the dominant source for the steep decline in selection efficiency towards small $D_s^-\pi^+\pi^-$ invariant masses.

Amplitude model construction

The construction of the amplitude model follows the same general strategy utilized for $D \to \pi\pi\pi\pi$ decays (*cf.* Section 6.3). In contrast to the spectrum of exited pions, the exited kaon resonances potentially contributing to the $K\pi\pi$ subsystem in $B_s \to D_s K\pi\pi$ decays are experimentally better but still not precisely constrained [10]. Contributions from the axial vector mesons $K_1(1270)$ and $K_1(1400)$ decaying to the $K\pi\pi$ final state and from the resonances $\rho(770)^0 \to \pi^+\pi^-$ and $K^*(892)^0 \to K^+\pi^-$ are apparent from the invariant mass distributions in Figure 11.3. These are considered for the model building procedure in a variety of decay topologies, together with several additional resonant states. The full list of considered intermediate-state amplitudes amounts to 45 and can be found in Table 11.5. A significant complication arises from the fact that two (quasi-independent) amplitude models need to be developed simultaneously: one amplitude describes decays via $b \to c$ ($A^c(\mathbf{x})$), the other decays via $b \to u$ ($A^u(\mathbf{x})$) quark-level transitions (compare Equation 3.13). These can only be disentangled as their relative contribution to the total $B_s \to D_s K\pi\pi$ decay rate changes over time (due to mixing) as outlined in Section 3.3.

The model building procedure is performed in two stages. The first stage identifies the set of intermediate-state amplitudes contributing (at a significant level) to either decays via $b \to c$ or $b \to u$ quark-level transitions or to both. To that end, the time-integrated and flavor-averaged phase-space distribution is examined. A single total amplitude, $A^{eff}(\mathbf{x}) = \sum_i a_i^{eff} A_i(\mathbf{x})$, is sufficient in this case, which effectively describes the incoherent superposition of the $b \to c$ and $b \to u$ amplitudes, $|A^{eff}(\mathbf{x})|^2 = |A^c(\mathbf{x})|^2 + r^2\,|A^u(\mathbf{x})|^2$. The significantly simplified fitting procedure allows to include the whole pool of considered intermediate-state amplitudes for the LASSO technique. Figure 11.4(left) shows the resulting BIC scan over the LASSO parameter λ. The minimum is found at $\lambda = 50$, where

nine intermediate-state amplitudes with a decay fraction above the threshold (0.5%) remain. These amplitudes are further considered for the second stage of the model selection, at which a full time-dependent amplitude fit is performed. The components selected by the first stage are included for both $b \to c$ and $b \to u$ transitions and a LASSO penalty term for each is added to the likelihood function. As shown in Figure 11.4(right), an optimal value of $\lambda = 6$ is found for the complexity parameter. The final step of the model construction removes two intermediate-state amplitudes from each of the total decay amplitudes $A^c(\mathbf{x})$ and $A^u(\mathbf{x})$.

Table 11.5: Intermediate-state components considered for the $B_s \to D_s K\pi\pi$ LASSO model building procedure. If no angular momentum is specified, the lowest angular momentum state compatible with angular momentum conservation and, where appropriate, parity conservation, is used.

(a) Cascade decays

$B_s \to D_s^- [K_1(1270)^+[S,D] \to \pi^+ K^*(892)^0]$
$B_s \to D_s^- [K_1(1270)^+ \to \pi^+ K_0^*(1430)^0]$
$B_s \to D_s^- [K_1(1270)^+[S,D] \to K^+ \rho(770)^0]$
$B_s \to D_s^- [K_1(1400)^+[S,D] \to \pi^+ K^*(892)^0]$
$B_s \to D_s^- [K_1(1400)^+[S,D] \to K^+ \rho(770)^0]$
$B_s \to D_s^- [K(1460)^+ \to K^+ \sigma^0]$
$B_s \to D_s^- [K(1460)^+ \to K^+ \rho(770)^0]$
$B_s \to D_s^- [K(1460)^+ \to \pi^+ K^*(892)^0]$
$B_s \to D_s^- [K(1460)^+ \to \pi^+ K^*(1430)^0]$
$B_s \to D_s^- [K^*(1410)^+ \to \pi^+ K^*(892)^0]$
$B_s \to D_s^- [K^*(1410)^+ \to K^+ \rho(770)^0]$
$B_s \to D_s^- [K_2^*(1430)^+ \to \pi^+ K^*(892)^0]$
$B_s \to D_s^- [K_2^*(1430)^+ \to K^+ \rho(770)^0]$
$B_s \to D_s^- [K^*(1680)^+ \to \pi^+ K^*(892)^0]$
$B_s \to D_s^- [K^*(1680)^+ \to K^+ \rho(770)^0]$
$B_s \to D_s^- [K_2(1770)^+ \to \pi^+ K^*(892)^0]$
$B_s \to D_s^- [K_2(1770)^+ \to K^+ \rho(770)^0]$
$B_s \to D_s^- [K_2(1770)^+ \to \pi^+ K_2^*(1430)^0]$
$B_s \to D_s^- [K_2(1770)^+ \to K^+ f_2(1270)^0]$
$B_s \to D_s^- [K_2^*(1980)^+ \to \pi^+ K^*(892)^0]$
$B_s \to D_s^- [K_2^*(1980)^+ \to K^+ \rho(770)^0]$
$B_s \to D_s^- [K_2^*(1980)^+ \to \pi^+ K_2^*(1430)^0]$
$B_s \to D_s^- [K_2^*(1980)^+ \to K^+ f_2(1270)]$
$B_s \to K^+ [D_{s1}(2536)^- \to D_s^- \ \rho(770)^0]$
$B_s \to K^+ [D_{s1}(2536)^- \to D_s^- \ \sigma^0]$

(b) Quasi two-body decays

$B_s \to \sigma^0 (D_s^- K^+)_S$
$B_s \to \sigma^0 (D_s^- K^+)_V$
$B_s \to \rho(770)^0 (D_s^- K^+)_S$
$B_s [S,P,D] \to \rho(770)^0 \, (D_s^- K^+)_V$
$B_s \to f_2(1270)^0 (D_s^- K^+)_S$
$B_s \to K^*(892)^0 \, (D_s^- \pi^+)_S$
$B_s [S,P,D] \to K^*(892)^0 \, (D_s^- \pi^+)_V$
$B_s \to K_0^*(1430)^0 \, (D_s^- \pi^+)_S$
$B_s \to K_2^*(1430)^0 \, (D_s^- \pi^+)_S$
$B_s \to (D_s^- K^+)_S \, (\pi^+ \pi^-)_S$

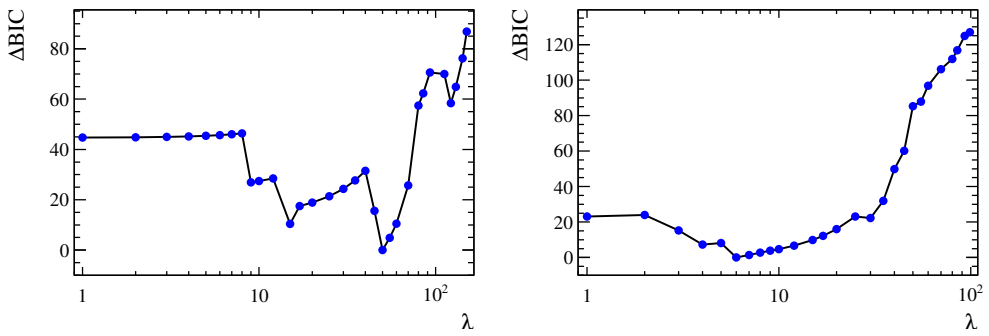

Figure 11.4: Difference in the BIC value from its minimum as function of the LASSO parameter λ for step-1 (left) and step-2 (right) of the model selection.

Resonant substructure

Table 11.7 lists the moduli and phases of the complex amplitude coefficients a_i^c and a_i^u obtained by fitting the LASSO model to the $B_s \to D_s K\pi\pi$ signal candidates. The corresponding decay fractions for the $b \to c$ and $b \to u$ amplitudes are individually normalized:

$$F_i^c \equiv \frac{\int |a_i^c\, A_i(\mathbf{x})|^2 \, \mathrm{d}\Phi_4}{\int |A^c(\mathbf{x})|^2 \, \mathrm{d}\Phi_4}, \qquad F_i^u \equiv \frac{\int |a_i^u\, A_i(\mathbf{x})|^2 \, \mathrm{d}\Phi_4}{\int |A^u(\mathbf{x})|^2 \, \mathrm{d}\Phi_4}, \tag{11.2}$$

and are given in Table 11.8. Invariant-mass projections are shown in Figure 11.5 indicating that the model provides a reasonable description of the data. A χ^2 per degree of freedom of 1.4 is obtained using a five-dimensional adaptive binning as described in Section 6.4. The decay-time projection and time-dependent asymmetries shown in Figure 11.6 are qualitatively consistent with those of the phase-space integrated fit in Figure 11.2.

Decays via $b \to c$ quark-level transitions are found to be dominated by the axial vector states $K_1(1270)$ and $K_1(1400)$. These resonances are produced by the external weak current (see Figure 3.6) such that the observed pattern is consistent with the $a_1(1260)^+$ meson dominance in $D^0 \to \pi^+\pi^-\pi^+\pi^-$ decays. The determined resonant substructure of the axial vector states is in agreement with other analyses [10]. The sub-leading contribution comes from the vector resonance $K^*(1410)$. In $b \to u$ quark-level transitions, the exited kaon states are produced by the spectator-quark interaction. Here, no clear hierarchy is observed. There are again sizable contributions from the axial vector resonances but also from the pseudoscalar state $K(1460)$ and from the quasi two-body process $B_s \to (D_s\,\pi)_P\; K^*(892)$. The spectator quark interaction produces the $K_1(1270)$ meson more abundantly than the $K_1(1400)$ meson, while the external weak current

Table 11.7: Moduli and phases of the amplitudes coefficients for decays via $b \to c$ and $b \to u$ quark-level transitions. In case of multiple decay modes of three-body resonances, the amplitude coefficients are defined relative to the one listed first. The first quoted uncertainty is statistical, while the second arises from systematic sources (discussed in Section 11.4). Additional fit parameters are listed below. Here, the third uncertainty arises from the alternative models considered.

Decay Channel	$A^c(\mathbf{x})$		$A^u(\mathbf{x})$	
	$\lvert a_i^c\rvert$	$\arg(a_i^c)[^\circ]$	$\lvert a_i^u\rvert$	$\arg(a_i^u)[^\circ]$
$B_s \to D_s\,(K_1(1270) \to K\,\rho(770))$	1.0	0.0	1.0	0.0
$K_1(1270) \to K^*(892)\,\pi$	0.72 ± 0.11 ± 0.08	50.2 ± 7.8 ± 5.3		
$K_1(1270) \to K_0^*(1430)\,\pi$	0.52 ± 0.05 ± 0.05	128.9 ± 5.8 ± 17.8		
$B_s \to D_s\,(K_1(1400) \to K^*(892)\,\pi)$	1.98 ± 0.26 ± 0.18	10.5 ± 7.6 ± 5.6	0.75 ± 0.21 ± 0.16	-64.3 ± 16.0 ± 11.2
$B_s \to D_s\,(K^*(1410) \to K^*(892)\,\pi)$	1.14 ± 0.09 ± 0.07	55.0 ± 6.3 ± 5.2		
$K^*(1410) \to K\,\rho(770)$	0.63 ± 0.05 ± 0.03	-164.1 ± 5.1 ± 2.7		
$B_s \to D_s\,(K(1460) \to K^*(892)\,\pi)$			0.87 ± 0.13 ± 0.08	-96.1 ± 13.1 ± 9.7
$B_s \to (D_s\,\pi)_P\ K^*(892)$	0.72 ± 0.13 ± 0.12	-17.2 ± 13.8 ± 11.3	1.13 ± 0.20 ± 0.14	-16.7 ± 17.7 ± 15.3
$B_s \to (D_s\,K)_P\ \rho(770)$			0.53 ± 0.08 ± 0.07	33.7 ± 11.4 ± 10.4

Fit parameter	Value
$m_{K_1(1400)}$ [MeV]	1397 ± 8 ± 5 ± 7
$\Gamma_{K_1(1400)}$ [MeV]	205 ± 17 ± 9 ± 8
$m_{K^*(1410)}$ [MeV]	1432 ± 13 ± 16 ± 8
$\Gamma_{K^*(1410)}$ [MeV]	345 ± 27 ± 36 ± 17
r	0.50 ± 0.04 ± 0.03 ± 0.02
$\delta\,[^\circ]$	46 ± 15 ± 6 ± 8
$\gamma - 2\beta_s\,[^\circ]$	61 ± 15 ± 6 ± 6

Table 11.8: Decay fractions of the intermediate-state amplitudes contributing to decays via $b \to c$ and $b \to u$ quark-level transitions. The uncertainties are statistical, systematic (discussed in Section 11.4) and due to alternative models considered.

Decay Channel	$F^c[\%]$	$F^u[\%]$
$B_s \to D_s\,(K_1(1270) \to K\,\rho(770))$	12.3 ± 1.4 ± 1.3 ± 1.9	29.1 ± 6.1 ± 6.4 ± 6.2
$B_s \to D_s\,(K_1(1270) \to K^*(892)\,\pi)$	6.3 ± 1.6 ± 1.5 ± 0.8	14.9 ± 4.5 ± 4.2 ± 4.3
$B_s \to D_s\,(K_1(1270) \to K_0^*(1430)\,\pi)$	3.4 ± 0.5 ± 0.9 ± 0.5	8.0 ± 2.1 ± 2.5 ± 1.7
$B_s \to D_s\,(K_1(1400) \to K^*(892)\,\pi)$	48.3 ± 4.5 ± 6.8 ± 4.5	17.2 ± 8.6 ± 7.6 ± 6.4
$B_s \to D_s\,(K^*(1410) \to K^*(892)\,\pi)$	15.5 ± 1.0 ± 1.0 ± 1.1	
$B_s \to D_s\,(K^*(1410) \to K\,\rho(770))$	6.7 ± 0.6 ± 0.7 ± 0.5	
$B_s \to D_s\,(K(1460) \to K^*(892)\,\pi)$		21.0 ± 4.6 ± 4.0 ± 5.1
$B_s \to (D_s\,\pi)_P\ K^*(892)$	6.8 ± 1.5 ± 2.4 ± 2.3	36.0 ± 8.0 ± 10.1 ± 13.2
$B_s \to (D_s\,K)_P\ \rho(770)$		9.7 ± 4.0 ± 4.1 ± 3.5
Sum	99.3 ± 4.7 ± 6.8 ± 4.0	135.9 ± 12.9 ± 12.5 ± 11.7

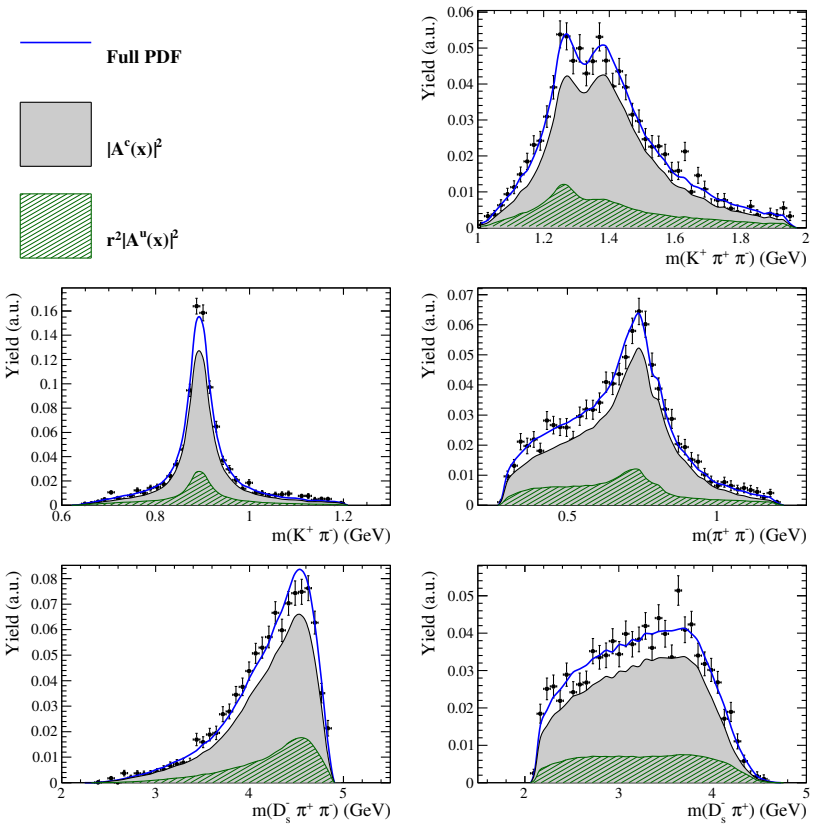

(a) Contributions from $b \to c$ and $b \to u$ decay amplitudes are overlaid.

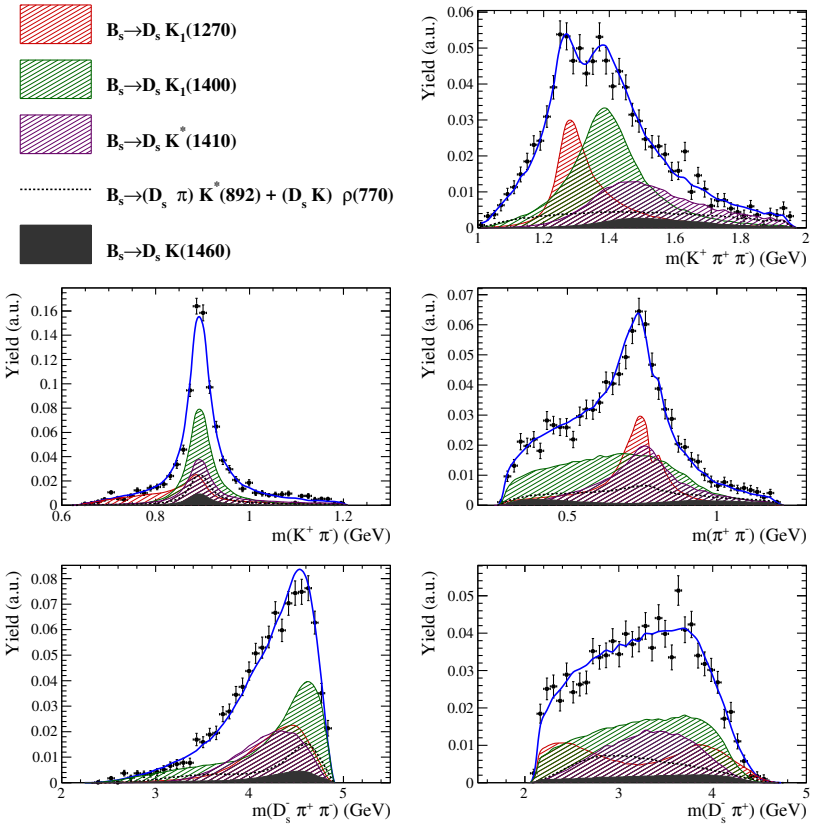

(b) Incoherent contributions from intermediate-state components are overlaid.

Figure 11.5: Invariant-mass distribution of background-subtracted $B_s \to D_s K\pi\pi$ candidates (data points) and fit projections (blue solid line).

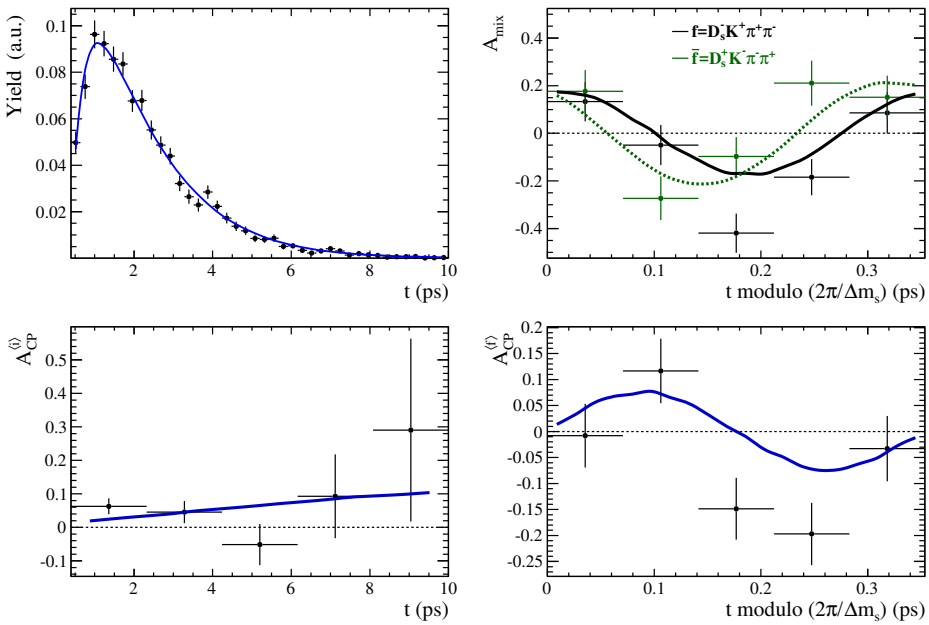

Figure 11.6: Decay-time distribution (top-left), mixing asymmetry (top-right) and time-dependent *CP* asymmetries (bottom) of background-subtracted $B_s \to D_s K\pi\pi$ candidates along with the projections of the time-dependent amplitude fit (blue solid line).

prefers the heavier state ($K_1(1400)$). A qualitatively consistent pattern is observed in $D^0 \to K^-\pi^+\pi^+\pi^-$ and $D^0 \to K^+\pi^-\pi^-\pi^+$ decays [191], where the axial vector resonances are produced by the spectator-quark and weak-current interaction, respectively.

Interference fractions of the $b \to c$ and $b \to u$ intermediate-state amplitudes are given in Tables E.8 and E.9. Sizable interference effects between the decay modes $B_s \to D_s\,(K_1(1270) \to K^*(892)\,\pi)$, $B_s \to D_s\,(K_1(1400) \to K^*(892)\,\pi)$ and $B_s \to (D_s\,\pi)_P\ K^*(892)$ (from $|I_{ij}| \approx 6\%$ to $|I_{ij}| \approx 20\%$) are observed since the overlap of their phase-space distributions is significant, see Figure 11.5b. Constructive and destructive interference effects of all amplitude components (21 interference fractions) approximately cancel each other (when integrated over the phase space) for $b \to c$ quark-level transitions, whereas a net destructive interference around -36% remains for $b \to u$ transitions.

The mass and width of the $K_1(1400)$ resonance determined from the fit(see Table 11.7) agree well with the PDG average values, $m^{PDG}_{K_1(1400)} = 1403 \pm 7\,\text{MeV}$ and $\Gamma^{PDG}_{K_1(1400)} = 174 \pm 13\,\text{MeV}$ [10], and their precision is competitive with the best single measurements. A good agreement is also observed for the measured mass of the $K^*(1410)$ meson ($m^{PDG}_{K^*(1410)} = 1421 \pm 9\,\text{MeV}$). The decay width is around 100 MeV larger than the PDG estimate ($\Gamma^{PDG}_{K^*(1410)} = 236 \pm 18\,\text{MeV}$), what corresponds to a deviation at the 2σ level. The PDG average value is dominated

by studies of decay modes where the $K^*(1410)$ meson decays to the $K\pi$ final state, for example $D^0 \to K_S^0 K^\pm \pi^\mp$ transitions [261]. The employed lineshape models considered only the partial decay width for this final state even though the branching fraction is no more than $\mathcal{B}(K^*(1410) \to K\pi) = (6.6 \pm 1.3)\%$ [10]. The measurement presented in this thesis is the first which takes the partial decay widths of both $K\pi\pi$ and $K\pi$ final states into account, see Appendix B.

Results for the ratio of the $B_s^0 \to D_s^- K^+\pi^+\pi^-$ and $\bar{B}_s^0 \to D_s^- K^+\pi^+\pi^-$ decay amplitudes (r) as well as their strong (δ) and weak phase ($\gamma - 2\beta_s$) difference are given in Table 11.7. They are discussed and compared to the results of the (model-independent) phase-space integrated fit in Section 11.5. Systematic uncertainties are discussed in the next section.

11.4 Systematic uncertainties

The systematic uncertainties on the measured observables are summarized in Table 11.9 for the decay-time fit to $B_s \to D_s\pi\pi\pi$, in Table 11.10 for the phases-space integrated fit to $B_s \to D_sK\pi\pi$ and in Table 11.11 for the time-dependent amplitude fit to $B_s \to D_sK\pi\pi$ decays. A description of each systematic effect is given in the following paragraphs starting with the ones common to all fits. Afterwards, systematic effects specific to the amplitude description are discussed.

Fit bias

Pseudo-experiments are performed, where MC event samples of the same size as the number of observed signal candidates are generated according to the nominal fit model and subsequently fitted with the same model. The means of the pull distributions are taken as systematic uncertainties, which are small ($\approx 0.1\sigma_{\text{stat}}$) with respect to the statistical uncertainties of the fit parameters. The width of the pull distributions are compatible with unity.

Background subtraction

The statistical subtraction of the residual background relies on the correct description of the reconstructed B_s mass distribution. Since the empirical choice of the employed PDFs is not unique, alternative parameterizations are tested for the signal and each background component [2]. To evaluate the possible source of systematic uncertainty arising from the fixed yields of the cross-feed contributions to the $B_s \to D_sK\pi\pi$ candidates estimated from a combination of simulated data and control modes (*cf.* Section 9.3), the yields are fixed to zero or doubled. In total nine (six) distinct combinations of the modifications discussed above are considered for the fit to the reconstructed mass distribution of $B_s \to D_sK\pi\pi$ ($B_s \to D_s\pi\pi\pi$) candidates. For each case, new sWeights are calculated and subsequently used in the fits to the decay-time (and phase-space) spectra. The standard deviation of the obtained differences to the nominal fit values are used as systematic uncertainty (between $0.2\sigma_{\text{stat}}$ and $0.5\sigma_{\text{stat}}$) due to the background subtraction.

Table 11.9: Systematic uncertainties on the fit parameters of the fit to $B_s \to D_s\pi\pi\pi$ data in units of statistical standard deviations.

Fit Parameter	Fit-bias	Background	Acceptance	Resolution	Asymmetries	Mom./z-Scale	Total
p_0^{OS} Run-I	0.05	0.09	0.00	0.99	0.01		1.00
p_1^{OS} Run-I	0.01	0.13	0.01	1.04	0.01		1.05
Δp_0^{OS} Run-I	0.14	0.03	0.15	0.02	0.00		0.21
Δp_1^{OS} Run-I	0.07	0.06	0.15	0.03	0.00		0.18
$\epsilon_{\text{tag}}^{OS}$ Run-I	0.06	0.17	0.01	0.00	0.00		0.18
$\Delta\epsilon_{\text{tag}}^{OS}$ Run-I	0.04	0.01	0.01	0.06	0.00		0.07
p_0^{SS} Run-I	0.03	0.03	0.00	0.56	0.01		0.56
p_1^{SS} Run-I	0.10	0.03	0.01	0.60	0.01		0.60
Δp_0^{SS} Run-I	0.04	0.01	0.10	0.00	0.00		0.11
Δp_1^{SS} Run-I	0.03	0.04	0.12	0.01	0.00		0.13
$\epsilon_{\text{tag}}^{SS}$ Run-I	0.02	0.02	0.01	0.00	0.00		0.04
$\Delta\epsilon_{\text{tag}}^{SS}$ Run-I	0.04	0.03	0.01	0.05	0.00		0.07
p_0^{OS} Run-II	0.02	0.20	0.00	0.93	0.02		0.96
p_1^{OS} Run-II	0.02	0.08	0.00	0.70	0.01		0.70
Δp_0^{OS} Run-II	0.07	0.08	0.00	0.02	0.00		0.11
Δp_1^{OS} Run-II	0.02	0.03	0.00	0.02	0.00		0.04
$\epsilon_{\text{tag}}^{OS}$ Run-II	0.01	0.16	0.00	0.00	0.00		0.16
$\Delta\epsilon_{\text{tag}}^{OS}$ Run-II	0.05	0.05	0.00	0.01	0.00		0.07
p_0^{SS} Run-II	0.10	0.06	0.00	0.60	0.01		0.62
p_1^{SS} Run-II	0.01	0.07	0.00	0.64	0.02		0.64
Δp_0^{SS} Run-II	0.07	0.02	0.00	0.02	0.00		0.08
Δp_1^{SS} Run-II	0.11	0.05	0.00	0.02	0.00		0.12
$\epsilon_{\text{tag}}^{SS}$ Run-II	0.03	0.03	0.00	0.00	0.00		0.04
$\Delta\epsilon_{\text{tag}}^{SS}$ Run-II	0.01	0.03	0.00	0.10	0.00		0.11
A_P Run-II	0.04	0.02	0.01	0.06	0.00		0.08
Δm_s	0.01	0.11	0.02	0.16	0.00	0.67	0.69

Table 11.10: Systematic uncertainties on the fit parameters of the phase-space integrated fit to $B_s \to D_s K\pi\pi$ data in units of statistical standard deviations.

Fit Parameter	Fit bias	Background	Acceptance	Resolution	Asymmetries	Δm_s	Total
C	0.15	0.03	0.06	0.04	0.15	0.06	0.23
D	0.00	0.18	0.10	0.04	0.01	0.01	0.21
$\bar{D}$	0.05	0.20	0.13	0.04	0.02	0.01	0.24
S	0.05	0.01	0.06	0.04	0.07	0.10	0.15
$\bar{S}$	0.07	0.02	0.03	0.04	0.05	0.10	0.14

Decay-time acceptance

The systematic uncertainties related to the decay-time acceptance as well as due to the limited experimental knowledge of Γ_s and $\Delta\Gamma_s$ are studied simultaneously as they are strongly correlated. The correlation between Γ_s and $\Delta\Gamma_s$ (which are fixed to the world-average values [35] in the nominal fit) is taken from Reference [35], whereas the correlation among the decay-time acceptance parameters is determined in the fit procedure described in Section 10.2. To obtain the correlation between Γ_s and the spline coefficients v_i, new sets of acceptance parameters are determined by varying the value of Γ_s by plus one (v_i^+) and minus one standard deviation (v_i^-). The correlation matrix is then computed as $\mathrm{corr}(\Gamma_s, v_i) = (v_i^+ - v_i^-)/(2\,\sigma_{v_i})$, where σ_{v_i} is the nominal statistical uncertainty of the parameter v_i. An analog procedure determines $\mathrm{corr}(\Delta\Gamma_s, v_i)$.

Pseudo-data sets are generated assuming the nominal configuration and subsequently fitted under both this nominal configuration and a configuration in which the acceptance parameters together with Γ_s and $\Delta\Gamma_s$ are randomized within their uncertainties (taking their correlation into account). For each pseudo-experiment, a pull is calculated by dividing the difference between the fitted values of the nominal and alternative (randomized) configurations by the nominal statistical uncertainty. The bias of the mean of the resulting pull distribution is added in quadrature to the pull width in order to arrive at the final systematic uncertainty (which is negligible with respect to the statistical uncertainty).

Decay-time resolution and flavor tagging

Systematic effects originating from the calibration of the decay-time error estimate are studied with two alternative approaches which either slightly overestimate or underestimate the decay-time resolution. The first approach performs a fit to the decay-time distributions of fake B_s candidates using the sum of two Gaussian

Table 11.11: Systematic uncertainties on the fit parameters of the full time-dependent amplitude fit to $B_s \to D_s K\pi\pi$ data in units of statistical standard deviations.

Fit Parameter	Fit bias	Background	Time-Acc.	Resolution	Asymmetries	Δm_s	Phsp-Acc.	Lineshapes	Resonances m, Γ	Form-Factors	Amp. Model	Total
$B_s \to D_s\,(K_1(1270) \to K^*(892)\,\pi)$ Mag	0.10	0.12	0.01	0.03	0.00	0.01	0.07	0.44	0.22	0.47		0.70
$B_s \to D_s\,(K_1(1270) \to K^*(892)\,\pi)$ Phase	0.07	0.09	0.01	0.04	0.01	0.01	0.26	0.35	0.32	0.38		0.68
$B_s \to D_s\,(K_1(1270) \to K_0^*(1430)\,\pi)$ Mag	0.04	0.23	0.00	0.01	0.00	0.00	0.05	1.00	0.10	0.16		1.04
$B_s \to D_s\,(K_1(1270) \to K_0^*(1430)\,\pi)$ Phase	0.04	0.13	0.00	0.02	0.00	0.00	0.05	3.01	0.13	0.43		3.05
$B_s \to D_s\,(K_1(1400) \to K^*(892)\,\pi)$ Mag$(b \to c)$	0.13	0.15	0.01	0.08	0.01	0.03	0.14	0.51	0.17	0.36		0.69
$B_s \to D_s\,(K_1(1400) \to K^*(892)\,\pi)$ Phase$(b \to c)$	0.14	0.17	0.01	0.09	0.01	0.02	0.25	0.44	0.25	0.40		0.73
$B_s \to D_s\,(K_1(1400) \to K^*(892)\,\pi)$ Mag$(b \to u)$	0.10	0.26	0.03	0.04	0.03	0.09	0.21	0.28	0.17	0.59		0.77
$B_s \to D_s\,(K_1(1400) \to K^*(892)\,\pi)$ Phase$(b \to u)$	0.02	0.08	0.04	0.03	0.03	0.09	0.23	0.55	0.20	0.28		0.70
$B_s \to D_s\,(K^*(1410) \to K^*(892)\,\pi)$ Mag$(b \to c)$	0.08	0.10	0.02	0.04	0.01	0.04	0.57	0.31	0.14	0.43		0.81
$B_s \to D_s\,(K^*(1410) \to K^*(892)\,\pi)$ Phase$(b \to c)$	0.35	0.11	0.01	0.05	0.01	0.01	0.09	0.41	0.16	0.58		0.83
$B_s \to D_s\,(K^*(1410) \to K\,\rho(770))$ Mag	0.35	0.13	0.01	0.01	0.00	0.01	0.07	0.41	0.08	0.24		0.61
$B_s \to D_s\,(K^*(1410) \to K\,\rho(770))$ Phase	0.18	0.25	0.00	0.01	0.00	0.01	0.15	0.34	0.09	0.22		0.54
$B_s \to D_s\,(K(1460) \to K^*(892)\,\pi)$ Mag$(b \to u)$	0.14	0.27	0.03	0.04	0.02	0.04	0.09	0.32	0.20	0.44		0.66
$B_s \to D_s\,(K(1460) \to K^*(892)\,\pi)$ Phase$(b \to u)$	0.13	0.14	0.03	0.07	0.02	0.04	0.05	0.53	0.34	0.32		0.74
$B_s \to (D_s\,\pi)_P\; K^*(892)$ Mag$(b \to c)$	0.03	0.21	0.01	0.05	0.01	0.02	0.17	0.71	0.10	0.49		0.91
$B_s \to (D_s\,\pi)_P\; K^*(892)$ Phase$(b \to c)$	0.20	0.31	0.01	0.08	0.01	0.01	0.30	0.58	0.11	0.32		0.82
$B_s \to (D_s\,\pi)_P\; K^*(892)$ Mag$(b \to u)$	0.14	0.08	0.03	0.05	0.01	0.05	0.21	0.50	0.17	0.38		0.71
$B_s \to (D_s\,\pi)_P\; K^*(892)$ Phase$(b \to u)$	0.24	0.22	0.02	0.09	0.01	0.03	0.23	0.70	0.13	0.28		0.87
$B_s \to (D_s\,K)_P\; \rho(770)$ Mag$(b \to u)$	0.35	0.23	0.03	0.02	0.02	0.05	0.22	0.53	0.28	0.54		0.93
$B_s \to (D_s\,K)_P\; \rho(770)$ Phase$(b \to u)$	0.12	0.54	0.02	0.04	0.01	0.05	0.10	0.37	0.31	0.53		0.91
$m_{K_1(1400)}$	0.09	0.15	0.01	0.08	0.01	0.01	0.25	0.22	0.14	0.40	0.80	0.98
$\Gamma_{K_1(1400)}$	0.01	0.11	0.01	0.01	0.01	0.01	0.14	0.37	0.10	0.35	0.50	0.74
$m_{K^*(1410)}$	0.05	0.07	0.01	0.01	0.00	0.01	0.21	0.23	0.04	1.19	0.59	1.37
$\Gamma_{K^*(1410)}$	0.25	0.13	0.00	0.01	0.00	0.01	0.08	0.14	0.04	1.29	0.65	1.48
r	0.11	0.31	0.03	0.06	0.02	0.08	0.33	0.39	0.08	0.17	0.52	0.83
δ	0.19	0.10	0.04	0.07	0.05	0.10	0.10	0.29	0.03	0.11	0.53	0.67
$\gamma - 2\beta_s$	0.10	0.13	0.07	0.13	0.02	0.07	0.04	0.28	0.03	0.11	0.42	0.56

functions, but (in contrast to the nominal method) only the width of the core Gaussian function is considered to represent the decay-time resolution. This reduces the average decay-time resolution $\langle\sigma_t\rangle$ by about 6 fs. Second, a single Gaussian function is used in which case the average resolution increases by about 3 fs. Due to the high correlation between the decay-time resolution and the calibration of the flavor taggers, their systematic uncertainty must be studied simultaneously. As a first step, the decay-time fit to the $B_s \to D_s\pi\pi\pi$ candidates is repeated using the alternative decay-time error calibration functions. New tagging calibration parameters are obtained (where deviations up to $1.0\sigma_{\text{stat}}$ are observed, see Table 11.9) which are then used (together with the respective decay-time error calibration function) for the fits to the $B_s \to D_sK\pi\pi$ candidates. The largest deviations of the central values from their nominal values are assigned as systematic uncertainty for each fit parameter. These are small ($\approx 0.1\sigma_{\text{stat}}$) with respect to the statistical uncertainty, see Tables 11.10 and 11.11.

Nuisance asymmetries and mixing frequency

The systematic uncertainty from the production and detection asymmetries and Δm_s (in case of $B_s \to D_sK\pi\pi$ decays) which are fixed in the fit are evaluated by means of pseudo-experiments, identical to the procedure performed for the decay-time acceptance. The parameters are assumed to be uncorrelated. The resulting systematic uncertainties are small ($\approx 0.1\sigma_{\text{stat}}$) with respect to the statistical uncertainty.

Length and momentum scales

The precision with which the B_s flight distance (and therefore the decay time) can be determined is limited by the knowledge of the overall length of the VELO detector and the position of the individual VELO modules. This z-scale uncertainty has been estimated to be at most 0.02% [142], which translates directly in a relative uncertainty on Δm_s of 0.02% with other parameters being unaffected. Similar, the momentum-scale uncertainty leads to a relative uncertainty on Δm_s of not more than 0.02% [142]. Together the uncertainties associated with the length and momentum scale of the detector are the dominant contribution to the systematic uncertainty on Δm_s ($0.7\sigma_{\text{stat}}$).

In the fit to the $B_s \to D_sK\pi\pi$ candidates, the length and momentum scale uncertainties are then implicitly included in the systematic error due to the Δm_s uncertainty described above.

Phase-space acceptance

The treatment of the phase-space acceptance relies on simulated data. The integration error due to the limited size of the MC sample used to normalize the signal PDF is below 0.2% and thus negligible small. To assess the uncertainty due to possible data-simulation differences, alternative phase-space acceptances are derived by varying the selection requirements (for the simulated sample only) on quantities that are expected not to be well described by the simulation. In particular, the following variations are considered:

- no (or a tighter) selection requirement on the multivariate classifier (trained against combinatorial background) is imposed;
- the simulated sample is reweighted to match the p_T and η distribution observed for B_s signal candidates from real data;
- the simulated PID variables are corrected in a data-driven way using $D^{*+} \to (D^0 \to K^-\pi^+)\,\pi^+$ decays as control sample (similar to the procedure to estimate the cross-feed yields discussed in Section 9.3);
- a tight cut on the B_s transverse momentum is applied ($p_T > 10\,\text{GeV}$);
- instead of the nominal trigger strategy (L0-TOS || L0-TIS), only candidates fulfilling the L0-TOS (L0-TIS) trigger requirement are used.

The standard deviation of the fit results using these alternative phase-space acceptances is taken as systematic uncertainty, which ranges from $0.1\sigma_{\text{stat}}$ to $0.6\sigma_{\text{stat}}$ depending on the fit parameter (see Table 11.11).

Resonance description

For the resonances $\rho(770)^0 \to \pi^+\pi^-$ and $K_0^*(1430)^0 \to K^+\pi^-$ more sophisticated lineshape parameterizations are used, see Appendix B. They are replaced by a relativistic Breit-Wigner propagator (Equation 2.19) as part of the systematic studies. Moreover, energy-dependent decay widths of three-body resonances are recomputed taking only the dominant $K\pi\pi$ decay mode into account. For each alteration, a time-dependent amplitude fit is performed and the standard deviation of the obtained fit results is assigned as systematic uncertainty (Table 11.11, *Lineshapes*). These are generally around half of the statistical uncertainty. A larger systematic uncertainty is observed for the magnitude and phase of the $B_s \to D_s\,(K_1(1270) \to K_0^*(1430)\,\pi)$ amplitude coefficient ($1\sigma_{\text{stat}}$ and $3\sigma_{\text{stat}}$) due to the specific choice of lineshape parameterization for the $K_0^*(1430)^0$ resonance (see Appendix B).

Systematic uncertainties due to fixed resonance masses and widths (given in Table B.1) are computed with the same procedure used for the other fixed parameters (nuisances asymmetries etc.) mentioned above. They are small ($\approx 0.2\sigma_{\text{stat}}$) with respect to the statistical uncertainty (Table 11.11, *Resonances* m, Γ).

Similarly, pseudo-experiments are performed in which the Blatt-Weisskopf radial parameter (set to $r_{BW} = 1.5\,\text{GeV}^{-1}$ by default) is varied uniformly within the interval $[0, 3]\,\text{GeV}^{-1}$ to assign a systematic uncertainty due to the form-factor modeling. This is the dominant contribution to the systematic uncertainty (slightly larger than the statistical uncertainty) on the mass and width of the $K^*(1410)$ meson. For the other fit parameters, the systematic uncertainty ranges from $0.1\sigma_{\text{stat}}$ to $0.6\sigma_{\text{stat}}$.

Alternative amplitude models

Several modifications to the LASSO model are tested to assign an additional uncertainty due to the choice of amplitude components:

- all amplitudes selected by the first stage of the model selection are included for both $b \to c$ and $b \to u$ transitions;
- the amplitudes with the smallest decay fraction are removed;
- additional subdecay modes of selected three-body resonances are considered;
- higher orbital angular momentum states are included where applicable;
- the orbital angular momentum state of non-resonant two-body states is set to other allowed values;
- additional cascade and quasi two-body amplitudes (which were removed by the first stage of the model selection) are considered.

In total twelve amplitude models with similar fit quality as the baseline model are identified. The fit results for those are summarized in Tables E.10 and E.11. The standard deviation of the results is taken as model uncertainty. The model uncertainty is the largest systematic uncertainty for the physical observables r, δ and $\gamma - 2\beta_s$ (between $0.4\sigma_{\text{stat}}$ and $0.8\sigma_{\text{stat}}$) and for the mass and width of the $K_1(1400)$ meson ($0.7\sigma_{\text{stat}}$), see Table 11.11 (*Amp. Model*). In case of the decay fractions, the model uncertainty is comparable to the statistical uncertainty (see Table 11.8). No model uncertainty is assigned to the amplitude coefficients since they are, by definition, parameters of a given model.

11.5 Interpretation of the results

To interpret the parameters determined in the model-independent fit, $P_{\text{obs}} \equiv (C, D, \bar{D}, S, \bar{S})$, in terms of the physical observables $\Lambda \equiv (r, \kappa, \delta, \gamma - 2\beta_s)$, the set of Equations in 3.17 expressing the *CP* coefficients as function of Λ, $P(\Lambda)$, need to be inverted. This is accomplished by minimizing the following likelihood function:

$$-2\mathcal{L}(\Lambda) = -2 \exp\left(-\frac{1}{2}(P(\Lambda) - P_{\text{obs}})^T V^{-1} (P(\Lambda) - P_{\text{obs}})\right), \tag{11.3}$$

as implemented in the GammaCombo [262, 263] tool. Here, V denotes the experimental (statistical and systematic) covariance matrix of the measured observables. To evaluate the confidence level of a certain parameter, say r, at a given value (r'), the likelihood difference with respect to the global minimum is computed: $\Delta\chi^2 \equiv -2\mathcal{L}(\Lambda') + 2\mathcal{L}(\Lambda_{\text{min}}) \geq 0$, where Λ_{min} denotes the parameter set at the global minimum and Λ' denotes the parameter set obtained when fixing the parameter r to $r = r'$. The p-value ($p \equiv 1 - \text{CL}$) is then given by the probability that the observed $\Delta\chi^2$ value is exceeded assuming a χ^2-distribution with one degree of freedom [79, 262]. Figure 11.7 displays the $1 - \text{CL}$ contours for the physical parameters Λ obtained from the model-independent method. The $1 - \text{CL} = 68.3\%$ (1σ) confidence intervals are given in Table 11.12 together with the results of the full time-dependent amplitude analysis. The coherence factor for the latter method is computed by numerically integrating over the phase space using the LASSO model (*cf.* Equation 3.18).

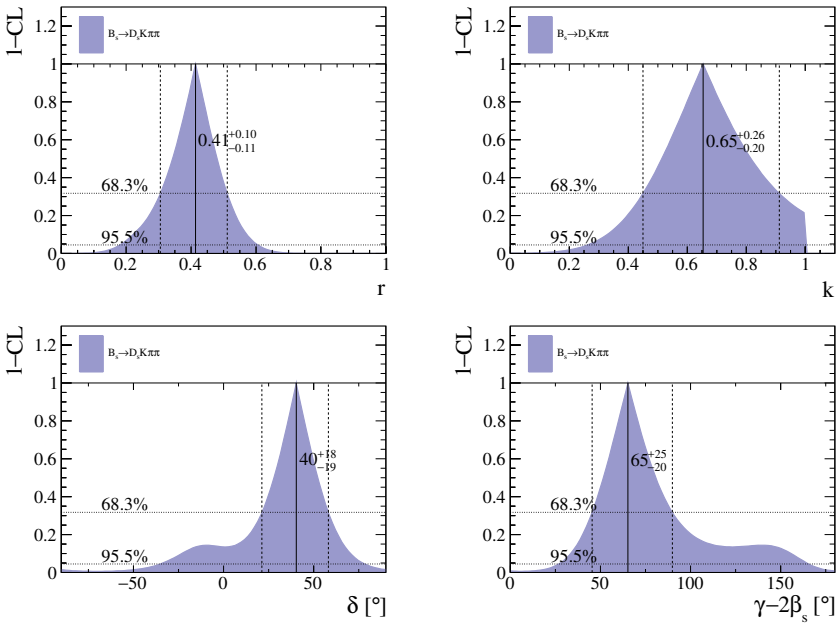

Figure 11.7: The 1-CL contours for the physical observable r, κ, δ and γ obtained with the model-independent fit.

Table 11.12: Parameters determined from the phase-space integrated (model-independent) and time-dependent amplitude fit (model-dependent) fit to the $B_s \to D_s K\pi\pi$ signal candidates. Statistical and systematic uncertainties are combined.

Parameter	Model-independent	Model-dependent	Difference [$\Delta\sigma$]
r	$0.41^{+0.10}_{-0.11}$	0.50 ± 0.05	1.0
κ	$0.65^{+0.26}_{-0.20}$	0.52 ± 0.11	0.6
δ [°]	40^{+18}_{-19}	46 ± 18	0.4
$\gamma - 2\beta_s$ [°]	65^{+25}_{-20}	61 ± 17	0.3

The precision of the phase-space integrated (model-independent) method is completely statistically limited. The time-dependent amplitude fit (model-dependent) reduces the statistical uncertainty by more than a factor two and three for the parameters r and κ, respectively. At the same time, the statistical precision of the strong and weak phase difference is improved by around 5°. The additional uncertainty originating from the amplitude modeling compensates the gained sensitivity to some extent. However, the total uncertainty is still statistically limited and superior to the one of the model-independent method. In case of the weak phase difference, the reduction of the total uncertainty with the model-dependent method is considerable but could have been much larger. In preliminary sensitivity studies performed with pseudo-experiments [2], the statistical uncertainty of the model-independent method was estimated to be between 20° and 50° by varying the coherence factor from 0.7 to 0.3 (the other parameters were chosen to be $r = 0.4$, $\delta = 10°$ and $\gamma - 2\beta_s = 70°$). The precision of the time-dependent amplitude fit, on the other hand, was estimated to be 17°, (almost) independent of the coherence factor of the amplitude model. The model-independent result ($\kappa = 0.65^{+0.26}_{-0.20}$) is close to the best case scenario considered in this study ($\kappa = 0.7$) and might be a fortunate upward fluctuation given that the model-dependent result is $\kappa = 0.52 \pm 0.06\,(\text{stat}) \pm 0.06\,(\text{syst}) \pm 0.08(\text{model})$.

As the results are obtained from the same data set, the comparison of the central values is more involved. A measure of their compatibility is defined as follows: first, the quadratic difference of the statistical uncertainties of both fits is computed: $\Delta\sigma_{\text{stat}} \equiv \sqrt{(\sigma^{\text{MI}}_{\text{stat}})^2 - (\sigma^{\text{MD}}_{\text{stat}})^2}$, where $\sigma^{\text{MI}}_{\text{stat}}$ is the statistical uncertainty of the model-independent method and $\sigma^{\text{MD}}_{\text{stat}}$ is the statistical uncertainty of the time-dependent amplitude fit. Second, the model-dependent uncertainty (including resonance lineshapes, form factors and alternative amplitude models) of the time-dependent amplitude fit, $\sigma^{\text{MD}}_{\text{model}}$, is added in quadrature to $\Delta\sigma_{\text{stat}}$ since the model-independent

fit is not impacted by these effects. The remaining systematic uncertainties (including time-acceptance, resolution, flavor tagging, etc.) are assumed to be 100% correlated between the two fit methods such that their effect should cancel. A good consistency of the methods is observed as the obtained results agree within a range of 0.3 to 1.0 $\Delta\sigma$ (see Table 11.12), with $\Delta\sigma \equiv \sqrt{\Delta\sigma^2_{\text{stat}} + (\sigma^{\text{MD}}_{\text{model}})^2}$.

The measured ratio of the $b \to u$ and $b \to c$ decay amplitudes is qualitatively consistent with the naive expectation based on the involved CKM elements ($r \approx 0.4$). Note that the parameters r, κ and δ are determined in a limited phase-space region ($m(K\pi\pi) < 1.95\,\text{GeV}$, *cf.* Section 9.2) and might differ when the full phase space is considered. To determine the CKM angle γ from the measured weak phase difference $\gamma - 2\beta_s$, it is assumed that the mixing phase $-2\beta_s$ is equivalent to $\phi_s = (-1.20 \pm 1.78)^\circ$ [35]. Within uncertainties an excellent agreement with the world-average value, the indirect determination of the CKMfitter group and the loop-level measurement is observed as shown in Table 11.13. The presented (tree-level) measurement is only the second in the B_s meson system, where previously a slight tension (up to almost 3σ) with other measurements was found. While the precision of the phase-space integrated fit is modestly worse than the sensitivity obtained from $B_s \to D_s K$ decays, the uncertainty of the time-dependent amplitude fit is a few degrees smaller. This is an impressive result, given that the analysis is significantly more complex and the $B_s \to D_s K$ signal yield is 20% higher (only Run-I data was used [141]).

Table 11.13: Measurements of the CKM angle γ.

Measurement	$\gamma[^\circ]$
$B_s \to D_s K\pi\pi$ (model-independent)	64^{+25}_{-20}
$B_s \to D_s K\pi\pi$ (model-dependent)	60 ± 17
World-average (tree-level) [30]	$72.1^{+5.4}_{-5.7}$
Indirect (CKMfitter [30])	$65.64^{+0.97}_{-3.42}$
Loop-level [104]	$63.5^{+7.2}_{-6.7}$
$B_s \to D_s K$ [141]	128^{+18}_{-22}

Part IV

SUMMARY AND IMPLICATIONS

Towards a precision measurement of the Unitarity Triangle

Several hadronic multi-body decays are investigated in this dissertation. The resonant substructures of the decays $D \to \pi\pi\pi\pi$ and $B_s \to D_s K\pi\pi$ are studied by means of an amplitude analysis, which disentangles the various intermediate-state components. For this purpose, the spin-dependent angular distributions of the final-state particles are calculated in a refined covariant tensor formalism [1,61–64], improving over previously used approaches [144,170,176,264,265] to the effect that orthogonal spin-states are produced. Advanced lineshape parameterizations for cascade decays are implemented which take the resonant three-body substructure and partial decay widths to additional final states into account. To limit the model complexity, caused by the abundance of potential intermediate-state amplitudes, the LASSO [180, 182] regularization procedure is applied to $D \to \pi\pi\pi\pi$ and $B_s \to D_s K\pi\pi$ decays (for the first time in context of amplitude analyses). For $B_s \to D_s K\pi\pi$ decays, a two stage model building procedure is developed to cope with the unprecedented challenge of determining two amplitude models simultaneously; one for decays via $b \to c$ quark-level transitions, the other for decays via $b \to u$ transitions.

The light axial vector resonances are identified as prominent contributions: $D \to a_1(1260)\pi \to \pi\pi\pi\pi$, $B_s \to D_s K_1(1400) \to D_s K\pi\pi$ ($b \to c$) and $B_s \to D_s K_1(1270) \to D_s K\pi\pi$ ($b \to u$). The mass and width of the pseudoscalar $\pi(1300)$, the vector $K^*(1410)$ and the axial vector mesons $a_1(1260), a_1(1640)$ and $K_1(1400)$ are determined. All results are among the most precise single measurements to date.

Beyond hadron spectroscopy, the intrinsic sensitivity to phases makes amplitude analyses particularly attractive to study *CP*-violating effects. An amplitude model for $D \to \pi\pi\pi\pi$ decays distinguishing between the initial flavor of the charm meson is presented for the first time [1]. The full CLEO-c legacy data set corresponding to an integrated luminosity of $818\,\mathrm{pb}^{-1}$ is used. No evidence for the breaking of *CP* symmetry in the amplitude components is found at the

level of a few percent. The fractional *CP*-even content of the decay and the average strong phase difference between D^0 and $\bar{D}^0$ decays in certain regions of phase space are calculated from the amplitude model. These hadronic parameters are found to be in good agreement with model-independent measurements exploiting quantum-entangled $D^0\bar{D}^0$ pairs [124]. This gives confidence in the chosen amplitude parameterization. Statistical and systematic uncertainties of the amplitude-model parameters are on a comparable scale. The statistical precision could be improved by analyzing the copious amount of charm mesons collected at the LHCb experiment, this would however demand an increase in model complexity. To some extent the systematic uncertainties can also be reduced with additional statistics, for example lineshape parameters which are currently fixed to the world-average values could be determined more precisely. A promising method to improve the robustness of the amplitude model involves simultaneous analyses of several decay modes which share resonant subsystems. For example, the decay channels $D \to \pi\pi\pi\pi$, $D \to K\pi\pi\pi$, $B_d \to D\pi\pi\pi$ and $B_s \to D_s\pi\pi\pi$ all have the three-pion subsystem in common. With increased statistical precision, the assumptions of the isobar model will eventually break down. To improve the phenomenological description of hadronic decay processes, additional constraints from theory such as unitarity [266,267] or crossing symmetry [268] of the scattering matrix [4,54] (which relates initial and final states and from which decay rates and cross-sections derive) should explicitly be built into the formalism. Rescattering effects [269–271] need to be accounted for. The form factor parameterization should be revisited as the Blatt-Weisskopf barrier factors are derived from non-relativistic quantum-mechanics and spoil the otherwise covariant amplitude formalism. The discovery of tetraquark and pentaquark candidates has triggered a resurgence of interest in hadron spectroscopy also in the theory community. Among many other possible interpretation of these states, rescattering effects have been suggested to be responsible for the observed structures [272, 273]. Theoretical work on these specific cases may lead to more general approaches which improve the amplitude analysis formalism substantially. The statistically limited model-independent measurement of the hadronic parameters could be improved with currently existing and future BES-III data sets. The presented results are vital input for a future determination of the CKM angle γ from direct *CP* violation in $B^\pm \to (D \to \pi\pi\pi\pi)K^\pm$ decays, where a sensitivity competitive with the current most precise single measurement is expected.

The phenomenon of neutral meson mixing is studied in the B_s system using $7\,\text{fb}^{-1}$ of proton-proton collision data recorded by the LHCb detector [2]. First, the B_s^0-$\overline{B}_s^0$ mixing frequency is measured from flavor specific $B_s \to D_s\pi\pi\pi$ decays to be:

$$\Delta m_s = (17.7651 \pm 0.0084 \pm 0.0058)\,\text{ps}^{-1},$$

where the precision surpasses the current world-average value [10] by more than a factor two. Note that the selection strategy was optimized to study the decay channel $B_s \to D_sK\pi\pi$. A dedicated study of $B_s \to D_s\pi\pi\pi$ decays could increase the signal yield by at least 10%. As the statistical uncertainty approaches the systematic uncertainty, new methods to calibrate the length and momentum scale of the LHCb detector need to be developed to further improve the precision of future measurements. The decay mode $B_s \to D_s\pi\pi\pi$ is also of interest for hadron spectroscopy. In analogy to $B_s \to D_sK\pi\pi$ decays, a prominent contribution from the light axial vector meson $a_1(1260)$ is expected. The large phase space of the decay would allow to investigate the hadronic spectrum contributing to the tri-pion system up to 3.4 GeV (in contrast to 1.7 GeV for $D \to \pi\pi\pi\pi$ decays) and to search for new resonances in the $D_s^-\pi^+\pi^-$, $D_s^-\pi^+$ or $D_s^-K^+$ subsystems.

The first time-dependent amplitude analysis of $B_s \to D_sK\pi\pi$ decays is presented. Evidence for mixing-induced *CP* violation is reported with a statistical significance of 3.5 standard deviations. The *CP*-violating weak phase $\gamma - 2\beta_s$ is extracted and subsequently used to determine the CKM angle γ by taking the mixing phase, $-2\beta_s$, as external input. With a total uncertainty of 17°, the obtained result,

$$\gamma = (60 \pm 15\,(\text{stat}) \pm 6\,(\text{syst}) \pm 6(\text{model}))^\circ,$$

represents the most precise measurement in the B_s meson system to date [141]. The measurement is performed in the low $K\pi\pi$ invariant mass region since the exited kaon spectrum above 2 GeV is not well understood experimentally. A simultaneous analysis with, for example, the decay modes $B_d \to D_sK\pi\pi$ and $B_u \to J/\psi K\pi\pi$ might allow to reliably model the full phase space. An alternative model-independent approach confirms the measured observables with a reduced statistical precision but free of model uncertainties related to the amplitude parameterization. In any case, the measurement of time-dependent *CP* asymmetries is currently statistically limited, in a large part due to the need to

determine the B_s production flavor. It is not expected that the flavor-tagging algorithms will improve significantly in the future. The measurement will thus profit from the additional $2\,\text{fb}^{-1}$ of data collected in 2018 by the LHCb detector and from future LHCb or Belle-II data sets. Unless amplitude analysis techniques improve significantly (see discussion above) and model uncertainties related to the choice of intermediate-state components or lineshape and form factor parameterizations can be reduced, the phase-space integrated fit will become the method of choice when a statistical uncertainty of a few degrees is reached for the CKM angle γ. Here, it might be possible to enhance the sensitivity by performing the analysis in several bins of phase space, similar to the model-unbiased method to measure the CKM angle γ from $B^\pm \to DK^\pm$ decays. To design and optimize such a strategy, the amplitude model determined in this thesis will be critical.

Both the measurement of the B_s^0-$\overline{B}_s^0$ mixing frequency and the CKM angle γ are important pieces of the Standard Model puzzle. The former allows to extract the ratio of the V_{td} and V_{ts} CKM matrix elements:

$$\left|\frac{V_{td}}{V_{ts}}\right| = \varepsilon \sqrt{\frac{m_{B_s}}{m_{B_d}} \frac{\Delta m_d}{\Delta m_s}} = 0.2065 \pm 0.0043,$$

with $m_{B_s}/m_{B_d} = 1.0165 \pm 0.0054$ [10], $\Delta m_d = 0.5065 \pm 0.0019\,\text{ps}^{-1}$ [35] and $\varepsilon = 1.213 \pm 0.024$ [30] as input. To improve the result further, the $B^0 - \bar{B}^0$ mixing frequency and, in particular, the constant ε (computed from lattice QCD) need to be determined more precisely.

Thanks to the combination of plenty of decay modes and advanced analysis techniques, an impressive overall precision on the CKM angle γ has been achieved. The measurement in $B_s \to D_s K\pi\pi$ decays and a future model-unbiased measurement in $B^\pm \to (D \to \pi\pi\pi\pi)K^\pm$ decays will add to that. With the Run-III data-taking period (2021-2024), the combination of LHCb results (with an expected integrated luminosity of $23\,\text{fb}^{-1}$ [206]) will enter the high precision region ($\mathcal{O}(1°)$ [206]) where discrepancies between direct measurement and indirect CKM prediction may be observed. An ultimate precision at the sub-degree level is achievable by the end of the LHCb experiment ($300\,\text{fb}^{-1}$ [206]). It remains thrilling to see whether new phenomena beyond the established theory can be uncovered or if the Standard Model triumphs.

The presented analyses are among the most complex performed so far at the LHCb and CLEO-c experiments and lay the foundation for similar studies. Some of the techniques and tools developed in context of the $D \to \pi\pi\pi\pi$ amplitude analysis have already been applied to analyze $D \to KK\pi\pi$ [184] and $D \to K\pi\pi\pi$ [191] decays at the LHCb experiment. In the same way, the generic implementation of the time-dependent amplitude fit allows a straightforward application to related analyses. These include for example the determination of the CKM phases $\gamma + 2\beta$ from $B_d \to D^- K^0_S \pi^+$ [274] or α from $B_d \to \pi\pi\pi\pi$ [275] decays as well as studies of charm mixing in four-body decays [129, 276–279]. The latter would be an intriguing synergy of the two analyses performed for this dissertation and would permit a measurement the charm mixing parameters, where so far only a non-zero decay-width difference is observed [35].

Spin Amplitudes

A

All spin factors relevant for $D \to \pi\pi\pi\pi$ and $B_s \to D_s K\pi\pi$ decays are given in Table A.1. A general method how to calculate them is outlined in the following. First, the spin-2 equivalents to the tensors introduced in Section 2.2 need to be defined. Starting with the spin-2 polarization tensors. They can be obtained by coupling two spin-1 states to a spin-2 state:

$$\varepsilon^{\mu\nu}(p,\lambda) = \sum_{\lambda_1,\lambda_2} \langle 1\,\lambda_1, 1\,\lambda_2 | 2\,m\rangle\, \varepsilon^{\mu}(p,\lambda_1)\, \varepsilon^{\nu}(p,\lambda_2) \tag{A.1}$$

where $\langle 1\,\lambda_1, 1\,\lambda_2|2\,\lambda\rangle$ are the *Clebsch-Gordon* coefficients [4]. By construction, they are symmetric, traceless and orthogonal to p. In other words, they fulfill the spin-2 Rarita-Schwinger conditions [65]:

$$p^{\mu}\,\varepsilon_{\mu\nu}(p,\lambda) \quad = 0, \quad \varepsilon_{\mu\nu}(p,\lambda) = \varepsilon_{\nu\mu}(p,\lambda), \quad g^{\mu\nu}\,\varepsilon_{\mu\nu}(p,\lambda) \quad = 0\,, \tag{A.2}$$

which reduce the sixteen elements of the rank-2 tensor $\varepsilon^{\mu\nu}(p,\lambda)$ to five independent elements corresponding to the polarization states $\lambda = \{0, \pm 1, \pm 2\}$. Similar than its spin-1 counterpart, the spin-2 projection operator, given by

$$\begin{aligned} P_{(2)}^{\mu\nu\alpha\beta}(p) &= \sum_{\lambda} \varepsilon^{\mu\nu}(p,\lambda)\, \varepsilon^{*\alpha\beta}(p,\lambda) \\ &= \frac{1}{2}\left(P_{(1)}^{\mu\alpha}(p)\, P_{(1)}^{\nu\beta}(p) + P_{(1)}^{\mu\beta}(p)\, P_{(1)}^{\nu\alpha}(p)\right) - \frac{1}{3}\, P_{(1)}^{\mu\nu}(p)\, P_{(1)}^{\alpha\beta}(p)\,, \end{aligned} \tag{A.3}$$

projects any second-rank tensor into the spin-2 subspace spanned by the polarization tensors. The angular momentum tensor is constructed by applying the spin-2 projection operator to the rank-2 tensor $q_R^{\mu}\, q_R^{\nu}$ constructed from the relative momentum of a two-body system:

$$L_{(2)}^{\mu\nu}(p_R, q_R) = P_2^{\mu\nu\alpha\beta}(p_R)\, q_{R_\alpha}\, q_{R_\beta}. \tag{A.4}$$

This concept is generalized to arbitrary integer spins in Reference [63]. For the sake of brevity, the following notation is introduced: $\varepsilon_{(S)}(R) \equiv \varepsilon_{(S)}(p_R, \lambda_R)$, $P_{(S)}(R) \equiv P_{(S)}(p_R)$, and $L_{(L)}(R) \equiv L_{(L)}(p_R, q_R)$. Now, consider a generic spin-S_R

isobar state, R, decaying via two isobar states, A and B with spins S_A and S_B, which have a relative orbital angular momentum L_{AB}. First, a polarization tensor is assigned to the decaying state and the complex conjugate tensors for each outgoing state. The daughter spins couple to a total intrinsic spin, S_{AB}, which can take on the following range of values in integer steps: $|S_A - S_B| \leq S_{AB} \leq S_A + S_B$. Within the covariant tensor formalism, this is accomplished by projecting the spin-S_A and spin-S_B polarization tensors into the spin-S_{AB} space, resulting in the spin wave tensor $\Phi_{(S_{AB})}$. The possible spin-orbit couplings to a total angular momentum J_{AB}, $|L_{AB} - S_{AB}| \leq J_{AB} \leq L_{AB} + S_{AB}$, are then restricted to those, which satisfy $J_{AB} = S_R$. Moreover, parity conservation imposes the condition $\eta_R = \eta_A \, \eta_B \, (-1)^{L_{AB}}$, where η_R, η_A and η_B are the intrinsic parities of the isobars R, A, and B, respectively. Thus in case of a strong decay, the relative orbital angular momentum is restricted to be either even or odd. A corresponding angular momentum tensor, $L_{(L_{AB})}(R)$, is assigned and properly contracted with the polarization vectors and the spin wave tensor to arrive at the isobar amplitude:

$$\begin{aligned} \langle R_{\lambda_R} | A_{\lambda_A} \, B_{\lambda_B}; L_{AB}, S_{AB} \rangle &= \varepsilon_{(S_R)}(R) \, X(S_R, L_{AB}, S_{AB}) \, L_{(L_{AB})}(R) \, \Phi_{(S_{AB})} \\ \Phi_{(S_{AB})} &= P_{(S_{AB})}(R) \, X(S_{AB}, S_A, S_B) \, \varepsilon^*_{(S_A)}(A) \, \varepsilon^*_{(S_B)}(B) \, . \end{aligned} \tag{A.5}$$

In some cases the tensor $\varepsilon_{\alpha\beta\gamma\delta} \, p_R^\delta$ needs to be included via the relation

$$X(j_a, j_b, j_c) = \begin{cases} 1 & \text{if } j_a + j_b + j_c \; \textit{even} \\ \varepsilon_{\alpha\beta\gamma\delta} \, p_R^\delta & \text{if } j_a + j_b + j_c \; \textit{odd} \end{cases} , \tag{A.6}$$

where $\varepsilon_{\alpha\beta\gamma\delta}$ is the *Levi-Civita* symbol. Indeed, its antisymmetric nature ensures the correct parity transformation behavior of the amplitude. Parity-odd amplitudes typically involve terms like $\mathcal{A}_{\text{P-odd}} \propto \varepsilon_{\alpha\beta\gamma\delta} \, p_1^\alpha \, p_2^\beta \, p_3^\gamma \, p_4^\delta$, where p_i^μ are four-momenta (or objects which transform like a four-momentum under parity). The p_i^μ have to be distinct otherwise the contraction with the antisymmetric tensor gives zero. This also motivates the usage of the total momentum in the tensor $\varepsilon_{\alpha\beta\gamma\delta} \, p_R^\delta$ as the relative momentum is already included in the orbital angular momentum tensors. The transformation under parity can be most easily demonstrated in the rest frames of one of the four-momenta, say p_4, where the expression evaluates to $\mathcal{A}_{\text{P-odd}} \propto \vec{p}_1 \cdot (\vec{p}_2 \times \vec{p}_3) \xrightarrow{\text{P}} -\vec{p}_1 \cdot (\vec{p}_2 \times \vec{p}_3)$. Parity-even amplitudes, on the other hand, typically include only scalar products such as $\vec{p}_1 \cdot \vec{p}_2 \xrightarrow{\text{P}} +\vec{p}_1 \cdot \vec{p}_2$.

The overall spin factor for a complete decay tree is obtained by combining the two-body amplitudes and performing a sum over all intermediary spin projections, *e.g.* for $M \to (R \to AB)\,(T \to CD)$:

$$\sum_{\lambda_R,\lambda_T} \langle M|R_{\lambda_R}\,T_{\lambda_T};L_{RT},L_{RT}\rangle\,\langle R_{\lambda_R}|A\,B;S_R,0\rangle\,\langle T_{\lambda_T}|C\,D;S_T,0\rangle \tag{A.7}$$

where $\lambda_M = \lambda_A = \lambda_B = \lambda_C = \lambda_D = 0$, $S_{AB} = S_{CD} = 0$, $L_{AB} = S_R$ and $L_{CD} = S_T$ as well as $S_{RT} = L_{RT}$ since only pseudo-scalar initial and final states are considered.

Table A.1: Spin factors for all $B \to P_1\,P_2\,P_3\,P_4$ topologies considered in this analysis, where B and P_i are pseudoscalar particles. In the decay chains, S, P, V, A, T and PT label scalar, pseudoscalar, vector, axial vector, tensor and pseudotensor states, respectively. If no angular momentum is specified, the lowest angular momentum state compatible with angular momentum conservation and, where appropriate, parity conservation, is used.

Decay chain	Spin factor
$B \to (P\,P_1)$, $P \to (S\,P_2)$, $S \to (P_3\,P_4)$	1
$B \to (P\,P_1)$, $P \to (V\,P_2)$, $V \to (P_3\,P_4)$	$L_{(1)\alpha}(P)\;L^{\alpha}_{(1)}(V)$
$B \to (A\,P_1)$, $A \to (V\,P_2)$, $V \to (P_3\,P_4)$	$L_{(1)\alpha}(B)\,P^{\alpha\beta}_{(1)}(A)\,L_{(1)\beta}(V)$
$B \to (A\,P_1)$, $A[D] \to (P_2\,V)$, $V \to (P_3\,P_4)$	$L_{(1)\alpha}(B)\,L^{\alpha\beta}_{(2)}(A)\,L_{(1)\beta}(V)$
$B \to (A\,P_1)$, $A \to (S\,P_2)$, $S \to (P_3\,P_4)$	$L_{(1)\alpha}(B)\,L^{\alpha}_{(1)}(A)$
$B \to (A\,P_1)$, $A \to (T\,P_2)$, $T \to (P_3\,P_4)$	$L_{(1)\alpha}(B)\,L_{(1)\beta}(A)\,L^{\alpha\beta}_{(2)}(T)$
$B \to (V_1\,P_1)$, $V_1 \to (V_2\,P_2)$, $V_2 \to (P_3\,P_4)$	$L_{(1)\mu}(B)\,P^{\mu\alpha}_{(1)}(V_1)\,\epsilon_{\alpha\beta\gamma\delta}\,L^{\beta}_{(1)}(V_1)\,p^{\gamma}_{V_1}\,L^{\delta}_{(1)}(V_2)$
$B \to (PT\,P_1)$, $PT \to (V\,P_2)$, $V \to (P_3\,P_4)$	$L_{(2)\alpha\beta}(B)\,P^{\alpha\beta\gamma\delta}_{(2)}(PT)\,L_{(1)\gamma}(PT)\,L_{(1)\delta}(V)$
$B \to (PT\,P_1)$, $PT \to (S\,P_2)$, $S \to (P_3\,P_4)$	$L_{(2)\alpha\beta}(B)\,L_{(2)}(PT)^{\alpha\beta}$
$B \to (PT\,P_1)$, $PT \to (T\,P_2)$, $T \to (P_3\,P_4)$	$L_{(2)\alpha\beta}(B)\,P^{\alpha\beta\gamma\delta}_{(2)}(PT)\,L_{(2)\gamma\delta}(T)$
$B \to (T\,P_1)$, $T \to (V\,P_2)$, $V \to (P_3\,P_4)$	$L_{(2)\mu\nu}(B)\,P^{\mu\nu\rho\alpha}_{(2)}(T)\,\epsilon_{\alpha\beta\gamma\delta}\,L^{\beta}_{(2)\rho}(T)\,p^{\gamma}_{T}\,P^{\delta\sigma}_{(1)}(T)\,L_{(1)\sigma}(V)$
$B \to (T_1\,P_1)$, $T_1 \to (T_2\,P_2)$, $T_2 \to (P_3\,P_4)$	$L_{(2)\mu\nu}(B)\,P^{\mu\nu\rho\alpha}_{(2)}(T_1)\,\epsilon_{\alpha\beta\gamma\delta}\,L^{\beta}_{(1)}(T_1)\,p^{\gamma}_{T_1}\,L^{\delta}_{(2)\rho}(T_2)$
$B \to (S_1\,S_2)$, $S_1 \to (P_1\,P_2)$, $S_2 \to (P_3\,P_4)$	1
$B \to (V\,S)$, $V \to (P_1\,P_2)$, $S \to (P_3\,P_4)$	$L_{(1)\alpha}(B)\,L^{\alpha}_{(1)}(V)$
$B \to (V_1\,V_2)$, $V_1 \to (P_1\,P_2)$, $V_2 \to (P_3\,P_4)$	$L_{(1)\alpha}(V_1)\,L^{\alpha}_{(1)}(V_2)$
$B[P] \to (V_1\,V_2)$, $V_1 \to (P_1\,P_2)$, $V_2 \to (P_3\,P_4)$	$\epsilon_{\alpha\beta\gamma\delta}\,L^{\alpha}_{(1)}(B)\,L^{\beta}_{(1)}(V_1)\,L^{\gamma}_{(1)}(V_2)\,p^{\delta}_{B}$
$B[D] \to (V_1\,V_2)$, $V_1 \to (P_1\,P_2)$, $V_2 \to (P_3\,P_4)$	$L_{(2)\alpha\beta}(B)\,L^{\alpha}_{(1)}(V_1)\,L^{\beta}_{(1)}(V_2)$
$B \to (T\,S)$, $T \to (P_1\,P_2)$, $S \to (P_3\,P_4)$	$L_{(2)\alpha\beta}(B)\,L^{\alpha\beta}_{(2)}(T)$
$B \to (V\,T)$, $T \to (P_1\,P_2)$, $V \to (P_3\,P_4)$	$L_{(1)\alpha}(B)\,L^{\alpha\beta}_{(2)}(T)\,L_{(1)\beta}(V)$
$B[D] \to (T\,V)$, $T \to (P_1\,P_2)$, $V \to (P_3\,P_4)$	$\epsilon_{\alpha\beta\delta\gamma}\,L^{\alpha\mu}_{2}(B)\,L^{\beta}_{2\mu}\,L^{\gamma}_{(1)}(V)\,p^{\delta}_{B}$
$B \to (T_1\,T_2)$, $T_1 \to (P_1\,P_2)$, $T_2 \to (P_3\,P_4)$	$L_{(2)\alpha\beta}(T_1)\,L^{\alpha\beta}_{(2)}(T_2)$
$B[P] \to (T_1\,T_2)$, $T_1 \to (P_1\,P_2)$, $T_2 \to (P_3\,P_4)$	$\epsilon_{\alpha\beta\gamma\delta}\,L^{\alpha}_{(1)}(B)\,L^{\beta\mu}_{(2)}(T_1)\,L^{\gamma}_{(2)\mu}(T_2)\,p^{\delta}_{B}$
$B[D] \to (T_1\,T_2)$, $T_1 \to (P_1\,P_2)$, $T_2 \to (P_3\,P_4)$	$L_{(2)\alpha\beta}(B)\,L^{\alpha\gamma}_{(2)}(T_1)\,L^{\beta}_{(2)\gamma}(T_2)$

B Lineshape models

Lineshape parameters for resonances contributing to $D \to \pi\pi\pi\pi$ or $B_s \to D_s K\pi\pi$ decays are fixed to the values given in Table B.1. The running-width distributions of the three-body resonances contributing to $D \to \pi\pi\pi\pi$ ($B_s \to D_s K\pi\pi$) decays are shown in Figure B.1 (Figure B.2).

For the broad scalar resonance σ, the model from Reference [280] is used. Besides $\sigma \to \pi\pi$ decays, it includes contributions from the decay modes $\sigma \to KK$, $\sigma \to \eta\eta$ and $\sigma \to \pi\pi\pi\pi$ as well as dispersive effects due to the channel opening of the latter. The explicit parameterization is given by:

$$
\begin{aligned}
T_\sigma(s) &= [M^2 - s - g_{\pi\pi}^2 \frac{s - s_A}{M^2 - s_A} z(s) - iM\Gamma_{\text{tot}}(s)]^{-1}, \\
M\Gamma_{\pi\pi}(s) &= g_{\pi\pi}^2 \frac{s - s_A}{M^2 - s_A} \rho_{\pi\pi}(s), \\
M\Gamma_{KK}(s) &= 0.6 g_{\pi\pi}^2(s) \frac{s}{M^2} \exp(-\alpha|s - 4m_K^2|)\rho_{KK}(s), \\
M\Gamma_{\eta\eta}(s) &= 0.2 g_{\pi\pi}^2(s) \frac{s}{M^2} \exp(-\alpha|s - 4m_\eta^2|)\rho_{\eta\eta}(s), \\
M\Gamma_{4\pi}(s) &= M g_{4\pi} \frac{\rho_{4\pi}(s)}{\rho_{4\pi}(M^2)}, \\
g_{\pi\pi}^2(s) &= M(b_1 + b_2 s) \exp[-(s - M^2)A^{-1}], \\
j_1(s) &= \frac{1}{\pi}[2 + \rho_{\pi\pi}(s) \log \frac{1 - \rho_{\pi\pi}(s)}{1 + \rho_{\pi\pi}(s)}], \\
z(s) &= j_1(s) - j_1(M^2),
\end{aligned}
$$

with $\Gamma_{\text{tot}}(s) = \Gamma_{\pi\pi} + \Gamma_{KK} + \Gamma_{\eta\eta} + \Gamma_{4\pi}$, $\rho_{\pi\pi}(s) = \sqrt{1 - 4m_\pi^2/s}$, $\rho_{KK}(s) = \sqrt{1 - 4m_K^2/s}$, $\rho_\eta(s) = \sqrt{1 - 4m_\eta^2/s}$ and $\rho_{4\pi}(s) = 1.0[1 + \exp(7.082 - 2.845s)]^{-1}$. The numerical values for the parameters are [280] $M = 0.953\,\text{GeV}$, $b_1 = 1.302\,\text{GeV}$, $b_2 = 0.340\,\text{GeV}^{-1}$, $A = 2.426\,\text{GeV}^2$, $g_{\pi\pi}^2 = 0.146\,\text{GeV}^2 g_{4\pi} = 0.011\,\text{GeV}$ and $s_A = 0.41 m_\pi^2$. For systematic studies, two alternative parameterization given in Reference [280] are tested.

Table B.1: Parameters of the resonances included in the $D \to \pi\pi\pi\pi$ or $B_s \to D_s K\pi\pi$ LASSO models.

Resonance	m [MeV]	Γ [MeV]	J^P	Source
$\rho(770)$	775.26 ± 0.25	149.1 ± 0.8	1^-	[10]
$K^*(892)$	895.55 ± 0.20	47.3 ± 0.5	1^-	[10]
$f_2(1270)$	1275.5 ± 0.8	186.7 ± 2.5	2^+	[10]
$f_0(1370)$	1475.1 ± 6.3	1474.4 ± 6.0	0^+	[284]
$K_1(1270)$	1289.81 ± 1.75	116.11 ± 3.4	1^+	[191]
$K(1460)$	1482.4 ± 15.64	335.6 ± 10.64	0^-	[191]
$K_0^*(1430)$	1425 ± 50	270 ± 80	0^+	[10]
$\pi_2(1670)$	1672.2 ± 3.0	260 ± 9	2^-	[10]

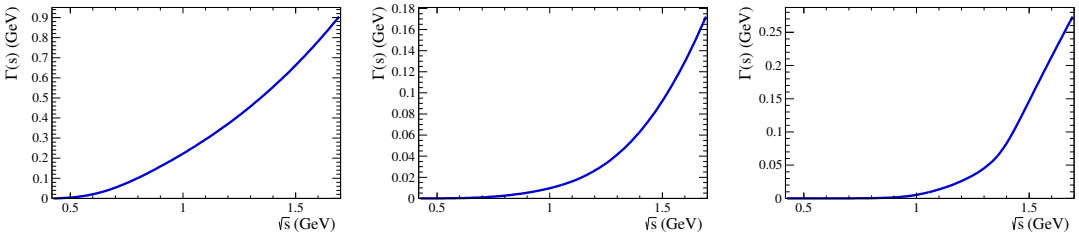

Figure B.1: Running width distributions of the three-body resonances included in the LASSO model for $D \to \pi\pi\pi\pi$ decays: $\pi(1300)$ (left), $a_1(1640)$ (middle) and $\pi_2(1670)$ (right).

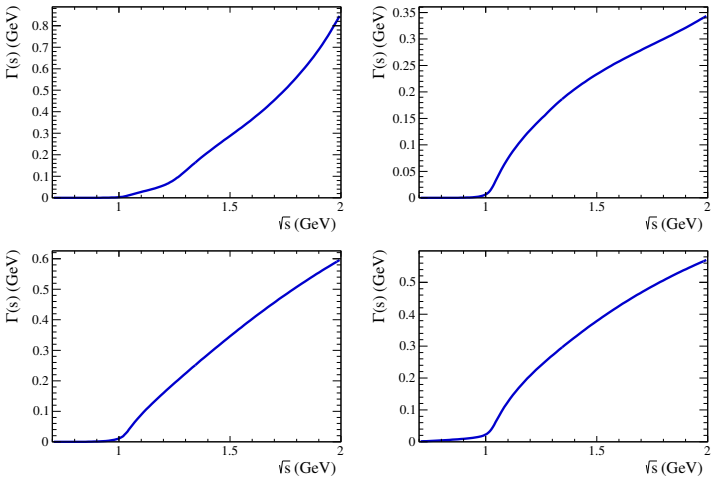

Figure B.2: Running width distributions of the three-body resonances included in the LASSO model for $B_s \to D_s K\pi\pi$ decays: $K_1(1270)$ (top-left), $K_1(1400)$ (top-right), $K(1460)$ (bottom-left) and $K^*(1410)$ (bottom-right).

The *LASS* parameterization is used to model the $K\pi$ S-wave contribution [281, 282]. It consists of the $K_0^*(1430)$ resonance together with an effective range non-resonant component:

$$T_{LASS}(s) = \frac{\sqrt{s}}{q\cot\delta_L - iq} + e^{2i\,\delta_L}\frac{m_0\,\Gamma_0\frac{m_0}{q_0}}{m_0^2 - s - i\,m_0\,\Gamma_0\,\frac{m_0}{\sqrt{s}}\,\frac{q}{q_0}} \tag{B.1}$$

with $\cot\delta_L = \frac{1}{aq} + \frac{1}{2}rq$. The values for the scattering length $a = 2.07 \pm 0.1\,\text{GeV}$ and effective range parameter $r = 3.32 \pm 0.34\,\text{GeV}$ are taken from Reference [281].

The *Gounaris-Sakurai* parametrization for the $\rho(770)^0 \to \pi\pi$ propagator is used [77]:

$$T_{GS}(s) = \frac{1 + f(0)/m_0^2}{m_0^2 + f(s) - s - i\,m_0\,\Gamma(s)}\,, \tag{B.2}$$

where $\Gamma(s)$ takes on the same form as in Equation 2.19 and the function $f(s)$ is defined as:

$$f(s) = \Gamma_R\,\frac{m_R^2}{q_R^3}\left[q^2\left(h(s) - h(m_R^2)\right) + \left(s - m_R^2\right)q_R^2\,\frac{dh}{dm}\bigg|_{m_R}\right], \tag{B.3}$$

$$h(s) = \frac{2}{\pi}\,\frac{q}{\sqrt{s}}\ln\left(\frac{\sqrt{s} + 2\,q}{2\,m_\pi}\right). \tag{B.4}$$

For the decay chain $K_1(1270) \to \rho(770)K$, mixing of the $\rho(770)$ meson with the $\omega(782)$ meson is included [283]:

$$T(s) = T_{GS}(s)\cdot\left(1 + \delta\frac{s}{m_\omega^2}T_\omega(s)\right) \tag{B.5}$$

where $T_\omega(s)$ is the relativistic Breit-Wigner propagator (Equation 2.19) of the $\omega(782)$ meson and the relative magnitude and phase between the $\rho(770)$ and $\omega(782)$ contributions is fixed to the values determined in Reference [184]: $|\delta| = 0.159 \pm 0.012 \pm 0.011$ and $\arg(\delta) = 1.36 \pm 0.07 \pm 0.06$.

Probability density functions

C

ARGUS function

The ARGUS [171] function is used to describe the combinatorial background distribution for $D \to \pi\pi\pi\pi$ candidates (see Section 5.3) in the beam-constrained mass dimension. It is defined as:

$$\mathcal{P}(x|x_0, a) \propto x\sqrt{1-(x/x_0)^2}\, e^{a(1-(x/x_0)^2)}\, \theta(x_0 - x),$$

where x_0 denotes the kinematic cut-off of the the variable x and $\theta(x_0 - x)$ is the Heaviside step function.

Johnson's SU function

The Johnson's SU function [242], used to model the signal component in $B_s \to D_s K\pi\pi$ and $B_s \to D_s\pi\pi\pi$ decays (see Section 9.3), is approximately Gaussian but allows for asymmetric tails:

$$\begin{aligned}
\mathcal{P}(x|\mu,\sigma,\nu,\tau) &= \frac{e^{-\frac{1}{2}r^2}}{2\pi\cdot c\cdot\sigma\cdot\tau\cdot\sqrt{z^2+1}} \\
r &= -\nu + \frac{\operatorname{asinh}(z)}{\tau} \\
z &= \frac{x-(\mu - c\cdot\sigma\cdot e^{\tau}\sinh(\nu\cdot\tau))}{c\cdot\tau} \\
c &= \frac{e^{\tau^2}-1}{2\sqrt{e^{\tau^2}\cdot\cosh(2\nu\cdot\tau)+1}}.
\end{aligned}$$

It is conveniently expressed in terms of the central moments up to order four: The mean of the distribution μ, the standard deviation σ, the skewness ν and the kurtosis τ.

Additional material for Part II

D

Parameterization of the background PDF

The background function in Equation 6.5 is explicitly given by:

$$
\begin{aligned}
B(\mathbf{x}) &= \sum_{i=1}^{7} b_i \, |B_i(\mathbf{x})|^2, \\
B_1(\mathbf{x}) &= BW_{\sigma}(s_{12}) \cdot BW_{\sigma}(s_{34}), \\
B_2(\mathbf{x}) &= BW_{\rho(770)^0}(s_{12}) \cdot \exp(-\alpha_1 \cdot s_{34}), \\
B_3(\mathbf{x}) &= BW_{f_0(980)}(s_{12}) \cdot BW_{f_0(980)}(s_{34}), \\
B_4(\mathbf{x}) &= BW_{S_1^0}(s_{12}) \cdot \left(\sum_{i=1}^{5} c_i \cdot s_{34}^i \right), \\
B_5(\mathbf{x}) &= BW_{S_2^-}(s_{124}), \\
B_6(\mathbf{x}) &= \exp(-\alpha_2 \cdot s_{14}) \cdot \exp(-\alpha_3 \cdot s_{23}), \\
B_7(\mathbf{x}) &= \left(\sum_{i=1}^{4} d_i \cdot s_{124}^i \right) \cdot \left(\sum_{i=1}^{3} e_i \cdot s_{12}^i \right),
\end{aligned}
\tag{D.1}
$$

with $s_{ij} = m^2(\pi_i \, \pi_j)$, $s_{ijk} = m^2(\pi_i \, \pi_j \, \pi_k)$ and $D^0 \to \pi_1^+ \pi_2^- \pi_3^+ \pi_4^-$. The functions $BW_R(s)$ are of the form given in Equation 2.18 with constant (running) mass and width, where the indices refers to the resonant state. The (real) parameters b_i, α_i, d_i, e_i and the mass and width of the ad-hoc resonances S_1^0 and S_2^- are extracted from a fit to the sideband samples.

Signal model

Table D.1 lists the interference fractions, ordered by magnitude, for the baseline LASSO model of $D^0 \to \pi^+\pi^-\pi^+\pi^-$ decays. The decay fractions of the baseline LASSO model and several alternative models are summarized in Tables D.2 and D.3.

Table D.1: Interference fractions $|I_{ij}| > 0.5\%$ ordered by magnitude, for the nominal $D \to \pi\pi\pi\pi$ amplitude fit. Only the statistical uncertainties are given.

Channel i	Channel j	I_{ij}[%]
$D^0 \to \pi^-[a_1(1260)^+ \to \sigma\pi^+]$	$D^0 \to \pi^-[a_1(1260)^+ \to \rho(770)^0\pi^+]$	20.01 ± 1.19
$D^0 \to \pi^-[\pi(1300)^+ \to \sigma\pi^+]$	$D^0 \to f_0(1370)\,\sigma$	-10.77 ± 0.84
$D^0 \to \rho(770)^0\,\sigma$	$D^0 \to \pi^-[a_1(1260)^+ \to \rho(770)^0\pi^+]$	-6.94 ± 0.75
$D^0 \to \pi^-[a_1(1260)^+ \to \sigma\pi^+]$	$D^0 \to \pi^-[a_1(1640)^+ \to \sigma\pi^+]$	-6.15 ± 1.10
$D^0 \to \pi^-[a_1(1260)^+ \to \rho(770)^0\pi^+]$	$D^0[D] \to \rho(770)^0\,\rho(770)^0$	-5.24 ± 0.33
$D^0 \to \pi^-[a_1(1640)^+ \to \sigma\pi^+]$	$D^0 \to \pi^-[a_1(1260)^+ \to \rho(770)^0\pi^+]$	-5.07 ± 0.69
$D^0 \to \pi^+[\pi(1300)^- \to \sigma\pi^-]$	$D^0 \to f_0(1370)\,\sigma$	-4.50 ± 0.87
$D^0 \to \pi^-[a_1(1260)^+ \to \sigma\pi^+]$	$D^0[D] \to \rho(770)^0\,\rho(770)^0$	-4.30 ± 0.34
$D^0 \to \pi^-[\pi_2(1670)^+ \to \sigma\pi^+]$	$D^0 \to \pi^-[\pi_2(1670)^+ \to f_2(1270)\pi^+]$	-3.06 ± 0.43
$D^0 \to \pi^-[\pi(1300)^+ \to \sigma\pi^+]$	$D^0 \to \pi^+[\pi(1300)^- \to \sigma\pi^-]$	2.90 ± 0.34
$D^0 \to \pi^-[a_1(1260)^+ \to \rho(770)^0\pi^+]$	$D^0 \to \pi^+[a_1(1260)^- \to \rho(770)^0\pi^-]$	2.75 ± 0.13
$D^0 \to \pi^-[a_1(1260)^+ \to \sigma\pi^+]$	$D^0 \to f_0(1370)\,\sigma$	2.65 ± 0.18
$D^0 \to f_2(1270)\,f_2(1270)$	$D^0 \to \pi^-[\pi_2(1670)^+ \to f_2(1270)\pi^+]$	-2.60 ± 0.53
$D^0 \to f_0(1370)\,\sigma$	$D^0 \to \pi^-[a_1(1260)^+ \to \rho(770)^0\pi^+]$	2.41 ± 0.14
$D^0 \to \pi^-[\pi_2(1670)^+ \to \sigma\pi^+]$	$D^0 \to f_2(1270)\,f_2(1270)$	2.18 ± 0.27
$D^0[S] \to \rho(770)^0\,\rho(770)^0$	$D^0[D] \to \rho(770)^0\,\rho(770)^0$	2.04 ± 0.44
$D^0 \to \pi^-[a_1(1640)^+[D] \to \rho(770)^0\pi^+]$	$D^0[D] \to \rho(770)^0\,\rho(770)^0$	1.99 ± 0.30
$D^0 \to \pi^-[a_1(1260)^+ \to \sigma\pi^+]$	$D^0[S] \to \rho(770)^0\,\rho(770)^0$	-1.80 ± 0.40
$D^0 \to \pi^+[a_1(1260)^- \to \rho(770)^0\pi^-]$	$D^0[D] \to \rho(770)^0\,\rho(770)^0$	-1.75 ± 0.09
$D^0 \to \pi^+[a_1(1260)^- \to \rho(770)^0\pi^-]$	$D^0[S] \to \rho(770)^0\,\rho(770)^0$	-1.74 ± 0.29
$D^0 \to \pi^+[a_1(1260)^- \to \sigma\pi^-]$	$D^0 \to \pi^+[a_1(1260)^- \to \rho(770)^0\pi^-]$	1.61 ± 0.10
$D^0 \to \pi^-[a_1(1260)^+ \to \sigma\pi^+]$	$D^0 \to \pi^+[a_1(1260)^- \to \rho(770)^0\pi^-]$	1.60 ± 0.07
$D^0 \to \pi^-[a_1(1260)^+ \to \sigma\pi^+]$	$D^0 \to \pi^+[a_1(1260)^- \to \sigma\pi^-]$	1.51 ± 0.17
$D^0 \to f_0(1370)\,\sigma$	$D^0[D] \to \rho(770)^0\,\rho(770)^0$	-1.40 ± 0.09
$D^0 \to \pi^-[a_1(1260)^+ \to \sigma\pi^+]$	$D^0 \to \pi^-[\pi_2(1670)^+ \to \sigma\pi^+]$	1.33 ± 0.12
$D^0 \to \pi^-[a_1(1640)^+[D] \to \rho(770)^0\pi^+]$	$D^0 \to f_2(1270)\,f_2(1270)$	1.28 ± 0.15
$D^0 \to \pi^+[a_1(1260)^- \to \rho(770)^0\pi^-]$	$D^0 \to \pi^-[a_1(1640)^+[D] \to \rho(770)^0\pi^+]$	-1.21 ± 0.09
$D^0 \to \pi^-[a_1(1260)^+ \to \sigma\pi^+]$	$D^0 \to \pi^+[\pi(1300)^- \to \sigma\pi^-]$	1.19 ± 0.16
$D^0 \to \pi^-[a_1(1260)^+ \to \sigma\pi^+]$	$D^0 \to \pi^-[\pi_2(1670)^+ \to f_2(1270)\pi^+]$	-1.18 ± 0.16
$D^0 \to \pi^-[a_1(1260)^+ \to \sigma\pi^+]$	$D^0 \to \pi^-[\pi(1300)^+ \to \sigma\pi^+]$	-1.14 ± 0.10
$D^0 \to \pi^+[a_1(1260)^- \to \sigma\pi^-]$	$D^0[S] \to \rho(770)^0\,\rho(770)^0$	-1.07 ± 0.12
$D^0 \to \pi^+[a_1(1260)^- \to \sigma\pi^-]$	$D^0 \to \rho(770)^0\,\sigma$	-1.02 ± 0.12
$D^0 \to \pi^-[a_1(1640)^+[D] \to \rho(770)^0\pi^+]$	$D^0[S] \to \rho(770)^0\,\rho(770)^0$	-1.01 ± 0.13
$D^0 \to \pi^-[a_1(1640)^+ \to \sigma\pi^+]$	$D^0 \to f_0(1370)\,\sigma$	-1.00 ± 0.16
$D^0 \to \pi^-[a_1(1640)^+ \to \sigma\pi^+]$	$D^0[D] \to \rho(770)^0\,\rho(770)^0$	0.96 ± 0.15
$D^0 \to \pi^-[\pi_2(1670)^+ \to \sigma\pi^+]$	$D^0 \to f_0(1370)\,\sigma$	-0.95 ± 0.08
$D^0 \to \pi^+[a_1(1260)^- \to \sigma\pi^-]$	$D^0[D] \to \rho(770)^0\,\rho(770)^0$	-0.90 ± 0.10
$D^0 \to \pi^-[a_1(1640)^+ \to \sigma\pi^+]$	$D^0 \to \pi^+[a_1(1260)^- \to \rho(770)^0\pi^-]$	-0.89 ± 0.13
$D^0 \to \pi^+[\pi(1300)^- \to \sigma\pi^-]$	$D^0 \to \pi^-[\pi_2(1670)^+ \to \sigma\pi^+]$	-0.86 ± 0.12
$D^0 \to \pi^-[\pi(1300)^+ \to \sigma\pi^+]$	$D^0 \to \pi^-[a_1(1260)^+ \to \rho(770)^0\pi^+]$	-0.83 ± 0.09
$D^0 \to \pi^+[a_1(1260)^- \to \sigma\pi^-]$	$D^0 \to \pi^-[a_1(1640)^+ \to \sigma\pi^+]$	-0.81 ± 0.18
$D^0 \to f_0(1370)\,\sigma$	$D^0 \to \pi^+[a_1(1260)^- \to \rho(770)^0\pi^-]$	0.80 ± 0.03
$D^0 \to \rho(770)^0\,\sigma$	$D^0 \to \pi^-[a_1(1640)^+[D] \to \rho(770)^0\pi^+]$	0.78 ± 0.11
$D^0 \to \pi^-[a_1(1640)^+ \to \sigma\pi^+]$	$D^0 \to \pi^-[\pi(1300)^+ \to \sigma\pi^+]$	0.75 ± 0.10
$D^0 \to \pi^-[\pi_2(1670)^+ \to \sigma\pi^+]$	$D^0 \to \pi^+[a_1(1260)^- \to \rho(770)^0\pi^-]$	-0.69 ± 0.05
$D^0 \to \pi^-[a_1(1260)^+ \to \rho(770)^0\pi^+]$	$D^0 \to f_2(1270)\,f_2(1270)$	0.67 ± 0.07
$D^0 \to \pi^-[a_1(1640)^+ \to \sigma\pi^+]$	$D^0 \to \pi^+[\pi(1300)^- \to \sigma\pi^-]$	-0.67 ± 0.15
$D^0 \to f_0(1370)\,\sigma$	$D^0[S] \to \rho(770)^0\,\rho(770)^0$	-0.66 ± 0.11
$D^0 \to \rho(770)^0\,\sigma$	$D^0 \to \pi^+[a_1(1260)^- \to \rho(770)^0\pi^-]$	-0.64 ± 0.19
$D^0 \to \pi^-[a_1(1260)^+ \to \rho(770)^0\pi^+]$	$D^0 \to \pi^-[\pi_2(1670)^+ \to f_2(1270)\pi^+]$	-0.63 ± 0.15
$D^0 \to \pi^-[\pi_2(1670)^+ \to \sigma\pi^+]$	$D^0[S] \to \rho(770)^0\,\rho(770)^0$	0.62 ± 0.08
$D^0 \to \pi^-[a_1(1640)^+ \to \sigma\pi^+]$	$D^0 \to f_2(1270)\,f_2(1270)$	-0.62 ± 0.14
$D^0 \to \pi^-[a_1(1640)^+ \to \sigma\pi^+]$	$D^0[S] \to \rho(770)^0\,\rho(770)^0$	0.61 ± 0.17
$D^0 \to \pi^-[\pi_2(1670)^+ \to \sigma\pi^+]$	$D^0 \to \pi^-[a_1(1640)^+[D] \to \rho(770)^0\pi^+]$	-0.61 ± 0.06
$D^0 \to \pi^-[\pi(1300)^+ \to \sigma\pi^+]$	$D^0[D] \to \rho(770)^0\,\rho(770)^0$	-0.60 ± 0.07
$D^0 \to \pi^-[a_1(1260)^+ \to \sigma\pi^+]$	$D^0 \to f_2(1270)\,f_2(1270)$	0.59 ± 0.13
$D^0 \to \pi^-[a_1(1640)^+ \to \sigma\pi^+]$	$D^0 \to \pi^-[\pi_2(1670)^+ \to \sigma\pi^+]$	-0.57 ± 0.09
$D^0 \to \pi^-[\pi_2(1670)^+ \to \sigma\pi^+]$	$D^0 \to \rho(770)^0\,\sigma$	0.52 ± 0.10
$D^0 \to \rho(770)^0\,\sigma$	$D^0 \to \pi^-[\pi_2(1670)^+ \to f_2(1270)\pi^+]$	-0.52 ± 0.08
$D^0 \to \pi^+[\pi(1300)^- \to \sigma\pi^-]$	$D^0 \to \pi^-[a_1(1260)^+ \to \rho(770)^0\pi^+]$	0.51 ± 0.05
$D^0 \to \pi^-[a_1(1640)^+ \to \sigma\pi^+]$	$D^0 \to \pi^-[a_1(1640)^+[D] \to \rho(770)^0\pi^+]$	0.51 ± 0.12
$D^0 \to \pi^-[a_1(1260)^+ \to \rho(770)^0\pi^+]$	$D^0 \to \pi^-[a_1(1640)^+[D] \to \rho(770)^0\pi^+]$	0.50 ± 0.07

Table D.2: Decay fractions in percent for each component of various alternative models for $D^0 \to \pi^+\pi^-\pi^+\pi^-$ decays. Resonance parameters, fractional CP-even content F_+ and χ^2/ν are also given.

Decay mode	Alt. 1	Alt. 2	Alt. 3	FOCUS
$D^0 \to \pi^- \left[a_1(1260)^+ \to \pi^+ \rho(770)^0\right]$	37.3	41.0	36.7	38.2
$D^0 \to \pi^- \left[a_1(1260)^+[D] \to \pi^+ \rho(770)^0\right]$	-	-	2.6	7.0
$D^0 \to \pi^- \left[a_1(1260)^+ \to \pi^+ \sigma\right]$	8.1	5.5	5.1	6.6
$D^0 \to \pi^+ \left[a_1(1260)^- \to \pi^- \rho(770)^0\right]$	2.1	3.0	1.0	-
$D^0 \to \pi^+ \left[a_1(1260)^-[D] \to \pi^- \rho(770)^0\right]$	-	-	0.07	-
$D^0 \to \pi^+ \left[a_1(1260)^- \to \pi^- \sigma\right]$	0.5	0.4	0.14	-
$D^0 \to \pi^- \left[\pi(1300)^+ \to \pi^+ \sigma\right]$	8.6	-	10.7	-
$D^0 \to \pi^+ \left[\pi(1300)^- \to \pi^- \sigma\right]$	5.0	-	2.8	-
$D^0 \to \pi^- \left[a_1(1640)^+[D] \to \pi^+ \rho(770)^0\right]$	2.9	6.5	-	-
$D^0 \to \pi^- \left[a_1(1640)^+ \to \pi^+ \sigma\right]$	3.0	-	-	-
$D^0 \to \pi^- \left[a_1(1640)^+ \to \pi^+ f_2(1270)\right]$	-	2.1	-	-
$D^0 \to \pi^+ \left[a_1(1640)^-[D] \to \pi^- \rho(770)^0\right]$	1.0	-	-	-
$D^0 \to \pi^+ \left[a_1(1640)^- \to \pi^- \sigma\right]$	1.1	-	-	-
$D^0 \to \pi^- \left[\pi_2(1670)^+ \to \pi^+ f_2(1270)\right]$	0.8	2.6	3.4	-
$D^0 \to \pi^- \left[\pi_2(1670)^+ \to \pi^+ \sigma\right]$	3.3	3.4	1.0	-
$D^0 \to \pi^+ \left[\pi_2(1670)^- \to \pi^- f_2(1270)\right]$	0.3	-	-	-
$D^0 \to \pi^+ \left[\pi_2(1670)^- \to \pi^- \sigma\right]$	1.3	-	-	-
$D^0 \to \sigma\,(\pi\,\pi)_S$	-	-	-	24.7
$D^0 \to \sigma\, f_0(1370)$	26.1	9.4	28.4	-
$D^0 \to f_0(980)\,(\pi\,\pi)_S$	-	-	-	4.6
$D^0 \to \sigma\, \rho(770)^0$	10.6	6.3	7.4	-
$D^0[S] \to \rho(770)^0\, \rho(770)^0$	0.9	3.2	0.8	5.0
$D^0[P] \to \rho(770)^0\, \rho(770)^0$	6.8	6.5	6.9	6.3
$D^0[D] \to \rho(770)^0\, \rho(770)^0$	13.2	3.7	11.8	3.2
$D^0 \to f_2(1270)\,(\pi\,\pi)_S$	-	-	-	2.4
$D^0 \to f_2(1270)\,\sigma$	-	1.1	1.4	-
$D^0 \to f_2(1270)\, f_0(980)$	-	4.6	-	-
$D^0 \to f_2(1270)\, f_2(1270)$	2.1	7.9	4.0	-
Sum	135	107	124	98
$m_{a_1(1260)}$ [MeV]	1225	1225	1230	1304
$\Gamma_{a_1(1260)}$ [MeV]	442	460	421	529
$m_{\pi(1300)}$ [MeV]	1093	-	1135	-
$\Gamma_{\pi(1300)}$ [MeV]	314	-	308	-
$m_{a_1(1640)}$ [MeV]	1710	1727	-	-
$\Gamma_{a_1(1640)}$ [MeV]	201	141	-	-
χ^2/ν	1.52	1.79	1.55	2.36
F_+ [%]	70.8	70.8	72.6	61.7

Table D.3: Decay fractions in percent for each component of various alternative models for $D^0 \to \pi^+\pi^-\pi^+\pi^-$ decays. Resonance parameters, fractional CP-even content F_+ and χ^2/ν are also given.

Decay mode	Alt. 4	Alt. 5	Alt. 6	Alt. 7	Alt. 8
$D^0 \to \pi^- \left[a_1(1260)^+ \to \pi^+ \rho(770)^0\right]$	37.1	38.3	35.2	38.4	35.7
$D^0 \to \pi^- \left[a_1(1260)^+ \to \pi^+ \sigma\right]$	11.3	9.8	9.4	11.6	11.4
$D^0 \to \pi^+ \left[a_1(1260)^- \to \pi^- \rho(770)^0\right]$	2.1	3.3	3.7	3.1	4.0
$D^0 \to \pi^+ \left[a_1(1260)^- \to \pi^- \sigma\right]$	0.6	0.9	1.0	0.9	1.3
$D^0 \to \pi^- \left[\pi(1300)^+ \to \pi^+ (\pi^+\pi^-)_P\right]$	-	-	-	-	6.4
$D^0 \to \pi^- \left[\pi(1300)^+ \to \pi^+ \sigma\right]$	8.1	8.6	6.0	7.7	4.3
$D^0 \to \pi^+ \left[\pi(1300)^- \to \pi^- (\pi^+\pi^-)_P\right]$	-	-	-	-	2.5
$D^0 \to \pi^+ \left[\pi(1300)^- \to \pi^- \sigma\right]$	4.3	4.0	6.8	4.9	1.7
$D^0 \to \pi^- \left[a_1(1640)^+[D] \to \pi^+ \rho(770)^0\right]$	2.7	4.5	3.9	5.2	3.7
$D^0 \to \pi^- \left[a_1(1640)^+ \to \pi^+ \sigma\right]$	3.2	1.4	2.4	3.0	1.2
$D^0 \to \pi^- \left[\pi_2(1670)^+ \to \pi^+ f_2(1270)\right]$	1.8	0.6	1.2	1.7	1.6
$D^0 \to \pi^- \left[\pi_2(1670)^+ \to \pi^+ \rho(770)^0\right]$	2.7	-	-	-	-
$D^0 \to \pi^- \left[\pi_2(1670)^+ \to \pi^+ \sigma\right]$	2.1	3.9	3.3	3.8	3.5
$D^0 \to \sigma\, f_0(1370)$	20.7	19.3	21.3	21.8	20.4
$D^0 \to \sigma\, \rho(770)^0$	5.5	8.7	8.7	-	4.8
$D^0 \to f_0(980)\, \rho(770)^0$	-	-	3.6	-	-
$D^0 \to f_0(1370)\, \rho(770)^0$	-	-	-	5.8	-
$D^0[S] \to \rho(770)^0\, \rho(770)^0$	-	1.5	0.8	1.2	0.9
$D^0[P] \to \rho(770)^0\, \rho(770)^0$	7.3	6.8	6.9	6.8	6.4
$D^0[D] \to \rho(770)^0\, \rho(770)^0$	10.4	8.3	11.4	10.9	16.0
$D^0 \to f_2(1270)\, f_2(1270)$	2.5	-	1.2	1.4	1.1
Sum	122	120	127	128	127
$m_{a_1(1260)}$ [MeV]	1198	1220	1213	1215	1231
$\Gamma_{a_1(1260)}$ [MeV]	429	408	434	420	459
$m_{\pi(1300)}$ [MeV]	1110	1079	1075	1077	1180
$\Gamma_{\pi(1300)}$ [MeV]	314	347	330	377	297
$m_{a_1(1640)}$ [MeV]	1694	1681	1672	1686	1644
$\Gamma_{a_1(1640)}$ [MeV]	177	171	250	209	222
χ^2/ν	1.50	1.42	1.43	1.50	1.33
F_+ [%]	71.7	72.9	73.0	73.3	73.5

Additional material for Part III

E

Summary of selection criteria

The selection of D_s candidates is summarized in Table E.1. For the $KK\pi$ final state, the well known resonance structure is exploited; the decay proceeds either via the narrow $\phi(1020)$ resonance, the broader $K^*(892)$ resonance or (predominantly) non-resonant. Within the $\phi(1020)$ resonance region loose cuts on the PID information and the D_s flight-distance are sufficient. For the $K^*(892)$ and non-resonant regions consecutively tighter requirements are applied. Table E.2 summarizes the selection of $B_s \to D_s K\pi\pi$ and $B_s \to D_s\pi\pi\pi$ candidates. The following selection variables are used in addition to the ones introduced in Chapter 9:

- χ^2_{IP}: the impact parameter significance is calculated from the increase of the vertex fit χ^2 when adding the respective track (or composite particle) to the fit of the primary vertex
- ZFD: the flight distance in z-direction
- RFD: the flight distance projected to the transverse plane
- χ^2_{FD}: the flight distance significance is derived from the flight distance taking also the uncertainties on the vertex positions into account
- DIRA: the cosine of the angle between the B_s momentum and the vector connecting the primary and secondary vertices
- χ^2_{DTF}/ndf: the fit quality of the DTF with primary vertex constrain
- $\theta_{D_s h_i}$: the opening angle between the D_s and a companion track h_i in the plane transverse to the beam
- DOCA: the distance of closest approach of two tracks

- ghostProb: the probability for a track to be a reconstruction artifact originating from the combination of unrelated hits (ghost) is computed from the information provided by the tracking system such as the track fit χ^2, the kinematics of the track and the detector occupancy

Table E.1: Offline selection requirements for $D_s \to 3h$ candidates.

	Description	Requirement
$D_s \to hhh$	$m(hhh)$	$= m_{D_s} \pm 25\,\text{MeV}$
	Vertex fit χ^2/ndf	< 10
	χ^2_{IP}	> 36
	Daughter DOCA	$< 0.5\,\text{mm}$
	ZFD	$> 0\,\text{mm}$
$D_s^- \to KK\pi^-$	D^0 veto	$m(KK) < 1840$ MeV
$D_s^- \to \phi(1020)\pi^-$	$m(KK)$	$= m_\phi \pm 12$ MeV
	$\Delta\ln\mathcal{L}_{K\pi}(K^+)$	> -10
	$\Delta\ln\mathcal{L}_{K\pi}(K^-)$	> -10
	$\Delta\ln\mathcal{L}_{K\pi}(\pi^-)$	< 20
	χ^2_{FD}	> 0
	D^- veto	$m(K^+K^-_\pi\pi^-) \neq m(D^-) \pm 40$ MeV $\|\|$ $\Delta\ln\mathcal{L}_{K\pi}(K^-) > 5$
	Λ_c veto	$m(K^+K^-_p\pi^-) \neq m(\Lambda_c) \pm 40$ MeV $\|\|$ $\Delta\ln\mathcal{L}_{K\pi}(K^-) - \Delta\ln\mathcal{L}_{p\pi}(K^-) > 2$
$D_s^- \to K^*(892)K^-$	$m(KK)$	$\neq m_\phi \pm 12$ MeV
	$m(K^+\pi^-)$	$= m_{K^*(892)} \pm 75$ MeV
	$\Delta\ln\mathcal{L}_{K\pi}(K^+)$	> -10
	$\Delta\ln\mathcal{L}_{K\pi}(K^-)$	> 0
	$\Delta\ln\mathcal{L}_{K\pi}(\pi^-)$	< 10
	χ^2_{FD}	> 0
	D^- veto	$m(K^+K^-_\pi\pi^-) \neq m(D^-) \pm 40$ MeV $\|\|$ $\Delta\ln\mathcal{L}_{K\pi}(K^-) > 15$
	Λ_c veto	$m(K^+K^-_p\pi^-) \neq m(\Lambda_c) \pm 40$ MeV $\|\|$ $\Delta\ln\mathcal{L}_{K\pi}(K^-) - \Delta\ln\mathcal{L}_{p\pi}(K^-) > 5$
$D_s^- \to (KK\pi^-)_{NR}$	$m(KK)$	$\neq m_\phi \pm 12$ MeV
	$m(K^+\pi^-)$	$\neq m_{K^*(892)} \pm 75$ MeV
	$\Delta\ln\mathcal{L}_{K\pi}(K^+)$	> 5
	$\Delta\ln\mathcal{L}_{K\pi}(K^-)$	> 5
	$\Delta\ln\mathcal{L}_{K\pi}(\pi^-)$	< 10
	χ^2_{FD}	> 4
	D^- veto	$m(K^+K^-_\pi\pi^-) \neq m(D^-) \pm 40$ MeV $\|\|$ $\Delta\ln\mathcal{L}_{K\pi}(K^-) > 15$
	Λ_c veto	$m(K^+K^-_p\pi^-) \neq m(\Lambda_c) \pm 40$ MeV $\|\|$ $\Delta\ln\mathcal{L}_{K\pi}(K^-) - \Delta\ln\mathcal{L}_{p\pi}(K^-) > 5$
$D_s^- \to \pi\pi\pi$	$\Delta\ln\mathcal{L}_{K\pi}(\pi)$	< 10
	$\Delta\ln\mathcal{L}_{p\pi}(\pi)$	< 20
	D^0 veto	$m(\pi^+\pi^-) < 1700$ MeV
	χ^2_{FD}	> 9
$D_s^- \to K^-\pi^+\pi^-$	$\Delta\ln\mathcal{L}_{K\pi}(K)$	> 8
	$\Delta\ln\mathcal{L}_{K\pi}(\pi)$	< 5
	$\Delta\ln\mathcal{L}_{p\pi}(\pi)$	< 20
	D^0 veto	$m(K^-\pi^+) < 1750$ MeV
	χ^2_{FD}	> 9
	D^- veto	$m(K^-_\pi\pi^+\pi^-) \neq m(D^-) \pm 40$ MeV $\|\|$ $\Delta\ln\mathcal{L}_{K\pi}(K^-) > 15$
	Λ_c veto	$m(K^-_p\pi^+\pi^-) \neq m(\Lambda_c) \pm 40$ MeV $\|\|$ $\Delta\ln\mathcal{L}_{K\pi}(K^-) - \Delta\ln\mathcal{L}_{p\pi}(K^-) > 5$

Table E.2: Offline selection requirements for $B_s \to D_s X_s$ and $B_s \to D_s X_d$ candidates, where X_s and X_d label the $K\pi\pi$ or $\pi\pi\pi$ companion particles. The label $X \to h\pi\pi$ is used if no distinction between the final states is necessary.

	Description	Requirement
$B_s \to D_s h\pi\pi$	$m(D_s h\pi\pi)$	$\in [5200, 5700]\,\text{MeV}$
	Vertex Fit χ^2/ndf	< 8
	DIRA	> 0.99994
	χ^2_{FD}	> 100
	χ^2_{IP}	< 16
	χ^2_{DTF}/ndf	< 15
	$\Delta\chi^2_{add-track}$	> 2
	$\cos(\max\theta_{D_s h_i})$	> -0.9
	t	$> 0.4\,\text{ps}$
	δ_t	$< 0.15\,\text{ps}$
	Phasespace region	$m(h\pi\pi) < 1.95\,\text{GeV}$
		$m(h\pi) < 1.2\,\text{GeV}$
		$m(\pi\pi) < 1.2\,\text{GeV}$
	BDTG	> 0.35 [Run-I,L0-TOS]
		> 0.45 [Run-I,L0-TIS]
		> 0.25 [Run-II,L0-TOS]
		> 0.45 [Run-II,L0-TIS]
$X^+ \to h^+\pi^+\pi^-$	Vertex fit χ^2/ndf	< 8
	χ^2_{IP}	> 16
	Daughter DOCA	$< 0.4\,\text{mm}$
$X_s^+ \to K^+\pi^+\pi^-$	$\Delta\ln\mathcal{L}_{K\pi}(\text{K})$	> 10
	$\Delta\ln\mathcal{L}_{K\pi}(\pi^+)$	< 10
	$\Delta\ln\mathcal{L}_{K\pi}(\pi^-)$	< 0
$X_d^+ \to \pi^+\pi^+\pi^-$	$\Delta\ln\mathcal{L}_{K\pi}(\pi^+)$	< 0
	$\Delta\ln\mathcal{L}_{K\pi}(\pi^-)$	< 10
All tracks	p_T	$> 100\,\text{MeV}$
	p	$> 1000\,\text{MeV}$
	χ^2_{IP}	> 4
	Track fit χ^2/ndf	< 3
	ghostProb	< 0.4

Details of multivariate classifier

A decision tree with gradient boosting (BDTG) is trained to discriminate signal and combinatorial background using the Toolkit for Multivariate Analysis (TMVA [285]) implementation. Due to the limited statistics of the training samples the classifier could be overtrained, which means that the algorithm learns statistical fluctuations rather than actual signal or background properties. The issue of overtraining becomes particularly relevant if the classifier is trained on a sub-sample which is supposed to be used in the final analysis. In this case, the training events might be selected more efficiently, potentially biasing the measurement. It is therefore ensured that the BDTG is always applied to a statistically independent sample as follows: the total data samples are split into two disjoint categories according to whether the event number is even or odd; the classifier is then trained on the even (odd) training samples and applied to the odd (even) sample (cross-training). The following discriminating variables are used for the BDTG training: the impact parameter significance of the B_s candidate, the smallest impact parameter significance of the D_s daughters, the smallest impact parameter significance of the companion particles, the largest distance of closest approach of the companion particles, the largest ghost probability of all tracks, the cosine of the largest opening angle between the D_s candidate and a companion track, the DIRA of the B_s candidate, the flight distance significance and ZFD of the D_s candidate. In addition, the isolation variables $A_{p_T}^{cone}$ and $\Delta\chi^2_{add-track}$ are included. Figure E.1 shows the distributions of the input variables for signal and background. These distributions differ between data-taking period and L0 trigger category. In particular variables depending on the B_s kinematics and the event multiplicity are affected (*e.g.* the opening angle $\theta_{D_s h_i}$ or isolation variables). The BDTG is consequently trained separately for these categories. The resulting classifier response is shown in Fig. E.2 for each category (even and odd samples combined).

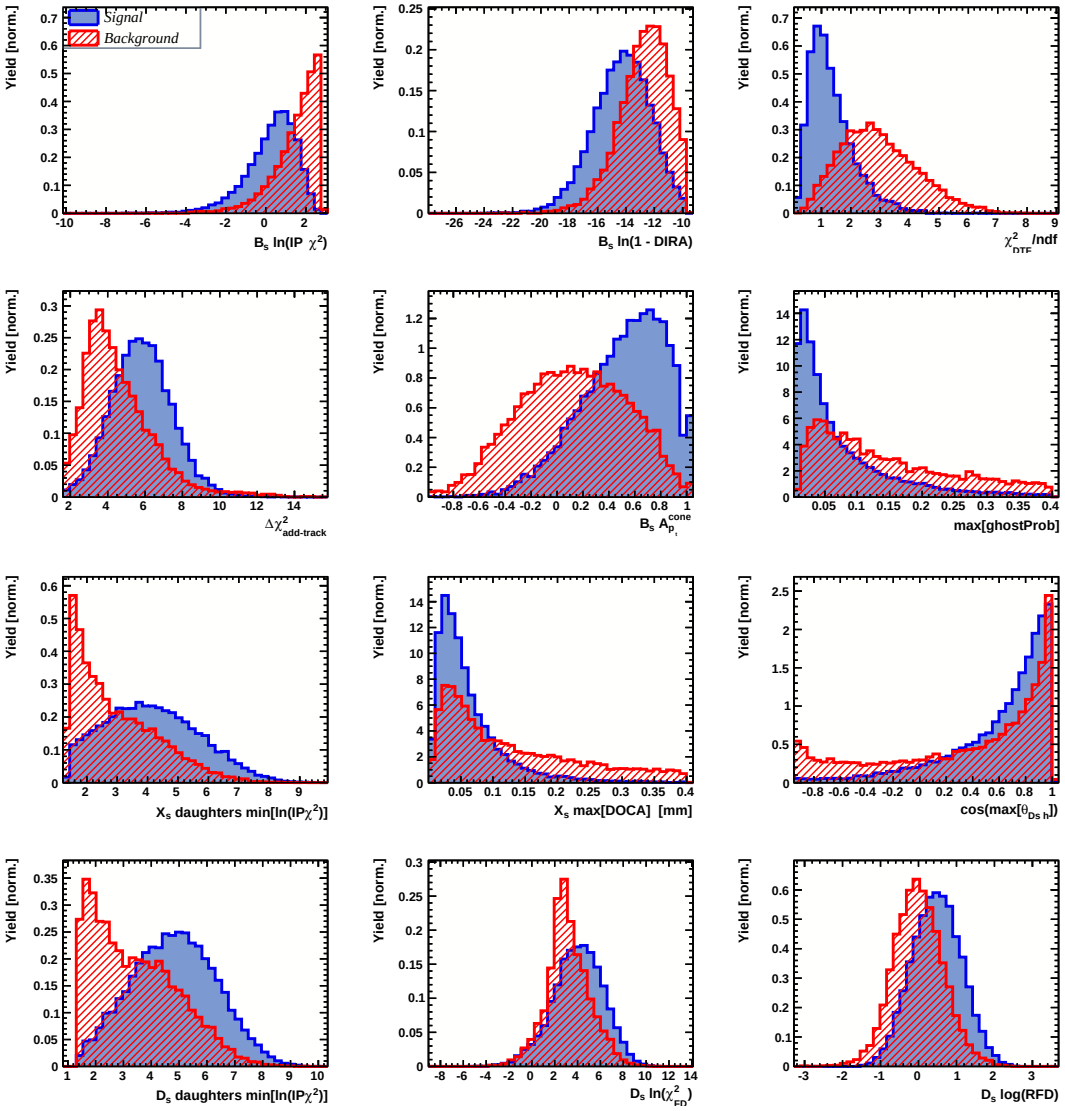

Figure E.1: Discriminating variables used to train the BDTG for signal (red) and combinatorial background (blue). All data categories are combined.

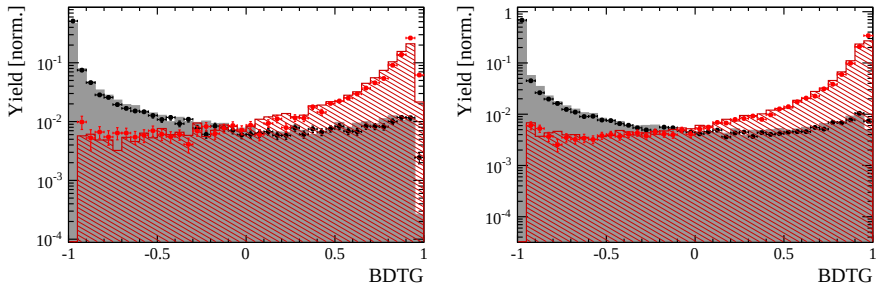

Figure E.2: Signal (red) and background (black) distributions for the BDTG response for Run-I (left) and Run-II (right) data. Filled histograms (data points) show the BDTG response for the L0-TOS (L0-TIS) category. Even and odd samples are combined.

Details on decay-time studies

Decay-time resolution

Table E.3 details the selection criteria applied to the fake B_s candidates used to calibrated the decay-time error estimates. For technical reasons the prompt $D_sK\pi\pi$ data sample is only available for Run-II data. Instead, for Run-I data, the time-resolution calibration uses prompt D_sK candidates. The calibration on this sample was done in context of the $B_s \to D_sK$ analysis [141] using an identical procedure as outlined in Section 10.1. The usage of this calibration also for $B_s \to D_sK\pi\pi$ decays is justified by the fact that the decay-tree fit correctly propagates the momentum and vertex uncertainties; the main effects expected to be influenced by the decay topology. In contrast, the influence of the detector alignment is assumed to be decay channel independent. It is verified on simulated data that the calibration functions for $B_s \to D_sK\pi\pi$ and $B_s \to D_sK$ decays are indeed equivalent [2].

Table E.3: Offline selection requirements for fake B_s candidates from promptly produced D_s candidates combined with random prompt $K\pi\pi$ bachelor tracks. The PID and veto cuts depending on the D_s final state and Dalitz plot position are the same as in Table E.1.

	Description	Requirement
$B_s \to D_sK\pi\pi$	χ^2_{vtx}/ndof	< 8
	χ^2_{DTF}/ndof	< 15
	t	$< 0\,\text{ps}$
$D_s \to hhh$	χ^2_{vtx}/ndof	< 5
	DIRA	> 0.99994
	χ^2_{FD}	> 9
	p_T	> 1800 MeV
	χ^2_{IP}	< 9
	$\chi^2_{IP}(h)$	> 5
	Wrong PV veto	nPV $= 1$ || $\min(\Delta\chi^2_{IP}) > 20$
$X_s \to K\pi\pi$	$\chi^2_{IP}(h)$	< 40
	$\Delta \ln \mathcal{L}_{K\pi}$(K)	> 10
	$\Delta \ln \mathcal{L}_{K\pi}(\pi)$	< 5
	isMuon(h)	False
All tracks	p_T	> 500 MeV

Decay-time acceptance

As the candidates selected by the L0-TIS and L0-TOS requirements (see Section 9.2) have different kinematic properties, the decay-time acceptance has to be studied separately for these categories. As the trigger conditions have changed for Run-II, a further splitting in two data-taking periods (Run-I and Run-II) is necessary. Tables E.4 to E.7 list the determined decay-time acceptance parameters for different data-taking periods and trigger categories. One of the coefficients (v_{N-1}) is fixed to unity in as the overall efficiency scale does not matter. To stabilize the B-spline curve at large decay times where the statistics is low, the last coefficient (v_N) is fixed by a linear extrapolation from the two previous coefficients.

Table E.4: Time acceptance parameters for events in category [Run-I,L0-TOS].

Knot position	Coefficient	$B_s^0 \to D_s K\pi\pi$ data	$B_s^0 \to D_s K\pi\pi$ MC	Ratio
0.4	v_0	0.309 ± 0.018	0.410 ± 0.007	1.007 ± 0.029
0.5	v_1	0.694 ± 0.031	0.776 ± 0.011	0.936 ± 0.021
1.4	v_2	0.858 ± 0.043	0.896 ± 0.015	1.004 ± 0.024
2.5	v_3	1.090 ± 0.028	1.099 ± 0.009	0.992 ± 0.015
6.5	v_4	1.0 (fixed)	1.0 (fixed)	1.0 (fixed)
10.0	v_5	0.921 (interpolated)	0.913 (interpolated)	1.007 (interpolated)

Table E.5: Time acceptance parameters for events in category [Run-I,L0-TIS].

Knot position	Coefficient	$B_s^0 \to D_s K\pi\pi$ data	$B_s^0 \to D_s K\pi\pi$ MC	Ratio
0.4	v_0	0.158 ± 0.014	0.216 ± 0.005	0.986 ± 0.040
0.5	v_1	0.422 ± 0.029	0.524 ± 0.010	0.965 ± 0.029
1.4	v_2	0.802 ± 0.047	0.860 ± 0.017	0.982 ± 0.029
2.5	v_3	1.099 ± 0.034	1.098 ± 0.011	1.002 ± 0.019
6.5	v_4	1.0 (fixed)	1.0 (fixed)	1.0 (fixed)
10.0	v_5	0.913 (interpolated)	0.914 (interpolated)	0.998 (interpolated)

Table E.6: Time acceptance parameters for events in category [Run-II,L0-TOS].

Knot position	Coefficient	$B_s^0 \to D_s K\pi\pi$ data	$B_s^0 \to D_s K\pi\pi$ MC	Ratio
0.4	v_0	0.285 ± 0.009	0.368 ± 0.005	1.023 ± 0.020
0.5	v_1	0.663 ± 0.017	0.749 ± 0.009	0.911 ± 0.016
1.4	v_2	0.856 ± 0.025	0.893 ± 0.012	1.016 ± 0.019
2.5	v_3	1.060 ± 0.017	1.071 ± 0.008	0.996 ± 0.013
6.5	v_4	1.0 (fixed)	1.0 (fixed)	1.0 (fixed)
10.0	v_5	0.948 (interpolated)	0.938 (interpolated)	1.004 (interpolated)

Table E.7: Time acceptance parameters for events in category [Run-II,L0-TIS].

Knot position	Coefficient	$B_s^0 \to D_s K\pi\pi$ data	$B_s^0 \to D_s K\pi\pi$ MC	Ratio
0.4	v_0	0.117 ± 0.008	0.171 ± 0.003	0.965 ± 0.034
0.5	v_1	0.422 ± 0.019	0.474 ± 0.008	0.952 ± 0.024
1.4	v_2	0.733 ± 0.027	0.777 ± 0.013	0.973 ± 0.025
2.5	v_3	1.071 ± 0.020	1.046 ± 0.010	0.989 ± 0.015
6.5	v_4	1.0 (fixed)	1.0 (fixed)	1.0 (fixed)
10.0	v_5	0.938 (interpolated)	0.959 (interpolated)	1.009 (interpolated)

Amplitude model

Tables E.8 ($b \to c$ amplitudes) and E.9 ($b \to u$ amplitudes) lists the interference fractions, ordered by magnitude, for the baseline LASSO model of $B_s \to D_s K\pi\pi$ decays. The decay fractions for several alternative models are summarized in Tables E.10 and E.11.

Table E.8: Interference fractions (ordered by magnitude) of the $b \to c$ intermediate-state amplitudes included in the LASSO model. Only the statistical uncertainties are given.

Decay Channel i	Decay Channel j	I_{ij}[%]
$B_s \to D_s\,(K_1(1400) \to K^*(892)\,\pi)$	$B_s \to (D_s\,\pi)_P\ K^*(892)$	-10.1 ± 4.2
$B_s \to D_s\,(K_1(1270) \to K^*(892)\,\pi)$	$B_s \to D_s\,(K_1(1400) \to K^*(892)\,\pi)$	8.8 ± 4.1
$B_s \to D_s\,(K_1(1270) \to K^*(892)\,\pi)$	$B_s \to (D_s\,\pi)_P\ K^*(892)$	-5.6 ± 1.3
$B_s \to D_s\,(K_1(1400) \to K^*(892)\,\pi)$	$B_s \to D_s\,(K_1(1270) \to K\,\rho(770))$	5.3 ± 0.5
$B_s \to D_s\,(K^*(1410) \to K^*(892)\,\pi)$	$B_s \to D_s\,(K^*(1410) \to K\,\rho(770))$	5.1 ± 0.3
$B_s \to D_s\,(K_1(1270) \to K_0^*(1430)\,\pi)$	$B_s \to D_s\,(K_1(1270) \to K\,\rho(770))$	-2.3 ± 0.8
$B_s \to (D_s\,\pi)_P\ K^*(892)$	$B_s \to D_s\,(K_1(1270) \to K\,\rho(770))$	0.5 ± 0.2
$B_s \to D_s\,(K_1(1270) \to K^*(892)\,\pi)$	$B_s \to D_s\,(K_1(1270) \to K\,\rho(770))$	-0.2 ± 0.4
$B_s \to D_s\,(K_1(1400) \to K^*(892)\,\pi)$	$B_s \to D_s\,(K_1(1270) \to K_0^*(1430)\,\pi)$	-0.1 ± 0.0
$B_s \to (D_s\,\pi)_P\ K^*(892)$	$B_s \to D_s\,(K_1(1270) \to K_0^*(1430)\,\pi)$	0.0 ± 0.0
$B_s \to D_s\,(K_1(1400) \to K^*(892)\,\pi)$	$B_s \to D_s\,(K^*(1410) \to K\,\rho(770))$	-0.0 ± 0.0
$B_s \to D_s\,(K_1(1400) \to K^*(892)\,\pi)$	$B_s \to D_s\,(K^*(1410) \to K^*(892)\,\pi)$	-0.0 ± 0.0
$B_s \to D_s\,(K^*(1410) \to K^*(892)\,\pi)$	$B_s \to D_s\,(K_1(1270) \to K\,\rho(770))$	0.0 ± 0.0
$B_s \to D_s\,(K^*(1410) \to K^*(892)\,\pi)$	$B_s \to D_s\,(K_1(1270) \to K_0^*(1430)\,\pi)$	-0.0 ± 0.0
$B_s \to D_s\,(K^*(1410) \to K\,\rho(770))$	$B_s \to D_s\,(K_1(1270) \to K\,\rho(770))$	-0.0 ± 0.0
$B_s \to D_s\,(K_1(1270) \to K^*(892)\,\pi)$	$B_s \to D_s\,(K_1(1270) \to K_0^*(1430)\,\pi)$	-0.0 ± 0.0
$B_s \to D_s\,(K^*(1410) \to K^*(892)\,\pi)$	$B_s \to (D_s\,\pi)_P\ K^*(892)$	-0.0 ± 0.0
$B_s \to (D_s\,\pi)_P\ K^*(892)$	$B_s \to D_s\,(K^*(1410) \to K\,\rho(770))$	0.0 ± 0.0
$B_s \to D_s\,(K^*(1410) \to K\,\rho(770))$	$B_s \to D_s\,(K_1(1270) \to K_0^*(1430)\,\pi)$	-0.0 ± 0.0
$B_s \to D_s\,(K_1(1270) \to K^*(892)\,\pi)$	$B_s \to D_s\,(K^*(1410) \to K^*(892)\,\pi)$	-0.0 ± 0.0
$B_s \to D_s\,(K_1(1270) \to K^*(892)\,\pi)$	$B_s \to D_s\,(K^*(1410) \to K\,\rho(770))$	0.0 ± 0.0

Table E.9: Interference fractions (ordered by magnitude) of the $b \to u$ intermediate-state amplitudes included in the LASSO model. Only the statistical uncertainties are given.

Decay Channel i	Decay Channel j	I_{ij}[%]
$B_s \to D_s\,(K_1(1270) \to K^*(892)\,\pi)$	$B_s \to (D_s\,\pi)_P\ K^*(892)$	-20.7 ± 4.9
$B_s \to D_s\,(K_1(1270) \to K^*(892)\,\pi)$	$B_s \to D_s\,(K_1(1400) \to K^*(892)\,\pi)$	-20.0 ± 8.7
$B_s \to D_s\,(K_1(1400) \to K^*(892)\,\pi)$	$B_s \to (D_s\,\pi)_P\ K^*(892)$	18.9 ± 9.7
$B_s \to D_s\,(K(1460) \to K^*(892)\,\pi)$	$B_s \to (D_s\,\pi)_P\ K^*(892)$	-8.4 ± 1.2
$B_s \to (D_s\,K)_P\ \rho(770)$	$B_s \to D_s\,(K_1(1270) \to K_0^*(1430)\,\pi)$	-6.3 ± 1.2
$B_s \to D_s\,(K_1(1270) \to K_0^*(1430)\,\pi)$	$B_s \to D_s\,(K_1(1270) \to K\,\rho(770))$	-5.5 ± 1.7
$B_s \to (D_s\,\pi)_P\ K^*(892)$	$B_s \to (D_s\,K)_P\ \rho(770)$	3.1 ± 0.6
$B_s \to D_s\,(K_1(1400) \to K^*(892)\,\pi)$	$B_s \to (D_s\,K)_P\ \rho(770)$	2.0 ± 0.6
$B_s \to D_s\,(K_1(1400) \to K^*(892)\,\pi)$	$B_s \to D_s\,(K_1(1270) \to K\,\rho(770))$	2.0 ± 1.3
$B_s \to (D_s\,\pi)_P\ K^*(892)$	$B_s \to D_s\,(K_1(1270) \to K\,\rho(770))$	1.7 ± 0.8
$B_s \to D_s\,(K(1460) \to K^*(892)\,\pi)$	$B_s \to (D_s\,K)_P\ \rho(770)$	-1.5 ± 0.3
$B_s \to D_s\,(K_1(1270) \to K^*(892)\,\pi)$	$B_s \to (D_s\,K)_P\ \rho(770)$	-1.3 ± 0.4
$B_s \to D_s\,(K_1(1270) \to K^*(892)\,\pi)$	$B_s \to D_s\,(K_1(1270) \to K\,\rho(770))$	-0.6 ± 1.0
$B_s \to (D_s\,\pi)_P\ K^*(892)$	$B_s \to D_s\,(K_1(1270) \to K_0^*(1430)\,\pi)$	0.1 ± 0.0
$B_s \to (D_s\,K)_P\ \rho(770)$	$B_s \to D_s\,(K_1(1270) \to K\,\rho(770))$	-0.1 ± 2.9
$B_s \to D_s\,(K(1460) \to K^*(892)\,\pi)$	$B_s \to D_s\,(K_1(1270) \to K\,\rho(770))$	0.1 ± 0.0
$B_s \to D_s\,(K_1(1270) \to K^*(892)\,\pi)$	$B_s \to D_s\,(K(1460) \to K^*(892)\,\pi)$	0.0 ± 0.0
$B_s \to D_s\,(K_1(1400) \to K^*(892)\,\pi)$	$B_s \to D_s\,(K(1460) \to K^*(892)\,\pi)$	-0.0 ± 0.0
$B_s \to D_s\,(K_1(1270) \to K^*(892)\,\pi)$	$B_s \to D_s\,(K_1(1270) \to K_0^*(1430)\,\pi)$	-0.0 ± 0.0
$B_s \to D_s\,(K_1(1400) \to K^*(892)\,\pi)$	$B_s \to D_s\,(K_1(1270) \to K_0^*(1430)\,\pi)$	0.0 ± 0.0
$B_s \to D_s\,(K(1460) \to K^*(892)\,\pi)$	$B_s \to D_s\,(K_1(1270) \to K_0^*(1430)\,\pi)$	0.0 ± 0.0

Table E.10: Decay fractions in percent for the baseline and several alternative amplitude models (Alt. 1 - Alt. 6). Resonance parameters and the physical observables $r, \kappa, \delta, \gamma - 2\beta_s$ are also given.

		Baseline	Alt.1	Alt.2	Alt.3	Alt.4	Alt.5	Alt.6
$b \to c$	$B_s \to D_s\,(K_1(1270) \to K^*(892)\,\pi)$	6.2	6.5	6.7	5.2	5.4	6.1	6.0
	$B_s \to D_s\,(K_1(1270)[D] \to K^*(892)\,\pi)$			1.3				
	$B_s \to D_s\,(K_1(1270) \to K\,\rho(770))$	12.3	10.3	9.8	9.4	13.9	11.2	12.9
	$B_s \to D_s\,(K_1(1270) \to K\,\rho(1450))$							
	$B_s \to D_s\,(K_1(1270) \to K_0^*(1430)\,\pi)$	3.3	2.5	2.3	2.6	3.5	2.8	3.5
	$B_s \to D_s\,(K_1(1400) \to K^*(892)\,\pi)$	47.9	54.3	53.5	58.8	47.0	53.7	43.7
	$B_s \to D_s\,(K_1(1400) \to K\,\rho(770))$							
	$B_s \to D_s\,(K^*(1410) \to K^*(892)\,\pi)$	15.9	15.0	15.6	15.7	17.6	15.7	16.1
	$B_s \to D_s\,(K^*(1410) \to K\,\rho(770))$	6.5	5.5	6.2	6.3	6.5	6.5	6.6
	$B_s \to D_s\,(K(1460) \to K^*(892)\,\pi)$		0.8					
	$B_s \to D_s\,(K(1460) \to K\,\rho(770))$							
	$B_s \to D_s\,(K(1460) \to K\,\sigma)$							
	$B_s \to D_s\,(K^*(1680) \to K^*(892)\,\pi)$							
	$B_s \to D_s\,(K^*(1680) \to K\,\rho(770))$							
	$B_s \to D_s\,(K_2(1770) \to K^*(892)\,\pi)$							
	$B_s \to (D_s\,\pi)_S\ K^*(892)$							
	$B_s \to (D_s\,\pi)_P\ K^*(892)$	6.7	9.2	7.9	10.3	13.9	6.8	6.4
	$B_s[P] \to (D_s\,\pi)_P\ K^*(892)$					0.1		
	$B_s[D] \to (D_s\,\pi)_P\ K^*(892)$					0.9		
	$B_s \to (D_s\,K)_S\ \sigma$							
	$B_s \to (D_s\,K)_P\ \sigma$							
	$B_s \to (D_s\,K)_S\ f_0(980)$							
	$B_s \to (D_s\,K)_S\ f_2(1270)$							0.0
	$B_s \to (D_s\,K)_P\ f_2(1270)$							
	$B_s \to (D_s\,K)_S\ f_0(1370)$							
	$B_s \to (D_s\,K)_S\ \rho(770)$							
	$B_s \to (D_s\,K)_P\ \rho(770)$		0.7				0.1	
	$B_s[P] \to (D_s\,K)_P\ \rho(770)$							
	$B_s[D] \to (D_s\,K)_P\ \rho(770)$							
	Sum	98.9	104.7	103.2	108.3	108.8	103.1	95.2
$b \to u$	$B_s \to D_s\,(K_1(1270) \to K^*(892)\,\pi)$	15.0	20.9	21.0	18.2	11.5	19.1	13.8
	$B_s \to D_s\,(K_1(1270)[D] \to K^*(892)\,\pi)$			4.0				
	$B_s \to D_s\,(K_1(1270) \to K\,\rho(770))$	29.5	33.3	30.8	33.0	29.8	35.2	29.6
	$B_s \to D_s\,(K_1(1270) \to K\,\rho(1450))$							
	$B_s \to D_s\,(K_1(1270) \to K_0^*(1430)\,\pi)$	8.0	8.2	7.2	9.2	7.5	8.9	8.2
	$B_s \to D_s\,(K_1(1400) \to K^*(892)\,\pi)$	15.5	29.5	21.2	22.1	23.5	15.4	19.6
	$B_s \to D_s\,(K_1(1400) \to K\,\rho(770))$							
	$B_s \to D_s\,(K^*(1410) \to K^*(892)\,\pi)$		2.2					
	$B_s \to D_s\,(K^*(1410) \to K\,\rho(770))$		0.8					
	$B_s \to D_s\,(K(1460) \to K^*(892)\,\pi)$	22.3	19.1	12.9	17.2	15.1	21.7	21.9
	$B_s \to D_s\,(K(1460) \to K\,\rho(770))$				3.5			
	$B_s \to D_s\,(K(1460) \to K\,\sigma)$				2.3			
	$B_s \to D_s\,(K^*(1680) \to K^*(892)\,\pi)$							
	$B_s \to D_s\,(K^*(1680) \to K\,\rho(770))$							
	$B_s \to D_s\,(K_2(1770) \to K^*(892)\,\pi)$							
	$B_s \to (D_s\,\pi)_S\ K^*(892)$							
	$B_s \to (D_s\,\pi)_P\ K^*(892)$	37.6	16.3	23.1	17.3	61.2	29.3	41.8
	$B_s[P] \to (D_s\,\pi)_P\ K^*(892)$					0.6		
	$B_s[D] \to (D_s\,\pi)_P\ K^*(892)$					3.8		
	$B_s \to (D_s\,K)_S\ \sigma$							
	$B_s \to (D_s\,K)_P\ \sigma$							
	$B_s \to (D_s\,K)_S\ f_0(980)$							
	$B_s \to (D_s\,K)_S\ f_2(1270)$							0.2
	$B_s \to (D_s\,K)_P\ f_2(1270)$							
	$B_s \to (D_s\,K)_S\ f_0(1370)$							
	$B_s \to (D_s\,K)_S\ \rho(770)$							
	$B_s \to (D_s\,K)_P\ \rho(770)$	8.4	8.2	4.8	13.3	8.4	12.6	7.5
	$B_s[P] \to (D_s\,K)_P\ \rho(770)$						0.9	
	$B_s[D] \to (D_s\,K)_P\ \rho(770)$						0.8	
	Sum	136.4	138.7	124.9	136.0	161.5	143.8	142.6
	$m_{K_1(1400)}$ [MeV]	1397	1389	1389	1394	1410	1392	1403
	$\Gamma_{K_1(1400)}$ [MeV]	205	210	207	220	222	207	205
	$m_{K^*(1410)}$ [MeV]	1432	1435	1436	1429	1435	1428	1432
	$\Gamma_{K^*(1410)}$ [MeV]	345	351	348	347	360	346	347
	r	0.50	0.46	0.48	0.49	0.51	0.49	0.51
	κ	0.52	0.61	0.54	0.30	0.53	0.51	0.51
	$\delta\,[^\circ]$	46	58	57	46	42	55	45
	$\gamma - 2\beta_s\,[^\circ]$	61	70	57	60	54	67	62

Table E.11: Decay fractions in percent for several alternative amplitude models (Alt. 7 - Alt. 12). Resonance parameters and the physical observables $r, \kappa, \delta, \gamma - 2\beta_s$ are also given.

		Alt.7	Alt.8	Alt.9	Alt.10	Alt.11	Alt.12
$b \to c$	$B_s \to D_s\,(K_1(1270) \to K^*(892)\,\pi)$	6.9	7.6	6.1	6.7	8.1	6.3
	$B_s \to D_s\,(K_1(1270)[D] \to K^*(892)\,\pi)$						
	$B_s \to D_s\,(K_1(1270) \to K\,\rho(770))$	13.8	12.8	13.2	11.0	14.7	14.9
	$B_s \to D_s\,(K_1(1270) \to K\,\rho(1450))$						
	$B_s \to D_s\,(K_1(1270) \to K_0^*(1430)\,\pi)$	3.8	3.1	3.3	3.3	4.0	3.3
	$B_s \to D_s\,(K_1(1400) \to K^*(892)\,\pi)$	47.8	45.7	49.8	52.6	46.4	49.9
	$B_s \to D_s\,(K_1(1400) \to K\,\rho(770))$						0.6
	$B_s \to D_s\,(K^*(1410) \to K^*(892)\,\pi)$	15.4	15.5	18.8	15.2	15.5	15.9
	$B_s \to D_s\,(K^*(1410) \to K\,\rho(770))$	5.8	6.0	5.2	6.3	6.2	6.3
	$B_s \to D_s\,(K(1460) \to K^*(892)\,\pi)$						
	$B_s \to D_s\,(K(1460) \to K\,\rho(770))$						
	$B_s \to D_s\,(K(1460) \to K\,\sigma)$						
	$B_s \to D_s\,(K^*(1680) \to K^*(892)\,\pi)$			0.8			
	$B_s \to D_s\,(K^*(1680) \to K\,\rho(770))$			0.9			
	$B_s \to D_s\,(K_2(1770) \to K^*(892)\,\pi)$				0.7		
	$B_s \to (D_s\,\pi)_S\ K^*(892)$						
	$B_s \to (D_s\,\pi)_P\ K^*(892)$	7.8	5.7	7.7	7.3	7.1	6.5
	$B_s[P] \to (D_s\,\pi)_P\ K^*(892)$						
	$B_s[D] \to (D_s\,\pi)_P\ K^*(892)$						
	$B_s \to (D_s\,K)_S\ \sigma$	1.6	0.4				
	$B_s \to (D_s\,K)_P\ \sigma$	2.9					
	$B_s \to (D_s\,K)_S\ f_0(980)$		0.6				
	$B_s \to (D_s\,K)_S\ f_2(1270)$						
	$B_s \to (D_s\,K)_P\ f_2(1270)$						
	$B_s \to (D_s\,K)_S\ f_0(1370)$						
	$B_s \to (D_s\,K)_S\ \rho(770)$						
	$B_s \to (D_s\,K)_P\ \rho(770)$						
	$B_s[P] \to (D_s\,K)_P\ \rho(770)$						
	$B_s[D] \to (D_s\,K)_P\ \rho(770)$						
	Sum	105.7	97.4	105.8	103.1	102.0	103.8
$b \to u$	$B_s \to D_s\,(K_1(1270) \to K^*(892)\,\pi)$	9.7	14.3	14.4	19.3	8.0	13.3
	$B_s \to D_s\,(K_1(1270)[D] \to K^*(892)\,\pi)$						
	$B_s \to D_s\,(K_1(1270) \to K\,\rho(770))$	19.3	24.1	31.3	31.7	14.5	31.5
	$B_s \to D_s\,(K_1(1270) \to K\,\rho(1450))$						
	$B_s \to D_s\,(K_1(1270) \to K_0^*(1430)\,\pi)$	5.3	5.9	7.8	9.5	4.0	7.1
	$B_s \to D_s\,(K_1(1400) \to K^*(892)\,\pi)$	6.8	14.3	12.0	18.7	8.9	15.7
	$B_s \to D_s\,(K_1(1400) \to K\,\rho(770))$						0.2
	$B_s \to D_s\,(K^*(1410) \to K^*(892)\,\pi)$						
	$B_s \to D_s\,(K^*(1410) \to K\,\rho(770))$						
	$B_s \to D_s\,(K(1460) \to K^*(892)\,\pi)$	29.4	27.0	23.1	22.6	28.9	22.8
	$B_s \to D_s\,(K(1460) \to K\,\rho(770))$						
	$B_s \to D_s\,(K(1460) \to K\,\sigma)$						
	$B_s \to D_s\,(K^*(1680) \to K^*(892)\,\pi)$						
	$B_s \to D_s\,(K^*(1680) \to K\,\rho(770))$						
	$B_s \to D_s\,(K_2(1770) \to K^*(892)\,\pi)$				0.8		
	$B_s \to (D_s\,\pi)_S\ K^*(892)$						
	$B_s \to (D_s\,\pi)_P\ K^*(892)$	45.5	40.9	39.3	27.0	46.6	35.3
	$B_s[P] \to (D_s\,\pi)_P\ K^*(892)$						
	$B_s[D] \to (D_s\,\pi)_P\ K^*(892)$						
	$B_s \to (D_s\,K)_S\ \sigma$	0.3	0.7				
	$B_s \to (D_s\,K)_P\ \sigma$	0.6					
	$B_s \to (D_s\,K)_S\ f_0(980)$		0.9				
	$B_s \to (D_s\,K)_S\ f_2(1270)$						
	$B_s \to (D_s\,K)_P\ f_2(1270)$						
	$B_s \to (D_s\,K)_S\ f_0(1370)$						
	$B_s \to (D_s\,K)_S\ \rho(770)$					4.1	
	$B_s \to (D_s\,K)_P\ \rho(770)$	4.6	8.4	8.6	7.9		7.3
	$B_s[P] \to (D_s\,K)_P\ \rho(770)$						
	$B_s[D] \to (D_s\,K)_P\ \rho(770)$						
	Sum	121.6	136.5	136.5	137.5	115.0	133.1
	$m_{K_1(1400)}$ [MeV]	1401	1393	1399	1394	1400	1393
	$\Gamma_{K_1(1400)}$ [MeV]	195	199	200	208	194	205
	$m_{K^*(1410)}$ [MeV]	1444	1438	1413	1432	1435	1433
	$\Gamma_{K^*(1410)}$ [MeV]	329	342	400	351	337	346
	r	0.44	0.46	0.49	0.46	0.46	0.49
	κ	0.46	0.51	0.51	0.54	0.56	0.44
	$\delta\,[^\circ]$	34	49	47	49	34	44
	$\gamma - 2\beta_s\,[^\circ]$	54	69	57	68	51	61

Bibliography

[1] P. d'Argent *et al.*, *Amplitude Analyses of $D^0 \to \pi^+\pi^-\pi^+\pi^-$ and $D^0 \to K^+K^-\pi^+\pi^-$ Decays*, JHEP **05** (2017) 143, arXiv:1703.08505.

[2] P. d'Argent, E. Gersabeck, M. T. Schiller, and M. Kecke, *Measurement of the CKM angle γ using $B_s \to D_s K\pi\pi$ decays*, LHCb-ANA-2018-021.

[3] LHCb Outer Tracker Group, P. d'Argent *et al.*, *Improved performance of the LHCb Outer Tracker in LHC Run 2*, JINST **12** (2017), no. 11 P11016, arXiv:1708.00819.

[4] M. E. Peskin and D. V. Schroeder, *An Introduction To Quantum Field Theory (Frontiers in Physics)*, Westview Press, 1995.

[5] S. L. Glashow, J. Iliopoulos, and L. Maiani, *Weak interactions with lepton-hadron symmetry*, Phys. Rev. D **2** (1970) 1285.

[6] A. Salam and J. C. Ward, *Weak and electromagnetic interactions*, Il Nuovo Cimento Series 10 **11** (1959), no. 4 568.

[7] S. Weinberg, *A model of leptons*, Phys. Rev. Lett. **19** (1967) 1264.

[8] M. Bartelmann and P. Schneider, *Weak gravitational lensing*, Phys. Rept. **340** (2001) 291, arXiv:astro-ph/9912508.

[9] A. H. Broeils, K. G. Begeman, and R. H. Sanders, *Extended rotation curves of spiral galaxies: dark haloes and modified dynamics*, Monthly Notices of the Royal Astronomical Society **249** (1991) 523.

[10] Particle Data Group, M. Tanabashi *et al.*, *Review of particle physics*, Phys. Rev. D **98** (2018) 030001.

[11] H. J. Rothe, *Lattice gauge theories: An Introduction*, World Sci. Lect. Notes Phys. **43** (1992) 1.

[12] A. Lenz, *Lifetimes and heavy quark expansion*, Int. J. Mod. Phys. **A30** (2015), no. 10 1543005.

[13] N. Uraltsev, *Heavy quark expansion in beauty and its decays*, Proc. Int. Sch. Phys. Fermi **137** (1998) 329, arXiv:hep-ph/9804275.

[14] R. P. Feynman, M. Kislinger, and F. Ravndal, *Current matrix elements from a relativistic quark model*, Phys. Rev. D **3** (1971) 2706.

[15] L. Micu, *Decay rates of meson resonances in a quark model*, Nuclear Physics B **10** (1969), no. 3 521 .

[16] M. Gell-Mann, *A Schematic Model of Baryons and Mesons*, Phys. Lett. **8** (1964) 214.

[17] E. Noether, *Invariant variation problems*, Transport Theory and Statistical Physics **1** (1971) 186, arXiv:physics/0503066.

[18] C. S. Wu *et al.*, *Experimental test of parity conservation in beta decay*, Phys. Rev. **105** (1957) 1413.

[19] J. H. Christenson, J. W. Cronin, V. L. Fitch, and R. Turlay, *Evidence for the* 2π *Decay of the* K_2^0 *Meson*, Phys. Rev. Lett. **13** (1964) 138.

[20] A. D. Sakharov, *Violation of CP Invariance, C asymmetry, and baryon asymmetry of the universe*, Pisma Zh. Eksp. Teor. Fiz. **5** (1967) 32.

[21] A. Riotto, *Theories of baryogenesis*, in *Proceedings, Summer School in High-energy physics and cosmology: Trieste, Italy*, pp. 326–436, 1998. arXiv:hep-ph/9807454.

[22] Belle, S. K. Choi *et al.*, *Observation of a resonance-like structure in the* $\pi^+\psi'$ *mass distribution in exclusive* $B \to K\pi^+\psi'$ *decays*, Phys. Rev. Lett. **100** (2008) 142001, arXiv:0708.1790.

[23] LHCb collaboration, R. Aaij *et al.*, *Observation of the resonant character of the* $Z(4430)^-$ *state*, Phys. Rev. Lett. **112** (2014) 222002, arXiv:1404.1903.

[24] LHCb collaboration, R. Aaij *et al.*, *Observation of* $J/\psi p$ *resonances consistent with pentaquark states in* $\Lambda_b^0 \to J/\psi p K^-$ *decays*, Phys. Rev. Lett. **115** (2015) 072001, arXiv:1507.03414.

[25] S. Godfrey and N. Isgur, *Mesons in a relativized quark model with chromodynamics*, Phys. Rev. D **32** (1985) 189.

[26] I. I. Y. Bigi, *CP violation: An essential mystery in nature's grand design*, Surveys High Energ. Phys. **12** (1998) 269.

[27] M. Pospelov and A. Ritz, *Theta induced electric dipole moment of the neutron via QCD sum rules*, Phys. Rev. Lett. **83** (1999) 2526, arXiv:hep-ph/9904483.

[28] N. Cabibbo, *Unitary symmetry and leptonic decays*, Phys. Rev. Lett. **10** (1963) 531.

[29] M. Kobayashi and T. Maskawa, *CP Violation in the Renormalizable Theory of Weak Interaction*, Prog. Theor. Phys. **49** (1973) 652.

[30] CKMfitter Group, J. Charles *et al.*, *CP violation and the CKM matrix: Assessing the impact of the asymmetric B factories*, Eur. Phys. J. **C41** (2005), no. 1 1, arXiv:hep-ph/0406184.

[31] L. Wolfenstein, *Parametrization of the Kobayashi-Maskawa Matrix*, Phys. Rev. Lett. **51** (1983) 1945.

[32] W. Heisenberg, *Über den anschaulichen Inhalt der quantentheoretischen Kinematik und Mechanik*, Zeitschrift für Physik **43** (1927) 172.

[33] T. D. Lee, R. Oehme, and C. N. Yang, *Remarks on possible noninvariance under time reversal and charge conjugation*, Phys. Rev. **106** (1957) 340.

[34] I. Dunietz, R. Fleischer, and U. Nierste, *In pursuit of new physics with* B_s *decays*, Phys. Rev. **D63** (2001) 114015, arXiv:hep-ph/0012219.

[35] Heavy Flavor Averaging Group, Y. Amhis *et al.*, *Averages of b-hadron, c-hadron, and τ-lepton properties as of summer 2016*, Eur. Phys. J. **C77** (2017) 895, arXiv:1612.07233, updated results and plots available at https://hflav.web.cern.ch.

[36] T. Inami and C. S. Lim, *Effects of Superheavy Quarks and Leptons in Low-Energy Weak Processes $K_L \to \mu\bar{\mu}, K^+ \to \pi^+\nu\bar{\nu}$ and $K^0 \leftrightarrow \bar{K}^0$*, Prog. Theor. Phys. **65** (1981) 297, [Erratum: Prog. Theor. Phys.65,1772(1981)].

[37] S. L. Glashow, J. Iliopoulos, and L. Maiani, *Weak interactions with lepton-hadron symmetry*, Phys. Rev. D **2** (1970) 1285.

[38] M. Artuso, G. Borissov, and A. Lenz, *CP violation in the B_s^0 system*, Rev. Mod. Phys. **88** (2016), no. 4 045002, arXiv:1511.09466.

[39] A. Lenz and U. Nierste, *Theoretical update of $B_s - \bar{B}_s$ mixing*, JHEP **06** (2007) 072, arXiv:hep-ph/0612167.

[40] M. Blanke *et al.*, *Particle-Antiparticle Mixing, $\epsilon_K, \Delta\Gamma_q, A_{SL}^q, A_{CP}(B_s \to \psi\phi)$ and $B \to X_{s,d}\gamma$ in the Littlest Higgs Model with T-Parity*, JHEP **12** (2006) 003, arXiv:hep-ph/0605214.

[41] L. Di Luzio, M. Kirk, and A. Lenz, *Updated B_s-mixing constraints on new physics models for $b \to s\ell^+\ell^-$ anomalies*, Phys. Rev. **D97** (2018), no. 9 095035, arXiv:1712.06572.

[42] M. Ciuchini and L. Silvestrini, *Upper bounds on SUSY contributions to $b \to s$ transitions from B(s) - anti-B(s) mixing*, Phys. Rev. Lett. **97** (2006) 021803, arXiv:hep-ph/0603114.

[43] Y. Grossman, Y. Nir, and G. Raz, *Constraining the phase of $B_s - \bar{B}_s$ mixing*, Phys. Rev. Lett. **97** (2006) 151801, arXiv:hep-ph/0605028.

[44] Z. Ligeti, M. Papucci, and G. Perez, *Implications of the measurement of the $B_s^0 - \bar{B}_s^0$ mass difference*, Phys. Rev. Lett. **97** (2006) 101801, arXiv:hep-ph/0604112.

[45] Y. Nir, *CP violation in meson decays*, in *High-energy physics Proceedings, 3rd Latin American CERN-CLAF School, Malargue, Argentina*, pp. 79–145, 2006.

[46] B. Winstein and L. Wolfenstein, *The search for direct* CP *violation*, Rev. Mod. Phys. **65** (1993) 1113.

[47] U. Nierste, *Three Lectures on Meson Mixing and CKM phenomenology*, in *Heavy quark physics Proceedings, Helmholtz International School, HQP08, Dubna, Russia*, pp. 1–38, 2009. arXiv:0904.1869.

[48] A. Hocker and Z. Ligeti, *CP violation and the CKM matrix*, Ann. Rev. Nucl. Part. Sci. **56** (2006) 501, arXiv:hep-ph/0605217.

[49] KTeV Collaboration, A. Alavi-Harati *et al.*, *Observation of Direct CP Violation in $K_{S,L} \to \pi\pi$ Decays*, Phys. Rev. Lett. **83** (1999) 22.

[50] S. M. Bilen'kii, in *CP Violation in Decays of Neutral K-Mesons*, N. N. Bogolyubov, ed., pp. 146–164, Springer US, New York, NY, 1972.

[51] A. L. Kagan and M. D. Sokoloff, *On Indirect CP Violation and Implications for $D^0 - \bar{D}^0$ and $B_s - \bar{B}_s$ mixing*, Phys. Rev. **D80** (2009) 076008, arXiv:0907.3917.

[52] L. Wolfenstein, *Violation of CP Invariance and the Possibility of Very Weak Interactions*, Physical Review Letters **13** (1964) 562.

[53] E. Fermi, *Nuclear Physics*, University Of Chicago Press, 1974.

[54] E. Byckling and K. Kajantie, *Particle Kinematics*, John Wiley & Sons, 1973.

[55] R. H. Dalitz, *On the analysis of τ-meson data and the nature of the τ-meson*, The London, Edinburgh, and Dublin Philosophical Magazine and Journal of Science **44** (1953), no. 357 1068.

[56] R. H. Dalitz, *Decay of τ mesons of known charge*, Phys. Rev. **94** (1954) 1046.

[57] CLEO, D. Cronin-Hennessy *et al.*, *Searches for CP violation and $\pi\pi$ S-wave in the Dalitz-Plot of $D^0 \to \pi^+\pi^-\pi^0$*, Phys. Rev. **D72** (2005) 031102, arXiv:hep-ex/0503052, [Erratum: Phys. Rev.D75,119904(2007)].

[58] S Mandelstam and J. E Paton and Ronald F Peierls and A. Q Sarker, *Isobar approximation of production processes*, Annals of Physics **18** (1962), no. 2 198 .

[59] D. J. Herndon, P. Söding, and R. J. Cashmore, *Generalized isobar model formalism*, Phys. Rev. D **11** (1975) 3165.

[60] J. J. Brehm, *Unitarity and the isobar model: two-body discontinuities*, Annals of Physics **108** (1977), no. 2 454 .

[61] C. Zemach, *Use of angular momentum tensors*, Phys. Rev. **140** (1965) B97.

[62] C. Zemach, *Determination of the Spins and Parities of Resonances*, Phys. Rev. **140** (1965) B109.

[63] V. Filippini, A. Fontana, and A. Rotondi, *Covariant spin tensors in meson spectroscopy*, Phys. Rev. **D51** (1995) 2247.

[64] B. S. Zou and D. V. Bugg, *Covariant tensor formalism for partial wave analyses of ψ decay to mesons*, Eur. Phys. J. **A16** (2003) 537, arXiv:hep-ph/0211457.

[65] W. Rarita and J. Schwinger, *On a theory of particles with half integral spin*, Phys. Rev. **60** (1941) 61.

[66] F. von Hippel and C. Quigg, *Centrifugal-barrier effects in resonance partial decay widths, shapes, and production amplitudes*, Phys. Rev. D **5** (1972) 624.

[67] CLEO Collaboration, D. M. Asner *et al.*, *Hadronic structure in the decay $\tau^- \to \nu_\tau \pi^- \pi^0 \pi^0$ and the sign of the tau neutrino helicity*, Phys. Rev. D **61** (1999) 012002.

[68] V. Weisskopf and E. Wigner, *Berechnung der natürlichen Linienbreite auf Grund der Diracschen Lichttheorie*, Zeitschrift für Physik **63** (1930) 54.

[69] G. Breit and E. Wigner, *Capture of slow neutrons*, Phys. Rev. **49** (1936) 519.

[70] S. Willenbrock and G. Valencia, *On the definition of the Z-boson mass*, Physics Letters B **259** (1991), no. 3 373 .

[71] A. Sirlin, *Theoretical considerations concerning the Z^0 mass*, Phys. Rev. Lett. **67** (1991) 2127.

[72] A. R. Bohm and Y. Sato, *Relativistic resonances: Their masses, widths, lifetimes, superposition, and causal evolution*, Phys. Rev. **D71** (2005) 085018, arXiv:hep-ph/0412106.

[73] J. R. Argand, *Essai sur une manière de représenter les quantités imaginaires dans les constructions géométriques*, Paris Gauthier-Villars, Paris.

[74] BES Collaboration, M. Ablikim *et al.*, *Resonances in $J/\psi \to \phi\pi^+\pi^-$ and ϕK^+K^-*, Phys. Lett. **B607** (2005) 243, arXiv:hep-ex/0411001.

[75] N. Isgur, C. Morningstar, and C. Reader, *The a_1 in τ decay*, Phys. Rev. D **39** (1989) 1357.

[76] M. Vojik and P. Lichard, *Three-pion decays of the τ lepton, the $a_1(1260)$ properties, and the $a_1\rho\pi$ Lagrangian*, arXiv:1006.2919.

[77] G. J. Gounaris and J. J. Sakurai, *Finite-width corrections to the vector-meson-dominance prediction for $\rho \to e^+e^-$*, Phys. Rev. Lett. **21** (1968) 244.

[78] P. Lichard and M. Vojik, *An alternative parametrization of the pion form-factor and the mass and width of $\rho(770)$*, arXiv:hep-ph/0611163.

[79] G. Cowan, *Statistical Data Analysis*, Oxford science publications, Clarendon Press, 1998.

[80] R. J. Barlow, *Statistics: a guide to the use of statistical methods in the physical sciences*, Manchester physics series, Wiley, Chichester, 1989.

[81] F. James, *MINUIT Function Minimization and Error Analysis: Reference Manual Version 94.1*, 1994.

[82] X.-G. He and G. Valencia, *An extended scalar sector to address the tension between a fourth generation and Higgs searches at the LHC*, Phys. Lett. **B707** (2012) 381, arXiv:1108.0222.

[83] D. Das, A. Kundu, and I. Saha, *Higgs data does not rule out a sequential fourth generation with an extended scalar sector*, Phys. Rev. **D97** (2018), no. 1 011701, arXiv:1707.03000.

[84] A. Crivellin, *Effects of right-handed charged currents on the determinations of $|V_{ub}|$ and $|V_{cb}|$*, Phys. Rev. **D81** (2010) 031301, arXiv:0907.2461.

[85] F. U. Bernlochner, Z. Ligeti, and S. Turczyk, *New ways to search for right-handed current in $B \to \rho l \bar{\nu}$ decay*, Phys. Rev. **D90** (2014), no. 9 094003, arXiv:1408.2516.

[86] V. Barger, C.-W. Chiang, P. Langacker, and H.-S. Lee, *Z' mediated flavor changing neutral currents in B meson decays*, Phys. Lett. **B580** (2004) 186, arXiv:hep-ph/0310073.

[87] V. Barger *et al.*, *Family Non-universal U(1)-prime Gauge Symmetries and $b \to s$ Transitions*, Phys. Rev. **D80** (2009) 055008, arXiv:0902.4507.

[88] B. Gripaios, M. Nardecchia, and S. A. Renner, *Composite leptoquarks and anomalies in B-meson decays*, JHEP **05** (2015) 006, arXiv:1412.1791.

[89] G. Hiller and M. Schmaltz, *R_K and future $b \to s\ell\ell$ physics beyond the standard model opportunities*, Phys. Rev. **D90** (2014) 054014, arXiv:1408.1627.

[90] C. A. Dominguez, *Introduction to QCD sum rules*, Mod. Phys. Lett. **A28** (2013) 1360002, arXiv:1305.7047.

[91] Belle, A. Sibidanov *et al.*, *Study of Exclusive $B \to X_u \ell \nu$ Decays and Extraction of $\|V_{ub}\|$ using Full Reconstruction Tagging at the Belle Experiment*, Phys. Rev. **D88** (2013), no. 3 032005, arXiv:1306.2781.

[92] BaBar, J. P. Lees *et al.*, *Branching fraction and form-factor shape measurements of exclusive charmless semileptonic B decays, and determination of* $|V_{ub}|$, Phys. Rev. **D86** (2012) 092004, arXiv:1208.1253.

[93] LHCb collaboration, R. Aaij *et al.*, *Determination of the quark coupling strength* $|V_{ub}|$ *using baryonic decays*, Nature Physics **11** (2015) 743, arXiv:1504.01568.

[94] Fermilab Lattice, MILC, J. A. Bailey *et al.*, $|V_{ub}|$ *from* $B \to \pi\ell\nu$ *decays and (2+1)-flavor lattice QCD*, Phys. Rev. **D92** (2015), no. 1 014024, arXiv:1503.07839.

[95] W. Detmold, C. Lehner, and S. Meinel, $\Lambda_b \to p\ell^-\bar{\nu}_\ell$ *and* $\Lambda_b \to \Lambda_c\ell^-\bar{\nu}_\ell$ *form factors from lattice QCD with relativistic heavy quarks*, Phys. Rev. **D92** (2015), no. 3 034503, arXiv:1503.01421.

[96] ETM, N. Carrasco *et al.*, *B-physics from* $N_f = 2$ *tmQCD: the Standard Model and beyond*, JHEP **03** (2014) 016, arXiv:1308.1851.

[97] Belle, I. Adachi *et al.*, *Measurement of the CP violation parameters in* $B^0 \to \pi^+\pi^-$ *decays*, Phys. Rev. **D88** (2013), no. 9 092003, arXiv:1302.0551.

[98] M. Gronau and J. L. Rosner, *Improving the measurement of the CKM phase* $\phi_2 = \alpha$ *in* $B \to \pi\pi$ *and* $B \to \rho\rho$ *decays*, Phys. Lett. **B763** (2016) 228, arXiv:1608.06224.

[99] BaBar, B. Aubert *et al.*, *Measurement of Time-Dependent CP Asymmetry in* $B^0 \to c\bar{c}K^{*0}$ *Decays*, Phys. Rev. **D79** (2009) 072009, arXiv:0902.1708.

[100] LHCb, R. Aaij *et al.*, *Measurement of CP violation in* $B^0 \to J/\psi K^0_S$ *decays*, Phys. Rev. Lett. **115** (2015), no. 3 031601, arXiv:1503.07089.

[101] T. Gershon and V. V. Gligorov, *CP violation in the B system*, Rept. Prog. Phys. **80** (2017), no. 4 046201, arXiv:1607.06746.

[102] LHCb collaboration, R. Aaij *et al.*, *Measurement of the CKM angle* γ *from a combination of LHCb results*, JHEP **12** (2016) 087, arXiv:1611.03076.

[103] LHCb collaboration, M. W. Kenzie and M. P. Whitehead, *Update of the LHCb combination of the CKM angle* γ, LHCb-CONF-2018-002.

[104] LHCb collaboration, R. Aaij *et al.*, *Determination of* γ *and* $-2\beta_s$ *from charmless two-body decays of beauty mesons*, Phys. Lett. **B739** (2015) 1, arXiv:1408.4368.

[105] LHCb collaboration, R. Aaij *et al.*, *First measurement of time-dependent CP violation in* $B^0_s \to K^+K^-$ *decays*, JHEP **10** (2013) 183, arXiv:1308.1428.

[106] LHCb collaboration, R. Aaij *et al.*, *Measurement of CP asymmetries in two-body* $B^0_{(s)}$*-meson decays to charged pions and kaons*, Phys. Rev. **D98** (2018), no. 3 032004, arXiv:1805.06759.

[107] R. Fleischer, *New strategies to extract* β *and* γ *from* $B_d \to \pi^+\pi^-$ *and* $B_s \to K^+K^-$, Phys. Lett. **B459** (1999) 306, arXiv:hep-ph/9903456.

[108] M. Gronau and D. Wyler, *On determining a weak phase from CP asymmetries in charged B decays*, Phys. Lett. **B265** (1991) 172.

[109] J. Brod and J. Zupan, *The ultimate theoretical error on* γ *from* $B \to DK$ *decays*, JHEP **01** (2014) 051, arXiv:1308.5663.

[110] M. Gronau and D. London, *How to determine all the angles of the unitarity triangle from $B_d \to DK_s$ and $B_s^0 \to D\phi$*, Phys. Lett. **B253** (1991) 483.

[111] D. Atwood, I. Dunietz, and A. Soni, *Enhanced CP violation with $B \to \mathrm{KD}^0(\overline{\mathrm{D}}^0)$ modes and extraction of the Cabibbo-Kobayashi-Maskawa Angle γ*, Phys. Rev. Lett. **78** (1997) 3257, arXiv:hep-ph/9612433.

[112] A. Bondar, A. Dolgov, A. Poluektov, and V. Vorobiev, *Effect of direct CP violation in charm on γ extraction from $B^\pm \to DK^\pm$, $D \to K_s^0\pi^+\pi^-$ Dalitz plot analysis*, The European Physical Journal C **73** (2013) 2476.

[113] Y. Grossman and M. Savastio, *Effects of $K^0 - \bar{K}^0$ mixing on determining γ from $B^\pm \to DK^\pm$*, JHEP **03** (2014) 008, arXiv:1311.3575.

[114] A. Giri, Y. Grossman, A. Soffer, and J. Zupan, *Determining γ using $B^\pm \to \mathrm{DK}^\pm$ with multibody D decays*, Phys. Rev. D **68** (2003) 054018.

[115] Belle, A. Poluektov *et al.*, *Measurement of ϕ_3 with Dalitz plot analysis of $B^\pm \to D^{(*)}K^\pm$ decays*, Phys. Rev. D **70** (2004) 072003.

[116] J. Rademacker and G. Wilkinson, *Determining the unitarity triangle γ with a four-body amplitude analysis of $B^\pm \to (K^+K^-\pi^+\pi^-)_D K^\pm$ decays*, Phys. Lett. **B647** (2007) 400, arXiv:hep-ph/0611272.

[117] M. Neubert and B. Stech, *Nonleptonic weak decays of B mesons*, Adv. Ser. Direct. High Energy Phys. **15** (1998) 294.

[118] D. Berdine, N. Kauer, and D. Rainwater, *Breakdown of the Narrow Width Approximation for New Physics*, Phys. Rev. Lett. **99** (2007) 111601, arXiv:hep-ph/0703058.

[119] M. Nayak *et al.*, *First determination of the CP content of $D \to \pi^+\pi^-\pi^0$ and $D \to K^+K^-\pi^0$*, Phys. Lett. **B740** (2015) 1, arXiv:1410.3964.

[120] S. Malde, C. Thomas, and G. Wilkinson, *Measuring CP violation and mixing in charm with inclusive self-conjugate multibody decay modes*, Phys. Rev. D **91** (2015) 094032.

[121] LHCb collaboration, R. Aaij *et al.*, *Measurement of CP observables in $B^\pm \to DK^\pm$ and $B^\pm \to D\pi^\pm$ with two- and four-body D decays*, Phys. Lett. **B760** (2016) 117, arXiv:1603.08993.

[122] A. Bondar and A. Poluektov, *Feasibility study of model-independent approach to ϕ_3 measurement using Dalitz plot analysis*, Eur. Phys. J. **C47** (2006) 347, arXiv:hep-ph/0510246.

[123] A. Bondar and A. Poluektov, *On model-independent measurement of the angle ϕ_3 using Dalitz plot analysis*, arXiv:hep-ph/0703267.

[124] S. Harnew *et al.*, *Model-independent determination of the strong phase difference between D^0 and $\bar{D}^0 \to \pi^+\pi^-\pi^+\pi^-$ amplitudes*, JHEP **01** (2018) 144, arXiv:1709.03467.

[125] LHCb collaboration, R. Aaij *et al.*, *Measurement of CP violation and constraints on the CKM angle γ in $B^\pm \to DK^\pm$ with $D \to K^0_S\pi^+\pi^-$ decays*, Nucl. Phys. **B888** (2014) 169, arXiv:1407.6211.

[126] LHCb collaboration, R. Aaij *et al.*, *Model-independent measurement of the CKM angle γ using $B^0 \to DK^{*0}$ decays with $D \to K^0_S\pi^+\pi^-$ and $K^0_S K^+K^-$*, JHEP **06** (2016) 131, arXiv:1604.01525.

[127] BaBar, B. Aubert *et al.*, *Measurement of γ in $B^{\mp} \to D^{(*)}K^{\mp}$ decays with a Dalitz analysis of $D \to K^0_S\pi^-\pi^+$*, Phys. Rev. Lett. **95** (2005) 121802, arXiv:hep-ex/0504039.

[128] CLEO, R. A. Briere *et al.*, *First model-independent determination of the relative strong phase between D^0 and $\bar{D}^0 \to K^0_S\pi^+\pi^-$ and its impact on the CKM Angle γ/ϕ_3 measurement*, Phys. Rev. **D80** (2009) 032002, arXiv:0903.1681.

[129] S. Harnew and J. Rademacker, *Charm mixing as input for model-independent determinations of the CKM phase γ*, Phys. Lett. **B728** (2014) 296, arXiv:1309.0134.

[130] A. Bondar and A. Poluektov, *The use of quantum-correlated D^0 decays for ϕ_3 measurement*, The European Physical Journal C **55** (2008) 51.

[131] R. Fleischer, *New strategies to obtain insights into CP violation through $B_s \to D_s^{\pm}K^{\mp}, D_s^{*\pm}K^{\mp}$ and $B_d \to D^{\pm}\pi^{\mp}, D^{*\pm}\pi^{\mp}$ decays*, Nucl. Phys. **B671** (2003) 459, arXiv:hep-ph/0304027.

[132] K. De Bruyn *et al.*, *Exploring $B_s \to D_s^{(*)\pm}K^{\mp}$ Decays in the Presence of a Sizable Width Difference $\Delta\Gamma_s$*, Nucl. Phys. **B868** (2013) 351, arXiv:1208.6463.

[133] R. Fleischer, *CP violation in the B system and relations to $K \to \pi\ \nu\bar{\nu}$ decays*, Phys. Rept. **370** (2002) 537, arXiv:hep-ph/0207108.

[134] R. Aleksan, I. Dunietz, and B. Kayser, *Determining the CP-violating phase γ*, Zeitschrift für Physik C Particles and Fields **54** (1992) 653.

[135] I. Dunietz and R. G. Sachs, *Asymmetry between inclusive charmed and anticharmed modes in B^0, $\bar{B}^0$ decay as a measure of CP violation*, Phys. Rev. D **37** (1988) 3186.

[136] LHCb collaboration, R. Aaij *et al.*, *Precision measurement of CP violation in $B^0_s \to J/\psi K^+K^-$ decays*, Phys. Rev. Lett. **114** (2015) 041801, arXiv:1411.3104.

[137] LHCb collaboration, R. Aaij *et al.*, *Measurement of the CP-violating phase ϕ_s in $\overline{B}^0_s \to J/\psi\pi^-\pi^-$ decays*, Phys. Lett. **B736** (2014) 186, arXiv:1405.4140.

[138] LHCb collaboration, R. Aaij *et al.*, *Measurement of the CP violating phase and decay-width difference in $B^0_s \to \psi(2S)\phi$ decays*, Phys. Lett. **B762** (2016) 253, arXiv:1608.04855.

[139] LHCb collaboration, R. Aaij *et al.*, *Measurement of the CP-violating phase ϕ_s in $\overline{B}^0_s \to D_s^+D_s^-$ decays*, Phys. Rev. Lett. **113** (2014) 211801, arXiv:1409.4619.

[140] LHCb collaboration, R. Aaij *et al.*, *Measurement of the flavour-specific CP-violating asymmetry $a^s_{\rm sl}$ in B^0_s decays*, Phys. Lett. **B728** (2014) 607, arXiv:1308.1048.

[141] LHCb collaboration, R. Aaij *et al.*, *Measurement of CP asymmetry in $B^0_s \to D_s^{\mp}K^{\pm}$ decays*, JHEP **03** (2018) 059, arXiv:1712.07428.

[142] LHCb collaboration, R. Aaij *et al.*, *Precision measurement of the B^0_s–$\overline{B}^0_s$ oscillation frequency in the decay $B^0_s \to D_s^-\pi^+$*, New J. Phys. **15** (2013) 053021, arXiv:1304.4741.

[143] LHCb collaboration, R. Aaij *et al.*, *Measurement of CP asymmetry in $B^0_s \to D_s^{\mp}K^{\pm}$ decays*, JHEP **11** (2014) 060, arXiv:1407.6127.

[144] FOCUS Collaboration, J. M. Link *et al.*, *Study of the $D^0 \to \pi^-\pi^+\pi^-\pi^+$ decay*, Phys. Rev. **D75** (2007) 052003, arXiv:hep-ex/0701001.

[145] S. Godfrey and N. Isgur, *Mesons in a Relativized Quark Model with Chromodynamics*, Phys. Rev. **D32** (1985) 189.

[146] L. Roca, E. Oset, and J. Singh, *Low lying axial-vector mesons as dynamically generated resonances*, Phys. Rev. **D72** (2005) 014002, arXiv:hep-ph/0503273.

[147] BGR Collaboration, G. P. Engel *et al.*, *QCD with two light dynamical chirally improved quarks: Mesons*, Phys. Rev. D **85** (2012) 034508.

[148] S. Durr *et al.*, *Ab-Initio Determination of Light Hadron Masses*, Science **322** (2008) 1224, arXiv:0906.3599.

[149] C. B. Lang, L. Leskovec, D. Mohler, and S. Prelovsek, *Axial resonances $a_1(1260)$, $b_1(1235)$ and their decays from the lattice*, JHEP **04** (2014) 162, arXiv:1401.2088.

[150] Particle Data Group, C. Patrignani *et al.*, *Review of Particle Physics*, Chin. Phys. **C40** (2016), no. 10 100001.

[151] Y. Grossman, A. L. Kagan, and Y. Nir, *New physics and CP violation in singly Cabibbo suppressed D decays*, Phys. Rev. **D75** (2007) 036008, arXiv:hep-ph/0609178.

[152] S. Bianco, F. L. Fabbri, D. Benson, and I. Bigi, *A Cicerone for the physics of charm*, Riv. Nuovo Cim. **26N7** (2003) 1, arXiv:hep-ex/0309021.

[153] LHCb collaboration, R. Aaij *et al.*, *Observation of CP violation in charm decays*, arXiv:1903.08726, Submitted to Phys. Rev. Lett.

[154] LHCb, R. Aaij *et al.*, *Model-independent search for CP violation in $D^0 \to K^-K^+\pi^-\pi^+$ and $D^0 \to \pi^-\pi^+\pi^+\pi^-$ decays*, Phys. Lett. **B726** (2013) 623, arXiv:1308.3189.

[155] G. Zech and B. Aslan, *New test for the multivariate two-sample problem based on the concept of minimum energy*, Journal of Statistical Computation and Simulation **75** (2003) 109.

[156] LHCb, R. Aaij *et al.*, *Search for CP violation in the phase space of $D^0 \to \pi^+\pi^-\pi^+\pi^-$ decays*, Phys. Lett. **B769** (2017) 345, arXiv:1612.03207.

[157] CLEO, R. A. Briere *et al.*, *CLEO-c and CESR-c: A New frontier of weak and strong interactions*, CLNS-01-1742.

[158] D. Andrews *et al.*, *The CLEO detector*, Nuclear Instruments and Methods in Physics Research **211** (1983) 47.

[159] CLEO Collaboration, Y. Kubota *et al.*, *The CLEO-II detector*, Nucl. Instrum. Meth. **A320** (1992) 66.

[160] T. S. Hill, *The CLEO-II silicon vertex detector*, Nucl. Instrum. Meth. **A418** (1998) 32.

[161] CLEO Collaboration, G. Viehhauser, *CLEO III operation*, Nucl. Instrum. Meth. **A462** (2001) 146.

[162] Y. Kubota *et al.*, *The CLEO II detector*, Nuclear Instruments and Methods in Physics Research Section A: Accelerators, Spectrometers, Detectors and Associated Equipment **320** (1992), no. 1 66 .

[163] D. Peterson *et al.*, *The CLEO III drift chamber*, Nucl. Instrum. Meth. **A478** (2002) 142.

[164] M. Artuso *et al.*, *Construction, pattern recognition and performance of the CLEO III LiF-TEA RICH detector* , Nuclear Instruments and Methods in Physics Research Section A **502** (2003), no. 1 91 , Proceedings of the Fourth International Workshop on Ring Imaging Cherenkov Detectors.

[165] M. Artuso, *The Ring Imaging detector for CLEO III*, Il Nuovo Cimento A **109** (1996) 1035.

[166] R. Poling, *CLEO-c hot topics*, eConf **C060409** (2006) 005, `arXiv:hep-ex/0606016`.

[167] F. Bloch, *Zur Bremsung rasch bewegter Teilchen beim Durchgang durch Materie*, Annalen der Physik **408** no. 3 285.

[168] H. Bethe, *Zur Theorie des Durchgangs schneller Korpuskularstrahlen durch Materie*, Annalen der Physik **397** no. 3 325.

[169] CLEO Collaboration, S. Dobbs *et al.*, *Measurement of absolute hadronic branching fractions of D mesons and $e^+e^- \to D\overline{D}$ cross sections at the $\psi(3770)$*, Phys. Rev. D **76** (2007) 112001.

[170] CLEO Collaboration, M. Artuso *et al.*, *Amplitude analysis of $D^0 \to K^+K^-\pi^+\pi^-$*, Phys. Rev. **D85** (2012) 122002, `arXiv:1201.5716`.

[171] ARGUS Collaboration, H. Albrecht *et al.*, *Search for hadronic $b \to u$ decays*, Phys. Lett. **B241** (1990) 278.

[172] D. J. Lange, *The EvtGen particle decay simulation package*, Nucl. Instrum. Meth. **A462** (2001) 152.

[173] GEANT4 Collaboration, S. Agostinelli *et al.*, *GEANT4: A simulation toolkit*, Nucl. Instrum. Meth. **A506** (2003) 250.

[174] GEANT4 Collaboration, J. Allison *et al.*, *Geant4 developments and applications*, IEEE Trans. Nucl. Sci. **53** (2006) 270.

[175] LHCb collaboration, R. Aaij *et al.*, *Angular analysis of the $B^0 \to K^{*0}\mu^+\mu^-$ decay using $3\,fb^{-1}$ of integrated luminosity*, JHEP **02** (2016) 104, `arXiv:1512.04442`.

[176] MARK-III Collaboration, D. Coffman *et al.*, *Resonant substructure in $\overline{K}\pi\pi\pi$ decays of D mesons*, Phys. Rev. **D45** (1992) 2196.

[177] D. M. Penfold, *Monte carlo methods*, The Mathematical Gazette **51** (1967), no. 378 361.

[178] S. Weinzierl, *Introduction to Monte Carlo methods*, `arXiv:hep-ph/0006269`.

[179] K. Binder and D. Heermann, *The Monte Carlo Method in Statistical Physics*, 01, 1988. doi: 10.1007/978-3-642-51703-7.

[180] B. Guegan, J. Hardin, J. Stevens, and M. Williams, *Model selection for amplitude analysis*, JINST **10** (2015), no. 09 P09002, `arXiv:1505.05133`.

[181] F. E. Harrell, Jr. *Regression Modeling Strategies*, Springer-Verlag, Berlin, Heidelberg, 2006.

[182] R. Tibshirani, *Regression shrinkage and selection via the Lasso*, Journal of the Royal Statistical Society, Series B **58** (1994) 267.

[183] G. Schwarz, *Estimating the dimension of a model*, Ann. Statist. **6** (1978) 461.

[184] LHCb collaboration, R. Aaij *et al.*, *Search for CP violation through an amplitude analysis of $D^0 \to K^+K^-\pi^+\pi^-$ decays*, JHEP **02** (2019) 126, arXiv:1811.08304.

[185] BaBar Collaboration, B. Aubert *et al.*, *Measurements of CP-Violating Asymmetries in $B^0 \to a_1^{\pm}(1260)\pi^{\mp}$ decays*, Phys. Rev. Lett. **98** (2007) 181803, arXiv:hep-ex/0612050.

[186] Belle Collaboration, J. Dalseno *et al.*, *Measurement of Branching Fraction and First Evidence of CP Violation in $B^0 \to a_1^{\pm}(1260)\pi^{\mp}$ Decays*, Phys. Rev. **D86** (2012) 092012, arXiv:1205.5957.

[187] C. A. Baker *et al.*, *Evidence for a $J^{PC} = 1^{++}$ I=1 meson at 1640 MeV*, Physics Letters B **449** (1999), no. 1-2 114 .

[188] E852 Collaboration, S. U. Chung *et al.*, *Exotic and $q\overline{q}$ resonances in the $\pi^+\pi^-\pi^-$ system produced in π^-p collisions at 18 GeV/c*, Phys. Rev. D **65** (2002) 072001.

[189] A. Le Yaouanc, L. Oliver, O. Pène, and J.-C. Raynal, *"Naive" Quark-Pair-Creation Model of Strong-Interaction Vertices*, Phys. Rev. D **8** (1973) 2223.

[190] T. Barnes, F. E. Close, P. R. Page, and E. S. Swanson, *Higher quarkonia*, Phys. Rev. D **55** (1997) 4157.

[191] LHCb collaboration, R. Aaij *et al.*, *Studies of the resonance structure in $D^0 \to K^{\mp}\pi^{\pm}\pi^{\pm}\pi^{\mp}$ decays*, Eur. Phys. J. **C78** (2018), no. 6 443, arXiv:1712.08609.

[192] H.-Y. Cheng, C.-K. Chua, and A. Soni, *Final state interactions in hadronic B decays*, Phys. Rev. **D71** (2005) 014030, arXiv:hep-ph/0409317.

[193] P. Colangelo, F. De Fazio, and T. N. Pham, *The Riddle of polarization in $B \to VV$ transitions*, Phys. Lett. **B597** (2004) 291, arXiv:hep-ph/0406162.

[194] COMPASS Collaboration, M. Alekseev *et al.*, *Observation of a $J^{PC} = 1^{-+}$ exotic resonance in diffractive dissociation of 190-GeV/c π^- into π^- π^- π^+*, Phys. Rev. Lett. **104** (2010) 241803, arXiv:0910.5842.

[195] S. S. Wilks, *The large-sample distribution of the likelihood ratio for testing composite hypotheses*, Ann. Math. Statist. **9** (1938) 60.

[196] ALEPH Collaboration, S. Schael *et al.*, *Branching ratios and spectral functions of τ decays: Final ALEPH measurements and physics implications*, Phys. Rept. **421** (2005) 191, arXiv:hep-ex/0506072.

[197] ARGUS Collaboration, H. Albrecht *et al.*, *Analysis of the decay $\tau^- \to \pi^-\pi^-\pi^+\nu_\tau$ and determination of the $a_1(1260)$ resonance parameters*, Zeitschrift für Physik C Particles and Fields **58** (1993), no. 1 61.

[198] OPAL Collaboration, R. Akers *et al.*, *Measurement of the hadronic decay current in $\tau^- \to \pi^-\pi^-\pi^+\nu_\tau$*, Z. Phys. **C67** (1995) 45.

[199] E791, E. M. Aitala *et al.*, *Model independent measurement of S-wave $K^-\pi^+$ systems using $D^+ \to K\pi\pi$ decays from Fermilab E791*, Phys. Rev. **D73** (2006) 032004, arXiv:hep-ex/0507099, [Erratum: Phys. Rev.D74,059901(2006)].

[200] LHCb, R. Aaij *et al.*, *Observation of the resonant character of the $Z(4430)^-$ state*, Phys. Rev. Lett. **112** (2014), no. 22 222002, arXiv:1404.1903.

[201] G. Micula and S. Micula, in *Handbook of Splines*, pp. 79–102, 01, 1999. doi: 10.1007/978-94-011-5338-6_2.

[202] CLEO Collaboration, G. Bonvicini *et al.*, *Updated measurements of absolute D^+ and D^0 hadronic branching fractions and $\sigma(e^+e^- \to D\overline{D})$ at $E_{\rm cm}$ = 3774 MeV*, Phys. Rev. **D89** (2014), no. 7 072002, arXiv:1312.6775, [Erratum: Phys. Rev.D91,no.1,019903(2015)].

[203] CLEO collaboration, *Determination of Tracking Efficiencies*, CBX 06-29B.

[204] CLEO collaboration, *Pion and Kaon Identification Efficiencies for CLEO-c*, CBX 05-43.

[205] LHCb collaboration, R. Aaij *et al.*, *Measurement of the CKM angle γ using $B^\pm \to DK^\pm$ with $D \to K^0_S\pi^+\pi^-$, $K^0_SK^+K^-$ decays*, JHEP **08** (2018) 176.

[206] LHCb collaboration, R. Aaij *et al.*, *Physics case for an LHCb Upgrade II - Opportunities in flavour physics, and beyond, in the HL-LHC era*, arXiv:1808.08865.

[207] LHCb collaboration, R. Aaij *et al.*, *First observation of the decays $\overline{B}^0_{(s)} \to D_s^+K^-\pi^+\pi^-$ and $\overline{B}^0_s \to D_{s1}(2536)^+\pi^-$*, Phys. Rev. **D86** (2012) 112005, arXiv:1211.1541.

[208] L. Evans and P. Bryant, *LHC Machine*, Journal of Instrumentation **3** (2008), no. 08 S08001.

[209] LHCb collaboration, A. A. Alves Jr. *et al.*, *The LHCb detector at the LHC*, JINST **3** (2008) S08005.

[210] LHCb collaboration, *LHCb magnet: Technical Design Report*, CERN-LHCC-2000-007.

[211] LHCb collaboration, *LHCb VELO (VErtex LOcator): Technical Design Report*, CERN-LHCC-2001-011.

[212] R. Aaij *et al.*, *Performance of the LHCb Vertex Locator*, JINST **9** (2014) P09007, arXiv:1405.7808.

[213] R. Aaij *et al.*, *Performance of the LHCb trigger and full real-time reconstruction in Run 2 of the LHC*, arXiv:1812.10790.

[214] LHCb collaboration, *LHCb inner tracker: Technical Design Report*, CERN-LHCC-2002-029.

[215] LHCb collaboration, *LHCb outer tracker: Technical Design Report*, CERN-LHCC-2001-024.

[216] R. Arink *et al.*, *Performance of the LHCb Outer Tracker*, JINST **9** (2014) P01002, arXiv:1311.3893.

[217] LHCb collaboration, *LHCb RICH: Technical Design Report*, CERN-LHCC-2000-037.

[218] M. Adinolfi *et al.*, *Performance of the LHCb RICH detector at the LHC*, Eur. Phys. J. **C73** (2013) 2431, arXiv:1211.6759.

[219] LHCb collaboration, *LHCb calorimeters: Technical Design Report*, CERN-LHCC-2000-036.

[220] R. Aaij *et al.*, *Performance of the LHCb calorimeters*, LHCb-DP-2013-004, in preparation.

[221] LHCb collaboration, *LHCb muon system: Technical Design Report*, CERN-LHCC-2001-010.

[222] A. A. Alves Jr. *et al.*, *Performance of the LHCb muon system*, JINST **8** (2013) P02022, arXiv:1211.1346.

[223] LHCb collaboration, R. Aaij *et al.*, *LHCb detector performance*, Int. J. Mod. Phys. **A30** (2015) 1530022, arXiv:1412.6352.

[224] R. Aaij *et al.*, *Selection and processing of calibration samples to measure the particle identification performance of the LHCb experiment in Run 2*, arXiv:1803.00824.

[225] LHCb collaboration, *LHCb trigger system: Technical Design Report*, CERN-LHCC-2003-031.

[226] LHCb collaboration, *LHCb Trigger and Online Technical Design Report*, CERN-LHCC-2014-016.

[227] R. Aaij *et al.*, *The LHCb trigger and its performance in 2011*, JINST **8** (2013) P04022, arXiv:1211.3055.

[228] A. Puig, *The LHCb trigger in 2011 and 2012*, LHCb-PUB-2014-046.

[229] I. Belyaev *et al.*, *Handling of the generation of primary events in* Gauss*, the LHCb simulation framework*, Nuclear Science Symposium Conference Record (NSS/MIC) **IEEE** (2010) 1155.

[230] T. Sjöstrand, S. Mrenna, and P. Skands, *PYTHIA 6.4 physics and manual*, JHEP **05** (2006) 026, arXiv:hep-ph/0603175.

[231] T. Sjöstrand, S. Mrenna, and P. Skands, *A brief introduction to PYTHIA 8.1*, Comput. Phys. Commun. **178** (2008) 852, arXiv:0710.3820.

[232] LHCb collaboration, *The Moore project*, http://lhcb-release-area.web.cern.ch/LHCb-release-area/DOC/moore/.

[233] LHCb collaboration, *The Boole project*, http://lhcb-release-area.web.cern.ch/LHCb-release-area/DOC/boole/.

[234] W. D. Hulsbergen, *Decay chain fitting with a Kalman filter*, Nuclear Instruments and Methods in Physics Research A **552** (2005) 566, arXiv:physics/0503191.

[235] S. Tolk, J. Albrecht, F. Dettori, and A. Pellegrino, *Data driven trigger efficiency determination at LHCb*, Tech. Rep. LHCb-PUB-2014-039, CERN, Geneva, May, 2014.

[236] R. Aaij *et al.*, *The LHCb trigger and its performance*, arXiv:1211.3055.

[237] LHCb HLT project, J. Albrecht, V. V. Gligorov, G. Raven, and S. Tolk, *Performance of the LHCb High Level Trigger in 2012*, J. Phys. Conf. Ser. **513** (2014) 012001, arXiv:1310.8544.

[238] V. V. Gligorov and M. Williams, *Efficient, reliable and fast high-level triggering using a bonsai boosted decision tree*, JINST **8** (2013) P02013, arXiv:1210.6861.

[239] L. Breiman, J. H. Friedman, R. A. Olshen, and C. J. Stone, *Classification and regression trees*, Wadsworth international group, Belmont, California, USA, 1984.

[240] B. P. Roe *et al.*, *Boosted decision trees as an alternative to artificial neural networks for particle identification*, Nucl. Instrum. Meth. **A543** (2005) 577, arXiv:physics/0408124.

[241] M. Pivk and F. R. Le Diberder, *Plots: A statistical tool to unfold data distributions*, Nuclear Instruments and Methods in Physics Research A **555** (2005) 356, physics/04.

[242] N. L. Johnson, *Systems of frequency curves generated by methods of translation*, Biometrika **36** (1949), no. 1/2 149.

[243] Y. Xie, *sFit: a method for background subtraction in maximum likelihood fit*, ArXiv e-prints (2009) arXiv:0905.0724.

[244] LHCb collaboration, R. Aaij *et al.*, *Measurements of the B^+, B^0, B_s^0 meson and Λ_b^0 baryon lifetimes*, JHEP **04** (2014) 114, arXiv:1402.2554.

[245] *Geometric Modeling with Splines: An Introduction*, A. K. Peters, Ltd., Natick, MA, USA, 2001.

[246] P. L. Butzer, M. Schmidt, and E. L. Stark, *Observations on the history of central b-splines*, Archive for History of Exact Sciences **39** (1988), no. 2 137.

[247] T. M. Karbach, G. Raven, and M. Schiller, *Decay time integrals in neutral meson mixing and their efficient evaluation*, arXiv:1407.0748.

[248] LHCb collaboration, R. Aaij *et al.*, *Opposite-side flavour tagging of B mesons at the LHCb experiment*, Eur. Phys. J. **C72** (2012) 2022, arXiv:1202.4979.

[249] LHCb collaboration, R. Aaij *et al.*, *B flavour tagging using charm decays at the LHCb experiment*, JINST **10** (2015) P10005, arXiv:1507.07892.

[250] LHCb collaboration, R. Aaij *et al.*, *A new algorithm for identifying the flavour of B_s^0 mesons at LHCb*, JINST **11** (2016) P05010, arXiv:1602.07252.

[251] LHCb collaboration, R. Aaij *et al.*, *First measurement of the CP-violating phase in $B_s^0 \to \phi\phi$ decays*, Phys. Rev. Lett. **110** (2013) 241802, arXiv:1303.7125.

[252] LHCb collaboration, R. Aaij *et al.*, *Measurement of CP violation in $B \to D^+D^-$ decays*, Phys. Rev. Lett. **117** (2016) 261801, arXiv:1608.06620.

[253] E. Norrbin and R. Vogt, *Bottom production asymmetries at the LHC*, in *Fifth Workshop on electronics for LHC experiments, Snowmass, CO, USA, 20-24 Sep 1999: Proceedings*, 2000. arXiv:hep-ph/0003056.

[254] E. Norrbin and T. Sjostrand, *Production and hadronization of heavy quarks*, Eur. Phys. J. **C17** (2000) 137, arXiv:hep-ph/0005110.

[255] LHCb collaboration, R. Aaij *et al.*, *Measurement of B^0, B_s^0, B^+ and Λ_b^0 production asymmetries in 7 and 8 TeV pp collisions*, Phys. Lett. **B774** (2017) 139, arXiv:1703.08464.

[256] LHCb collaboration, R. Aaij *et al.*, *Measurement of the D_s^+–D_s^- production asymmetry in 7 TeV pp collisions*, Phys. Lett. **B713** (2012) 186, arXiv:1205.0897.

[257] LHCb collaboration, R. Aaij *et al.*, *Measurement of CP asymmetry in $D^0 \to K^-K^+$ and $D^0 \to \pi^-\pi^+$ decays*, JHEP **07** (2014) 041, arXiv:1405.2797.

[258] LHCb collaboration, R. Aaij *et al.*, *Measurement of the CP asymmetry in B_s^0–$\overline{B}_s^0$ mixing*, Phys. Rev. Lett. **117** (2016) 061803, arXiv:1605.09768.

[259] A. Davis *et al.*, *Measurement of the instrumental asymmetry for $K^-\pi^+$-pairs at LHCb in Run 2*, Tech. Rep. LHCb-PUB-2018-004, CERN, Geneva, Mar, 2018.

[260] G. Punzi, *Comments on likelihood fits with variable resolution*, eConf **C030908** (2003) WELT002.

[261] LHCb collaboration, R. Aaij *et al.*, *Studies of the resonance structure in $D^0 \to K^0_S K^\pm \pi^\mp$ decays*, Phys. Rev. **D93** (2016) 052018, arXiv:1509.06628.

[262] M. Karbach and M. Kenzie, *GammaCombo package*, 2014.

[263] LHCb collaboration, R. Aaij *et al.*, *Measurement of the CKM angle γ from a combination of LHCb results*, JHEP **12** (2016) 087, arXiv:1611.03076.

[264] FOCUS Collaboration, J. M. Link *et al.*, *Study of the $D^0 \to K^+K^-\pi^+\pi^-$ decay*, Phys. Lett. **B610** (2005) 225, arXiv:hep-ex/0411031.

[265] FOCUS Collaboration, J. M. Link *et al.*, *Study of the decay mode $D^0 \to K^-K^-K^+\pi^+$*, Phys. Lett. **B575** (2003) 190, arXiv:hep-ex/0308054.

[266] COMPASS, M. Mikhasenko, A. Jackura, B. Ketzer, and A. Szczepaniak, *Unitarity approach to the mass-dependent fit of 3π resonance production data from the COMPASS experiment*, EPJ Web Conf. **137** (2017) 05017.

[267] S. U. Chung *et al.*, *Partial wave analysis in K matrix formalism*, Annalen Phys. **4** (1995) 404.

[268] JPAC, M. Mikhasenko *et al.*, *What is the right formalism to search for resonances?*, Eur. Phys. J. **C78** (2018), no. 3 229, arXiv:1712.02815.

[269] M. Mikhasenko and B. Ketzer, *Beyond the isobar model: Rescattering in the system of three particles.*, PoS **BORMIO2016** (2016) 024.

[270] X. Zhang and J.-J. Xie, *The three-pion decays of the $a_1(1260)$*, Commun. Theor. Phys. **70** (2018), no. 1 060, arXiv:1712.05572.

[271] I. Bediaga and P. C. Magalhães, *Final state interaction on $B^+ \to \pi^-\pi^+\pi^+$*, arXiv:1512.09284.

[272] M. Mikhasenko, *A triangle singularity and the LHCb pentaquarks*, arXiv:1507.06552.

[273] S. X. Nakamura and K. Tsushima, *$Z_c(4430)$ and $Z_c(4200)$ as triangle singularities*, arXiv:1901.07385.

[274] BaBar, B. Aubert *et al.*, *Time-dependent Dalitz plot analysis of $B^0 \to D^\mp K^0 \pi^\pm$ decays*, Phys. Rev. **D77** (2008) 071102, arXiv:0712.3469.

[275] J. Dalseno, *Resolving the ϕ_2 (α) ambiguity in $B \to \rho\rho$*, JHEP **11** (2018) 193, arXiv:1808.09391.

[276] LHCb collaboration, R. Aaij *et al.*, *Measurement of the mass difference between neutral charm-meson eigenstates*, Submitted to: Phys. Rev. Lett. (2019) arXiv:1903.03074.

[277] CLEO, D. M. Asner *et al.*, *Search for $D^0 - \bar{D}^0$ mixing in the Dalitz plot analysis of $D^0 \to K^0_S \pi^+\pi^-$*, Phys. Rev. **D72** (2005) 012001, arXiv:hep-ex/0503045.

[278] LHCb collaboration, R. Aaij *et al.*, *Model-independent measurement of mixing parameters in $D^0 \to K^0_S \pi^+\pi^-$ decays*, JHEP **04** (2016) 033, arXiv:1510.01664.

[279] A. Di Canto *et al.*, *Novel method for measuring charm-mixing parameters using multibody decays*, Phys. Rev. **D99** (2019), no. 1 012007, arXiv:1811.01032.

[280] D. V. Bugg, *The mass of the σ pole*, Journal of Physics G Nuclear Physics **34** (2007) 151, arXiv:hep-ph/0608081.

[281] D. Aston *et al.*, *A Study of $K^-\pi^+$ Scattering in the Reaction $K^-p \to K^-\pi^+n$ at $11GeV/c$*, Nucl. Phys. **B296** (1988) 493.

[282] BaBar, B. Aubert *et al.*, *Dalitz-plot analysis of the decays $B^\pm \to K^\pm\pi^\mp\pi^\pm$*, Phys. Rev. **D72** (2005) 072003, arXiv:hep-ex/0507004, [Erratum: Phys. Rev.D74,099903(2006)].

[283] CMD-2, R. R. Akhmetshin *et al.*, *Measurement of $e^+e^- \to \pi^+\pi^-$ cross-section with CMD-2 around rho meson*, Phys. Lett. **B527** (2002) 161, arXiv:hep-ex/0112031.

[284] LHCb collaboration, R. Aaij *et al.*, *Analysis of the resonant components in $\overline{B}{}^0_s \to J/\psi\pi^+\pi^-$*, Phys. Rev. **D86** (2012) 052006, arXiv:1204.5643.

[285] A. Hoecker *et al.*, *TMVA: Toolkit for Multivariate Data Analysis*, PoS **ACAT** (2007) 040, arXiv:physics/0703039.

Acknowledgements

There are many people who made this thesis possible and I am deeply grateful for that. At the risk of forgetting some of you, I would like to use the opportunity to thank some persons explicitly.

First, I would like to thank Prof. Ulrich Uwer for supervising my Bachelor, Master and finally my PhD thesis. I appreciate the support throughout all the years and that you gave me the freedom to follow my research interests, even to work on a completely different experiment for the first part of my PhD. I am grateful that I could spend a lot of time at CERN, summer schools and conferences all around the world (credit goes also to the HGSFP and RTG). Moreover, I would like to thank the second referee of this thesis, Prof. Tilman Plehn, as well as Prof. Klaus Reygers and Prof. Ulrich Glasmacher who complete the examination committee.

I am grateful to all members of the Heidelberg LHCb group for a great working atmosphere. Especially, I would like to thank my friends and colleagues David Gerick, Dominik Mitzel and Matthieu Kecke with whom I started studying almost 10 years ago. It has been a great time! Evelina Gersabeck, thanks a lot for your continued support and guidance throughout all the years we worked together. I am indebted to Dominik Mitzel, Evelina Gersabeck and Nicole Skidmore for proofreading my thesis draft and giving me valuable feedback. I am also grateful for the technical support from Alexey Zhelezov and organizational support from Diana Horneck and Claudia Wallenwein. Moreover, I thank all members of the PI football squad, also known as the golden generation (two times HGSFP cup champions).

I would like to thank all members of the LHCb collaboration. In particular, I would like to thank Prof. Jonas Rademacker and Dr. Jeremy Dalseno. You first introduced me to the research field and this thesis would not have been possible without you. It was a pleasure to work with you and I felt like a honorary member of the Bristol LHCb group. Furthermore, I would like to thank Niels Tuning for being such a friendly and helpful person, even if I had to call you in the middle of the night. Lucia Grillo, thanks for all your help with the drift-time alignment.

I would like to express my gratitude to my friends from Mosbach: Patrick, Peter, Frieder, Lukas and Johannes. It is always fun to see you and I cannot thank you enough for keeping in touch, even though I did not manage to be around too often. I would also like to thank my high school teacher Jörg Leiprecht for sparking my interest in physics.

Most of all, I would like to thank my family, especially my parents Bettina and Rainer, my step-parents Angelika and Andreas and my brother Dominique, for always having my back. You supported every decision I ever made and I could always count on you. Thanks a lot!